Università degli Studi di Milano
Facoltà di scienze matematiche fisiche e naturali

Corso di Dottorato in Fisica, Astrofisica e Fisica Applicata
Ciclo XXVI

Interfacial properties of ionic liquids: electric properties of thin films and interaction with model membranes and living cells

Settore Scientifico Disciplinare FIS/03

Supervisore: Dr. Alessandro PODESTA'

Coordinatore: Prof. Marco BERSANELLI

Tesi di Dottorato di:
Massimiliano Galluzzi

Anno Accademico 2013/2014

Commission of the final examination:

External Referee:
Prof. Andrew Nelson

External Member:
Dr. Giorgio Ferrari

Internal Member:
Dr. Alessandro Podesta'

Final examination:

Date 24 Gennaio 2013

Università degli Studi di Milano, Dipartimento di Fisica, Milano, Italy

To my family

MIUR subjects:
FIS/03 -

PACS:
68.37.-d, 68.37.Ps, 68.08.-p, 68.55.-a 87.15.-v

Contents

Abstract

Room-Temperature Ionic Liquids (ILs) have attracted considerable interest in recent years. This interest is motivated by the physico-chemical properties of these systems, tunable modifying the chemical structure of ions. Generally, ILs show chemical and thermal stability, i.e. they do not easily decompose or react. Furthermore, these compounds remain liquid over an extended range of temperatures, in which they show also a remarkably low volatility. The low vapor pressure of ILs, promote them as good solvents for the growing field of the "Green Chemistry", in substitution of the volatile organic compounds. The fact that ILs are composed solely by ions, and can have a quite wide electrochemical window, make them very interesting as electrolytes. For these purposes, this PhD thesis is devoted to the investigation of ILs in contact with solid interfaces, primary targets of interaction. To deepen the analysis of electric properties at the solid interface, thin layers of ILs deposited on conductive substrates were investigated by means of AFM. The "Green" character of these compounds was investigated studying their interaction with biomembrane models and external membranes of living cells, by means of AFM and electrochemical methods.

Because of their ionic nature, ILs can be used as electrolytes in several devices aimed at conversion and storage of energy, such as electrochemical supercapacitors, Graetzel solar cells and batteries. In these devices a key role is played by the interface between the surface of the electrodes and the electrolyte; in particular, structural-morphological and electrical properties of the first few nanometers of IL interacting with the solid electrode surface are expected to have the strongest impact on device performance. AFM morphological analysis of small quantity of [C_4MIM] [NTf_2] IL, deposited on various insulating surfaces revealed a population of nanodroplets and new structures. Remarkably, the solid surfaces induce the organization of the ionic liquid into regular, lamellar solid-like nanostructures presenting a high degree of vertical structural order and high mechanical resistance to normal compressive stresses. Nanomechanical investigation reveals that the structures resist to normal compressive loads up to 1.5 MPa; beyond that limit, indentation, in discrete steps, occurs. Furthermore, lamellar [C_4MIM] [NTf_2] islands are not affected when scanned by a biased AFM tip under the influence of an electric field as intense as 10^8 V/m, while the liquid nano-and micro-droplets are easily swept away. These results confirm the solid-like character of the ordered lamellar nanostructures observed when thin films of [C_4MIM] [NTf_2] are deposited on solid surfaces, and suggest that these films may possess an insulating, dielectric behavior, at odd with the case of the bulk ionic liquids. Nanoscale impedance measurements (capacitance vs. distance) and electrostatic force spectroscopy (electric force vs. distance) between a conductive AFM tip and the IL structures confirmed that values of the dielectric constant (ε_r = 3-5) are significantly smaller than those measured in the bulk liquid (ε_r = 9-15). These results support the picture of solid-like ordered domains where the ion mobility is significantly inhibited with respect to the bulk liquid phase. These findings also highlight the potentialities of scanning probe techniques for the quantitative investigation of the interfacial

electrical properties of thin ionic liquid films, suggesting that ILs at electrified solid surfaces may possess unexpected electrical and structural properties, thus influencing the behavior of photo-electrochemical devices.

The "green" character of ionic liquids (ILs) is dependent on their negligible vapor pressure but in contrast to their environmental behavior their intrinsic toxicity is not at present completely understood. Accordingly, although ILs will not evaporate which alleviates air pollution problems, a potential hazard of Ils to living organisms via aqueous media cannot be ruled out. A rigorous investigation on the interaction of ILs with biomaterials is required to provide information about their intrinsic toxicity. In order to test the biocompatible character of ILs, as a first objective, the interaction of various ILs with biological membrane (biomembrane) models was studied using electrochemical methods. A series of imidazolium based ILs were investigated whose interactions highlighted the role of anion and lateral side chain of cation during the interaction with dioleoyl phosphatidylcholine (DOPC) monolayer. It was shown that the hydrophobic and lipophilic character of the IL cations is a primary factor responsible for this interaction. The modifications of the Hg supported monolayer caused by ILs were simultaneously monitored electrochemically in a well controlled manner using rapid cyclic voltammetry (RCV), alternating current voltammetry (ACV), and electrochemical impedance spectroscopy (EIS). Hg supported monolayers provide an accurate analysis of the behavior of ILs at the interface of a biomembrane leading to a comprehensive understanding of the interaction mechanisms involved. At the same time, these experiments show that the Hg-phospholipid model is an effective toxicity sensing technique as shown by the correlation between literature in vivo toxicity data and the data from this study. Cell membrane is the main target of ILs interaction, depending on the lipophilicity of hydrophobic lateral chain of cation. In order to test the biocompatible character of ILs, the interaction of various imidazolium-based ILs with supported DOPC phospholipid bilayers (as models of the cell membrane) and living MDA-MB-231 cells (@37 °C) was investigated. Atomic Force Microscopy (AFM) was used to carry on a combined topographic and mechanical analysis of supported DOPC bilayers as well as of living cells. During the analysis of DOPC bilayers we have observed modifications in breakthrough force and membrane elasticity related to the ingress of lateral chains of cations in the bilayer, demonstrating agreement with electrochemical results. The parallel nanomechanical analysis performed on living cells interacting with ILs at various concentrations showed modifications of elasticity (effective Young's modulus) and morphology of cells after exposure to ILs dispersed in their culture medium. The measurements confirmed the primary action of ILs on membrane and actin cytoskeleton, highlighting a subtoxic/toxic effect dependent on ILs concentration and chemical nature of cation. Our results may be helpful for filling existing gaps of knowledge about ionic liquids toxicity and their impact on living organisms. From these evidences, interaction of ILs with micro-organisms and single cells is an important step to assess the environmental sustainability of this novel and promising class of solvents and to attribute a "green" label to it.

Studying the interaction of ionic liquids, it has been recognized that the interface is a vital component. When the bulk symmetry of IL is broken by surfaces, the electrical properties are greatly affected, leading from a ion conductor to an insulator behavior. Also the interaction with biological entity is driven, in first instance, by surface interaction. Biomembrane models and cell membranes are affected by ILs that accumulate/penetrate the surface interface, leading to structural reorganization/damage of external membrane.

CHAPTER 1

Introduction

In this chapter I will introduce the compounds called room-temperature ionic liquids (shortly ionic liquids) and their applications. I will begin with a background about bulk properties, underlining their interactions with electric fields. Then I will introduce the properties of interface of ionic liquids and solid surfaces, focusing in particular on the electrical properties of thin layers supported on solid surface. In the end I will introduce the problem of biocompatibility and sustainability of ionic liquids.

1.1 Ionic liquids: background and bulk properties

In recent years, the scientific community focused the attention on the field of ionic liquids (acronym: ILs). ILs are salts with a low melting point, liquid at room temperature. Fluids consisting solely of ions such as plasmas or molten salts, possess several properties that are absent in liquids whose molecules are neutral. A limiting factor is that the traditional salts melt at temperatures of the order of 800-1000 K, which considerably restricts the field of applications. In the 1914 were developed the first salts with melting temperatures near to the ambient temperature [1]. However, the production of second generation ILs starts at the end of the '80. Compared to the first compounds synthesized, the liquids of the second generation resist to air and water without irreversible decomposition, thus ensuring a wide range of applicability. The lowering of the transition temperature from solid to liquid phase is due to the structure of the ions, which are not individual charged atoms, but complex and extended molecules. It has been demonstrated that one of the key points is to use large negative ions (anions) and asymmetrical positive ions (cations) with a delocalized charge: in this way an effective packing of the molecules is difficult due to the reduction of Coulomb binding energy which depresses the melting point.

However the remaining of the coulomb interaction, more than in conventional solvents, allows ILs to exhibit a very low vapor pressure at the limit of measurability (of the order of 1 Pa), which avoids the dispersion of dangerous vapors in the environment. For this reason, they are exceptional candidates for clean chemistry applications (green chemistry) [2; 3]. Unlike liquids and conventional solvents it is possible to engineer ad-hoc the chemical structure of anions and cations. In this way it is possible to create new ILs with chemical-physical properties adequate to meet the necessary requirements in the various fields of applicability. Some chemical-physical properties are tunable, for example: density, viscosity, melting point, chemical reactivity, thermal and ionic conductivity and electrochemical window [4]. Unfortunately, it is not easy to know a priori these properties, in fact the difficulty is in finding general rules telling scientists how a modification of an ion will influence the behavior of the IL. First of all, ions cannot be considered as isolated, because not only the coulombic interaction is present, but also Van Der Waals and hydrogen bonding must be considered. Van Der Waals forces

becomes relevant increasing the length of the alkyl chain of the cation [2]. Also the hydrogen bonding ability is important for ILs: usually the cation is an hydrogen bonding donor, while the anion can be hydrogen bonding acceptor.

In some processes and chemical reactions, ILs are advantageous compared to traditional solvents because recyclable many times and employable to obtain specific organic synthesis reactions [5], biphasic extraction of metal ions and aggregates [6], synthesis of metallic nanoparticles [7–9] and metal electrodeposition[10; 11]. A very interesting characteristics is also the ability of some ILs to dissolve complex sugars, like cellulose in $[C_4MIM][Cl]$ [12]. The peculiar structure of ILs offers the possibility to develop many processes impossible in conventional media and in particular in volatile organic compounds; nevertheless a big effort has still to be devoted to the study of their bulk properties in order to find general rules that allow scientists to specifically choice or design an IL that fits their purposes.

In the prospect of the use of ILs as solvents, in analogy with molecular solvents, it is important to know how these compounds mix (or solubilise) polar and apolar materials. An intuitive reasoning will drive to the idea that, because composed by ions, ILs will dissolve polar species. Actually the internal structure of an IL is quite complex. The complexity of a bulk of ILs is well shown in studies performed by Lopes et al.[13] and Triolo et al.[14; 15], showing how a pure IL has to be considered nanostructured, due to the formation of networks composed by the polar parts of the ions and segregated apolar parts. The nanostructured nature of ILs can be an explanation of their ability to dissolve both polar and apolar materials: polar molecules will be solvated in the polar domains while the apolar will be solvated into apolar domains.

1.1.1 Electrical properties

ILs subjected to electric fields behave similar to a standard electrolyte solutions but with some advantages. Being solvent free, while achieving maximum concentrations, they avoid the risk of salt precipitation. Having a high viscosity, ILs can be used in all applications with a reduced fluidity of active material (although they are not recommended where it is needed very high conductivity). Also the dielectric properties are important, in fact, the static dielectric constant is used as a quantitative index of the polarity for universal solvent. In the case of ILs the conductivity is an obstacle to the measurement of static dielectric constant which diverges for low frequencies. With high-frequency spectroscopy in the microwave range, it is possible to measure the dielectric constant and perform a posteriori extrapolation to obtain the static dielectric constant at zero frequency [16; 17]. As regards the electrical bulk properties of ILs, numerous works have been published primarily on study of conductivity and dielectric properties [16–22]. One of the criteria for choosing the fluid to be used in electrochemistry is electrochemical stability. This property is expressed by the voltage range within which the solvent is electrochemically inert. The 'window' of electrical potentials depends generally by reductive and oxidative stability of the solvent. The water has a potential oxidation of about 1.2 V, so electrolytes in aqueous base have electrochemical windows restricted to this range [23]. Salts dissolved in organic electrolytes possess electrochemical larger windows in order of 2.5 V, for example Et_4NBF_4, dissolved in acetonitrile (ACN), has an electrochemical window of 2.4 V (see Table 1.1). In the case of ILs this window depends on the resistance to the reduction potential of the cation and the oxidation resistance of the anion [24]. One of the most common techniques to establish the potential window is to measure the DC voltage between two electrodes. The oxidative and reductive voltage limits are assigned when the current in output reaches a certain threshold (typically 0.1 mA/cm^2).

These values can be subject to slight changes due to the type of material used for the electrodes, which affect the chemical reactions at the interface. The electrochemical window can also suffer strong variations when contaminants are present in IL, for example, contamination of water of 3% halve the window of electrochemical stability of the pure liquid [4]. The stability and the amplitude of the electrochemical window are quality important that may encourage the use of ILs in applications. Table 1.1 shows the limits of the potential at both electrodes and the electrochemical window [4].

Electrolyte	Cathodic lim(V)	Anodic lim(V)	Echem window(V)
1 mol dm^{-3} H_2SO_4/H_2O	-0.4	0.8	1.2
$[C_4MIM][Tf_2N]$	-2	2.6	4.6
$[C_4MIM][BF_4]$	-1.6	4.5	6.1
$[C_4MIM][PF_6]$	-1.1	2.1	3.2

Table 1.1: Potential of electrochemical reactions for some electrolytes present in literature [4].

Conductivity of ionic liquids

The conductivity of an electrolyte is a property describing the availability of charge carriers and their mobility. In principle, it is expected that ILs have very high conductivity because they are composed entirely of ions. Unfortunately it is not so, in fact the conductivity at room temperature, σ_{DC}, which can sweep a large range of values $0.1 - 18$ mS/cm [4], has a lower value than conventional aqueous solutions of electrolyte. For example, the specific conductivity of the aqueous solution KOH (29.4%), used in alkaline batteries, is 540 mS/cm. The smaller value than that expected is due to a decrease of charge carriers due to the effects of ionic pairing and aggregation and lowering of mobility due to the increase of viscosity. Assuming spherical symmetry for the ions and using Eq.1.1 of Nernst-Einstein, the expression of the DC conductivity at room temperature is obtained:

$$\sigma_{DC} = \frac{z^2 \varepsilon_0^2 N}{6V\pi r\eta} \tag{1.1}$$

where z represents the valence of the charge carriers, ε_0 is the elementary electronic charge and r the effective radius of the "spherical" ions. It may be noted, however, that conductivity σ_{DC}, is proportional to the number of carriers N and inversely proportional the viscosity η. The viscosity is a key parameter that describes an IL and generally depends not only on the size of the ions but especially by the dense network of Coulombian bonds, hydrogen bonds, Van der Waals forces between liquid particles [20]. Unfortunately N is a parameter difficult to know because of the strong ion-ion interaction and pairing and aggregation phenomena. Furthermore, the conductivity as a function of temperature shows a linear classical (Arrhenius), above room temperature, i.e. increasing proportionally with the increase of temperature. In contrast, for temperatures near to the temperature of glass transition T_g, the conductivity deviates from linear behavior showing a typical trend described by Vogel-Fulcher-Tammann (VFT) law (described in 1.2), characteristic of molecular liquids with tendency to vitrify [19]:

$$\sigma_{DC}(T) = \frac{A}{\sqrt{T}} \exp\left(\frac{B}{T - T_0}\right) \tag{1.2}$$

Where A and B are constants determined for the specific IL and $T_0 \approx T_g$ is the temperature at which σ_{DC} vanishes.

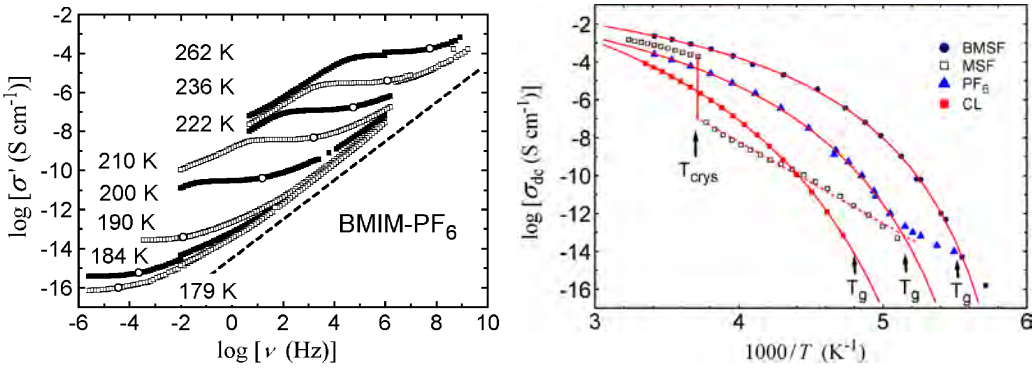

Figure 1.1: (left) Log-log plot of the real part σ of the conductivity of [C_4MIM][PF_6] IL vs frequency at indicated temperatures (taken from ref. [18]). The dashed line has a slope of 1 and corresponds to nearly constant loss. Open circles correspond to separation from long range DC conductivity to frequency dispersive regimes. (right) Arrhenius plot of the dc conductivity of various ILs (picture taken from ref. [18]). Solid lines: VFT fits; dashed line: temperature-activated behavior of the crystalline [C_4MIM][MSF] with an activation energy of 0.85eV.

It can be seen in figure 1.1 (from ref. [18]) that the performance of σ_{DC} follows well the VFT fit. In the case of IL crystallization (for example [C_4MIM][MSF]) there is a sudden drop of conductivity and a linear Arrhenius for temperatures below the crystallization temperature T_{crys}. Such a jump of the conductivity also indicates the presence of activation energy (in this case 0.85eV) to be overcome for the conduction process. Even after glass transitions, as in the case of [C_4MIM][PF_6], an Arrhenius trend is noted, but without discontinuity in conductivity because the liquid gradually solidifies (glass transition). If IL has a high structural order, conductivity decreases strongly because the ions are trapped in a stable structure and can not migrate. If no threshold is exceeded, the trapped ions behave like a classical dielectric insulator and this is the behavior of traditional ionic solids as NaCl. Exceeding the threshold potential for activation, the solid becomes an ionic conductor thanks to phenomena of charge hopping. Recent studies [18] show the trend of the conductivity $\sigma(\nu)$ of some imidazolium salts varying the frequency. In particular, it analyzed the [C_4MIM][PF_6] as a representative of this class which shows the typical behavior of an ionic conductor. In ionic conductors liquids both positive and negative ions act as current-carrying, although one of the two could prevail over the other having a more high "number of transport", defined as the conductivity provided by the species and expressed as a fraction of the total conductivity. In general, in ILs the anion provides the main contribution to the conductivity. The conductivity has a plateu that corresponds to the DC conductivity at long range. For very low frequencies, to the left of the plateau, the conductivity decreases strongly due to blockage of the ionic charge carriers on electrodes. This phenomenon is a characteristic of ion transport of charge that is usually absent in solid conductors. At higher frequencies the plateau intersects with a dispersive regime, in which the conductivity becomes frequency dependent. When the system temperature is low, the high-frequency conductivity is strongly dependent from the frequency. There is, therefore, a crossover frequency that separates the DC system with ion transport by diffusive-dispersive regime characterized by subdiffusive ionic motion (reorientations, dipole libration, rotation).

Dielectric constant of ionic liquids

The study of the dielectric properties of liquid or solid/glassy system, which are complementary and closely related to the conductivity, provides a more general framework for the interpretation of the behavior of ILs subjected to an electric field. In general, however, the complex dielectric function and the complex conductivity ε^* and σ^* are equivalent in fact:

$$\sigma^*(\omega, T) = i\varepsilon_0\omega\varepsilon^*(\omega, T) \tag{1.3}$$

which produces $\varepsilon' = \sigma''/(\varepsilon_0\omega)$ and $\varepsilon'' = \sigma'/(\varepsilon_0\omega)$. In principle, ε' and σ' describe physical processes distinct only in the DC case, where σ' describes the "free charges" (those that can move freely for arbitrarily large distances in response to a DC field) while ε' describes the "bound charge" (charges related to an equilibrium position only moving to a new equilibrium position in response to a DC field). In the case of an AC field this distinction is blurred. The free charges do not move arbitrarily far away, but oscillate with the frequency of the field, while the bound charges do not stay long in the new equilibrium positions, but also they oscillate at the frequency of the field. If the frequency of the field is sufficiently low, the distinction can still be preserved but with different consequences: the speed of the free charges responds in phase with the field (ie, $\sigma^*(\omega)$ is substantially real) while the speed of the bound charge will be out of phase with the electrical field (i.e. $\varepsilon^*(\omega)$ is substantially imaginary). For high frequencies, even this distinction disappears and the distinction between free and bound charges is purely conventional. Generally this distinction is maintained even at high frequency and the response of bound and free charges is described by the expression eq.1.4:

$$\varepsilon^*(\omega) = \varepsilon'(\omega) + i\frac{4\pi\sigma'(\omega)}{\omega} \tag{1.4}$$

The dielectric constant is a fundamental parameter, not only to describe an insulating behavior, but also to describe the solvent property. In correlation with molecular properties used in chemistry, dielectric constant is an important parameter to establish the polarity of the solvent [4][19]. Conventional techniques for measuring the dielectric constant of ILs, however, fail because the liquid is an ionic conductor (as shown in the previous paragraph) and the conductivity impacts heavily on the contribution of the dielectric constant. In some studies [19] an analysis of the $\varepsilon(\omega)$ response was performed using dielectric broadband spectroscopy techniques to investigate the interaction between electromagnetic radiation and IL (in this case, [C_4MIM][BF_4]) in a wide range of frequencies (10^{-2} 10^{12} Hz). It can be seen that the charge transport, as expected, dominates at low frequencies and dielectric relaxation phenomena, associated with dipole reorientation and libration, are observed at higher frequencies. Since there is transport of charge carriers, the migration of charge to the electrodes is inevitable at low frequencies with the consequent polarization. This phenomenon is characterized by a huge increase of $\varepsilon'(\nu)$ and a decrease of $\sigma'(\nu)$ decreasing in frequency. It can also be noted that, for very low temperatures, the mobility of the ions is much lowered and there is a system shift towards lower frequencies of dielectric relaxation. The decrease in temperature could cause a transition from a liquid to a glassy state and also a transition from ionic conductor regime to ionic dielectric regime. Other studies in literature

[16; 17; 21] are concentrated in deriving the dielectric constant using a high-frequency electric field with techniques of microwave dielectric spectroscopy (1MHz - 20GHz). In this case the electrodes polarization problem, which occurs at a low frequency and the dielectric constant diverges, is avoided. From these measurements, the value of the static dielectric constant ε_r is derived with an extrapolation at low frequencies. The fit, around 20 GHz, provides an indication of the contribution to high frequency, ε_∞, i.e. the dispersion caused by polarization of nuclear and electronic shift in infrared and optical regime. Singh et al. in ref. [22] use a thermodynamic approach and concepts of cohesive energy density (ced) to predict ε_r of various ILs. The predicted values of ε_r of the ILs using this theoretical approach comply well with experimental results in literature [16; 17; 21]. Since the polarity scales of the liquids rely on ε_r values, and direct measurements of ε_r of the ILs are not very easy, the technique discussed in this paper can be a very useful tool for the prediction of ε_r of the ILs. Useful information and characteristics are contained in Tab. 1.2.

Compound	ρ (g/cm^3)	η (cP)	T$_{melt}$ (°C)	σ_{DC} (mS/cm)	ε_r	ε_∞
[C_2MIM][Tf_2N]	1.50	35	-19	9.5	12.3	4.70
[C_4MIM][Tf_2N]	1.44	52	-4	4.23	13.7	4.25
[C_4MIM][BF_4]	1.20	100	-82	4.36	14.1	5.45
[C_4MIM][Cl]	1.10	sol	65	sol	15	/
[C_8MIM][Tf_2N]	1.32	95	/	1.37	16.8	3.72
[C_8MIM][Cl]	1.00	/	/	/	7	/
[C_{12}MIM][Tf_2N]	1.25	154	/	/	/	/
[Na][Cl]	2.17	sol	801	sol	5.90	2.34
[K][Cl]	1.98	sol	770	sol	4.84	2.19
[K][Br]	2.74	sol	734	sol	4.90	2.34
[Li][Cl]	2.07	sol	605	sol	11.9	2.78

Table 1.2: For ionic liquids present in our laboratory are presented some physicochemical quantities in this order: density, viscosity, temperature liquefaction, DC conductivity, dielectric constant at optical frequencies, the static dielectric constant measured by spectroscopy. All the data tabulated are published in refs. [4; 17; 25]

All procedures, presented in literature, refer to measurements of dielectric properties on bulk ILs. But how different is the dielectric constant when IL is confined in nanometric layers in close proximity to a solid surface? Answering this question is important for all applications (mentioned in the next section) in which the electrified interfaces in contact with the electrolyte play a fundamental role. Firstly, a morphological analysis of accurate IL on a surface is essential, in fact, when the surface effects prevail, the formation of new and interesting structures is favored. Moreover is required the application of new techniques of ad-hoc dielectric spectroscopy to study the electrical and dielectric properties of these nanostructures.

Dielectric properties of ionic solids

Due to the structural complexity of ILs confined on solid surface, domains with compact reorganization can not be ruled out. It is therefore necessary to possess a background about the electrical properties of ionic solids. Conventional ionic solids (most common example is sodium chloride, NaCl) are well known in scientific community and generally possess a crystalline structure at room temperature [25]. Since the electrons and ions of the crystal structure are well bound in equilibrium positions, in ionic solids there is substantial absence of carriers mobility and consequently they are good electrical insulators. Generally, in insulators without flow of free charges, the applied electric field can penetrate them. It is very important to know how the internal structure of the solid, both electronic and ionic, readjusts when an external electric field is superimposed to the natural electric field associated with the potential of the crystal lattice. When an insulator is placed in a static electric field there are therefore important consequences due to total internal distortion. In this sense, the dielectric constant ε_r relative to the material is a tensor, diagonal in cubic crystals, that summarize the macroscopic response of the material to an applied electric field. Microscopic theories of matter can provide through the electronic and ionic polarizability a prediction of the dielectric constant. Inversely, knowing the dielectric constant, it is possible to obtain additional information about the modifications suffered by the microscopic structure of the dielectric material [25].

As mentioned, in most ionic solids, the ions are trapped in their lattice sites and, though it will continue to vibrate, they rarely have a thermal energy enough to move from their positions. If they manage to escape and move to adjacent lattice sites, we realize the phenomenon called ionic conduction, migration or hopping charge. The ionic conduction occurs more easily at higher temperatures and, especially, in the presence of crystalline defects. In solids without defects there are not interstitial sites completely empty. For the ionic conductivity it is necessary that some sites are vacant, so that adjacent ions can move in such free holes, leaving vacancies in their own place. At higher temperatures the ionic conduction is favored because ions possess greater thermal energy, but also because the concentration of the defects is increased. For example, the conductivity of NaCl around 800 °C (just below the melting point) is about 1 mS/cm, while at room temperature NaCl is a pure dielectric insulator, with a much lower conductivity to 10^{-9} mS/cm.

There is, however, a small group of solids called solid electrolytes, fast ionic conductors or superionic conductors [26], in which a set of ions can move in a very fast way. Such materials often have special crystalline structures, open channels or layers allowing easy movement of the mobile ions. The conductivity values, e.g. 1mS/cm for the migration of ions in Na β-alumina at 25° C, are comparable with those observed for strong liquid electrolytes [27]. There is currently much interest for the study of the properties of solid electrolytes, for the development of new materials and for the expansion of their range of applications in solid-state electrochemical devices.

Generally in the crystals of the alkali halides the cations are normally more mobile than anions. It is therefore convenient to consider the vacancies as the main cationic charge carriers in NaCl. Anion vacancies are also present, but less mobile than cationic counterpart [28]. The ionic conductivity in NaCl depends also on the purity and the thermal history of the material. The vacancies are created in two ways. The first way is simply to heat the material. The number of intrinsic vacancies present in thermodynamic equilibrium increases exponentially with temperature representing the number of charge carriers for pure NaCl. The second method involves the addition of external impurities: vacancies are generated to preserve the charge balance. These carriers are ex-

trinsic and are not present in perfectly pure NaCl. At ordinary temperatures (eg 25 °C), the number of intrinsic vacancies thermally generated is very small and is much lower than the concentration of extrinsic vacancies. As the temperature increases there is a change from extrinsic to intrinsic behavior, when the concentration of intrinsic vacancies thermally generated exceeds the concentration of vacancies controlled by extrinsic impurities. The dependence of ionic conductivity on temperature has a trend of Arrhenius type entirely similar to the relation 1.2.

$$\sigma(T) = \frac{\sigma_0}{T} \exp\left(-\frac{E_m}{RT}\right) \tag{1.5}$$

where in this case, E_m is the activation energy for the process of hopping charge. For pure NaCl the activation energy for the migration of Na^+ is from 0.65 to 0.85 eV while for Cl^- is 0,9-1.1 eV [28]. For comparison the Arrhenius activation energy of liquid electrolyte like [C_2MIM][BF_4] is 0.18 eV [29].

1.2 The solid-liquid interface

As stated in the previous section, the behavior of IL in the proximity of a solid interface is a field not much explored but no less important. Many applications in photoelectrochemical and lubrication field could use ILs to advantage the interfacial properties performance. Some applications are presented below, with particular emphasis to the study of the electrical and interfacial properties, critical for the functioning of the device.

1.2.1 Ionic liquids in lubrication

Since the first paper appeared in 2001 by Ye et al.[30], ILs have shown good performances as lubricants. First of all, ILs show good thermal stability and lower flammability respect to ordinary lubricating fluids, so they are promising for those applications in which extreme temperatures or very low pressures are involved. Their strong electrostatic bonding compared to covalently bonded fluids, leads to very desirable lubrication properties. Unlike conventional lubricants that are electrically insulating, ionic liquids can minimize the contact resistance between sliding surfaces because they are conducting, and conducting lubricants are needed for various electrical applications (micro- and nano-electromechanical devices (MEMS/NEMS)). These liquids can also be used to mitigate arcing, which is a cause of electrical breakdown in sliding electrical contacts [31]. In addition, ILs have high thermal conductivity which helps to dissipate heat during sliding.

A recent study by Jimenez et al. [32], allows to depict some trends in the properties of different ILs used as lubricants. It appears that if an imidazolium cation is used, an increase in the alkyl chain length, that increases viscosity, induces a reduction in both friction and wear [32]. In contrast, it appears that cations with longer alkyl chains are less thermally stable and also more susceptible to tribochemical reactions, especially in presence of humidity: it seems that the cation loses its longer side chain[33], testified also by the browning of the IL. The mechanism proposed is the absorption of the anion containing carboxyl group on metal surface, forming an immobilized layer. By coulombic interaction, the ions of ILs tend to form a layered structure on top of the first bound layer. The first bound layer works as an anti-wear layer while the mobile IL layers on top of it reduces friction. An explanation similar to that provided by Ye, has been proposed also by Bhushan et al.[31] in a paper where an ultrathin (few nanometers-thick) IL layer

is deposited on top of Si(100). The behavior of ultrathin layers is of direct importance for the application of ILs in micro- and nano-electromechanical devices (MEMS/NEMS) lubrication. The lubrication of MEMS/NEMS is a definitely not simple task, because the mechanical components involved are very thin and delicate and the separation distances between moving part is reduced even to few nanometers. In these conditions a lack in lubrication can bring to immediate damaging of the device. Furthermore, an efficient lubricating fluid should provide good thermal and charge dissipation. The presence of wetting layers can be potentially harmful due to adhesion that can "glue" surfaces together. So also wettability is an issue that can be tailored with ILs. In MEMS and NEMS the behavior of the lubricant layer can change respect to the case in which bulk quantities of liquid contact a solid surface. In fact, in a nanometer-thick layer the surface to volume ratio is very high, and the interaction with the solid surface plays a fundamental role. In the work previously cited, Bhushan compares the behavior $[C_4MIM][PF_6]$ and $[C_4MIM][OctSO_4]$ with the reference Z-Tetraol (a PFPE lubricant). The comparison is performed both with a standard ball on disk tribometer and with an AFM using a diamond tip. $[C_4MIM][PF_6]$ shows comparable or better performances than the reference and it is more able to dissipate or screen the charges produced during the friction. In all the cases, the coatings of IL prepared annealing the samples just after deposition at 150°C for 30 minutes have the best durability and low friction coefficient. The authors ascribe this behavior to an immobilized layer formed by the reaction of the anions with OH groups on the surface, covered by a mobile fraction composed by the rest of the liquid. If the mobile fraction is removed by washing with isopropanol, the performances vanish.

1.2.2 Electrochemical devices

Generally, surface-induced effects at liquid/solid interfaces are expected to became more important when the surface to volume ratio increases. This is the case in all those applications in which the solid material is nanoporous or nanostructured. Due to the nature of ILs, they are appealing candidates for the substitution of standard electrolytes in electrochemistry and photo-electrochemistry. Two categories of those devices, that are gaining considerable attention in the last years, are super-capacitors or electrochemical capacitors (ECs), and Dye Sensitized Solar Cells (DSSCs).

Electrochemical supercapacitor

ECs are devices composed by electrodes with high specific active area, filled with an electrolyte. In an electrochemical capacitor the reversible adsorption of the ions of the electrolyte at electrodes is employed for energy storage [34–37]. Compared to traditional capacitors, their capacitances are huge: thousands of Farad capacitors are already available, with specific capacitance also exceeding 300 F/g. Differently respect to batteries, no reactions take place at the electrodes, only the physical accumulation of charges from the electrolyte: this leads to faster times of charge/discharge of ECs, that can be of the order of few seconds or less. Furthermore, batteries, even the most performing Lithium ion batteries available, can sustain at maximum few thousand cycles of fully charge/discharge, whereas supercapacitor durability is measured in hundred thousand or even million of cycles. Supercapacitors bridge the gap between standard capacitors and rechargeable batteries. In terms of specific energy, as well as in terms of specific power, this gap covers several orders of magnitude. However, batteries still have about ten times the capacity of supercapacitors. While existing supercapacitors have energy

densities that are approximately 10% of a conventional battery (100 to 250 Wh/kg for a lithium-ion battery), their power density is generally 10 to 100 times as great (the specific power of electric double-layer capacitors can exceed 6 kW/kg at 95% efficiency). Supercapacitors are then suitable for those applications in which high power and short time of charging/discharging, coupled with high durability, are needed [38]. The working principle of the EC was first described by Helmoltz in 1853 [39] and relates to the formation of a double layer of charge at the surface of the electrode once a potential is applied, that is responsible for the capacitance per unit area of the device:

$$C_d = \frac{\varepsilon_0 \varepsilon_r}{d} \tag{1.6}$$

where ε_0 and ε_r are respectively the dielectric constant of vacuum and dielectric and d is the thickness of the double layer. The separation of charge distance in a double-layer d (in 1.6) is on the order of a few Angstroms (0.3–0.8 nm) so they can have capacitance values of 10,000 times greater than conventional capacitors. The double-layer theory was further developed by Gouy and Chapman, who introduced a contribution to the capacitance due by a diffuse layer of accumulated ions close to the electrode, induced by a non-perfect screening of the ions in the double layer [40]. The dynamics of the formation of the layers of charge when the electrolyte and the shape of the surfaces of the armor change, how ions behave in the bulk of the solution, are the subject of current research. A key role is played by how the molecules are to be arranged on the surfaces, which should be investigated experimentally using techniques sensitive only to the contributions of the first layers. In literature, there are also theoretical studies that provide an interpretation of the behavior of ILs on an electrified interface [23; 41]. Because the double-layer model is not in full agreement with the experimental values, new models have been proposed when there is a partial ordering or well defined ordering of the first layers of IL in the vicinity of the interface [41]. The last two models reproduce very well the experimental data but the theory is still far from complete. For example in [23] the compact layer is modeled with a layer of arbitrary effective dielectric constant $\varepsilon_r \approx 4$. Studying the behavior of ILs close to electrified interface and direct analysis of the dielectric properties of compact layers may open the way to new and profitable applications in this field. Experimental measurements focused at the interface, where reactions take place, could provide an explanation of the phenomena occurring on the surface and also a validation for the theoretical models used. An interface sensitive approach is particularly important for ECs electrodes with enhanced surface area. This configuration is preferred for applications because the capacitance increases linearly with the surface area since a larger surface is available for charge storage. Usually the choice is to use graphitic carbon electrodes, because they are highly conductive and electrochemically stable. Different structures of the electrodes can be used [42], like nanofibers, nanotubes or carbide derived carbons (CDCs) and activated carbons: this materials can have surface areas exceeding 2000 m^2g-1. A fundamental ingredient for an efficient operation of a supercapacitor is the electrolyte. Usually, organic electrolytes, i.e. electrolytic solutions in an organic solvent, are used in ECs, because even if higher capacitances can be generally achieved in aqueous solutions, organic solvents have a wider electrochemical window. Since the energy stored in a capacitor is E = $\frac{1}{2}CV^2$, the largest is the electrochemical window, the greater the specific energy that can be hold in the device. This choice is driven by the fact that water is not electrochemically stable, compared to some organic solvents like acetonitrile. The problem is that usually organic solvents have high vapor pressure, so the sealing of ECs using organic electrolytes is crucial and anyway can lead to a shortened life of the devices and furthermore some of the solvents used are

very toxic. The use of ILs as electrolytes in ECs seems promising, because their vapor pressure is very low, but also more important, because they can have electrochemical windows exceeding 5 V (see for example Tab. 1.1), that is almost twice wider than that of an organic electrolyte. A problem in using ILs as electrolytes is related to their high viscosity and low conductivity. The conductivity of an IL is usually just few mS/cm and this directly affect the equivalent series resistance (ESR), and so the specific power, calculated as $P = V^2/4(ESR)$. Furthermore, also the details of the dynamics of the IL inside the pores affects the ESR, as well as the wetting properties of the liquid on the electrode surface [38]. A more local and accurate investigation of ILs behavior in high surface/volume ratio configurations is necessary for further improve the performances of these devices, along with the developing of new well suited ILs.

Dye sensitised solar cells

Dye sensitized solar cells belong to the third generation of solar cells. This kind of cells, at least in the current design, have been developed by Graetzel and O'Regan in 1988, and the first paper on the topic has been published in 1991 on Nature[43]. The working principle of DSSC is based on a cell composed by a transparent anode (conducting glass like ITO or FTO), on which is deposited a nanostructured wide gap semiconductor (from now on I will refer to TiO_2 because is the most diffused, even if also ZnO and other oxides can be used) few tens of nanometers thick. The surface of the nanostructured material is covered by a monolayer of the sensitizer, called dye, the component responsible for the light harvesting. The cell is then filled with an electrolyte containing a redox couple (the most common is I^-/I^{-3}). In contrast with conventional silicon cells, where light conversion and charge carrier transport are both performed by the semiconductor, here the light is absorbed by the dye, whereas the photo-generated electrons flow into the nanostructured oxide. The dye is carefully chosen in such a way that the energy of its excited states matches the energy of the conduction band of the TiO_2: the electrons can jump into the conduction band, they flow regenerated by the oxidation of redox couple and the circuit is closed once the redox couple reduces at the counter electrode. Here again, as in the case of ECs, the nanostructure is used in order to increase the active area. In fact, it has been seen that the better performances are obtained when a single layer of dye molecules is absorbed onto the surface, but the light capture by such monolayer on a flat surface would be very low. Instead, on a nanostructured material this single layer allow to reach efficiencies higher then 12%.

One of the crucial ingredients for the efficiency of the device is the electrolyte. In fact, the electrolyte should provide sufficient mobility to the redox couple, needs to maintain its performances for a long time (corresponding to at least 15-20 years of operation) and not be corrosive or toxic. Electrolytes based on organic solvents allow to have good diffusion coefficients for the redox couple, but their usage requires that the cell is perfectly sealed, even because some of them are toxic, so making their application in flexible devices difficult and furthermore they can permeate plastics in time. ILs offer a valid alternative to ordinary solvents. As already mentioned, ILs have a low vapor pressure and furthermore they do not tend to permeate plastics. Moreover ILs can be carefully chosen in order to dissolve the redox couple, to properly wet the nanoporous matrix and to match the desired conductivity and viscosity. A good mobility of the redox couple is fundamental, because the sensitizers molecules, once ionized, need to be regenerated as fast as possible. First of all, a faster regeneration of the dye allows a greater photoelectron density injection in the TiO_2, second, ionized dyes are centers of positive charge, so they can induce recombination of the electrons and slow down their diffusion and third,

even more important, an ionized dye molecule can undergo degradation [43]. Thus, it is extremely important to know how the IL electrolyte behave at the nanostructured-solid/liquid interface. In fact, as we actually observed, if an oxide surface can induce a structural change when the surface to volume ratio is high, as in the case of nanoporous structure of a DSSC, and especially if compact insulating layers are formed, the regeneration of the dye can be slowed, and also the mobility, because of the narrowing of the pores. There are several reasons suggesting that these devices may go to replace conventional solar cells in next future. In fact, DSSC reached efficiencies close to that of commercial silicon-based devices, furthermore the reduced cost of the materials compared to e.g. silicon or GaAs, the possibility of printing the cells over large areas, also on flexible substrates and their transparency make them very appealing.

1.3 The solid-liquid interface: thin ILs supported layers

The previous sections highlight how the study of the IL/solid interface can be of fundamental importance in a series of applications. Nonetheless the systematic study of those interfaces is more recent than the investigation of the bulk properties of the ILs. Among the studies of the IL/solid interfaces present in the literature, the major part has been conducted by electromagnetic spectroscopic techniques. The nature of the IL/solid interface buried under a macroscopically thick IL film(representing the bulk IL) has received considerable attention recently. In fact, these interfaces have been studied by sum frequency generation spectroscopy (SFG) [44–46] and X-Ray reflectivity [47; 48]. Moreover Druschler et al. [49] using electrochemical impedance spectroscopy (EIS) analysis studied the structure and dynamics of IL/Au electrode interface. EIS measurements probe two distinct capacitive processes taking place on different time scales. The time scale of the fast capacitive process exhibits virtually the same VFT-type temperature dependence as the bulk conductivity of the IL. Thus, this process can be identified with double layer formation governed by ion transport in the ionic liquid. The slow process exhibits a time scale of seconds at room temperature. Comparative VFT and Arrhenius fits for the temperature dependence of the time scale indicate an Arrhenius-type temperature dependence. This suggests that the slow process is caused by temperature-independent activation barriers, most likely barriers for the reconstruction of the electrode surface and/or barriers for the reorientation of strongly bound ions in the innermost layer. In addition, a third ultraslow process is probed by EIS, which might be related to ultraslow vacancy formation in the Au surface (observed by in situ STM measurements [49]). Other experiments on solid/liquid IL interface have been conducted with the surface force apparatus (SFA) [50]. SFA consist of two smooth cylindrically curved surfaces whose cylindrical axes are positioned at 90° to each other are made to approach each other in a direction normal to the axes. The distance between the cylinders is measured by optical interferometry and one of them is held by a cantilever spring in order to sense the interaction forces. The surface of the cylinders, normally made of mica, can be covered with the material of choice in order to match specific purposes. Fig. 1.2 (left), reproduced from the work of Ueno et al. [50], reports the results of a measurement performed on a bulk of $[C_4MIM][Tf_2N]$, between silica surfaces. An oscillatory profile of the force with an amplitude exponentially decreasing with the distance can be clearly seen. The oscillations are ascribed to the rupture of solvation layers formed by IL in contact with the silica surface and the thickness of each layer is about 0.8-0.9 nm.

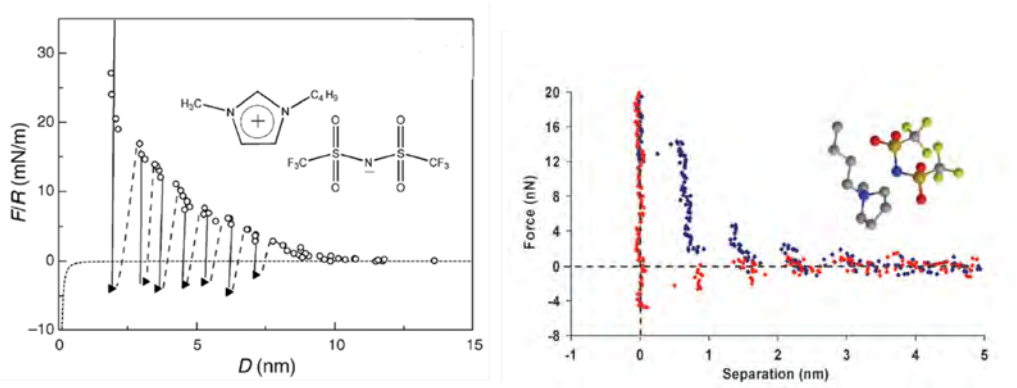

Figure 1.2: (left)Output of an SFA measurement performed in a bulk of $[C_4MIM][NTf_2]$ between 2 silica surfaces. Layering at the surface can be clearly detected as oscillation in the force between the surfaces (reproduced from ref. [50]. (right)Force curve acquired with an AFM in a bulk of $[C_4MPyr][NTf_2]$ with a silicon nitride tip on a mica substrate. As in SFA measurement, solvation layers are clearly visible in the force profile starting around 4nm from the substrate (reproduced from ref. [51]).

A different approach to obtain a better understanding of the IL/solid interface is to investigate very thin IL layers with thicknesses in the order of only a few nanometers or even in the sub-monolayer regime ("thin layers" in contrast to macroscopic IL films of a thickness in the order of micrometers up to millimeters). For example Cremer et al.[52; 53] on thin evaporated IL films with X-Ray photoelectron spectroscopy (XPS). In these systems, IL is confined in a 2D layered system leading to different physical properties. In another study [54], ultrathin films of ILs were deposited on mica by a physical vapor deposition method under UHV conditions, and were investigated using ARXPS. After IL deposition XP spectra of both ILs were collected from the submonolayer to the multilayer regime. On clean mica, 3D growth (complete dewetting) occurs, whereas on a fully carbon covered surface, initially a complete 2D wetting layer forms, followed by 3D growth. All the techniques mentioned before are sensitive only the first layers at the IL/solid interface, meaning that they have a resolution along the direction normal to the surface of fraction of nm or below, such that the orientation of the molecules at the interface can be detected. In these studies are evidenced ordering phenomena of the ions at the interface highlighted by the presence of electron density oscillations and interpreted as the signature of the formation of stacked double layers of anions and cations.

Spectroscopic techniques and SFA usually collect information coming from macroscopic or quasi-macroscopic areas of the sample. That means that, even if they are very sensitive to the the first layers at the interface, the measured quantities are averaged over large areas, so they suffer of a poor lateral resolution. For this reason in recent times the interest has grown in using scanning probe techniques in the study of IL/solid interfaces. Scanning probe microscopies (SPMs) use a probe with a radius of curvature that is usually around few nanometers in order to be sensitive to the local properties of the sample surface. The surplus value of SPMs respect the the spectroscopic techniques is the possibility of investigating the properties of the sample surface with a high lateral resolution. In fact, using these techniques is possible to acquire topographic map of the surface with resolution normal to the surface below 0.1 nm and lateral resolution of few nanometers, related to the size of the probe used. Furthermore other type of maps (friction maps, phase maps, mechanical map, electrical map), sensitive to dif-

ferent physico-chemical properties of the sample, can be collected in correspondence 1-1 simultaneously with topographic map. Among the SPMs the atomic force microscope (AFM) is the most versatile because it can be used equivalently on insulating or conducting sample, it doesn't require ultra high vacuum, in fact it is normally operated in air and it can work in liquids.

For example in ref. [55], drops on a IL-coated surface showed electrowetting at driving voltages as low as 70 mV. AFM revealed that the IL formed a solidlike adsorbate film, which was immiscible with liquids and formed a dielectric layer. The ultrahigh capacitance density of this IL dielectric layer led to low-voltage electrowetting. Also in a combined AFM and ARXPS studies [56] information on both the topography and molecular arrangement of ultrathin solid supported IL films were provided. They show that the overall structure is determined by the competition between the solid/IL attraction and the cohesion (surface tension) of ILs. When the film is thin, solid/IL attraction dominates and results in the layered structure and the film is very smooth. When the film is thicker, anion–cation cohesion dominates and the film shows a "drop-on-layer"/"sponge" structure and the film is rough.

Recently, few studies have been published in which AFM have been used to investigate the IL/solid interfaces. Atkin et.al. studied several bulk IL/solid interfaces using AFM [51; 57]. In these works the AFM has been used to perform force spectroscopy curves in order to sense the different forces experienced by the AFM tip approaching the surface. Different ILs on different surfaces have been used; the studies evidence that ILs tend to structure under the influence of the surface, forming solvation layers, that are subsequently broken by the tip, as shown in fig. 1.2 (right). The layering can extend few nanometers far from the surface and the intensity of the force needed to break the layers increases moving toward the substrate. The same authors performed also a study where they couple the AFM spectroscopy described above with electrochemical STM, were they see the reconstruction of gold surface immersed in an IL once the potential difference between the tip and the sample is changed [58; 59]. In this study it is also shown how an electrified interface influences the solvation layers; upon the application of a negative potential on the surface of gold, the number of detectable layers increases as well as the forces required to breakup. In these AFM studies the local structuring of the ILs in contact with solid surfaces is probed, differently respect with electromagnetic spectroscopies. Anyway the authors don't make use of the high lateral resolution of the AFM in order to explore the topography of the IL/interface. In fact it can be expected that the interface can be irregular, displaying different morphological and physico-chemical properties in different areas. Other groups actually performed AFM imaging of the bulk IL/solid interface. Yokota et al.[60] performed AFM imaging in bulk of $[C_4MIM][Tf_2N]$ and $[C_4MIM][BF_4]$ in contact with mica and HOPG surfaces, showing the presence of layered structures unevenly distributed. In an other work performed by the same group [61], the morphology of a thin film of $[C_4MIM][PF_6]$ on mica and HOPG is investigated by AFM, showing the tendency of the IL, more pronounced on mica, to coexist in a liquid and highly ordered form. This systems can be expected to show a different behavior than those systems in which a bulk of IL is in contact with a solid surfaces, since here the reduction of the volume means an increased surface to volume ratio and so the IL would be more influenced by the interaction with the substrate.

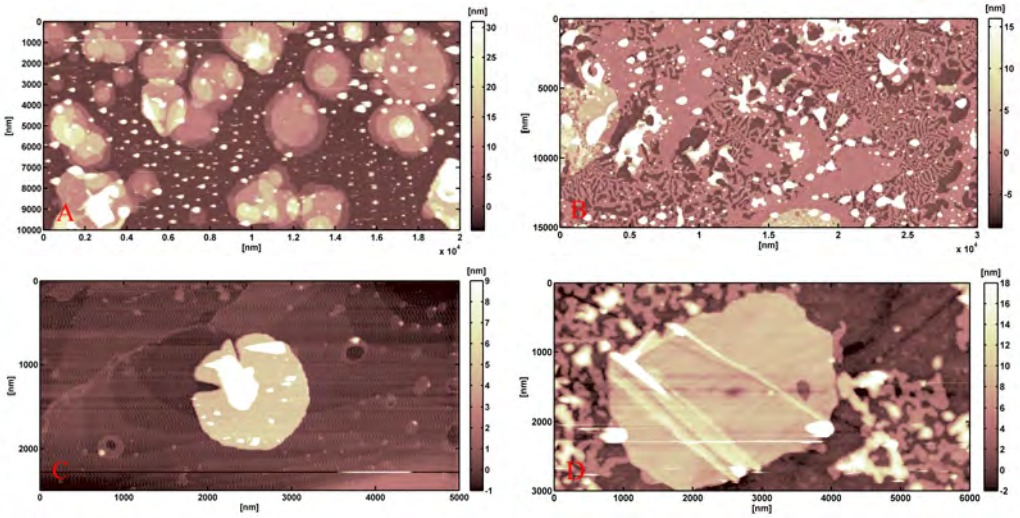

Figure 1.3: AFM morphological maps of thin layers of $[C_4MIM][NTf_2]$ deposited on different insulating surfaces: image A silicon with native oxide, image B mica, image C NaCl, image D polished MgO. Images are taken from refs. [62–64]

1.3.1 Thin films of solid-supported ILs investigated by Atomic Force Microscopy

Triggered by original work of Liu [61], Bovio et al. [62–64] continued and extended the investigation of IL/solid interfaces by means of atomic force microscopy. The important observation of coexistence of liquid and ordered phases at room temperature (called solid-like) is very interesting for a compound that is liquid in its bulk form at the same conditions. In particular $[C_4MIM][NTf_2]$ IL was used because it is hydrophobic and water stable, its bulk properties have been well characterized and because this IL or ILs very similar, are used in applications, in particular in photo-electrochemical devices.

The investigation has first been conducted on the morphological analysis of $[C_4MIM][NTf_2]$ thin films on different ideal solid surfaces (amorphous silica, silicon covered by its native oxide, mica, HOPG, MgO, TiO_2 and NaCl), chosen because they are smooth (some of them atomically flat) and so very suitable for an high-resolution AFM study (figure 1.3). The thin films have been realized by drop casting droplets of few μl of a IL/solvent solution in air. On all the substrates analyzed (not HOPG), IL coexists in the form of droplets and flat ordered domains behaving like solids under the AFM tip. Ordered flat layers can have an in-plane extension of several microns and can be thicker than 50nm. Those structures are usually arranged in a ziggurat-like configuration, composed by superimposed terraces.

A quantitative statistical analysis of the heights of the terraces as been performed by using height histogram. The internal structure of each terrace is interpreted using a simple model as the stacking of fundamental layers of thickness δ (see Fig. 1.4). A $\delta = 0.6$ nm has been found for all the set of data collected on different substrates (mica, amorphous silica and oxidized silicon) and using different deposition solvents (methanol, ethanol and chloroform), suggesting that the internal structure of the IL ordered domains does not depend on the kind of substrate and also that the solvent acts only as a fluidizing agent and support for the deposition, during surface reconstruction, without inclusions in solid-like layers. The obtained value of δ is in agreement with density oscillations

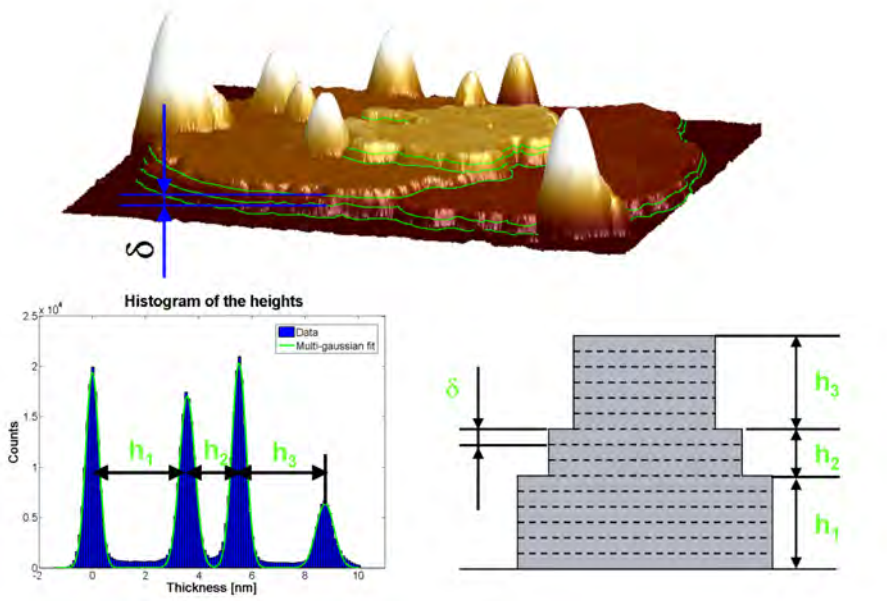

Figure 1.4: 3D AFM morphology of a layered structure on oxidised Si (2.2 μm lateral scale, 35nm vertical scale) and the corresponding histogram of the heights. On the AFM image the green lines are drawn in order to show the supposed internal structure of each layer, composed by vertically superimposed fundamental layers of thickness δ. At the bottom right is shown a scheme of the presumed structure of a generic ordered terrace.(reproduced from ref. [64])

found in a molecular dynamics simulations of a thin slab of $[C_4MIM][NTf_2]$ on silica in Fig. 1.5 [63]. In the field of the study of IL/solid interfaces, numerical simulation works have been performed. Pietro Ballone et al. [63] performed a molecular dynamics simulation of a thin slab (4 nm) of $[C_4MIM][NTf_2]$ on a silica surface. The simulation evidences density oscillation at the interfaces with a periodicity of 0.6 nm and extending for 2.5 nm from the silica surface at 300 K, whose amplitude decays away from the surface. If the silica surface is removed density oscillations disappear, restoring the symmetry of the slab, highlighting that the role of the substrate is responsible for the layering formation. It is apparent that the general properties of layered islands are far more solid-like than in the simulation results. The difference might be due to a limitation of simulation, unable to nucleate a crystal-like phase for the overlayer during the nanosecond scale computations. In another study Ballone et al. [65] performed a force spectroscopy experiment on the same thin IL slab indenting the liquid with a nanometric hard sphere (2 spheres with radius of 1.6nm and 2nm have been used). During indentation the dependence of the normal force Fz on Z is not monotonic, but displays both localized irregularities and longer-scale small-amplitude oscillations: the longer scale oscillations reflect the layering at the interface.

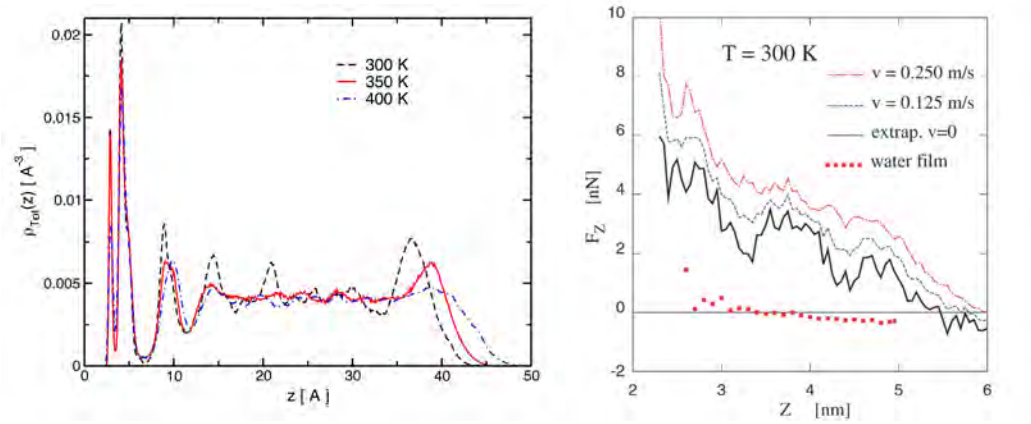

Figure 1.5: (left) Total density profiles (cation plus anion centres) at 300, 350 and 400 K obtained from MD simulations of a $[C_4MIM][NTf_2]$ film adsorbed on a hydroxylated SiO_2 surface. (reproduced from ref. [63]). (right) Average force on the incoming sphere as a function of distance from the silica surface. Dot-dashed line: approaching velocity v=0.25m/s; dashed line: approaching velocity 0.125 m/s; full line: extrapolation to v=0. Filled squares: force required to indent a water film of comparable thickness; single trajectory, v = 0.25 m/s, T = 300 K. (reproduced from ref. [65])

The mechanical resistance of the ordered domains has then been examined experimentally by nano-mechanical tests performed with the AFM [64]. Under the influence of forces parallel to the substrate exerted in contact mode scanning, the ordered domains are not easily removed and tend to be eroded as lamellar solids and a terrace-by-terrace erosion can be observed. Investigating the resistance to normal loads, discontinuities in force vs. tip-substrate distance curves have been found, highlighting a sequence of ruptures, separated by 1.8-2 nm, where the average rupture pressure is $\approx$ 2-3 KBar, very similar to the maximum pressure found in the mentioned MD simulations [65]. The first part of the force curve after contact shows a compression that has been treated as an elastic compression of the layer. A simple Hertz model has been applied to fit the com-

pression, leading to Young modulus E≈ 1.8 GPa, similar to that of some plastic material like nylon. The peculiar mechanical properties of these layers suggest a structure with reduced ionic mobility. If ions are trapped in a stable structure, confined in a 2D layers, the electrical properties could be greatly modified, passing from ionic conductor to ionic insulator. The first aim of this thesis presented in section 1.5 will be devoted to the AFM investigation of electrical properties.

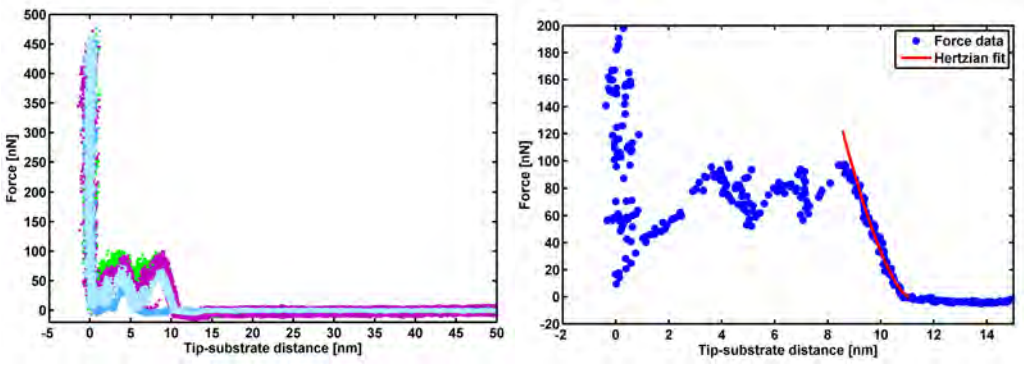

Figure 1.6: (left) Different force curves acquired on the same island in the same P&S measurements are reported. (right) Example of a fit performed using the Hertz model on first part of the contact in a force curves on a solid-like island.

The modifications of electrical properties can have important consequences for the applications. In particular when a nanoporous matrix is impregnated by an IL, if mechanically-resistant ordered domains are formed on the surface, electrical properties (since immobilized ions can behave like electrical insulators) and flow properties (since they can shrink or even block the nanopores) can be strongly influenced (See some examples and discussions in Appendix A). The study of the electrical properties of the layers with a high order of ionic liquid grown on insulating surfaces is critical because beyond the transition temperature of solid-liquid is not known if the material behaves as a conductor or an insulator. Measurements of the static dielectric constant may provide insights into the nature of that structures. A high static dielectric constant, ideally infinite, will demonstrate a metallic-like character of these layers, while values in a neighborhood of the unit will demonstrate an insulator-like nature.

1.4 Biocompatibility and toxicity of ionic liquids

1.4.1 Sustainability of ionic liquids

In the last twenty years an increasing effort has been devoted to the development of a less environmentally harmful chemistry, i.e. what is now called Green Chemistry[66]. The aim of Green Chemistry is to try to find more efficient processes of synthesis, especially at industrial scale, using as few as possible toxic solvents, or no solvents at all. To this regard, a useful tool providing a qualitative scale of the "goodness" of a process is the E factor, introduced by R. Sheldon [67], that is the amount of waste produced in the process divided by the amount of the desired products produced in the process, where in the waste also the amount of energy spent in the whole process is considered. ILs are good candidates for Green Chemistry especially because they are non volatile in

the whole liquid range and their ions can be tailored ad-hoc for the specific application. Normally the volatility of organic compounds is dangerous for the environment and is costly, because the solvent that evaporates cannot be reused any more. Furthermore sometimes the extraction of the products of a reaction is obtained by solvent evaporation, or by distillation, that wastes at least a 10% of the solvent itself. The low vapor pressure of ILs is due to their nature of ionic compounds. In these systems the coulombic interaction is limited by the size and structure of the ions, and differently respect to molten salts, it is not energetically favorable to evaporate ion couples. If the temperature is raised, the ions in an IL will generally decompose before undergoing evaporation. Other important aspects in favor of the greenness of ILs are the low flammability (compared with conventional solvents), controlled miscibility and the possibility of tailoring the physical-chemical properties by the ad-hoc synthesis of the ions. In fact, given the limited number of available organic solvents, some processes are not very efficient. The possibility of a targeted synthesis of an IL will take care of this issue. Anyway it will be quite ingenuous to assert that ILs are green just because they possess good chemical properties. In fact, in order to be considered green, the synthesis and also the disposal of that compound should be green too. In a study conducted by Deetlefs and Seddon [68], the environmental impact of the laboratory production of imidazolium-based ILs is performed. In the study is evidenced the fact that in the synthesis as well as in the purification or decolourisation of the ILs, several volatile solvents can be used, and also that a quite high amount of energy is usually necessary. Furthermore, common ILs are usually not designed to be biodegradable, so the study concludes with the statement that ILs are green, (if compared to ordinary compounds used in synthesis), but not green enough. The replacement in industrial processes of volatile solvents with ILs needs to be careful and should be motivated and sustained by a proper life cycle assessment study (see for example [69]).

1.4.2 Eco-toxicity and cyto-toxicity of ILs

As stated before, the risk of air pollution by ILs is minimal due to their nonvolatile characteristics. However, if large-scale industrial applications of ILs commence, their entry to the aquatic environment through accidental spills or as effluents is the most probable pathway for their contributing to environmental hazards [70]. Consequently, toxicology investigations were the earliest topic of interest concerning IL environmental safety. The studies of ILs toxicity have advanced at a significant rate and a great deal of information has been accumulated. Jastorff and co-workers undertook the first expert study concerning the toxic hazard nature of ILs in 2002 [71]. They estimated theoretically the metabolizing fate of a frequently used cation, 1-butyl-3-methylimidazolium ([C_4MIM]). If this ionic molecule actually reaches the cytochrome P450 system located in the endoplasmatic reticulum of any cell, it can be oxidized in different positions of the alkyl side chains. The resulting metabolites can further be broken down metabolically to biocompatible fatty acids and imidazole. In experimental ecotoxicological studies focused on algae (Scenedesmus vacuolatus) and invertebrates (Daphnia Magna), various cations were examined in a freshwater toxicity investigation measuring EC_{50} values (reviewed in ref. [72]). The half maximal effective concentration (EC_{50}) refers to the concentration of a drug, antibody or toxicant which induces a response halfway between the baseline and maximum after a specified exposure time. It is commonly used as a measure of drug potency. The EC_{50} is usually measured in linear multiples of mol dm^{-3} or in logharitmic scale derived from μmol dm^{-3} (see for example table 1.3). The EC_{50} of a dose response curve represents the concentration of a compound where 50% of the pop-

ulation exhibit a response, after a specified exposure duration. A clear trend of EC_{50} for various ILs is presented in table 1.3 and compared with conventional solvents. Shorter alkyl substituted chains (C_1–C_4) demonstrate lower toxicity to algae and invertebrates, whereas the toxicity of C_8–C_{18} substituted salts worsens severely, irrespective of the type of cation present. All ILs show much higher toxicities, in comparison with data of inorganic sodium salts containing the same anions. Regarding inhibition assays used in assessment of environmental potential risk of a compound in aquatic milieu, the bioluminescence assay Vibrio fischeri bacteria is one of the most applied [73]. This is a rapid, cost effective, and well-established method for toxicity determination focusing on environmental issues, and also a standard ecotoxicological bioassay in Europe [74]. Although it has been claimed that modifications of the anion lead to changes in chemical and physical properties of ILs, no clear increase in toxicity caused by the anion could be observed, and toxicity seemed to be determined mainly by the cationic component [75]. This is likely explained by the fact that lipophilic part of the molecules can be intercalated into the membrane composed by phospholipid bilayers, whereas their ionic head group is at least partially solvated in the aqueous solution. The ILs toxicity was also observed to correlate directly with the length of the n-alkyl residues in the methylimidazolium cation [76]. Concerning the anionic influence, compounds with $[PF_6]$ were found to be slightly more toxic than compounds with other anions in their study [75]. The anion $[NTf_2]$ showed no intrinsic toxicity to V. fischeri in the reference [77]; in contrast, an increased in toxicity was found for all tested compounds combined with $[NTf_2]$ for V. fischeri [74].

	$Log_{10}(EC_{50}$ (μM))					
Compound	Vibrio Fischeri	Scenedesmus vacuolatus	IPC-81	HeLa	Lemna minor	Daphnia magna
Methanol	7.00[75]	/	6.2[75]	/	/	/
Acetone	5.47[75]	/	6.8[75]	/	/	/
$[C_4MIM][Cl]$	3.47[74]	2.26 [77]	3.55[78]	3.44[79]	2.82[77]	1.99[80]
$[C_4MIM][BF_4]$	3.55[81]	2.11[77]	3.12[78]	3.66[79]	2.49[77]	1.67[80]
$[C_4MIM][Tf_2N]$	3.39[81]	1.81[77]	2.68[78]	3.07[79]	2.45[77]	/
$[C_8MIM][Cl]$	1.01[74]	-2.67[74]	2.01[78]	/	/	-1.33[81]
$[C_8MIM][Tf_2N]$	/	/	1.64[78]	2.28[79]	/	/

Table 1.3: Toxicity of ILs to different levels of biological complexity including bacteria, algae, rat cell line, human cell lines, duckweed and invertebrate from ref. [82].

Cytotoxicity is the quality of being toxic to cells. The use of mammalian cell cultures for a screening risk evaluation is a pioneering approach in environmental science. As a cellular test system, promyelotic leukemia rat cell line IPC-81 has been frequently used in cytotoxicity assays of ILs, with the reduction of the WST-1 dye as an indicator of cell viability ([75; 77; 79; 83; 84]). It was observed that ILs with polar ether, hydroxyl and nitrile functional groups within the side chains exhibited low cytotoxicity compared to those incorporated with 'simple' alkyl side chains ([79; 85]). Those functional groups were thought to impede cellular uptake by membrane diffusion and reduce interactions with the cell membrane [79]. The side chain length effect (decrease of EC_{50} values with elongation of the alkyl side chain) could also be confirmed in these studies. Many stud-

ies have analyzed the toxicity of ILs on human cell lines ([85–87]). These in vitro systems have been extremely beneficial in studying the molecular basis of chemical's biological activity, including its toxic mode of action and could facilitate extrapolation of in vitro data with regard to possible effects on humans. Most studies dealt with HeLa cells exemplifying prototypical cells of the human epithelium which is normally the site of first contact of an organism with toxicants. According to Stepnowski et al. [87], the cytotoxicity data implied that effects of [C_4MIM] cation coupled with [Cl], [BF_4], [PF_6] were probably dependent on the anionic moieties. The EC_{50} value for [BF_4] species were found to be 0.63 mmol dm^{-3}, whereas [PF_6] and Cl inhibited HeLa cell growth at comparably high concentrations of 10 mmol dm^{-3}. Surprisingly, when the anion effect was compared, the strongest inhibition was found for [PF_6] alone. This might be due to hydrolysis affecting fluoride formation, thus causing serious toxicological consequences through the decomposition product. A similar phenomenon was observed by Ranke et al.[75] in IPC-81 leukemia cells, where the lower toxicity of [C_4MIM][PF_6] in comparison to the [PF_6] anion alone was explained by reduced anion activity due to the formation of an ion pair. For each cation class the toxicity increased with increasing chain length of the alkyl substitute for a given anion: [C_2MIM][Br] yielded an EC_{50} of 8.4 mmol dm^{-3}, substituting the ethyl moiety for a butyl group led to an EC_{50} of 2.8 mmol dm^{-3}, and for an octyl moiety an EC_{50} of 0.3 mmol dm^{-3}. This result was consistent with what has been observed in other studies. Salts containing the [BF_4] anion showed the highest EC_{50}, followed closely by bromide and chloride. [NTf_2] salts were significantly more toxic than their halide counterparts. However, the effect of changing the anion was smaller than that of changing the alkyl substituent, e.g. while [C_2MIM][BF_4] was observed to have an EC_{50} of 9.9 mmol dm^{-3}, the corresponding [Br] and [NTf_2] salts had EC_{50} of 8.4 and 1.8 mmol dm^{-3}, respectively, all considerably less toxic than [C_8MIM][Br]. The CaCo-2 cells were used in the study of Garcia-Lorenzo [86] with the purpose of a screening method for obtaining first rough estimates for the toxic potential of ILs. The obtained data showed that in general, ILs with longer alkyl chains were more lipophilic than those with shorter alkyl chains. It can be presumed to have a tendency to be incorporated into the phospholipid bilayers of biological membranes. In this respect, some authors have indicated that the increased toxicity of longer ILs can be accounted for enhanced membrane permeability altering the physical properties of the lipid bilayer ([75; 87]). Additionally, it has been proposed that the mode of toxic action for ILs takes place through membrane disruption because of the structural similarity of imidazolium-based ILs to detergent and antibiotics able to cause membrane-bound protein disturbance. Recently, in refs [78; 83] it was demonstrated that lipophilicity of ILs dominates their in vitro cytotoxicity over a wide range of structural variations. This indicates that ILs toxicity seems to be related to the alkyl chain branching and to the hydrophobicity of the imidazolium cation, but not to the various anions. In this respect, a recent study using the IPC-81 rat leukemia cell line with a large pool of anions demonstrated that most of the commercially available anions showed no or only marginal cytotoxic effects. However, anionic compartments with lipophilic and hydrolysable structural elements are likely to be of considerable relevance with respect to the toxicity of ILs [84].

Although a variety of experimental conditions are involved, all the studies (reviewed in refs [82; 88–90]) ensure a general interdependency between IL cation lipophilicity and toxicity, suggesting a mode of action which can be termed baseline toxicity. In particular, baseline toxicity is related to the hydrophobic interactions between chemicals and biological membranes resulting in a nonspecific toxicity, which is governed by solubility and lipophilicity. The observed toxic effects are explained based on the assumption that these cationic compounds adsorb on to and/or intercalate into biomembranes

[75; 84; 91; 92] resulting in a biomembrane perturbation which is at present poorly understood. The octanol/water partitioning coefficients of long imidazolium IL molecules which are correlated with toxicity data support this hypothesis and indicate their potential to interact with the biomembrane and to accumulate inside organisms. This is significant since the biomembrane is the most critical interface between the living organisms and their environment. Very recent molecular dynamics simulations of imidazolium-based ILs interacting with lipid cholesterol bilayers [93] and POPC bilayers[94] indicate a clear tendency of IL cations being incorporated tail-first into the bilayer, with overall destabilizing effects on the lipid structures. Experimental studies carried out by different techniques including AFM, quartz microbalance, fluorescence microscopy, differential scanning calorimetry, and electrophoretic light scattering showed that imidazolium-based ILs are capable of strongly interacting with phospholipid structures (liposomes or bilayers), creating defects and perturbations, including desorption from the solid support, structural rearrangement and fluidification, formation of sparse holes, and complete disintegration of the assemblies [95–98]. From these experimental works, molecular mechanisms are evidenced in explanation of observed toxic effects. This stimulates us to employ techniques of investigation focused on model cell membranes and external parts of living cells (glycocanes, phospholipid membranes, protein membranes, cytoskeleton)

1.4.3 The importance of cytoskeleton

The cytoskeleton, especially in its most external part of actin microfilaments, interacts with the cell membrane. Actin microfilaments are the thinnest filaments of the cytoskeleton, composed of linear polymers of actin subunits, and generate force by elongation at one end of the filament coupled with shrinkage at the other, causing net movement of the intervening strand. The bond between actin filaments net and the external membrane is so tight that, often, these interactions lead to a reorganization of cytoskeletal internal structure. It is evident that studying the elastic properties of a cell, the coupling of the membrane with the underlying net of actin must be considered. For this reason, in the last years it became more and more evident that surface tension and modification of the cell's mechanical properties has a great impact on its behavior [99; 100]. Many physiological cellular processes (i.e. cell division and migration) involve rapid morphological rearrangements which coincide with drastic alterations of the mechanical state of the cell membrane and cytoskeletal components [101–104]. In addition, the cells can feel changes in physical-chemical parameters that characterize the surrounding environment [105; 106], rearranging their cytoskeletal structure and consequently modulating the elasticity. These changes can also occur at the nanoscale, and induce differentiation from stem cell samples [107; 108]. Recently it has been demonstrated a strong correlation between the mechanical properties of the cells and their patho-physiological state: for example, the carcinogen cells show typically less stiffness than the corresponding healthy, in agreement with a greater ability to spread and migrate through the blood vessels and tissues during metastasis [109; 110]; similarly, the decrease in elasticity cell can be put in correlation with the change of the metastatic potential [110; 111]. Recent studies show that membrane tension directly affects polarisation of cells and migration related processes [101; 112]. The membrane tension is regulated and determined by the composition of the lipid bilayer (i.e. by cholesterol content and membrane reservoirs (caveolae)), the hydrostatic pressure and the engagement of the membrane with the cytoskeleton [102; 113; 114]. Of particular importance is the actin network. Indeed, changes of the dynamics and structure of the actin network play an important role dur-

ing the implementation of cell morphological changes. They are mediated by actin filament (de-)polymerization ("treadmilling"), crosslinking, contraction and coupling to the cell membrane via molecular clutches which altogether produce and transmit the necessary forces [115]. Microtubules are another component of the cytoskeleton and have very versatile tasks in cellular processes. They are essential in cell division generating and transducing the mechanical tension for chromosome segregation [116]. In migration they are involved in cellular traffic (vesicles and receptors) but they also participate in cell shape determination and cell polarisation by their mechanical properties and in the regulation of focal adhesion turnover. In addition there is a complex interplay between the mentioned components [115].

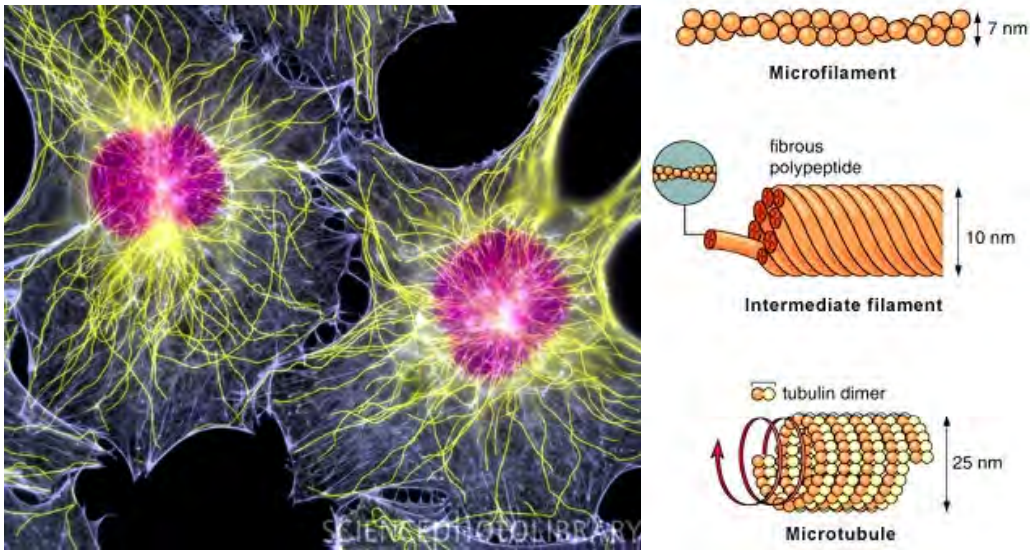

Figure 1.7: (left) Fibroblast cells. Fluorescent light micrograph of two fibroblast cells, showing their nuclei (purple) and cytoskeleton. The cytoskeleton is made up of microtubules of the protein tubulin (yellow) and actin filaments (blue) (taken from `http://amit1b.wordpress.com/the-molecules-of-life/about/` (right) The proteins that make up the cytoskeleton include: intermediate filaments are intermediate in size and include a variety of proteins that are similar in structure. These filaments enable the cell to maintain its physical structure by resisting pulling and stretching forces. Microfilaments consists of actin molecules. Microfilaments provide structural support for the cell but are also involved in cell motility and changing the shape of the cell. Microtubules are tube-like and determine the overall shape of the cell and the distribution of organelles. `http://www.mhhe.com/biosci/`

Hence, having a precise and reproducible method to measure the mechanical properties of cells is of certain interest and relevance. The atomic force microscope is broadly used to study the morphology of cells, but it can also probe the mechanics of cells. A new trend of applying AFM based technology to elucidate the mechanical basis of the cellular structure and its interaction with the extracellular matrix including cell to cell interaction is an hot research topic (reviewed in ref. [117–120]). As mentioned previously, the AFM allows to fully characterize some physico-chemical properties of the sample, including elasticity[121–123], thus allowing to realize topographic maps and elasticity in correspondence (the so-called combined topographic-mechanical imaging).

1.5 Aims and objectives

Since structural and mechanical investigations confirm the solid-like character of [C_4MIM][NTf_2] ordered lamellar nanostructures deposited on solid surfaces, an insulating, dielectric behavior, differently from the case of the bulk ILs is suggested. The first part of my work has been devoted to study in further details the electrical behavior of thin IL films on solid surfaces using the atomic force microscope, since its versatility in the electrical properties investigation of this kind of systems. The aims and objectives of this part are summarized as follows:

- Investigation of structural resistance of ILs solid-like islands applying large electrical fields between tip and sample.
- Test the conductivity properties of ILs solid-like domains
- Measure the dielectric constant of thin layers measuring the capacitance between the tip sample interface induced by an alternate voltage.
- Confirm the dielectric measures using an alternative technique consisting in to monitor the tip deflection induced by electrostatic field.

The findings of my PhD work highlight the potentialities of scanning probe techniques for the quantitative investigation of the electrical, mechanical and morphological properties of thin IL films. In fact my AFM investigation establishes how heterogeneous can be the IL/solid interfaces and so how is of fundamental importance to deal with local properties.

Furthermore, if confinement of ILs in solid-like structure is noticeable on flat ideal surface, a natural question arises about the behavior of ILs on more real nanostructured electrodes, very important for applications. For this reason, also preliminary studies have been conducted on nanostructured substrates(see Appendix A).

Considering the 'green' oriented properties of ILs, but at the same time their lipophilic character, the second part of my work has been devoted to study the interaction of ILs with biological materials, in particular focusing on biomembrane models and living cells. The aims and objectives of this part are summarized as follows:

- Perform a systematic investigation, carried out by electrochemical characterization techniques, of the interaction of different ILs belonging to the imidazolium cation family with phospholipid monolayers supported on Hg electrodes as a biomembrane model.
- Deepen the AFM morphological analysis of supported DOPC lipid bilayers interacting with various ILs, trying to capture the evolution of the sample and the kinetics of interaction through the AFM time-lapse imaging.
- Study the elastic properties of lipid bilayers supported by a rigid substrate interacting with various ILs, using combined AFM imaging/force spectroscopy analysis
- Run a combined topographical and mechanical imaging on living MDA-MB-231 (breast metastatic cancer cell line) at controlled temperature T= 37°C, with the purpose of quantitatively measuring the effect of exposure to ILs of external parts

of cell (membrane and cytoskeleton), through the measurement of morphological-structural (topography and cell spreading) and mechanical (Young's modulus) parameters.

The results obtained will be discussed, seeking a common trend between measures on phospholipid membrane models and cell membrane, performing comparative analysis of characteristic parameters of interaction.

Thesis outline

This thesis is organized into four chapters. Following this introduction (Chapter 1):

- Chapter 2 is focused on materials used to perform experiments and preparation of samples for analysis. The chapter continues presenting and explaining all the experimental setups and techniques used during the thesis.
- In Chapter 3 are described the results obtained measuring the electrical properties of thin layers of ILs and measuring the interaction of various ILs with biomembranes (model cell membrane) and living cells.
- Conclusions and outlooks follow in Chapter 4.
- In Appendix A is reported a study about characterization of thin ILs layers deposited on nanostructured films.

CHAPTER 2

Materials and methods

2.1 Ionic liquids in experiments: sample preparation

To study the electrical properties of thin ILs layers supported on solid surface, 1-butyl-3-methyl imidazolium bis(trifluoro methyl sulfonyl)imide ([C_4MIM] [Tf_2N]) was the most studied and characterized IL. The range of used ILs was enlarged to explore the interaction with biomaterials (phospholipid membrane and cells) analyzing the effect of the specific anion and cation lateral side chain length. As follows, the ILs added, with their specific nomenclature and abbreviation, are: 1-butyl -3-methyl imidazolium chloride ([C_4MIM][Cl]), 1-butyl- 3-methyl imidazolium tetrafluoroborate ([C_4MIM] [BF_4]), 1-ethyl-3-methyl imidazolium bis(trifluoro methyl sulfonyl)imide ([C_2MIM] [Tf_2N]), 1-methyl- 3-octyl imidazolium chloride ([C_8MIM] [Cl]), 1-methyl- 3-octyl imidazolium bis(trifluoro methyl sulfonyl)imide ([C_8MIM] [Tf_2N]), and 1-dodecyl- 3-methyl imidazolium bis(trifluoro methyl sulfonyl)imide ([C_{12}MIM] [Tf_2N]). All the ionic liquids were purchased from Sigma Aldrich, each with purity grade greater than 98.0%. In order to be stored in a clean way and to reduce water contamination, all the used ILs have been maintained in a desiccator under mild vacuum condition (around 10^{-2} mbar). All the used solvents (methanol, ethanol, acetone and chloroform) were purchased from Sigma, originally HPLC purity grade. The solvents, employed to dissolve ILs for drop coating deposition, were distilled twice prior the preparation of the solutions, in order to decrease the amount of non-volatile contaminants as well as water content. After the distillation, test samples were prepared by spotting the solvents onto a cleaned substrate. The distillation steps usually produce solvents that do not form any visible trace on the substrate surface, and the investigation with AFM shows a good cleaning level comparable with freshly clean samples.

For electrochemical analysis, the diluted working solutions were obtained by mixing an aliquot of the sample solution with a suitable amount of standard electrolyte solution to obtain the desired concentration of ILs (as standard electrolyte solutions, pH 7.4 phosphate buffered saline, PBS, of composition 0.1 mol dm^{-3} KCl and 0.01 mol dm^{-3} phosphate buffer, or 0.1 mol dm^{-3} KCl, all KCl calcined at 600 °C, were used). For hydrophobic ILs, a methanol(50%)$-$water(50%) solvent was employed to prepare IL sample solutions at 0.1 mol dm^{-3} concentration. Methanol concentration in diluted working solutions was always below 5% in volume. Due to its polar nature, methanol at such concentration should not have any marked influence on phospholipid layer structure, i.e. it should not interact with apolar phospholipid tails. Moreover, in previous work testing the effect of pharmaceuticals and gramicidin on the phospholipid monolayer methanol

working solutions were added to the electrolyte [124] and control experiments showed no effect of methanol on the monolayer. Prior to injection in the electrochemical cell, these working solutions were bubbled with argon gas to remove O_2.

2.1.1 Thin films of ionic liquids supported on solid surfaces

The depositions have been carried out using the method of the drop-casting of a dilute solution of IL into a volatile solvent. The reason is that in this way very thin coverages can be obtained, suitable for AFM investigation of the behavior of the first layers of IL in contact with a solid surface. As will be discussed in a section of the next chapter, the dissolution of the ionic liquid into a solvent, allows to deposit very small quantities of the IL on the substrate during the evaporation procedure. This gives the possibility to observe the effect of substrate-IL interactions that will be suppressed increasing the amount of liquid, but that are extremely important in the optics of understanding the behavior of ILs in confined geometries, like in nanoporous matrices. The deposition by drop coating has been performed on different substrates, principally smooth flat surfaces [62–64]. The most studied substrates have been amorphous silica coverslips, single crystal silicon covered by its native oxide layer and mica. These substrates have been chosen because they are smooth surface, even atomically flat (mica), so particularly suitable for an AFM investigation of the behavior of thin layers of ionic liquids. Some depositions have been performed also on MgO, TiO_2 and NaCl single crystal in order to see the behavior of $[C_4MIM][NTf_2]$ on other insulating surfaces. On the insulating substrates checked, ILs coexist in the form of micro and nanodroplets and flat ordered domains with solid-like character, as shown in the figure 1.3. The $[C_4MIM][NTf_2]$ thin films depositions consist in spotting a droplet of few microliters (on the order of 3-10 μl) of $[C_4MIM][NTf_2]$-solvent solution on the substrate of choice and allowing the volatile solvent to completely evaporate in air. Using solutions in which the IL concentration is typically maintained below 10^{-3} mg/ml, thin ILs films can be deposited. The density and the dimension of solid-like structures resulting from the solvent-free deposition are very different respect to those obtained in a drop coating deposition. It is possible that several factors contribute to this difference. First of all, the solvent decreases the strong interaction between the ions in the ionic liquid [13] so increasing the number of available conformations. During a deposition by drop casting, the ionic liquid is added to the surface in very tiny amounts since it comes from a solution. This means that the influence of the substrate, that is clearly the key factor in the formation of solid-like domains, becomes very important because the surface to volume ratio of small amounts of IL is very high. Moreover, the solvent evaporation induces the formation of terraces stacked one on top of the other, thanks to a driving force that pulls the IL molecules along the z direction.

Substrates were freshly prepared immediately before deposition of the $[C_4MIM][NTf_2]$ solution. Mica substrate was stripped with adhesive tape in order to obtain atomically smooth, cleaned surfaces. NaCl was mechanically cleaved in locally flat layers. Discs (13 mm-diameter) of amorphous silica (glass coverslips), squared specimens of polished oxidized Si(110), MgO and TiO_2 polished single crystal were all treated in acetone and in aqua-regia solution (HCl-HNO3 from, respectively, 37% and 69.5% solutions at ratio 3:1) before use, to remove organic contaminants and rehydroxilyse the surface. After aqua-regia the substrates are usually rinsed copiously with distilled water and then dried under nitrogen flux.

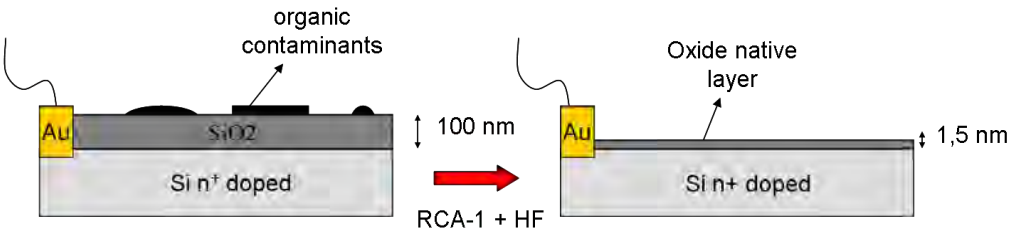

Figure 2.1: Diagram that represents the procedure of preparation and cleaning of silica substrate for electrical measurements before IL drop coating deposition.

2.1.2 Supporting substrates for electrical characterization

As shown previously, the preparation of the IL supported sample is an important step to obtain high ordered structure formation. Below is presented a new procedure with particular attention to the implementation of a deposition on a substrate suitable for capacitive measurements. Before the deposition and electrical measurements, the substrate must possess some important prerequisites:

- The substrate must be as clean and smooth as possible to avoid contaminants and morphological effects that could distort the interpretation of data obtained.
- The substrate should be insulator and hydroxylated to favor the formation of ordered layers.
- The sample should possess a conductive sublayer to act as counter electrode.
- The sample should be designed to minimize as much as possible the parasitic capacitance.

A sample that meets well these requirements and that can also ensure the formation of ionic liquids layers is a chip 1 cm x 1 cm of n^+ doped silicon with its native oxide layer (thickness ≈1.5 nm). These substrates, courtesy by M. Sampietro and G. Ferrari, Department of Electrical Engineering of the Polytechnic of Milan, have a golden pad dynamically connected to the conductive substrate for easy electrical connections. The sample provided is entirely covered with about 100 nm thick thermal oxide, a thickness too high for capacitive measurements with AFM. Chemical etching is used to remove quickly SiO_2 overlayer: bath in hydrofluoric acid solution with 7.7 nm/s etch rate. After several tests a standard procedure of cleaning and treatment of the substrate, in figure 2.1, has been established. Morphological analysis by AFM has confirmed the cleaning of the substrate according to the requested standards. Typically, during this procedure, a part of the chip is left out of the HF bath in order to obtain a step in the thermal oxide layer with a thickness roughly controlled by means of the etching rate.

The layer of thermal oxide is used in calibration procedures for capacitive measurements because has a mean dielectric constant, measured by Gomila et al. in [125] with nanoscale impedance microscopy, of $\varepsilon_r = 4.6 \pm 1.2$. The thickness is measured with a profilometer because the step gradient, extended for more than 100 μm due to the corrosive vapors, is too wide for AFM analysis. Moreover, to decrease the parasitic capacitance in the AFM capacitive measurements, the sample sizes are reduced obtaining

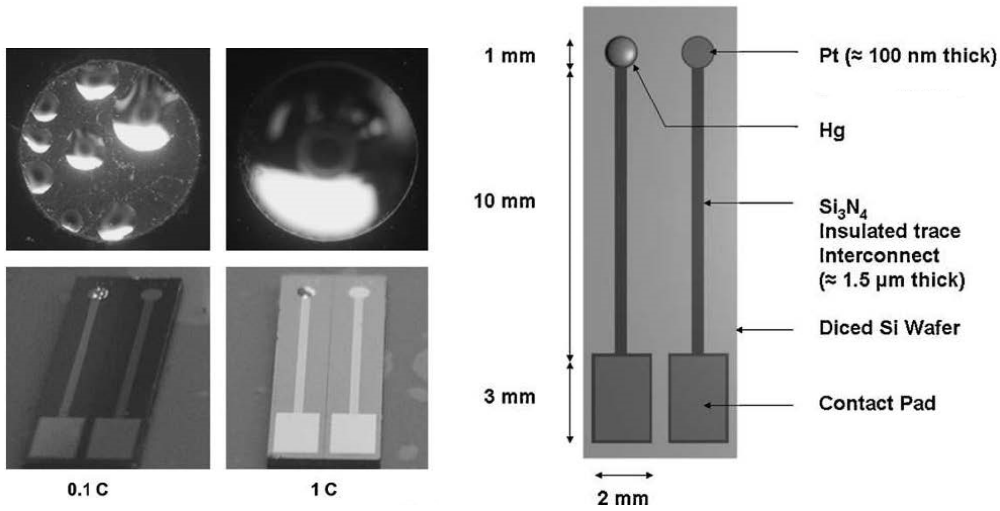

Figure 2.2: (left) Pt/Hg electrodes differing in the charge passed to electrodeposit Hg. Above each charge value is showed a photograph of the electrode and a low magnification reflection optical microscope image. (right) Schematic diagram of the Pt/Hg electrode . Images reproduced from ref. [126]

a thin strip of silicon large 1-2 mm, so that the AFM tip, approaching the surface of the sample, will have a large part of the support (cantilever, chip and tip-holder) away from the counter-electrode, enhancing local contributions in the output signal coming from the tip.

For silicon surface, aqua regia is used to eliminate metallic/organic contaminants and to restore hydroxyl groups on the surface (as explained in section 2.1.1). Since the sample has gold connections the aqua regia treatment is not indicated. A mild treatment is however sufficient to obtain a clean and smooth substrate: a bath in acetone for 15 min with sonication followed by RCA-1 procedure (H_2O: NH_4OH: H_2O_2 - 5:1:1) for 30 min. The sample is subsequently rinsed in distilled water and methanol. The drop-coating deposition was finally performed with $[C_4MIM][Tf_2N]$/methanol solution on the silicon native oxide substrate.

2.1.3 Samples for electrochemical analysis

The microfabricated Pt/Hg film electrodes were supplied by the Tyndall National Institute and are exhaustively described elsewhere [126][127]. Briefly Pt discs with a radius of 0.480 mm were embedded on a silicon wafer substrate, addressed via Si_3N_4 -insulated interconnections to 2.54 mm Pt electrical contacts. Electrodeposition of Hg on to these Pt discs was carried out in a standard three electrode cell with 0.05 mol dm^{-3} $Hg(NO_3)_2$ (Sigma-Aldrich Co.) at -0.4 V. One coulomb of charge was passed during the deposition in order to produce a Hg film with surface area of 0.744 mm^2, calculated for the semioblate spheroid geometry [128].

The Hg film electrode (MFE) was then rinsed with 18.2 MΩ Milli-Q water and dried under nitrogen gas before use. Before each experiment, all glassware and internal com-

ponents of the electrochemical cell were cleaned with piranha solution (30 wt% H_2O_2 + 98 wt % H_2SO_4 in ratio 2:1) then rinsed with 18.2 MΩ Milli-Q water. Hg indeed can present a toxicity risk in its use in a sensing device. However, in the system used by the authors this risk is minimized by a fabricated wafer-based electrode system where the amount of Hg used is so small that it is below the legal toxic threshold. Moreover, the Hg is supported on a Pt base to which it is bound. This maintains the Hg in a stable robust configuration. Its stability was evidenced by putting the electrode in a high vacuum for SEM measurement[129] with no ensuing loss of Hg following the measurement. For rapid cyclic voltammetry measurements (RCV described in section 2.3.1), the phospholipid coating was deposited on to the Hg from 0.2 mg cm^{-3} DOPC (Avanti Polar lipids Inc.) dispersion in water of which $0.1-0.2$ cm^3 was injected into the flow cell. For alternate cyclic voltammetry and electrochemical impedance spectroscopy measurements (ACV and EIS described in section 2.3.2), DOPC monolayers were prepared by carefully spreading $10-20$ μcm^3 of a 2 mg cm^{-3} DOPC solution in pentane at the argon/electrolyte interface. Upon the evaporation of pentane, DOPC lipids form a collapsed monolayer at this gas$-$water interface. By slowly lowering the MFE through this lipid layer at the interface, a monolayer can be transferred to the MFE. Following the work of Scheuring et al. in ref. [130], another deposition method was used. A 15 ml drop of PBS solution was deposited into a Teflon well and a 0.2 ml drop of lipid mixture (2 mg cm^{-3} DOPC solution in pentane) was spread on the drop to form a monolayer. The monolayer was adsorbed to freshly MFE, touching the top of the confined drop with the surface of electrode.

2.1.4 Deposition of supported phospholipid bilayers

The phospholipid molecules (in this case of DOPC: dioleoyl phosphatidylcholine from Avanti polar lipids) are dissolved in a chloroform solution at a concentration of 10 mg/ml. The solution is then dried with a stream of nitrogen until the chloroform is completely evaporated. The amount of lipid is selected to prepare a final concentration in solution between 0.1-0.2 mg/ml . This parameter is important for the formation of lipid bilayers, in fact, the surface density of lipid vesicles on the substrate must be sufficiently high to promote their rupture on surface and the subsequent formation of the lipid bilayers. The dried lipids are subsequently rehydrated making use of 1 ml of high ionic strength buffer solution 450 mmol dm^{-3} KCl, 25 mmol dm^{-3} HEPES(4-(2-hydroxy ethyl)-1-piperazine ethane sulfonic acid). Understanding how the buffer solution influences the phenomena of adhesion and spreading of the vesicles is an essential point to understand the formation processes of the lipid membrane [131–133].

An high ionic strength is necessary to shield effectively the electrostatic repulsive interaction between the negatively charged mica surface and phospholipids heads. After rehydration, lipids are vortexed for a few minutes, until all the lipids are suspended in solution. After being vortexed, the lipids are found suspended in the solution and thanks to the hydrophobic effect form vesicles and liposomes. These vesicles have a tendency to merge together and form larger and multi-layered liposomes (onion-like). Subsequently, the lipids solution is inserted in a sonicator for 15 minutes. This step appears to be important for the production of a sample of lipid bilayers of good quality. The effect of sonication is to break the bigger multi-layered vesicles, favoring the formation of smaller single-layered vesicles. The sonication is decisive for the quality of the sample: clean and uniform single bilayers are deposited. After sonication, the solution containing the

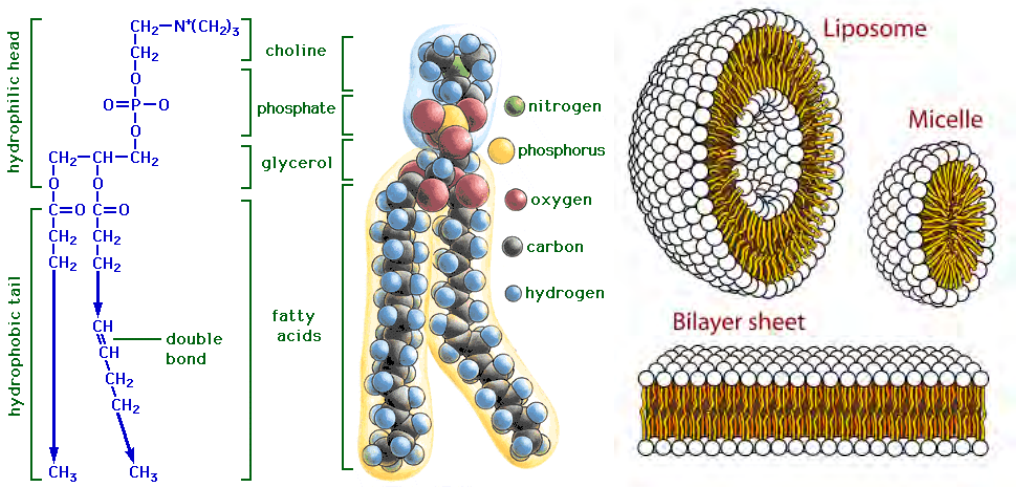

Figure 2.3: (left) Molecular phospholipid structure. The three main structures phospholipids form in water solution; liposome (a closed bilayer), micelle and bilayer sheet.

lipids is deposited on a freshly cleaved mica surface in the amount of 40 μl with 15 minutes incubation time. During this period, the deposition takes place: vesicles adhere to the substrate and merge to form supported bilayers. The protocol proceeds with the elimination of deposition buffer (HEPES + NaCl), obtained with a regular and gentle flux of nitrogen, useful for the fixing of the lipids. Finally, the sample is rehydrated to perform AFM measurement in fluid environment, using the so-called imaging buffer. Pure solution of pH 7.4 phosphate buffered saline, PBS, of composition 0.1 mol dm^{-3} KCl and 0.01 mol dm^{-3} phosphate buffer, was used as imaging buffer. The amount of imaging buffer is set to 3 ml to not overcome the petri capability. On this quantity, the concentrations of tested compounds are calculated.

2.1.5 Preparation of live cells specimens for AFM analysis

The cell lines used in the context of this work are coded as MDA-MB-231 (breast adenocarcinoma). It was not available in the literature reports on AFM nanomechanical measurements and investigation of interaction of MDA-MB-231 with ionic liquids. For more details on the line MDA-MB-231, see refs. [134; 135]. The MDA-MB-231 cell line were cultured in Dulbecco's modified eagle medium (DMEM) (Lonza) supplemented with 10% fetal bovine serum (FBS; Sigma-Aldrich), L-glutamine 5 mM, 100 units/ml penicillin and 100 units/ml streptomycin in 5% CO2, 98% air-humidified incubator (Galaxy S, RS Biotech, Irvine, California, USA) at 37°C. Cells were detached from culture dishes using a 0,25% Trypsin-EDTA in HBSS (Sigma-Aldrich), centrifuged at 1000 x g for 5 minutes, and resuspended in culture medium. Subcultures or culture medium exchanges were routinely established every 2nd to 3rd day into Petri dishes (d $\approx$ 10 cm).

In order to obtain results comparable to those exhibited by in vivo cells, and at the same time, to make the largest number of AFM measurements out of the same sample, it is necessary to recreate (as far as possible) the physiological conditions for the survival

of cells (atmosphere with addition of 5% CO_2 and 37 °C). In particular, the temperature is the most critical parameter for the stability and viability of cells. In order to thermalize the culture plates at a temperature close to 37 °C, a custom fluid cell for AFM measurements was then realized (see Fig. 2.4). The petri dish containing the cells and the culture medium is represented by the more internal petri, magnetically attached to the bottom of external petri with larger diameter; the interspace formed between the two plates is filled with distilled water. The correct temperature for the culture medium is achieved by means of a resistor contained in a strip of very thin and transparent plastic material attached to the bottom of the external petri and sandwiched , during measurements, between the two petri dishes, which are thermally connected by water in the interspace. The resistor (R≈40Ω) is powered by an external current supply, while temperature is measured with a thermocouple immersed in the internal petri. After testing, it turned out that instead of controlling the current supply by means of PID controller fed by the thermocouple, it was more reliable to set a constant current which, upon heat dissipation, was able to maintain the desired temperature. It is necessary to calibrate the system to obtain the correct correspondence between voltage applied to the resistor and the temperature measured by thermocouple in culture medium. A problem is represented by evaporation of the solution, which changes the concentrations of the individual components of the culture medium, with harmful consequences for the health of the cells. To solve this problem, a plastic cap with a special hole to favor the passage of the AFM head (containing piezoelectric element, detection system and tip-holder) was realized. This expedient has the defect of partially limit the movement of sample, but allows to solve the evaporation problem to good extent, forming a local atmosphere saturated with vapor. The whole system does not affect significantly the optical microscope visibility, and allows to keep the temperature of the culture medium at values close to 37 °C, allowing in turn to acquire measurements on the same sample for several hours (typically up to 5h) before the cells manifest obvious signs of distress. Thanks to the thermostatic cell, up to 10 cells from the same culture can be imaged for the sake of statistics.

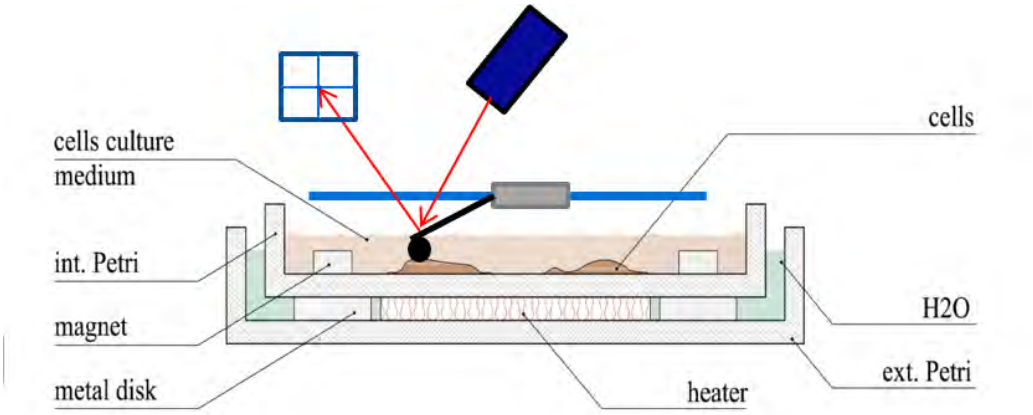

Figure 2.4: Schematic of of the system used for thermalization and fixing of the cell culture plates

2.2 Atomic force microscopy

The major part of the investigation during my PhD work was carried on by Atomic Force Microscopy (AFM). AFM is a scanning probe technique that allows to obtain quantitative information on the topography of conductive and insulated materials with nanometer resolution [136; 137].

During AFM imaging procedure, the sample is scanned by a nanometric tip mounted on a elastic lever. The force between tip and sample is controlled by monitoring the deflection (static or dynamic) of the lever spring (cantilever). The topographic image is reconstructed by recording the vertical position of the piezoelectric, which moves to maintain constant a signal coming from cantilever deflection, as a function of the xy position of the tip.

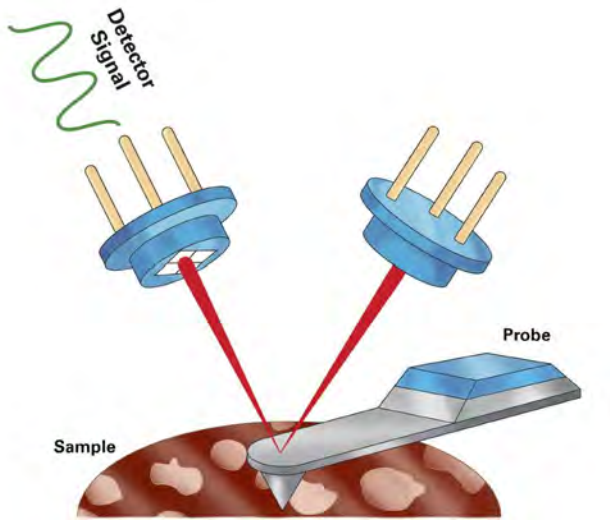

Figure 2.5: Schematic of light source, cantilever, and photo detector reassembling the basic components of the light-lever AFM detection system.

Contact mode (CM) works while maintaining a continuous and constant contact between the tip and sample. CM images are taken at small tip-surface distances, where the total tip-surface force is repulsive (the vdW interaction is smaller than the short range atomic repulsion) (review for high resolution CM in ref. [138]). The small (angular) movement of the lever is commonly measured by a laser beam that is reflected off the cantilever and directed onto a split photodetector, as shown in figure 2.5. Due to the feedback loop that monitors the deflection, if the tip encounters an obstacle on the flat surface, the deflection increases, and thus the feedback makes sure to retract the tip to restore the value of the deflection setpoint. In contact mode, tip is always in contact with the surface, thanks to an applied load. The movement of the z-piezo then becomes the sample topography that is plotted as a function of xy. The feedback loop, controlled by gain, must be fast enough to allow the z-piezo to respond to changes in sample topography but slow enough to avoid noise. Even though reasonably easy to operate, additional concerns arise when working with soft samples, such as biological samples or liquid drops, in fact contact mode has the inherent drawback that lateral force exerted on the sample can be quite high. This can result in sample damage or in drift of relatively

loosely attached objects.

The solution to the problem of having high lateral forces between the cantilever and surface, but still maintaining very high lateral resolution, is performed with the tip touching the surface only for a short time, thus avoiding the issue of lateral forces and drag across the surface. This mode was hence referred to as tapping mode (TM) (review for TM explanation in refs. [139; 140]). In tapping mode cantilevers with higher force constants are used (30-60N/m). In TM operation, the cantilever is oscillated near its resonance frequency (usually around 200-400KHz) normal to the sample surface. Typical amplitudes of oscillation are in the range of tens of nanometers, and thus very small compared to the cantilever length. Assuming air damping is the dominant factor, the movement of the cantilever can be described using the (sinusoidal) driven damped harmonic oscillator. Instead of the cantilever deflection (i.e. of the constant applied force), the amplitude of oscillation is monitored by the feedback loop. In this way the time in which the tip contacts the surface during the movement of the sample for the scan is very limited, so greatly reducing the problematic lateral forces. Even though normal loads can be high even in this modality (pressures can be of the order of 0.2KBar), in air environment the high reduction of friction forces allows the acquisition of high resolution maps on fragile samples like lipid bilayers, proteins and even liquid droplets. Drawbacks to use tapping mode is the difficulty to perform analysis in liquid environment, due to increase of noise and additional oscillation modes coming from petri cell. Moreover, the direct force control of CM imaging is lost in TM operations.

2.2.1 Force curves

Along with the operation with the scanning modalities, it as to be remembered that AFM is one of the most sensitive force sensor existent (along with optical and magnetic tweezers). For this reason AFM can be used to perform force spectroscopy measurements, by ramping the AFM tip against the sample surface and monitoring the force between them as a function of the tip-sample distance (review for force curves explanation and analysis in ref. [141]). It is important to underline that force spectroscopy can be coupled to the imaging, so allowing to find the area of interest and then to perform measurements on specific positions located from the morphological map (See for example P&S in section 2.2.3). The basic output obtained performing a standard force spectroscopy measurement with an AFM, is a force curve (FC). The force curve is a curve acquired recording the variation of a quantity of interest (deflection, TM deflection, amplitude of oscillation, lateral force), as a function of the distance traveled by the piezoelectric crystal.

A typical force curve, in the specific case a deflection vs. distance curve, is shown in Figure 2.6. The FC is performed ramping the tip against the surface of the sample (or the sample against the tip, depending on the type of instrument used), along the vertical axis (z-axis). In the absence of long-range forces, during the first part of the approaching the deflection remains constant (point 1 in Figure 2.6). At point 2 there is the jump-in event, i.e. the tip jumps to contact under the action of surface attractive force (capillary meniscus formation or van der Waals); the region 3 is the contact region, in which a strong repulsion acts between the tip and the surface. Normally, when performing force spectroscopy, a threshold on the deflection is fixed, the trigger setpoint: once the trigger is reached, the motion of the tip is reversed, increasing the tip-sample distance. The region 4 in figure 2.6 extends from the trigger to the point 5, where there is the jump-off event, i.e. the tip detaches from surface and comes back to the non-interaction part,

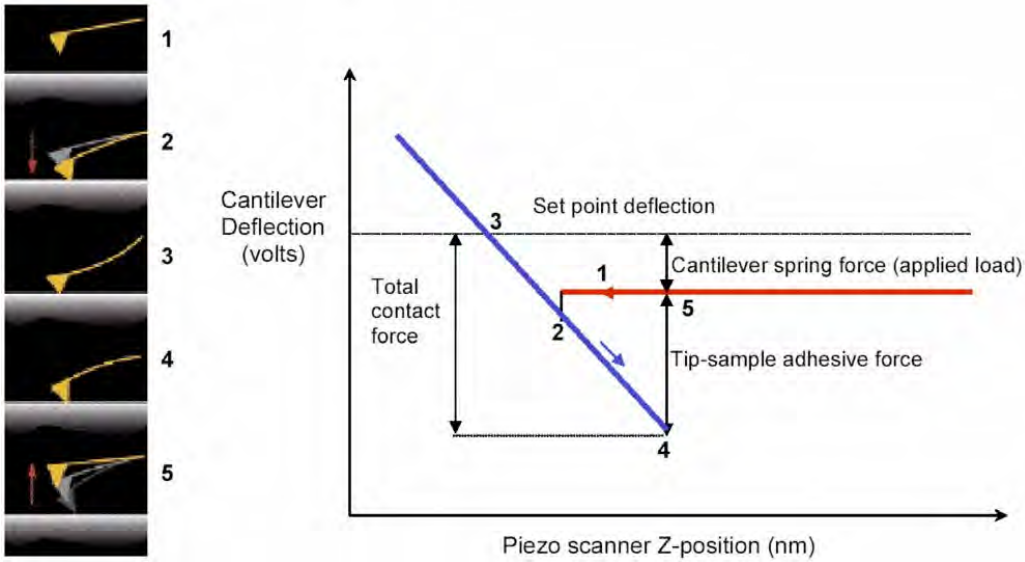

Figure 2.6: Force distance curve. The approach (red) and withdraw (blue) curves are shown on the right. Note that the total contact force is dependent on the adhesion as well as the applied load.

returning to the starting position. As can be noticed, point 2 and point 5 are not located at the same tip-sample distance, because of the interaction with the sample that traps the tip until a certain deflection, and so a certain force, necessary to free it is reached: this force is the adhesion force, and is related to the details of the interaction between the tip and the sample. At this step, the raw FC has in abscissa the distance traveled by the piezo during the ramp, that is set by the user, while in ordinate does not report a force, but a deflection signal in Volts.

In order to get a real force curve, i.e. reporting a force, for example in nN, versus the distance between the tip and the sample, two operations must be fulfilled: first, it has to be measured the deflection sensitivity (zsens) and then the cantilever force constant has to be calibrated. The zsens is necessary to convert from V to nm the deflection signal. In order to obtain a correct conversion, the acquisition of a force curve (usually more than one to measure an average) is performed on a cleaned rigid substrate, whose stiffness provides negligible deformations compared to the deflection on the cantilever in the range of forces applied. The contact part of this FC in nm units, is expected to be linear with unitary slope, because the only contribution is due to the cantilever bending and the amount of deflection in volts is equal to the distance travelled by the piezo driving the tip: the correction factor, i.e. the zsens, is the inverse of the slope of the contact part of FC. Now the FC is converted in deflection in nm vs. the distance traveled by the piezo. Anyway it is more physically significant to show the deflection as a function of the tip-sample distance. To this purpose the z-axis needs to be rescaled in such a way that the point of contact (jump-in, point 2 in figure 2.6) corresponds to zero. If there is no indentation, all the points of the part of the FC should lie on a vertical line at deflection d=0.

The tip-sample distance is calculated as $z = (z_p\text{-}z_0)+d$ (see Fig. 2.7), where z_p is the distance travelled by the piezo, d is the tip deflection in nm, and z_0 is the offset to shift the contact point (jump-in) at $d = 0$. At this point a force vs. tip-sample distance curve

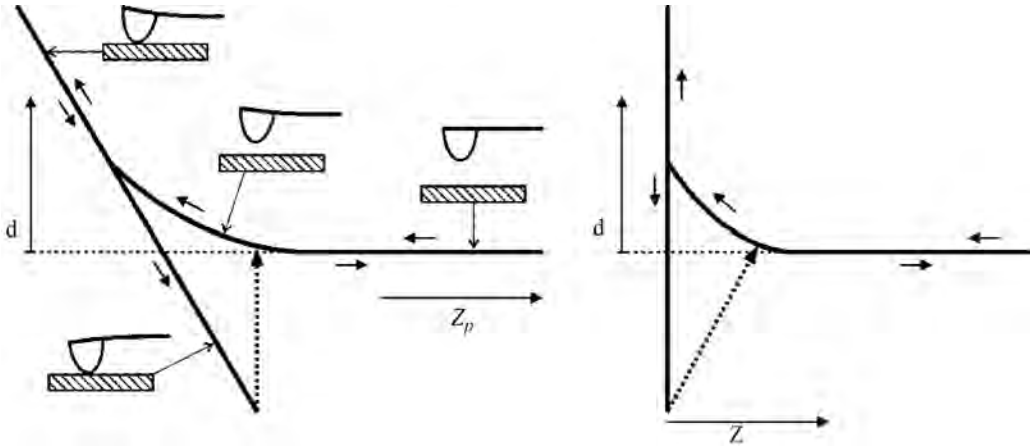

Figure 2.7: Schematic of a typical cantilever deflection-vs.-piezo height (d-vs.-Z_p) curve (left) and corresponding d-vs.z plot, with z = (z_p-z_0)+d. Figure taken from ref. [141]

can be obtained multiplying the deflection by the elastic constant k of the cantilever. Among several methods that can be used for the calibration of a cantilever (see Ref. [142] for a review on the argument), the thermal noise [143–145] was chosen. Thermal noise is a non invasive method for the calibration of the force constant based on the measurement of the free oscillation of the cantilever due to thermal energy, that is based on the equipartition theorem. For the k calibration it is only necessary to measure the temperature of the room, perform some force curves in order to calculate the zsens and then acquire the thermal spectrum. If standard rectangular cantilevers are used, the force constant can be calculated with an accuracy of 5-10%.

Force curves alone can reveal a variety of sample properties, such as adhesion and stiffness. As an aside, there is an imaging mode called Force Volume (FV See section 2.2.2) that is based on pixel-by-pixel analysis of force curves. The most common use of force curves is in combination with any of the forms of AFM imaging in a "point-and-shoot" fashion.

2.2.2 Force Volume

Force volume (FV) is force spectroscopy methodology in which, a force curve is made on every point of a regular matrix defined on that area [146; 147] (see Figure 2.8). FV measurements were mainly used for nanomechanical characterization of ionic liquid thin layers, supported phospholipid bilayers and living cells. In order to perform a FV, first of all an area of interest has to be selected. The area is then scanned in FV mode, collecting force curves by ramping the tip until a common maximum force (deflection) is reached. The morphology is reconstructed from the ensemble of FC by recording the absolute vertical positions at which the trigger deflection is reached, for each point defined in the matrix. The morphology in a FV is then always acquired at a force corresponding to the trigger force (see Figure 2.8).

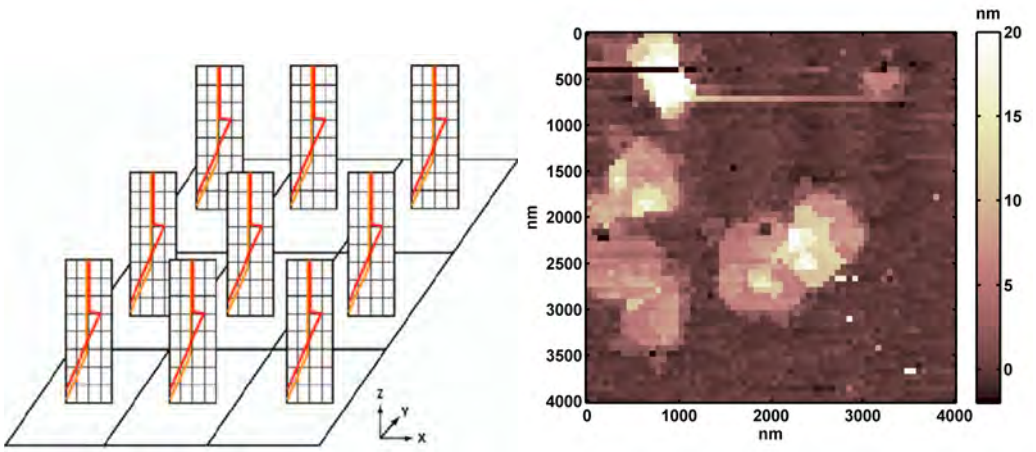

Figure 2.8: (left) Scheme showing the principle of FV measurement. A force curve is acquired in every point on a matrix defined on an area of the sample. (right) Example of a topographic image acquired in FV mode.

In a typical force volume 64x64 force curves can be collected. Force curves, in the specific case of my work, are usually performed using ramps 500 nm long for phospholipid bilayers and 5 μm for living cells analysis, with 2048 points each curve. In general the resolution of force curve depends on the size of object under analysis. Ramp rates usually ranges between 1 and 6Hz. The measurements were generally performed in liquid environment (PBS buffer solution). The output of a FV consists of a 3D matrix containing, for each position defined along the scan area, a force curve. The output of a force volume is analyzed by using specific routines developed in Matlab environment. In order to acquire reliable data, the scan area have to be chosen in such a way that always a reference part, i.e. the substrate, is visible and available for comparison. On the topography acquired in FV, a mask can be defined in order to mask out all the points that don't belong to the substrate. The mask is then passed in input to a routine that selects only those curves corresponding to the point not excluded by the mask. If the curves have been acquired on the rigid substrate, from their slope the deflection sensitivity can be calculated and successively used to convert the deflection signals from Volts to nanometers, as described in the previous section. This is very useful in the characterization of nanomechanical properties of soft material on which the zsens calculation is difficult. From a FV output, different maps in 1-1 correspondence with topography can be calculated. For example, adhesion map is a map reporting, for each point, the vertical distance (in force units), between the non-interaction part of the force curve (at high distances) and the pull-off point, immediately before tip detachment. The adhesion force, that is mainly related in air to capillary forces, can reveal heterogeneities on the surface that are not evidenced in the topography or, on the contrary, can show how different domains visible in the topography can have compatible physico-chemical properties. Another example is the stiffness map, built collecting the elasticity modulus of the sample. The contact part of each rescaled FC is analyzed using suitable models.

There are several drawbacks working in force volume. First of all, the number of points in FV 3D matrix is limited, because for each point a force curve is acquired too, and memory limits do not allow more than 64x64x2048 points. If the image resolution is increased, the resolution must be decreased and viceversa. Furthermore the FV is a

technique intrinsically slow: for example the acquisition of 128x128 curves with a ramping rate of 5Hz, will take about one hour. This is a problem for systems in temporal evolution like living cells. Special expedients will be considerate in section 2.2.5 to solve the problem. Therefore, the slow topographic map, built during the ramping, limits an extensive exploration of the sample surface needed to locate the areas of interest.

PeakForce tapping

In this framework a special mention must be devoted to the new high-speed FV also called PeakForce tapping [148–150]. PeakForce Tapping is a new imaging mode that operates similarly to tapping mode in that it avoids lateral forces by intermittently contacting the sample. For this reason, PeakForce tapping could substitute the tapping mode in fluid. All the morphology measurements on phospholipid bilayers were carried on using this nem modality. However, it is very different from tapping mode, in fact it operates in a non-resonant mode. The PeakForce tapping oscillation is performed at frequencies well below the cantilever resonance, thus avoiding the filtering effect and dynamics of a resonating system. As in FV mode, the tip, approaching the sample surface, will experience long-range van der Waals attraction, causing the cantilever to jump into contact with the sample. After contact, the short range repulsive forces dominate the interaction, leading to the peak point at the approaching curve. When the tip begins to retract it goes through an adhesion minimum, usually caused by capillary meniscus and finally becomes free. PeakForce tapping refers to the individual peak force points as triggering mechanisms to force the z-piezo to retract. PeakForce tapping also avoids another phenomena that plagues TappingMode. The cantilever amplitude in conventional TappingMode can change as a result of both long range and short range interactions. As a result, the height data represents the system response to a combination of interactions. PeakForce Tapping only responds to short range interaction. The long range interactions (adhesive and electrostatic forces) are basically ignored for height control. The system operates also at very low forces, which in turn is crucial for obtaining high resolution data on soft samples like phospholipid bilayers.

2.2.3 Point & Shoot

If AFM operates in FV mode it is possible to directly look for a good area on the surface through the FV topographic map, that as explained previously is very time-consuming. For these reasons, another spectroscopic technique was sometime used: the Point & Shoot (P&S). P&S measurements were mainly used for electrical characterization of ILs layers and only marginally for nanomechanical characterization of supported phospholipid bilayers.

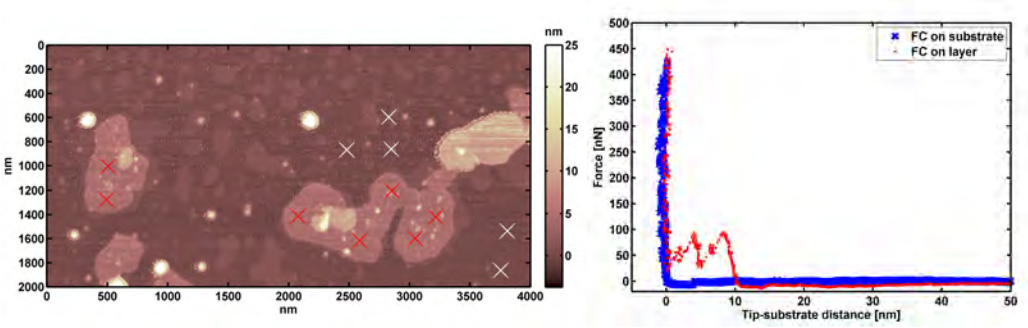

Figure 2.9: (left) Scheme showing the principle of P&S measurement. A force curve is acquired in every point on a custom grid (or sparse series) defined on an area of the sample. (right) Example of different FC acquired on IL layer (red crosses) and substrate (white crosses)

In general a P&S can be executed after the acquisition of a morphological maps: several points on the map can be marked by the user, as the crosses in Figure 2.9 show. For each point specified by a cros,s one (or multiple) force curve is acquired. This technique has several advantages compared to FV. The main advantage is the possibility to locate the area of interest during standard imaging, and then using the same tip to perform standard deflection vs. distance curves. Before a standard P&S all imaging mode are available, allowing the acquisition of high-resolution maps, useful to carefully choose the places where to perform the force curves and also for looking to the effect of the spectroscopy on the area of interest by a subsequent morphology acquisition. A second important advantage respect to FV is that the acquisition times are greatly reduced, because the high-resolution map permits to carefully select the points of interest where to acquire force curves. In the case of nanoscale impedance measurements, i.e. flat islands on flat substrates, a limited number of curves (100-150) is usually enough to have a good statistics. In the time needed to acquire an FV, several PS can be acquired moving on different areas of the sample. Another advantage of P&S combined mode is the possibility to acquire multiple signals for each force curve, for example z capacitance vs. z_p simultaneously to deflection vs. z_p. As shown in section 2.2.6, the force curves acquired on solid-like islands are in 1-1 correspondence with capacitive curves acquired simultaneously. For biological materials (biomebranes and cells) P&S was generally used in the first preliminar analysis to check the feasibility of nanomechanical setup, then a FV approach was chosen to have at least 4096 points every image.

2.2.4 Characterization by AFM of phospholipid bilayers

Time-lapse AFM imaging

The lipid bilayers were analyzed morphologically by means of PeakForce Tapping mode particularly suitable for measurements on biological samples in fluid due to absence of lateral force and controlled normal load. Sharpened contact silicon tips (Vista probes), with a nominal radius of curvature below 10nm and a typical spring constant of 0.3 N/m were used. Preliminarily, the sample is explored in order to find an area that is sufficiently good, i.e. that present an adequate population of lipid bilayers and exhibiting a sufficient portion of the substrate in order to compare them. Time-lapse AFM imaging is a technique whereby AFM images are acquired at well defined time intervals. If the frequency at which imaging frames are captured (the frame rate) is high enough, it is possi-

ble to follow the temporal evolution of the sample, in particular the effect of compound on phospholipid bilayers (for examples and discussion see section 3.2.2). PeakForce tapping at medium-low resolution (512x256 points) is suitable also to perform time-lapse imaging, leading the time acquisition interval to 3-4 minutes.

Force spectroscopy

The force spectroscopy by means of atomic force microscopy in total, covers a range of interaction ranging from 10-10^4 pN, the curve that contains the greatest number of information is the approaching curve, but some sensitive data of importance can also be extracted from the retracting curve in particular as regards the adhesion forces. Sharpened contact silicon tips (Vista probes), with a nominal radius of curvature below 10nm and a typical spring constant of 0.1N/m were used. Most of the studies regarding the nanomechanics of lipid bilayers, especially the most recent ones, concentrate on the quantitative determination of the breaktrough force threshold. However, prior to the plastic failure, a variety of interaction forces arising between the cantilever tip and the phospholipid surface can be detected. This is schematically exemplified in raw FC in Fig. 2.10 and treated FC in 2.11. Starting from a non interaction zone, the tip gradually approaches to the surface of bilayer. No interaction is observed at distances much larger than the film thickness.

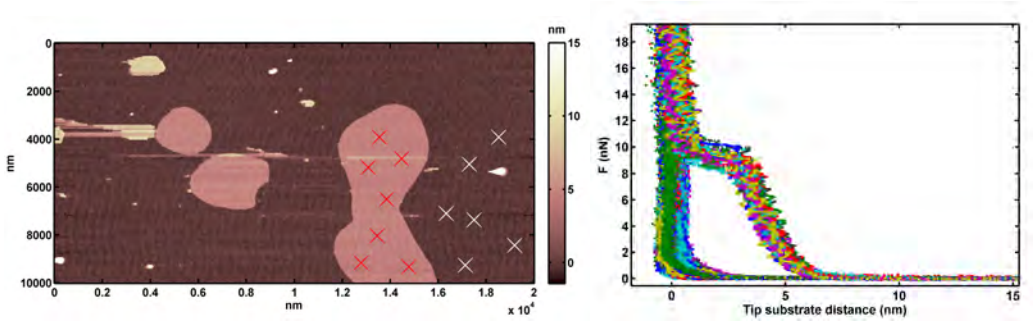

Figure 2.10: Typical point and shoot output. On the left-hand side the morphology, in this case acquired in PeakForce tapping mode, is reported. Each cross on the image represent a point where a force curve has been acquired. Red crosses represent FC on lipid bilayer, white crosses are performed on substrate. On the right-hand side, there is a plot reporting a raw force curve acquired on flat lipid bilayer, highlighting electrostatic force, jump to contact and breakthrough force event.

At closer distance, but before the mechanical contact between the two elements, a DLVO electrostatic interaction is detected by the tip with the deflection signal [141]. In general, the majority of phospholipid molecules are negatively charged. On the other hand, the silicon tips used to perform force spectroscopy experiments are known to be slightly negatively charged at neutral pH [141]. So, the interaction between the silicon tip and a layer of phospholipids neutral pH is repulsive as they are both negatively charged (Figure 2.11). The surface charge is balanced by the dissolved counterions which are attracted to the surface by the electric field, but spread away from the surface to increase the entropy. At large distances, this electrostatic double-layer force decays roughly exponentially. The decay length of this interaction, called Debye length [151], depends on

the ionic strength of the solution. For a salt solution it is:

$$\lambda_D = \sqrt{\frac{\varepsilon\varepsilon_0 k_B T}{2ce^2}} \qquad \text{(monovalent salt):} \quad \lambda_D = 0.304[nm]/\sqrt{c} \tag{2.1}$$

The Debye length λ_D is determined by the salt concentration; c_i is the bulk concentration in mol/l of the i_{th} ion species and Z_i their valency [141]. For PBS buffer solution used in this experiment, the predicted theoretical Debye length with eq.2.1 is calculated λ_D=0.76 nm. For the force curve in Figure 2.11 λ_D =0.93 in agreement with theoretical value.

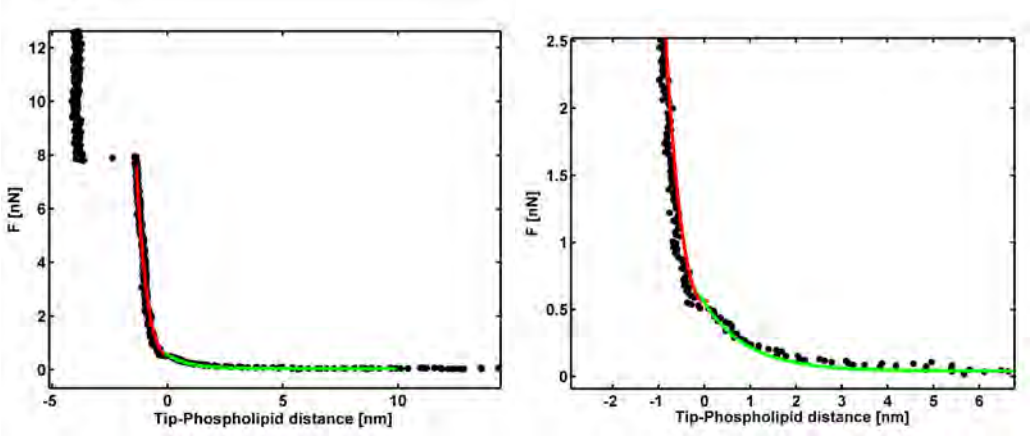

Figure 2.11: Typical force curve correctly rescaled, performed on lipid bilayers in PBS buffer solution supported on mica surface (left). For each curve a recursive fitting procedure is performed to individuate the contact point that separate the electrostatic DLVO interaction (green fit line) and mechanical compressive interaction (red fit line). To underline the nanometer resolution of this analysis, a magnification is presented in the right image.

Sometimes also additional repulsive forces are detected, related to steric interactions and hydration of the water molecules in proximity of hydrophilic heads of the phospholipids [141]. In the configuration used in experiments these forces are not visible. The electrostatic interaction must be taken into account before mechanical analysis because it could mislead the determination of tip-bilayer contact point. For this purpose, a recursive fitting procedure with constrained optimization, performed in Matlab environment, was used to determine the contact point with surface of bilayer. Knowing the contact point, it is possible to fit the non-contact part with DLVO model 2.2 and extract useful parameters. For constant charge conditions (insulating surfaces) the electrostatic double-layer force is:

$$F = \frac{2\pi R\varepsilon\varepsilon_0}{\lambda_D}\left[2\sigma_S\sigma_T e^{-z/\lambda_D} + (\sigma_S^2 + \sigma_T^2)e^{-2z/\lambda_D}\right] \tag{2.2}$$

Where z represents the tip-surface distance, σ_S and σ_T represent the tip surface charge of surface and tip respectively and R the tip radius. Surpassing the area of repulsive interaction, so after the contact point, the tip is directly in contact between the lipid bilayer and start to elastically deform the layer. Connel et al. [152] consider a theoretical model to interpret the mechanical interaction, in which a supported lipid bilayer

of thickness 2d is probed by an AFM tip of radius R in contact mode and the force is measured as a function of the indentation δ from the unperturbed surface of the layer. For small penetration δ, a simple function fits the experimental range of forces and especially for R > d, is:

$$F = \frac{\pi \kappa_A R}{4} \left(\frac{2\delta}{2d - \delta} \right)^2 \tag{2.3}$$

The force diverges as z_0 approaches 2d because the area per lipid diverges in order to preserve molecular volume. Experimentally this divergence is pre-empted by pore formation during breakthrough event. In Figure 2.11 For comparison, the contact force between two solid elastic bodies much larger than the radius of contact (Hertzian contact) F is proportional to $\delta^{3/2}$ [152](see for comparison Hertz equation 2.4).

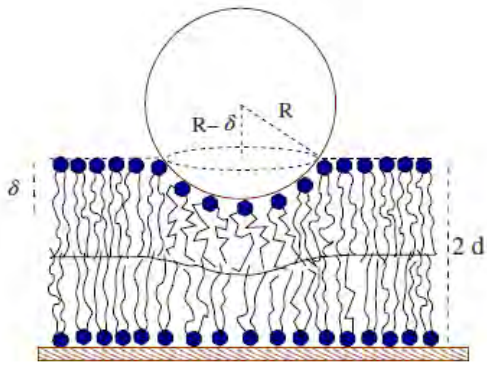

Figure 2.12: Schematic geometry of an AFM tip of radius R indenting a bilayer of thickness 2d by an amount δ. Image taken from ref. [152]

More relevant for AFM experiments, the response in Eq. 2.3 scales differently than this scenario, and force is proportional to the area compressibility modulus instead of Young's modulus Eq. 2.4. The developed model [152] provides an excellent fit until 2d$-\delta \approx$2.5 nm, at which point the elastic energy of the deformed bilayer overcomes the cost of forming a hole and the tip penetrates the full bilayer. This effect is also called breakthrough event. It is an event that depends on the kinetic force applied and is stochastic [151; 153]. The breakthrough force will be distributed around the most probable value. May possibly appear even two steps to jump-through, due to the penetration of two bilayers, but the statistical analysis will be restricted to the single bilayers. The penetration mechanism of an AFM tip through a supported lipid bilayer has already been successfully connected to the spontaneous formation of lipid pores (hydrophilic or hydrophobic) [153]. Most likely, the penetration of an AFM tip in a supported lipid bilayer involves the formation of a larger hole with respect to the spontaneous formation of a lipid pore in an unsupported lipid bilayer. The connection results from considering the role that fluctuations have with respect to the formation of a hole. Most of the studies concentrated on the force value at which the jump-through phenomenon occurs whereas, typical elastic properties which could be extracted from the force indentation has received less attention. It is more precise to define the properties related to the jump-through event as concerning "mechanical stability" rather than "mechanical properties",

which could suggest to examine, for example, the variation of the area compressibility modulus of the bilayer.

To calibrate analysis routine, 64x64 resolution force volume measurements were performed on DOPC bilayer suspended on mica in PBS solution at 25°C. A typical example of basic force curve on this system is showed in Fig. 2.11. As explained, temperature (25°C) and ionic strength (PBS saline buffer) are important parameters to be maintained in steady state.

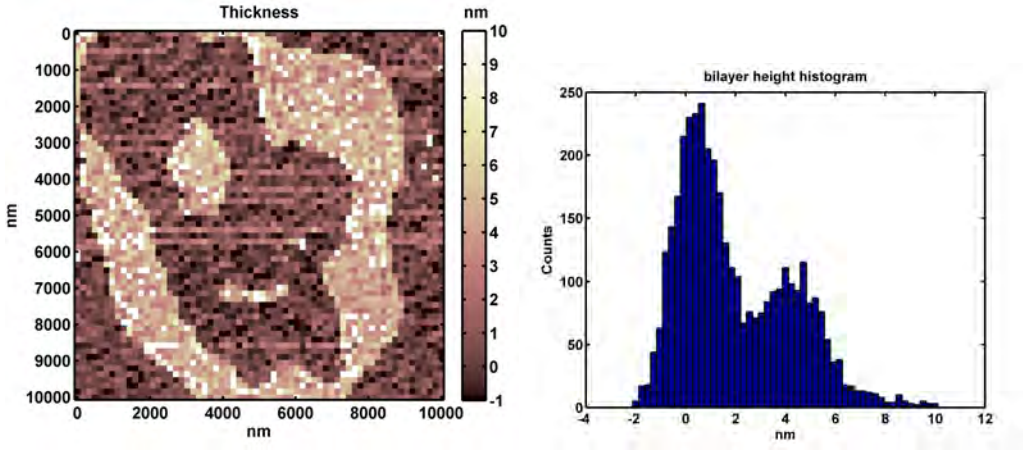

Figure 2.13: Thickness map (left) of DOPC bilayer. The image is reconstructed analyzing all the single FC and is completely equivalent to morphology. The quantitative analysis is performed with histograms(right) and Gaussian distribution fit

In the recursive fitting procedure with constrained optimization, the height of bilayer depends by the contact point, so is a free parameter during the procedure. This parameter separates the fits of mechanical and DLVO interaction. This method is useful to characterize the bilayer thickness with good precision, so that calculated thickness map is perfectly equivalent to standard morphology. Moreover, the thickness value obtained here (2d = 4.2$\pm$0.4 nm) is in agreement with theoretical (2d=4.1 nm at 22°C) and experimental values (2d = 4.0 nm at 22°) from ref. [154]. The authors in ref. [154] also performed force spectroscopy analysis on DOPC and DPPC bilayers revealing that the interaction between the tip and the surface was governed by electrostatic forces for longer range and by steric forces at shorter range. Electrostatic repulsion originates from an effective charge density at the bilayer-water interface, where headgroups interact with water molecules. Using pure water as buffer solution the electrostatic DLVO interaction is not screened, leading errors in the correct determination of contact point with DOPC bilayers. Using force spectroscopy analysis the authors overestimate the bilayer thickness (2d = 6.1 nm at 22°).

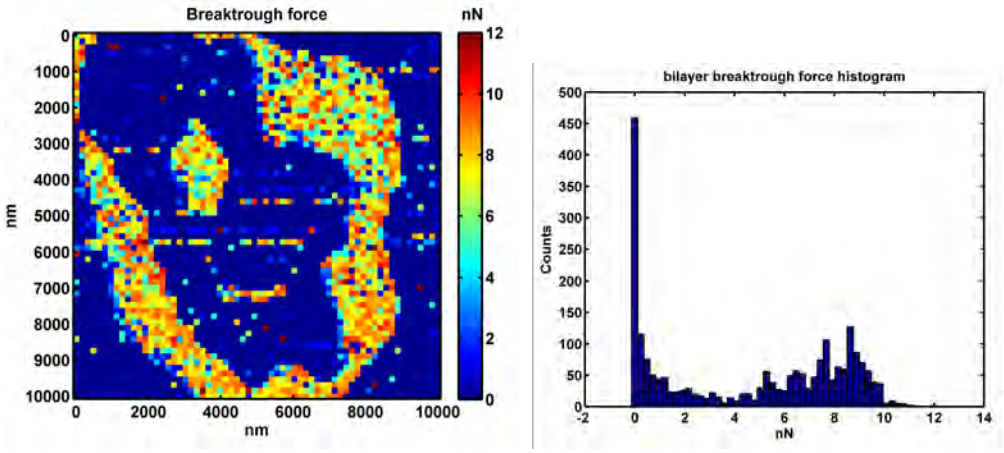

Figure 2.14: Breaktrough force map (left) of DOPC bilayer. The map is reconstructed analyzing all the single FC. The quantitative analysis is performed with histograms(right) and Gaussian distribution fit

Interestingly, the chemistry of the hydrophilic supporting substrate where the bilayers are adsorbed does not significantly affect the yield threshold determination [155]. By contrast, the chemistry of the AFM tip has shown to have a significant effect on the nanomechanics properties of the measured supported bilayers [156]. In general, typical experiments are performed with hydrophilic tips, either using bare silicon tips. Furthermore, when bare silicon tips are used, especially under high ionic strength conditions, a second bilayer can form on the cantilever tip apex. Upon approaching the "sample" bilayer, the force plots exhibit two consecutive breakthrough events; in these cases, the resulting force plot recordings are not taken into account for data statistics. The force value at which such breakthrough events occur, is strongly dependent on the physicochemical parameters (tip status, ionic strength, temperature) used in the experiment. Dealing with the jump-through event, if one describes it as a chemical reaction, it is to be expected the rate of the process be modified by temperature with an Arrhenius type trend. So, an increase of the temperature will induce the transition across the intermediate state for lower force values. The role of ionic strength of divalent and monovalent cations was known to have an effect on the packing properties of lipid bilayers, thus increasing the mechanical stability (and the breakthrough force) of lipid bilayers. The tip status is the main source of uncertainty because can not be controlled in a simple method. For this reason the breakthrough force values in literature span huge interval [153; 155] (from 4nN to 20nN) depending on different experimental conditions. If breakthrough force parameter is very sensitive to tip chemical status and dimension, the area compressibility modulus is a more stable parameter to describe the mechanical properties of lipid bilayers.

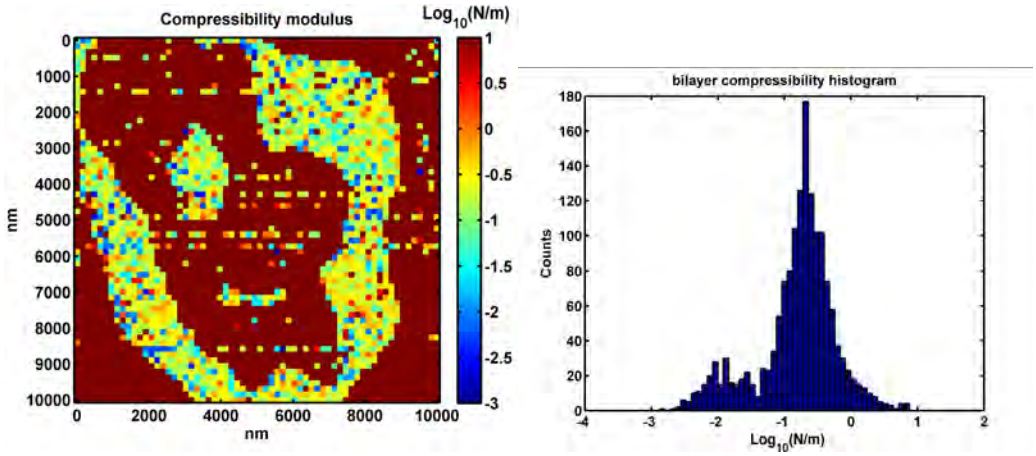

Figure 2.15: Compressibility modulus map (left) of DOPC bilayer in logarithmic scale. The image is reconstructed analyzing all the single FC. The quantitative analysis is performed with histograms(right) and Gaussian distribution fit

The best fit for the area compressibility modulus for R=10 nm, using eq. 2.3, is κ_A =0.21 N/m. Because of the uncertainty in the tip radius, the range of κ_A for R between 5 and 15 nm is between 0.32 and 0.11 N/m, respectively. Our estimate compares well with the literature values κ_A=0.13–0.6 N/m from osmotic pressure measurements [152] and κ_A=0.18-0.04 N/m from micropipette aspiration of giant unilamellar vesicles (GUVs) made of pure DOPC [152] and 0.265N/m from theoretical work in ref. [157]. Also with this parameter, the main uncertainty in experiments and fitting procedures is due to the uncertainty in the tip radius R. However, the simple linear dependence on R means that relative measurements taken with the same tip can be compared very accurately.

2.2.5 Live Cells

The general procedure used for nanomechanical measurements on living cells and the complete analysis is exhaustively discussed in [158]. The measurements were performed with spherical colloidal tips manufactured and characterized in the laboratory[159]. Borosilicate glass microspheres were strongly attached to commercial AFM cantilevers exploiting the capillary adhesion force due to the formation of a water meniscus, and then soldered to the cantilever by thermal annealing of the sphere-cantilever system at a temperature slightly below the softening point of borosilicate glass (800°C for 3 hours). The radius of the tip is statistically characterized with a protocol based on the AFM inverse imaging of colloidal probes on spiked gratings. In comparison with standard sharp tips, these spherical tips are particularly suitable for nanomechanical experiments on cell because their geometry is controlled and well defined (very useful for implementation of contact mechanics model) and the pressure applied to the soft sample is reduced thanks to increased surface area. Using a large probe in force spectroscopy experiments is also useful to obtain non-local properties averaged on cell surface to measure the mean effect of cytoskeletal components. A big tip radius decreases the lateral resolution during imaging, but in the case of cells, typical lateral dimension are between 50 and 90 μm, well wider than dimension of colloidal probe. As shown in Fig. 2.16 a good image quality is achieved.

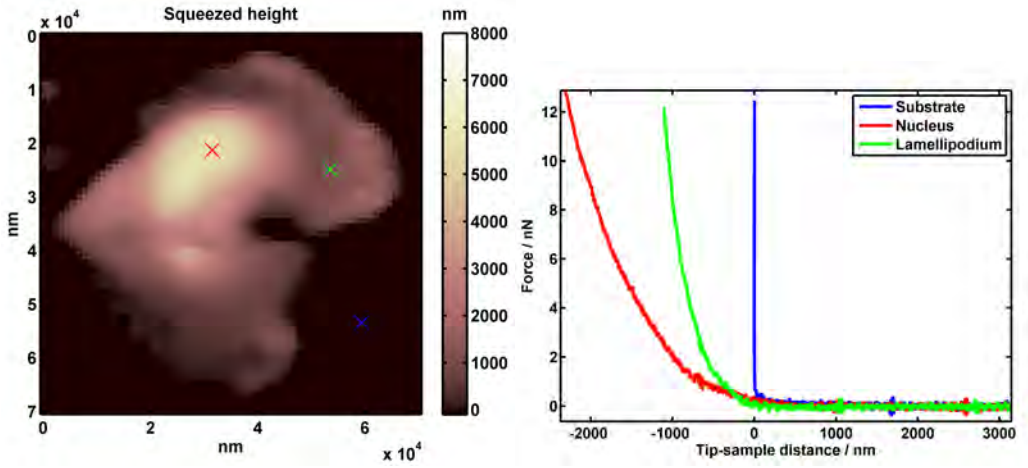

Figure 2.16: (left) FV topography map for a MDA-MB-231 living cell. Force curves on subtrate, cell nucleus and cell lamellipodium are represented by blue, red, green crosses respectively. (right) Using the same scale of colors (blue, red, green), the force curves rescaled and aligned are shown

Given the complexity of the system under consideration and the strong variability of the elastic parameters, the Young's modulus data were acquired in logarithmic scale, fitted with Gaussian distribution and subsequently transferred with log-normal distribution TO linear scale. For microscopy experiments, this kind of measurements are very time expensive, in fact a standard acquisition procedure consists in:

- Transport of sample with MDA-MB-231 culture from incubator (37°C and CO_2 atmosphere) to microscope stage (37°C)
- Investigation of sample with optical microscope searching cells suitable for AFM nanomechanical experiments
- Nanomechanical analysis in FV mode of few (2-3) cells.
- Contamination of sample with compound at controlled concentration (incubation time ≈20 min).
- Nanomechanical experiments trying to follow the cells analyzed in previous step.
- Repetition of experiments varying the concentration of contaminants.
- At the end of experiments the sample is washed with bleach and disposed of.

In analogy with nanomechanical experiments on phospholipid bilayers also in this situation the force curve is the basic element to investigate the sample, but the analysis is widened in μm range. A typical nanomechanical experiment is performed with spherical tip with a measured radius about 4900 nm, and attached on a rectangular cantilever with elastic constants of 0.21 N/m. Standard parameters for force volume: length of ramp gained 5 μm , force trigger setpoint $F_{MAX} \approx$ 10nN, approaching velocity v_a = 43.4 μm/s scan rate 7.1 Hz. The experiment is performed in FV mode at maximum resolution 64X64, containing 4096 curves, each of which consists of 2048 points, leading to resolution of about 2.5 nm/point per curve. All the experiments were performed in the cell culture medium, using the fluid cell described in section 2.1.5. The topography of the sample is acquired using the setpoint value of maximum cantilever deflection. In parallel, it is possible to analyze the contact part of each force curve to obtain a local map of elasticity (Young's modulus). In summary, developing an appropriate set of algorithms ([158]), it is possible to realize, through a single measure, a combined topographic-mechanical imaging.

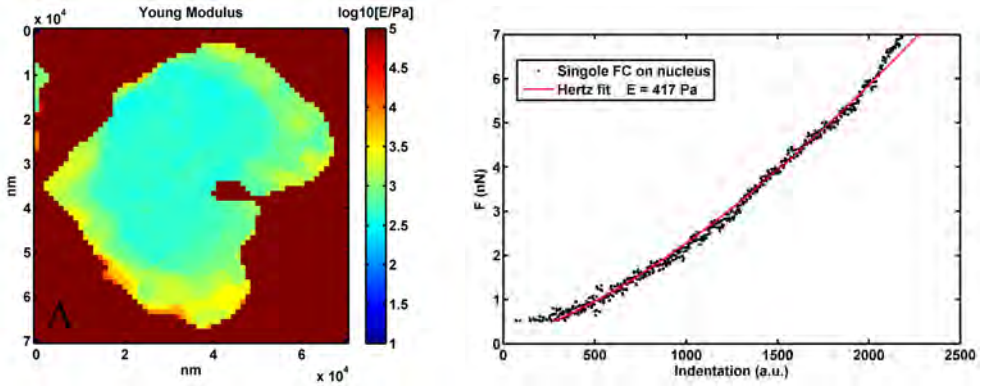

Figure 2.17: (left) Young's modulus map for a MDA-MB-231 living cell obtained with Hertzian fit. (right) Single force curves on nucleus showing the fit (red solid line) obtained using equation 2.4

The contact part of a force curve is analyzed using well discussed ([158]) Hertz model and the Young's modulus is extracted as a characteristic parameter of material (see Fig. 2.17). Young's modulus, also known as the tensile modulus or elastic modulus, is a measure of the stiffness of an elastic material. It is defined as the ratio of the stress along an axis over the strain along that axis in the range of stress in which Hooke's law holds. It can be experimentally determined from the slope of a stress-strain curve created during tensile tests conducted on a sample of the material. In anisotropic materials, Young's modulus may have different values depending on the direction of the applied force with respect to the material's structure. The Hertzian classical theory of contact focused primarily on non-adhesive contact where no tension force is allowed to occur within the contact area, i.e., contacting bodies can be separated without adhesion forces. For the validity of the Hertz model [160], it is supposed that sample must be homogeneous, isotropic and perfectly elastic (no friction), the deformation should not exceed the limit of elasticity of the material (the model is therefore not valid to describe plastic deformation), and more general deformations must be small compared to the characteristic size of the analyzed system (radius of curvature of the probe, height and width of the

sample). For these systems holds:

$$F = \frac{4}{3}\left(\frac{E}{1-\nu^2}\right)\sqrt{R}\delta^{3/2} \tag{2.4}$$

Where F is the applied force, δ the indentation in soft sample, ν the Poisson's ratio, E the Young's modulus of the material, and R the radius of the colloidal tip. When a material is compressed in one direction, it usually tends to expand in the other two directions perpendicular to the direction of compression. This phenomenon is called the Poisson effect. Poisson's ratio ν is a measure of this effect. The Poisson ratio is the fraction of expansion divided by the fraction of compression, for small values of these changes. An important question arises about the basic limit of elastic deformation of the sample. Dimitriadis et al. [161] studied in detail the question, and calculated the axial strain in function of the applied force (according to the model of Hertz). They note, in particular, that for 100 nm curvature radius the strain of the sample is significantly higher than in the case of micrometric probes with the same force applied, in addition, this value is not negligible even for law forces (1 pN), below the sensitivity limit of the AFM cantilever with the softest commercially available (k 0.01 N/m). Using micrometric probes, however, the order of some nN forces can be reached, with equal indentation: also in this case, the strain may be not negligible. The authors assume conservatively a value equal to 20% of strain as a limit for elastic behavior. For this reason traditional sharp probes involves substantial risks regarding the damage of the cell and not precise calculation of mechanical parameters misleading the actual properties exhibited by cells in vivo and in physiological conditions.

The fundamental part of the analysis is the treatment of raw force curve. For each FV the zsens is calculated using a topography mask built on the substrate, to select force curves acquired on hard flat surface. Knowing the zsens, all of the curves are rescaled in force vs. piezoelectric distance. To convert the x-axis in useful tip-sample distance, the recognition of the contact point is required but definitely not a simple task because of low adhesion in fluid environment and indentation of soft sample.

The contact point

For the determination of the contact point, the following strategy has been developed, applicable automatically on each force curve. The single curve, rescaled in force vs. piezoelectric distance, is aligned vertically, then in function of the applied force. The contact point on the surface δ_0 is detected binning the vertical axes of force and recognizing the non-contact part as a maximum peak. In fact, most of the values are concentrated around the origin, corresponding to the region not to contact, while the values for the contact zone are dispersed in a long tail. To obtain such a distribution it is necessary to have a large non-contact region (from which the choice to set a ramp size of the order of several micrometers), and assume a correct alignment of this region. The presence of large fluctuations and distortions (for example, if some object floating in the cell intercepts the laser beam incident on the cantilever) can introduce significant errors and invalidate the procedure for the curve in question. Also a possible offset, due to an imperfect alignment of laser, cantilever and detector must be taken in to account, aligning the non-contact region. The distribution obtained binning the vertical axis is fitted with a Gaussian function, and all the points of the force curve below the mean value are sub-

jected to smoothing to reduce the noise level. The new curve is reshaped, discarding all points below the mean value of the distribution + 1 std value. The contact zone has the lower extreme sufficiently close to the true contact. In this way, the part of non-contact, usually quite noisy, is eliminated. The final step is similar to the method described previously to find the contact point δ_0 on phospholipid bilayers. The selected contact region is fitted using the equation 2.4 (or more complex equations described later) leaving the contact point δ_0 as variable in the fit procedure. When δ_0 is known, the x-axis of each force curve is rescaled subtracting that value, thus aligning all the FC set at the contact point.

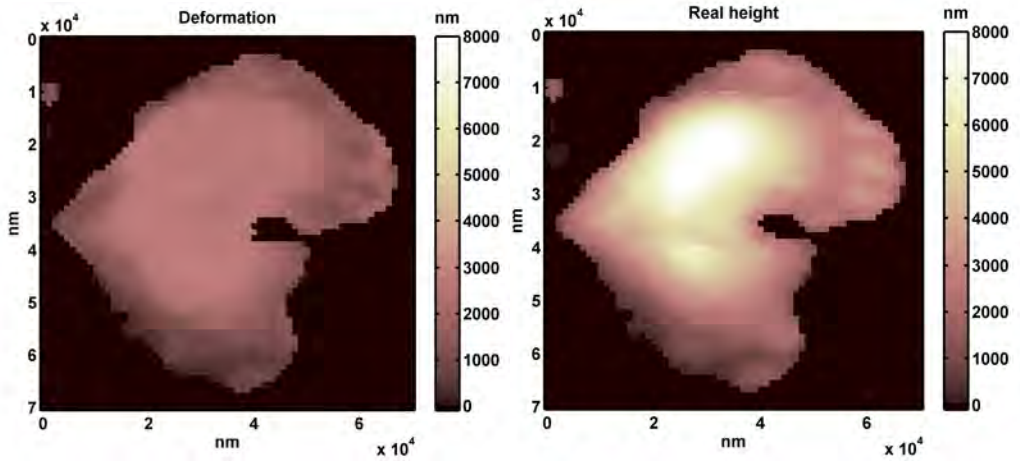

Figure 2.18: (left) FV deformation map for a MDA-MB-231 living cell obtained considering the contact point δ_0. (right) Real topography map of a MDA-MB-231 living cell, obtained summing the compressed morphology in Fig. 2.16 with deformation map.

However, the image obtained does not corresponds to the real height of sample, but represents a compressed topography: the cantilever reaches the value of maximum deflection indenting the sample of a quantity corresponding to the difference between the maximum value of indentation (in rescaled force curve) and the contact point δ_0. It is therefore necessary a post-processing of the data, using appropriate algorithms for each curve (and consequently for each point on the map) to calculate a map of the local deformations. At the end of morphological analysis the real topographical map of the system is obtained adding, to the compressed topography, the deformation map as shown in Fig.2.18.

Finite thickness correction

A fundamental prerequisite for Hertz model is an amplitude deformation negligible compared to the size of the sample (ideally infinite thickness). For elastic film supported on incompressible surface, when thickness is small (comparable to indentation), an apparent Young's modulus typically larger is measured; this is called finite thickness effect. Therefore a correction in Hertz model is necessary. Dimitriadis et. al [161] introduce a correction factor in the force-indentation relationship for spherical tips, that is function of Poisson's ratio ν and a parameter χ linked to the tip radius, indentation and sample height $\chi = \sqrt{R\delta}/\mathrm{h}$. The final expression of the corrected force linearized with inden-

tation, in the case of biological sample almost incompressible ($\nu \approx 0.5$) linked to the substrate is the following:

$$\delta = \alpha F^* \text{ where } \alpha = \left(\frac{9\left(1-\nu^2\right)}{16E\sqrt{R}}\right)^{2/3} \text{ and } F^* = \left(\frac{F}{\Delta}\right)^{2/3} \tag{2.5}$$

$$\text{The correction parameter } \Delta = [1 + 1.009\chi + 1.032\chi^2 + 0.578\chi^3 + 0.051\chi^4]$$

From Eq. 2.5 the correction is not relevant if R and δ are small compared with the thickness of sample. It was then obtained again a model in Hertzian form, where the correction for the effect of finite thickness is included in the effective force F*. In addition, the linearization process which led to Eq.2.5 brings several advantages. At a computational level, it allows to drastically reduce the computation time compared to a non-polynomial fitting, it is also possible to apply the procedure of matrix-fitting to the whole map of force curves acquired through force volume.

From a physical point of view, this procedure allows to recognize, in a clear and direct way, the presence of different indentation regimes, corresponding to different slopes (and thus different values of effective Young's modulus), demonstrating the heterogeneity and complexity of cytoskeletal structure. In figure 2.19 different regimes, hidden in standard FC curves, are well visible plotting $(\text{force})^{2/3}$ vs. distance. These regimes could hypothetically correspond to membrane+actin contribution for low indentation interval and actin+tubulin contribution for high indentation interval.

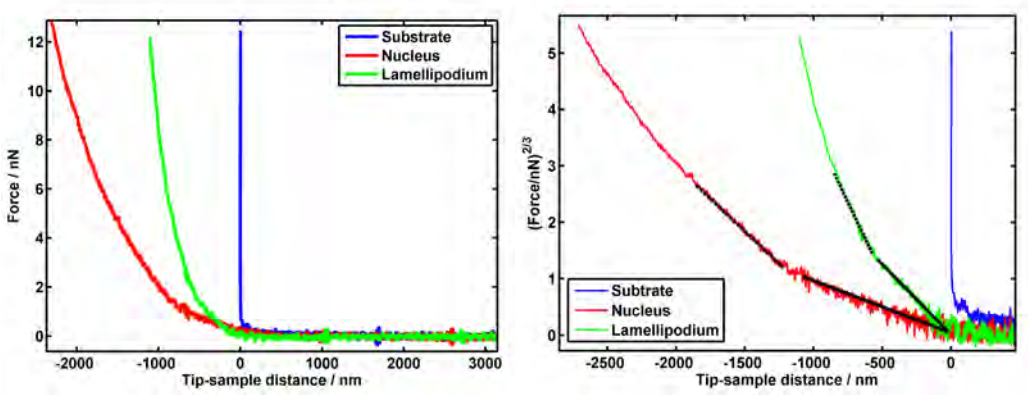

Figure 2.19: Comparison between force vs. distance curves for substrate(blue), nucleus (red) and lamellipodium (green) presented in Fig.2.16 and $(\text{force})^{2/3}$ vs. distance for the same 3 FC. Using flat black segments, different slopes are evidenced.

Moreover, it is possible to distinguish at first sight the non-validity region for the Hertz model, corresponding to the indentation range over which the scaled curve is non linear. It should be however noted that the presence and the characteristics of these effects depends on the single force curve, and is not always possible to notice in a direct way without computing with appropriate algorithms. Returning to the merits of

the finite thickness correction, it is important to highlight the dependence of the factor χ to indentation, either directly through the variable δ, and indirectly through the height h (necessity to rebuild the real topographical map of the sample from the compressed topographical map, calculating the deformation). The indentation also depends on the correct identification of the point of contact. it follows that this parameter must be estimated as accurately as possible, in order to obtain reliable results quantitatively. Ultimately, the correction developed by Dimitriadis et al. is implementable in a relatively simple way for the case of cells and spherical probes, without having a significant cost in computational terms and allowing to remove the artifacts induced on Young's modulus by the presence of a rigid substrate (regardless of the height of the single sample) and to fully exploit the entire surface of the cell, without the elimination of areas potentially rich in information such as lamellipodia, or cytoplasmic protrusions in general.

A deeper analysis of effective Young's modulus requires also the identification of different elastic regimes for all FC as in figure 2.19. The automatic recognition is based on the definition of percentages, calculated on the maximum indentation (or similarly the height real). This type of approach is based on the assumption that height variations (inside the single cell), can modify the amount of cytoskeletal material proportionally. Consequently the thickness of the different components (actin, tubulin, intermediate filaments) and the width (in absolute indentation) of the different regimes of elasticity are proportional to the total indentation,divisible in percentages (low indentation interval and high indentation interval). This hypothesis is very strong, although reasonable, and an empirical validation is required on a significant number of curves, selected possibly on different cells and different areas within the same cell [158].

Figure 2.20 highlights the effect of finite thickness correction on the same MDA-MB-231 cell. As expected, the finite thickness correction has the tendency to homogenize the effective Young's modulus of whole cell showing only minor differences between the nucleus, cell body and lamellipodium. The quantitative analysis with histograms is depicted in figure 2.21. Differently from simple Hertz model, with finite thickness correction only slight differences are shown for different indentation regimes. Correction on high indentation regime has more influence because of substrate, leading to similar behavior for all hertzian indentation.

Estimation of errors

To estimate a quantitative value of the error attributable to the mean value of Young's modulus, the presence of different sources of error must be considered, including the statistical errors on population of different cells, the experimental noise and the uncertainties related to the characterization of the experimental parameters (elastic constant of the cantilever deflection sensitivity, radius of the probe) and the determination of the point of contact.

Considering a number of FV measurements of many cells (8-10 cells) of the same sample in the same experimental conditions, the average value of single-cell Young's modulus is representative of the entire population of cells. It is necessary to calculate an error to associate with this value, which takes into account errors associated to the analysis of individual FV and the variability of the cellular sample, ie the dispersion of the average values associated with individual cells. The total error is obtained adding in quadrature the standard deviation of the mean relative to the average values of different cell population ($\sigma_{cellsAVE}$=$\sigma_{cells}/\sqrt{N_{cells}}$ where N_{cells} represents the total number of

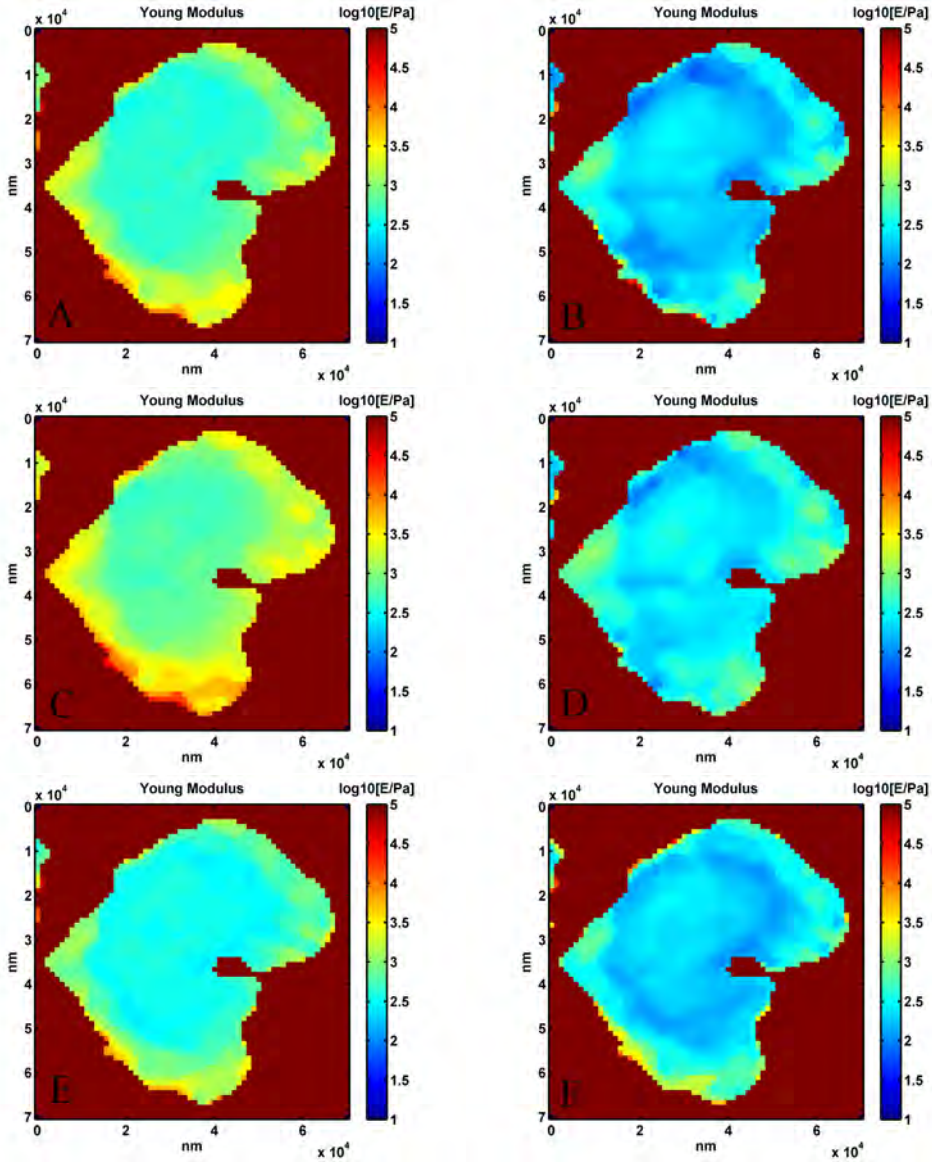

Figure 2.20: (left column) Young's modulus maps for a MDA-MB-231 living cell obtained with Hertzian fit from eq. 2.4. Image A represents the Young's modulus mediated on extended indentation interval, image C represents the modulus isolated on high indentation interval and image E represents the modulus isolated on low indentation interval. (right column) Young's modulus map for a MDA-MB-231 living cell obtained with hertzian fit and finite thickness correction in Eq. 2.5. Image B represents the Young's modulus mediated on extended indentation interval, image D represents the modulus for high indentation and image F represents the modulus for low indentation interval.

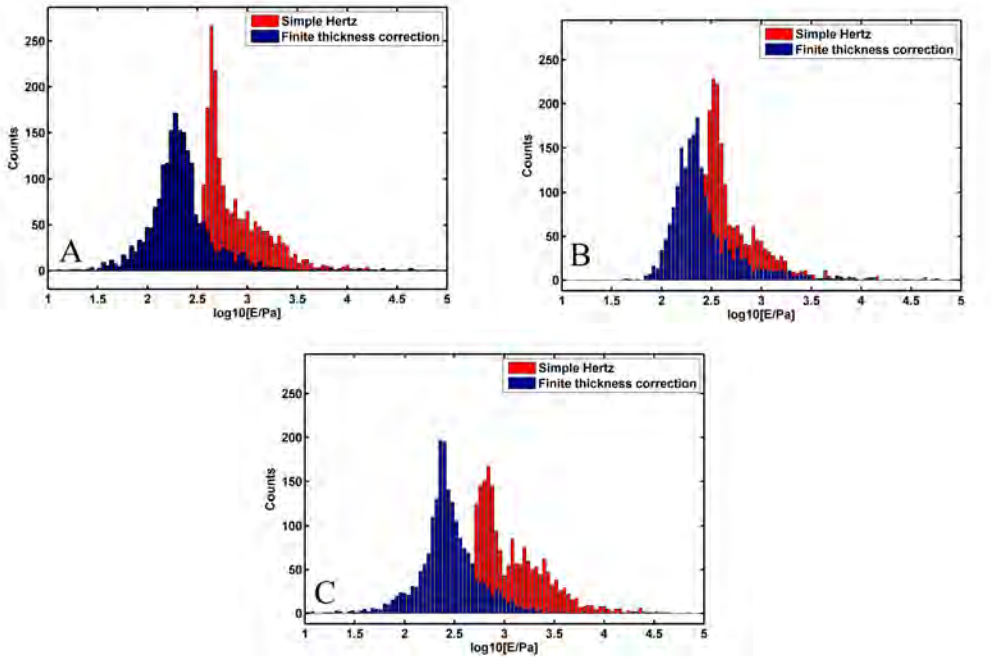

Figure 2.21: Quantitative analysis performed with histograms comparing the treatment using simple Hertzian fit (red bars, Eq. 2.4) and hertzian fit with finite thickness correction (blue bars, Eq. 2.5). Graphic A represents the Young's modulus mediated on the extended indentation range, graphic B represents the modulus isolated on low indentation interval and graphic C represents the modulus isolated on high indentation interval.

cells measured) with the error associated to the single cell (σ_{SINGLE}):

$$\sigma_{TOT} = \sqrt{\sigma^2_{cellsAVE} + \sigma^2_{SINGLE}} \tag{2.6}$$

The error for the single cell (σ_{SINGLE}) is propagated trough the average formula from error of individual FV (σ_{FV}):

$$\sigma_{SINGLE} = \frac{1}{N_{cells}} \sqrt{\sum_{i=1}^{N_{cells}} \sigma^2_{FV}} \tag{2.7}$$

If a FV of a single cell is considered, and we assume that force curves pertain to an area that can be considered (in first approximation) homogeneous (eg nucleus or lamellipodium), the total error for individual FV is obtained:

$$\sigma_{FV} = \sqrt{\sigma^2_{STAT} + \sigma^2_{FIT}} \qquad \text{where} \qquad \sigma_{STAT} = \frac{\sigma_E}{\sqrt{n}} \tag{2.8}$$

where σ_E is the standard deviation of the E values fitted out from single force curves, and n is the number of force curves analyzed. σ_{FIT} represents an estimate of the error associated to the mean value of E of a single cell, due to the uncertainties in the calibration of the experimental parameters (elastic constant of the cantilever deflection sensitivity, radius of the probe).

The uncertainty about spring constant and deflection sensitivity is of the order of respectively $\delta_k\%$=10% and $\delta_{zsens}\%$=5%, while the error in the characterization of the radius of the probe can be considered negligible (2%), if this parameter is measured with the care required (ref. [159]), the error at the point of contact can instead be estimated (in absolute value) of the order of 10 nm [158]. All the errors considered must be summed up in quadrature to obtain the final error value. Once familiar with the uncertainties on the various parameters, an effective method to estimate the overall effect on the value of Young's modulus is a simulation of Monte-Carlo type: starting from a single FC acquired experimentally, for each point of the curve is generated a new set of points Gaussianly distributed around the force value F, with the width calculated from experimental errors. For each force value of the force curve the associated error is calculated as:

$$\delta F = \sqrt{(\Delta V \cdot z_{sens})^2 \, \delta_k^2 + (k \cdot \Delta V)^2 \, \delta^2_{zsens}} \tag{2.9}$$

where δ_k and δ_{zsens} respectively represent the absolute uncertainties on the elastic constant of the cantilever ($\delta_k = \delta_k\% \cdot k$) and the deflection sensitivity ($\delta_{zsens} = \delta_{zsens}\% \cdot zsens$). This error is added to the original experimental values to produce a family of noisy curves. Similarly, the uncertainty on the abscissa is evaluated: the error in the determination of contact point is taken into account translating rigidly the axis of the indentation using an offset obtained Gaussianly around the experimental value with 10nm precision. In this way it is possible to build N force curves and repeat the fit to determine Young's modulus values: the result is a statistical distribution from which the mean value and the confidence interval of 68% is obtained.

Examples of measurements

The automated data analysis for each set of data can be summarized as follow

- Topography flattening procedure, individuating masks for substrate, cell body and lamellipodium.
- Zsens calibration on substrate. FC are rescaled in F vs. z piezo travel distance.
- Contact point individuation using Hertz model.
- Construction of indentation map, real height map and parameter χ for finite thickness correction.
- Contact point individuation using Hertz model + finite thickness correction.
- Reconstruction of indentation map, real height map and parameter χ for finite thickness correction.
- FC are rescaled in F vs. z tip-sample distance.
- Individuation of indentation regimes and fit of contact region using Hertz+ finite thickness model.
- Analysis of log-normal Young's modulus distributions using Gaussian fit.
- Error analysis and results representation.

A first test of measurements was performed on a single MDA-MB-231 cell using the heater, recreating (as close as possible) the physiological conditions for the survival of cells (controlled temperature at 37 °C), in order to make the largest number of AFM measurements out of the same sample. Morphology maps, Young's modulus (maps and quantitative histograms) of the same cell after 6 consecutive FV measurements (each measurements takes 15 min, total 90 min) were compared with original status. From Fig. 2.22, slight modifications in morphology are evidenced, in fact live cells, especially this line derived from metastatic cancerous tissue, move, spread and reorganize the cytoskeletal structure, as auto-defense mechanism, to avoid the contact with the tip. Also a small decrease of Young's modulus, restricted to low indentation range, is noticed, probably due to mechanical stress induced by 6 consecutive investigations.

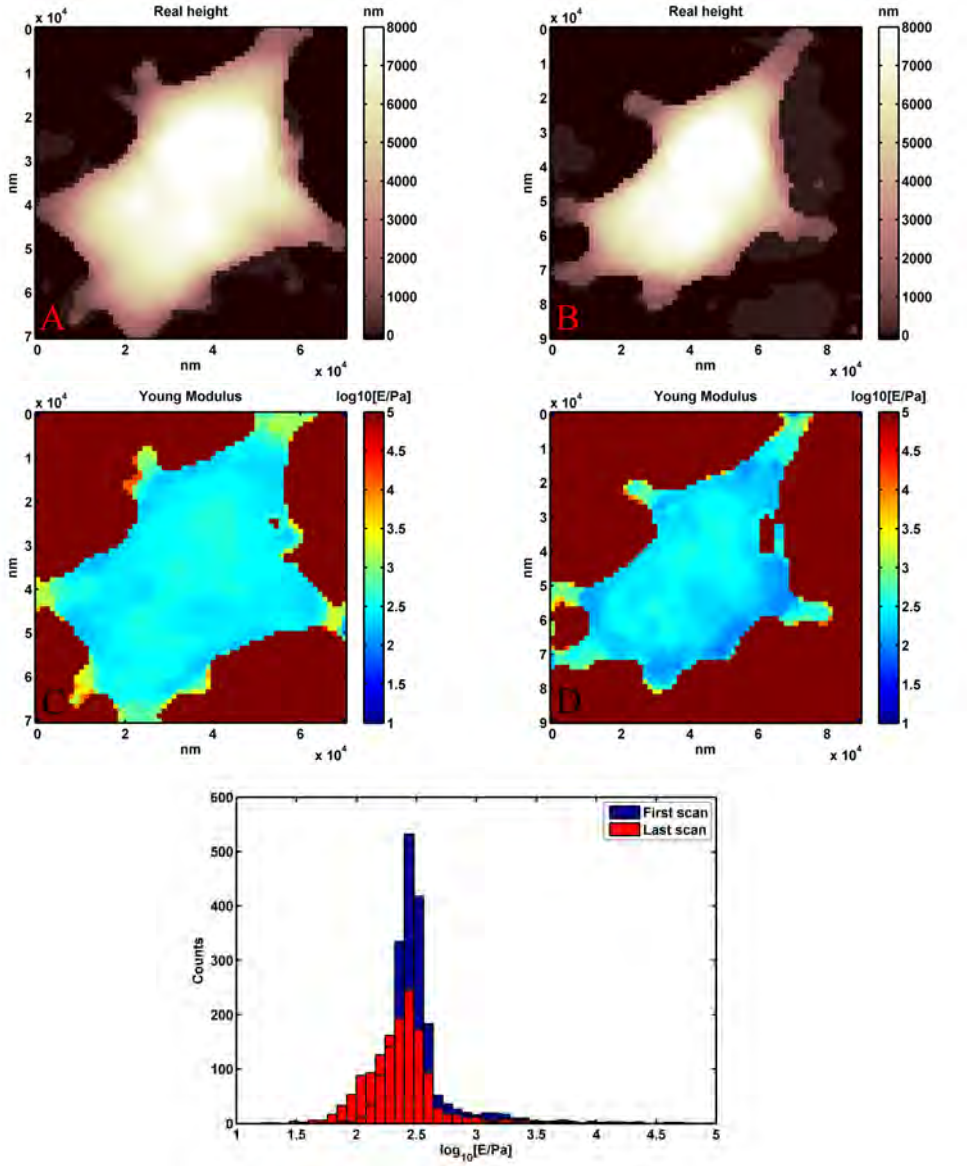

Figure 2.22: Evolution of morphology and Young's modulus for a cell of MDA-MB-231 after 6 consecutive FV analysis (15 min each). The total time elapsed between left and right column is 90 min. Image A and B represent the correct morphology of the cell respectively before and after time evolution, image C and D represent the Young's modulus (with finite thickness correction) map respectively before and after time evolution, the graph represents the quantitative analysis of Young's modulus for image C and D.

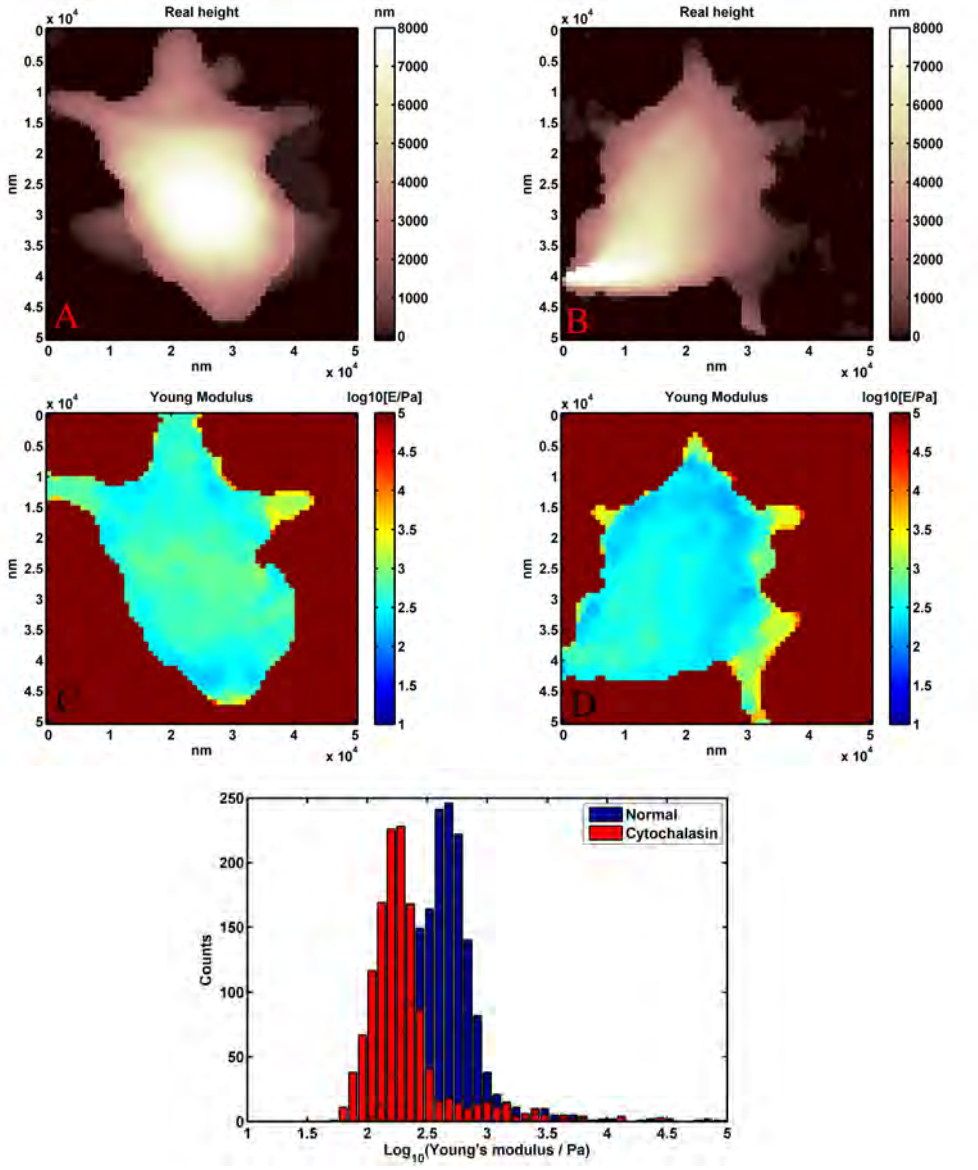

Figure 2.23: Evolution of morphology and Young's modulus for a cell of MDA-MB-231 before and after interaction with 25 μl cytochalasin. Image A and B represent the correct morphology of the cell respectively before and after cytochalasin treatment, image C and D represent the Young's modulus (with finite thickness correction) map respectively before and after cytochalasin treatment, The graph represents the superposition of quantitative analysis of Young's modulus for image C and D, showing a noticeable difference of stiffness after treatment.

The interaction compounds investigations were performed only on cells that showed a good spreading and lamellipodia evident. I then followed the morphological and mechanical evolution of the cells varying the concentration of contaminant, avoiding, in the case of obvious death, to acquire measurements that would have been distorted and focusing on cells showing good health after optical microscope investigation.

Before analysis with unknown compounds, as ionic liquids,a relatively simple way to test the complete protocol developed consisted in quantifying, at the level of nanomechanical interaction, the effect of the cytochalasin-D, a compound able to depolymerize the network of actin filaments, penetrating inside the cell. This choice is justified both by the possibility of comparing the data obtained with the results already present in the literature ([123; 162]), both from the possibility to investigate the contribution of actin on the different Young's modulus regimes within the force curves. Actin, in fact, can contribute to the effective Young's modulus of both regimes (low indentation and high indentation range), or only one of them. This is an experiment to determine if in principle it is possible deconvolve the contribution of the various components of the cytoskeleton from the effective Young's modulus measured by AFM.

From Fig. 2.23 it can be observed qualitatively a decrease of the Young's modulus of the cell in the area of the cell body and for both regimes, in relation to the two conditions, it is also possible to note how the effect of the toxin on the cytoskeleton entails a modification of the morphology of the cell, especially in relation to lamellipodia. According to the hypothesis of layered structure of cytoskeleton, it is very difficult, if not for special cases, to deconvolve the contribution of the different components of the cytoskeleton from the effective Young's modulus obtained by AFM measurements [158]. However focusing on the first regime (low indentation range) the effect of cytochalasin-D is well confirmed, in fact the Young's modulus is greatly affected, decreasing of an order of magnitude (See maps and quantitative histograms of Young's modulus in Fig. 2.23).

2.2.6 Characterization of electrical properties of ionic liquids by AFM

The atomic force microscope (AFM) is a powerful and versatile tool generally used to measure the topography of a surface with nanometer spatial resolution. As explained in the previous sections, simultaneously with the topography, it is possible to have quantitative information of other properties such as friction, elasticity, conductivity and magnetism. For the analysis of these local properties at the nanoscale, the AFM is a powerful technique because it is possible to correlate directly these properties with the morphology of the surface. Characterization of electrical properties at the nanoscale has become very important for modern science and technologies. Therefore, a number of scanning force microscopes have been designed with enhanced capabilities for probing local surface properties, notably electrical properties, and correlating them with surface topography. Modified AFMs have been employed as tools for measuring conductivity, surface potential, capacitance and impedance with nanometer spatial resolution. However, compared to the performance attained in standard surface imaging, nanoscale electrical characterization using atomic force microscopy is still underdeveloped and hot research topic. Up to date, several scanning force techniques have been implemented based on the same principle as AFM, i.e. using the force as feedback control parameter to map the surface topography, and simultaneously detecting a specific tip surface interaction. The most used conductive-AFM techniques can be divided into two main categories, according to the principle of operation: detection of force and current [163].

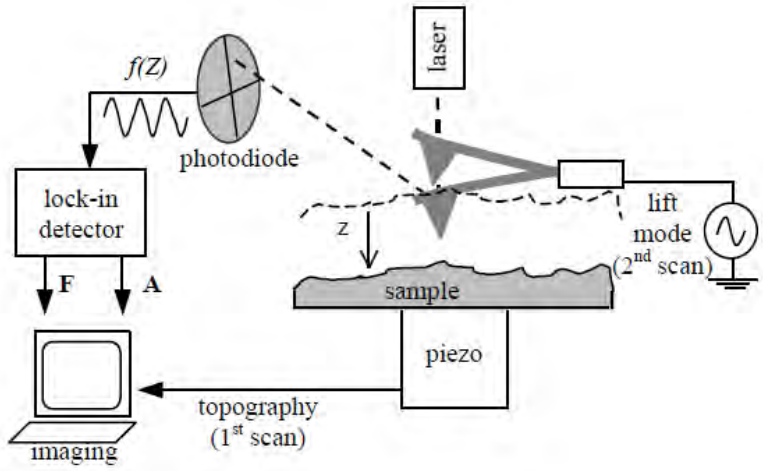

Figure 2.24: Basic principle of operation of the EFM. Electrostatic force is measured with changes in static or dynamic deflection signal during lift-mode.

Electrostatic force microscopy (EFM) [164] and Kelvin probe microscopy (KPM) [165–167] are techniques for the detection of force. In these techniques the electrostatic tip-sample electrostatic interaction can be detected directly by measuring changes in deflection or in the characteristic frequency of vibration of the probe approaching the surface [168]. In fact, applying a bias between conductive probe and sample, an electrostatic force is generated. This force can change the deflection of cantilever or resonance frequency. These are non-contact techniques that do not give information about electronic transport through the sample. An other approach for electrical measurements by SPM is based on current detection. To this aim, the local resistance and impedance, i.e. the resistance in the frequency domain, has been probed. This requires the tip-sample contact to perform a direct DC and AC measurement respectively. For this purpose, contact-mode techniques using AFM, have been recently developed, including conductive atomic force microscopy (C-AFM) [169; 170], scanning capacitance microscopy (SCM) [171; 172] and nanoscale impedance microscopy (NIM) [125; 173–176]. These contact-mode techniques measure the DC resistance and impedance respectively by DC and AC current detection. The tip-sample impedance, and hence tip-sample capacitance, is measured using the tip as a nanometric electrode and the sample as the counter electrode. Using this measurement setup, the measured capacitance involves both the local contribution of the tip apex (in the range of tens of aF) and the non-local stray capacitance contributions associated to the probe and chip holder (in the range of hundreds fF). Furthermore, both contributions during tip scanning may change in comparable amounts (in aF range), thus making difficult the extraction of the local variation in many cases. Therefore, in order to perform a nanoscale impedance microscopy and spectroscopy, three requirements need to be fulfilled:

- An high-resolution detector with aF capacitance resolution.
- The parasitic capacitance variations have to be much smaller than the local contributions during scanning.

- A wide frequency bandwidth detector has to be accomplished (not trivial to obtain simultaneously to high-resolution).

In the next section, the instrumentation allowing characterization of local electrical properties of the materials at the nanoscale, will be presented.

Nanoscale Impedance Microscopy

Since all the morphological studies the structured ionic liquid at the interface were performed by AFM, it was a natural choice to use the AFM set up for electrical measurements equipped with conductive tips, to investigate the electrical properties of the solid-like ILs layers. Measurements in this direction can be useful for electrochemical applications and also for a deeper understanding of the mechanisms of stratification of ILs at the interface. A particular technique was used: NIM (nanoscale impedance microscopy) consisting in just an AFM microscope, enabled by electrical measurements on conductive samples.

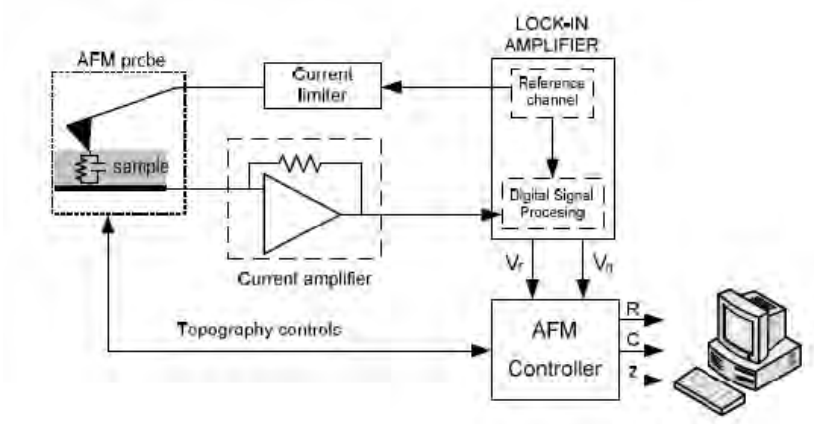

Figure 2.25: Schematic of the instrumentation used to implement impedance measurements at the nanoscale (NIM). The low noise transimpedance amplifier coupled with a lock-in for the detection of the signal, enables the AFM for capacitance and impedance measurements.

The instrument for wide-bandwidth electrical characterization at the nanoscale is presented. The novelty of the instrument is the use of a fully-customized current amplifier, specifically designed to combine high resolution with wide-bandwidth. To show the full capabilities of the instrument and before the measurements on unknown system like IL solid-like layers, a calibration of the NIM apparatus measuring the local dielectric constant of a thin film of SiO_2 with known dielectric constant ($\varepsilon_r \approx 4$) was performed. These measurements demonstrate that the instrument enables high-resolution local AC electrical characterization of thin films with excellent electrical performance.

In order to have large bandwidth and low noise performance, a classical solution is the series of an integrator and differentiator stages, to perform amplification of circulating current. This scheme is not able to manage DC currents, requiring a periodic discharge of capacitive element. A custom-made transimpedance amplifier, based on a original idea of M. Sampietro and G. Ferrari [177], represents an excellent solution, implemented to allow a multifunctional electrical characterization with AFM. It is based on the integrator-differentiator scheme, but provided with an additional feed-

back loop to discharge the DC current. The combination of this wide-bandwidth transimpedance amplifier with a lock-in stage is able to perform nanoscale impedance spectroscopy/imaging with wide-bandwidth measurements (from 100Hz up to 1MHz) and high resolution (down to aF capacitance and TΩ resistance). As a further advantage over above-mentioned works, DC current up to 1μA can be simultaneously measured with impedance with a input current noise of about 10 fA/$\sqrt{Hz}$.

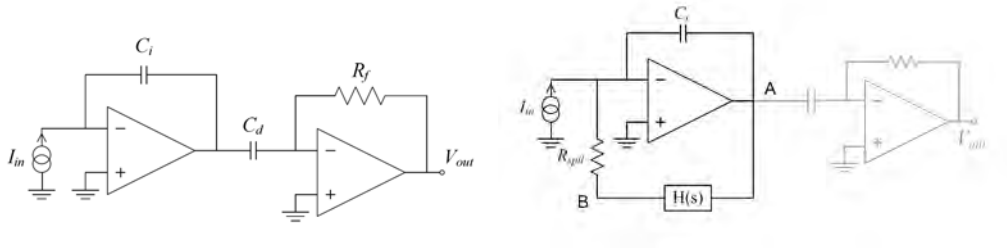

Figure 2.26: (left) Diagram of the low-noise wide-bandwidth amplifier, using the series of an integrator and derivator stage. The purely capacitive feedback at the input stage converts the input current to voltage with minimum instrumental noise. The derivator stage makes the overall conversion factor independent by the frequency over a large bandwidth up to MHz range. (right) Simplified diagram of the integrator/derivator scheme with additional feedback added to the integrator stage in order to discharge and measure the input DC current.

As mentioned before, the optimal solution that allows to have low noise and wide bandwidth is represented by two stages of amplifiers in sequence: an integrator and a differentiator [163; 177; 178] (See Fig. 2.26). The output of the stage integrator is connected to the input using a second feedback, constituted by an amplification block connected in series to a resistance. The amplification block H(s) is designed to have unitary gain in correspondence of DC signals and a strong attenuation in correspondence of AC signals. The AC output of the circuit is V_{OUT} = $|G_{ac}|$ I_{IN}, where $|G_{ac}|$ is the gain of the integrator-derivator expressed by Eq. 2.10 and in this case about 30MΩ. Simultaneously and continuously, the DC output is provided by the voltage at the node B (See Fig. 2.26), that is V_{OUT} = $|G_{dc}|$ I_{IN}, where $|G_{dc}|$= R_{spill} that can be choose 10MΩ or 1GΩ

$$|G_{ac}| = \frac{V_{out}(f)}{V_{in}(f)} = -\frac{1}{2\pi f C_i} 2\pi f C_i R_f = -\frac{C_d}{C_i} R_f \tag{2.10}$$

In the integrator, the feedback capacitance converts the input current into voltage without add a direct contribution to the noise, because it is a component of low noise. Since there is a first amplification due at the first stage, the resistive component of the second stage can be chosen smaller, in order of 10kΩ, extending the bandwidth up to MHz. Although in derivator stage there is a resistance which introduces thermal noise in the signal, this contribution is reduced by a factor C_d/C_i at the input of the amplifier. This type of amplifier is used to measure only AC currents, in fact with a input DC signal, the feedback capacitance during integration saturates the output signal (see Fig. 2.26). To prevent the saturation, the integrator stage must be discharged periodically, thereby limiting the measuring time at the discharge period. To eliminate this problem there is an additional branch of feedback in the first stage which continuously discharges the DC current path [177].

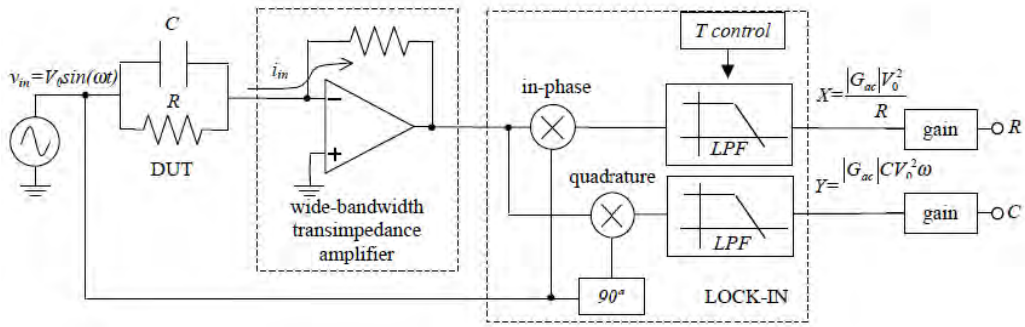

Figure 2.27: Schematic of dual phase lock-in.

The lock-in is a very sensitive system capable of isolating a single frequency signal superimposed on noise fluctuations and returning a DC signal proportional to the amplitude of the AC signal [163]. Acting as a narrow bandpass filter centered ('locked') on the frequency of interest, reduces random noise and interference by increasing the signal to noise ratio of the measurement. The AC signal in input is converted into DC with a bandpass filter with integration time τ. The resolution of the lock-in is then set to the width of the filter: the smaller the bandwidth , the more the noise fluctuations are suppressed, all at the expense of total measurement time. To directly extract the real and imaginary part is used the principle of dual-phase lock-in Fig. 2.27. While the first part uses as reference the applied voltage V_{IN}, the second uses as a reference the voltage phase shifted by 90°. In this way, the real parts (in phase) and imaginary (in quadrature) of the impedance are measured. In mathematical form, assuming that there is an incoming oscillating signal $V_{IN} = V_0 \sin(\omega t)$ the AC output from the sample, that has a resistance R and a capacitance C, is:

$$V_{out}(t) = \frac{|G_{ac}|V_0}{R}\sin(\omega t) + |G_{ac}|CV_0\cos(\omega t) \tag{2.11}$$

From this law using the principle of operation of the dual-phase lock-in that allows to obtain the part in phase and in quadrature v_f, v_q displayed directly on display, is obtained [163]:

$$\begin{aligned}\langle v_f\rangle &= \langle V_{out}(t)\cdot\sin(\omega t)\rangle = \left\langle |G_{ac}|\frac{V_0}{R}\sin^2(\omega t) + |G_{ac}|\omega CV_0\cos(\omega t)\sin(\omega t)\right\rangle = |G_{ac}|\frac{V_0}{2R}\\ \langle v_q\rangle &= \langle V_{out}(t)\cdot\cos(\omega t)\rangle = \left\langle |G_{ac}|\frac{V_0}{R}\sin(\omega t)\cos(\omega t) + |G_{ac}|\omega CV_0\cos^2(\omega t)\right\rangle = |G_{ac}|\frac{\omega CV_0}{2}\end{aligned} \tag{2.12}$$

Thus, from Eq. 2.12, the R and C of the sample are extracted and displayed in real-time as digital outputs:

$$R = \frac{V_0}{v_f}|G_{ac}| \qquad C = \frac{v_q}{V_0\omega|G_{ac}|} \tag{2.13}$$

where it is considered that the lock-in had just multiplied for 2 the outputs in order to compensate the 2 at denominator. Using the formula 2.13 we can easily derive the total capacitance perceived by the tip.

All the measuring system, consisting microscope AFM and integrated amplifiers, is placed in a Faraday cage in order to obtain an efficient electromagnetic shielding. The Faraday cage was built with a steel mesh and covered with aluminum, and the whole is then connected to the ground of the amplifier system. Removing the shielding implies an increase of the noise by a factor 2. As the AFM tip is very sensitive to mechanical vibrations from the external environment, all equipment is placed on a platform suspended by elastic cords. This design minimizes noise from low-frequency mechanical vibrations.

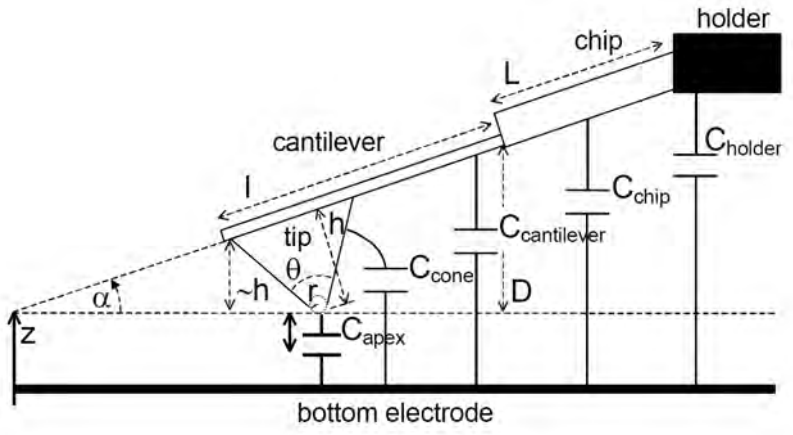

Figure 2.28: Schematic of the AFM tip in the proximity of the electrode surface. The total capacity is modeled by 5 capacitors in parallel (tip apex, cone tip, cantilever, chip and tip- holder). Only the capacitance of the tip apex is local, while the other contributions are parasitic. Image taken from ref. [178]

When the conductive AFM tip, which acts as nano-electrode, approaches the conductive surface of sample, the total capacity measured can have strong parasitic contributions due to the structure that supports the tip [125; 176].

In particular, one can identify five parallel capacitance that contribute to total capacity: C_{APEX}, C_{CONE}, $C_{CANTILEVER}$, C_{CHIP}, C_{HOLDER}. Although the capacitance C_{APEX} is negligible compared to the other contributions, its variations become dominant when the tip is very close to the surface. It is also pointed out in recent studies [125] that changes in capacity in the range of the aF are due, for the most part (about 80%) to local variations of the capacity below nanometric apex of the tip. Performing an accurate calibration of the instrumentation is essential for the proper implementation of the capacitive measures. If the measurements performed on layers, whose dielectric constant is known, provide expected results, we could proceed on layers whose dielectric constant is unknown, i.e. the solid-like layers of IL. The conductive AFM tips available are made in silicon with a conductive coating on both cantilever and tip. The processes of conduction are ensured by typically metallic or heavily doped diamond external coat-

ings. Depending on the applications we can choose the type of tip to use. The metallic coating is highly conductive but can be destroyed easily by friction or melting because of the very high local electric fields. The coatings in doped diamond is much more resistant but possesses a conductivity that is 3 orders of magnitude lower than the metal coatings. A second criterion to be fulfilled is the radius of curvature of the tip apex: sharp tips with radii of curvature small (30 nm) have a great lateral resolution but the capacitive signal coming from the tip is very small and consequently there is an increase of experimental error associated with the measurement.

The best results were obtained with tips coated with heavily doped CVD diamond, in fact, with regard to the measures of capacitive electrode or on the dielectric, there is no need for very-high conductivity and possess an ideal radius of about 150 nm. Unfortunately, even with these tips the coating can be damaged and is subject to wear, especially in scan mode or with high potential applied.

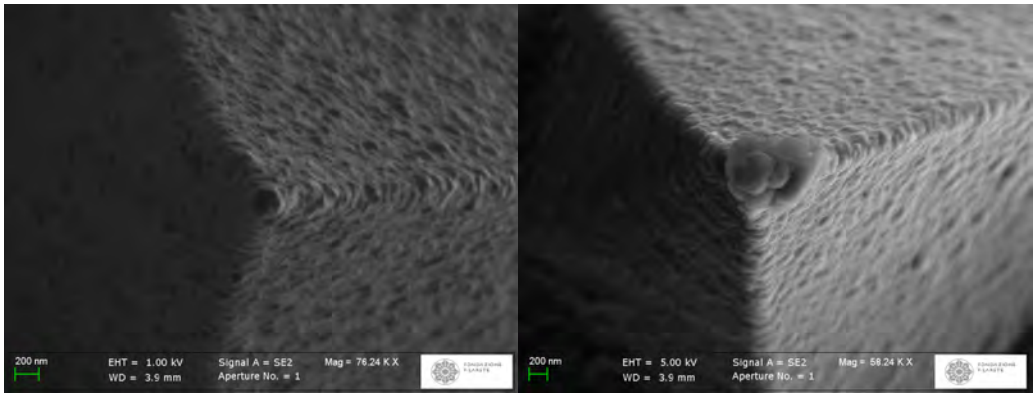

Figure 2.29: (left) SEM image of a new tip covered by heavy doped diamond conductive layer. The laminar structure of the coating doped diamond is evidenced in the image. (right) SEM image of a tip stressed in many capacitive measurements, the apex is worn out and unusable because it is no longer conductive.

The SEM images of the tips coated in doped diamond can be seen (Fig. 2.29). In the right picture, the conductive film ruined after repeated scans is evidenced. The shape of the tips (triangular-based pyramid) is quite different from that used in the model 2.17 (with conical hemisphere). The calibration procedure is used precisely to obtain an effective apex radius to be used later to make measurements on the dielectric film. The AFM tip is therefore a critical parameter often controlled for proper implementation of the measures. For this purpose, a production of metalized colloidal tip, could be useful to simplify the unknown geometry problem and to increase the capacitive signal sensed by the apex. The sample to be analyzed should be in good condition: dirty surfaces or inadequate electrical contacts can lead to misleading results. The sample must also show a low parasitic capacitance to enhance the contribution coming from the apex of the tip. In the first measurements calibration was therefore appropriate to use copper microelectrodes with gold coating which present a very low parasitic capacitance.

The first step of the calibration, which is the measure of the effective radius of the tip-sample electrical contact, could be performed with AFM engaging on the copper/gold microelectrode. While force curves are made with an alternating voltage applied to the tip, the lock-in returns a capacitive signal by integrating over a time τ.The capacity of cantilever, tip, chip and holder can be modeled with the capacitance of an inclined plane.

The analytical formula [125] is given by 2.14:

$$C = \varepsilon_0 \frac{w}{\tan(\alpha)} \ln\left(1 + \frac{l\tan(\alpha)}{d+z}\right) \tag{2.14}$$

Where w, l and α are respectively the width, the length and the tilt angle of the plane, d is the distance between the plane and the apex of the cone and z the distance between the apex of the cone and the substrate. The contribution of the tip cone is more complex because the analytical form comes from the integration of the electrostatic force used in the EFM measurements:

$$C = 2\varepsilon_0 \frac{4\pi}{(\pi-\alpha)^2}\left\{f_1(\ln(f_1/h)-1) - \sin(\vartheta/2)(h\ln(f_1/h) - \delta\ln(f_2/h))\right\} \tag{2.15}$$

Where $f_1 = z + h - \delta/2$, $f_2 = z + \delta/2$, $\delta = r/\tan(\vartheta/2)$, ϑ and h are respectively the opening and the height of the cone. These contributions can be hundreds of fF because of the macroscopic dimensions of the components, but for small z can be approximated linearly thanks to the great distance from the electrode surface.

Finally, the capacitance sensed by the tip apex is given by:

$$C_{APEX} = 2\pi\varepsilon_0 R \ln\left(1 + \frac{R(1-\sin(\vartheta/2))}{z}\right) \tag{2.16}$$

Where R is the radius of curvature of the tip apex, ϑ is the opening angle of the cone, z is the tip-electrode distance. In this way, the capacity-distance curve can be divided into two parts [125; 179]: the first, when the tip is far from the contact surface, given by the contribution of the cone, cantilever, chip and tip-holder is almost linear due to the great distance. The second, when the tip is close to contact with the surface, is given by the contribution of the apex and shows a logarithmic trend. In total, the law that describes well the capacity-distance curves on a clean electrode is given by [125]:

$$C^{metal}_{TOTAL}(z) = A + Bz + 2\pi\varepsilon_0 R \ln\left(1 + \frac{R(1-\sin(\vartheta/2))}{z}\right) \tag{2.17}$$

The linear part includes all parasitic contributions, while the logarithmic part includes the contribution of the apex. By fitting the experimental data with this law is possible to obtain the value of the effective radius of the tip. The radius has to be considered effective because the real geometry of the nanoelectrode is only approximately described by the formula.

For conductive surfaces covered by thin films of insulating material [174; 180] between the tip and the underlying electrode there is a layer with a dielectric constant that can be different from 1, must be considered [125]:

$$C^{dielectric}_{TOTAL}(z, \varepsilon_r, h) = A + Bz + 2\pi\varepsilon_0 R \ln\left(1 + \frac{R(1-\sin(\vartheta/2))}{z + h/\varepsilon_r}\right) \tag{2.18}$$

Where z represents the distance between the tip and top of the film, h is the thickness of the film on the electrode, R is the effective radius and ϑ the cone angle. From this equation it can be noted that the capacity of the apex depends on the ratio h/ε_r and the geometry of the tip, mainly the effective radius R. Since the dielectric constant ε_r and the effective radius are strongly correlated with each other, a quantitative measure of the dielectric constant requires an independent and accurate measurement of the effective

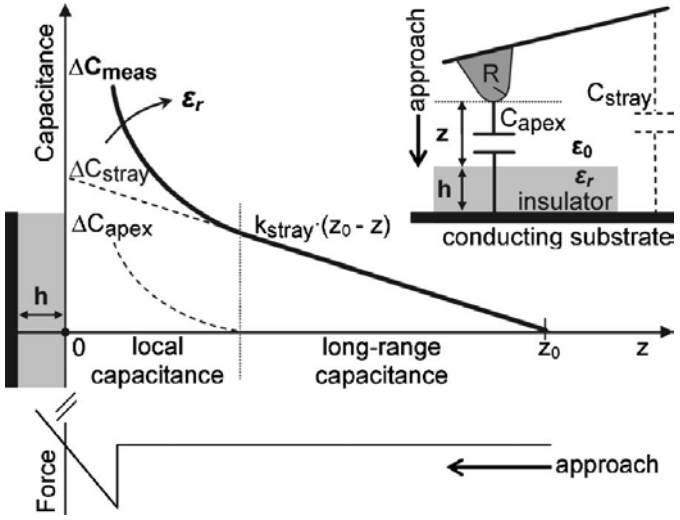

Figure 2.30: Schematic representation of simultaneous capacitance and force vs distance curves on an insulating film of thickness h and relative dielectric constant ε_r using nanoscale capacitance microscopy. The force-distance curve is used to determinate the tip-sample distance z. Inset: tip-sample measurement configuration. Taken from ref. [174]

radius. Unfortunately it is not possible to perform a 2 parameters fit trying to derive the radius R and the dielectric constant ε_r because they are closely related and the obtained results may be misleading. The parameter R instead must be derived in part on electrode and then be fixed in Eq.2.18. The dielectric constant of an insulating film can be quantified at the nanoscale using a two-step procedure. First, capacity-distance curve is measured on a conductive clean electrode. Eq. 2.17 provides the value of the effective radius (calibration point). Second, capacity-distance curves are measured on the thin dielectric film and using Eq. 2.18 the ratio h/ε_r is obtained. Finally, to obtain the dielectric constant ε_r is necessary to know with accuracy the thickness of the film through AFM topographic measurements or with profilometer. Simultaneously to the curves C(z), are acquired force curves F(z) in order to determine exactly the tip-sample distance z.

Since the capacity-distance curves are still quite noisy, is performed the average of about 100 curves acquired in the same conditions. The final resolution is obviously enhanced increasing measurement time i.e. by increasing the integration time $\tau$and lowering the ramp rate, or by increasing the number of curves in the final media.

The raw capacitance curves can not be used because they represent the capacity as a function of travel distance from of the piezoelectric element. This distance is arbitrary and must be converted to absolute tip-sample distance. The force curves are acquired simultaneously to capacitance curves. To this purpose the F vs. Z_{piezo} curve is converted in F vs. distance curve according to the procedure explained in section 2.2.1. Then the distance axis is used to obtain C vs. distance. It must be noticed that the distance from the first contact point is called z in equations. The curves obtained are then averaged to further lower the experimental noise.

# curves	V_{IN} (V)	$\lvert G_{ac}\rvert$ (MΩ)	FREQ (KHz)	L (nm)
100	0.5	28.3	90	300
v_{appr} (nm/s)	v_{ret} (nm/s)	FC freq (Hz)	# points	τ (ms)
20	150	0.058	1024	30
Conversion factor V F	$1.2497 \cdot 10^{-16}$			
points per nm	1.67			
Total time (min)	28			

Table 2.1: Standard parameters used for the ramps of capacity. In sequence is shown: the number of curves acquired, the amplitude of the input signal V_{IN}, the input signal frequency, the amplification factor $|G_{ac}|$ of amplifier circuit, the length L of the force curve ramp, the approaching velocity v_{appr}, the retracting velocity v_{ret}, the force curve frequency, the number of points for each curve and the integration time of the lock-in. At the bottom are shown the conversion factor, points relevant for each nanometer and the total time of the data set.

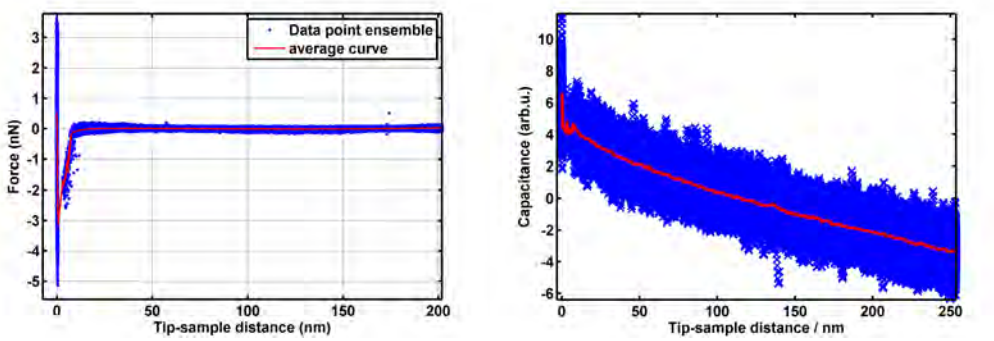

Figure 2.31: (left) 100 force curves acquired on Si native oxide as a function of the tip electrode. In blue are represented together all the data, while in red the average curve with 0.3 nm binning step is presented. (right) 100 capacitance curves acquired simoultaneously to FC curves of the left side. In blue are represented together all the data, while in red the average curve with 0.3 nm binning step is presented.

In figure 2.31 the single C vs. distance curves and their average are shown in comparison with F vs. distance curves. In this framework, the important values obtained from the fit, using Eq. 2.17, are B and R. B is the slope (in aF/nm) of the parasitic capacitance at long distances. If B is small, the contribution of the parasitic capacitance is minimized and the contribution coming from the apex is maximized. R is the radius of the effective electrical contact represented by tip apex. The errors of all the parameters of the fit are calculated with the method of Lybanon [181]. The error of the parameter R represents the confidence interval of 68% and is calculated in accordance with the optimized strategy discussed by Lybanon.

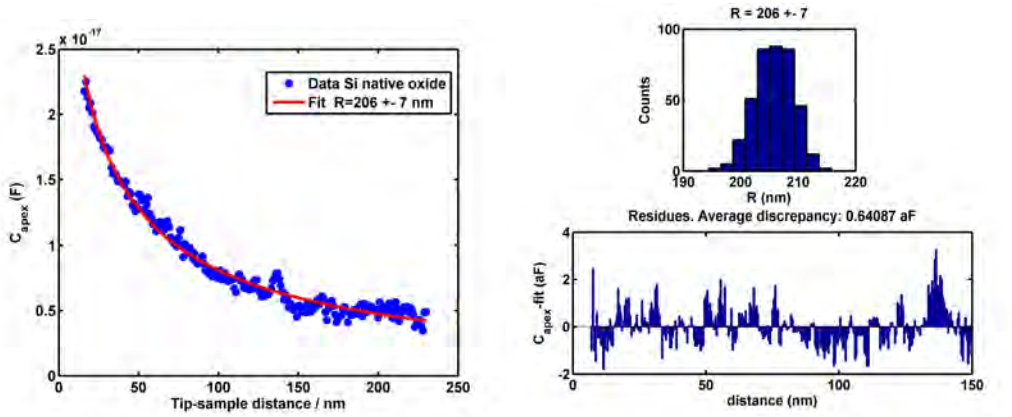

Figure 2.32: (left)Contribution from the tip apex, it is clear the logarithmic trend at small distances. The fit is shown in red while in blue experimental values obtained through average process. (right) Distribution of the R values extracted from the fit of the experimental data and diagram of the discrepancy between experimental data and fit.

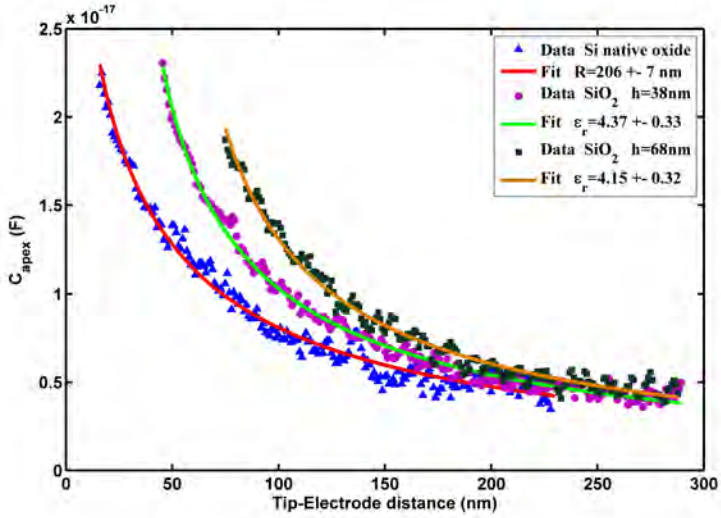

Figure 2.33: Fit of the experimental data obtained on electrode with native oxide and SiO_2 film thickness of 38 nm and 58 nm

The graph shows the distribution of the best values of the radius, h/ε_r and ε_r obtained by fitting simulated data constructed from the original experimental data by adding noise consistent with the error associated with each point. The values are Gaussian distributed around the best value of the fit, the half-width represents the error associated to the mean value. In view of the execution of measurements on ILs is appropriate to conduct the calibration of the radius of the tip electrode using a n^+silicon doped with native oxide layer thickness of about 1.5 nm. The native oxide, with dielectric constant static about 4, introduces a propagated error in the calibration of the order of $h/\varepsilon_r \approx 0.3$ nm (see Eq.2.18), then lesser than the spatial resolution of experiments. Since this error

is negligible, it is not necessary to calibrate the tip on bare electrode metal, which would have to change the experimental setup, it is possible to calibrate R in a region of the clean substrate with its oxide native, so having an 'electrode' reference and a dielectric film on the same sample. After the calibration procedure performed on Si doped electrode with native oxide, the procedure was tested on a thick thermal oxide layer, deposited on silicon by CVD.

This oxide is used as the dielectric film to test the validity of the models. With targeted HF etching, layers of thickness 58nm and 38nm were produced consecutively and measured by profilometer. The fit of the logarithmic law requires the use of Eq. 2.17 for radius calibration and Eq. 2.18 for the dielectric constant. The characterization of thermal silicon oxide dielectric constant shows that the experimental setup and measurement protocol are accurate and well calibrated, the logarithmic fit follows very well the experimental values calculated using the radius of the electrode. The dielectric constant is in good agreement with literature values (ε_r =4.6 $\pm$ 1.2 [125]) and is rightly independent of the value of the thickness of the dielectric material.

Concerning the sensibility and applicability of this technique (deeply discussed in refs. [174]), it is worth mentioning that, in its present state, it is limited to very thin dielectric films (5-50 nm thick dielectric layers). A thick dielectric layer decreases the current sensed by the tip, resulting in a decrease of the signal to noise ratio. Also the precision in the observed value of dielectric constant diminishes when decreasing the tip radius due to the fact that the capacitance noise of the instrument is constant in front of the decreasing apex signal. A metallic spherical colloidal probe

Electrostatic Force Microscopy

A different but simpler method to measure the static dielectric constant of thin films with nanometric spatial resolution consists in monitoring the static deflection of the biased cantilever. The dielectric constant is extracted from DC electrostatic force measurements with the use of an accurate analytical model [168].

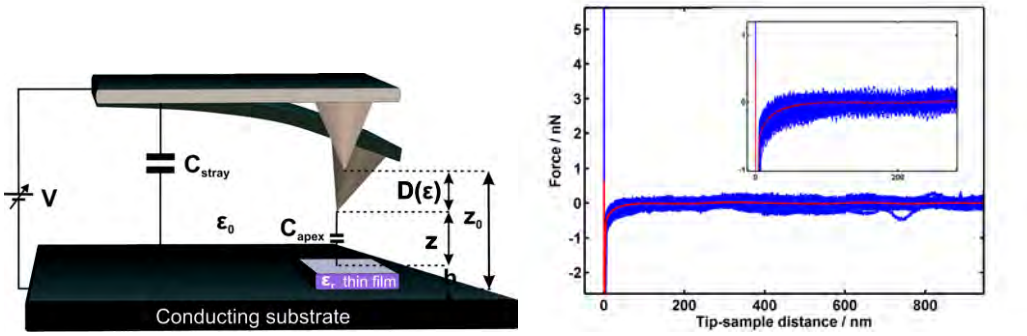

Figure 2.34: (left)Schematic representation of a DC electrostatic force microscopy measurement on a thin film for dielectric constant extraction. A DC voltage bias is applied between a conducting probe and substrate, resulting in a deflection D of the cantilever, which depends on the static dielectric constant of the thin film. Image taken from ref. [168]. (right) 100 force curves acquired on Si native oxide as a function of the tip electrode, applying a ΔV =3 V between tip and sample. In blue are represented together all the data, while in red the average curve with 0.3 nm binning step is showed. The inset is a zoom focused on a few nanometers near the interface

As in the previous AC measures, the method is validated here on thin silicon dioxide films and then used on IL layers. The main advantage of the force detection approach consists in its simplicity and direct application on atomic force microscope with no need of additional electronics to amplify the current. In this setup (see fig. 2.34), the conductive AFM probe positioned above the dielectric film of the thickness h with the tip apex separated by an initial distance z_0 from the conductive substrate. When a DC voltage is applied between the probe and the substrate, the cantilever deflects by an amount D, yielding a new equilibrium position of the apex at a distance $z = z_0 - D - h$ from the thin film. The deflection D depends on the spring constant k of the cantilever, the potential difference between tip and sample (the applied voltage V reduced by the surface potential V_{SP}) and the total capacitance C_{TOT} between the probe and the sample, according to the relation:

$$D(z) = z_0 - h - z = -\frac{1}{2k}\frac{\partial C_{TOT}}{\partial z}\left(V - V_{SP}\right)^2. \tag{2.19}$$

From the theory of the previous section, the total probe–sample capacitance C_{TOT} can be modeled as the sum of two contributions, the stray capacitance C_{STRAY} given by the micrometric components of the probe (cone and cantilever) and the apex contribution, C_{APEX}. The static deflection signal is proportional to the derivative of the total capacitance C_{TOT}. Substituting equation 2.17 for bare electrodes and equation 2.18 for thin dielectric films inside equation 2.19, the total DC electrostatic deflection of the cantilever over an electrode or over thin dielectric film can then be expressed as:

$$D^{metal}_{TOTAL}(z) = A + Bz + \frac{\left(V - V_{SP}\right)^2 \cdot \pi\varepsilon_0 R^2 \cdot (1 - \sin(\vartheta/2))}{k \cdot (z + R\,(1 - \sin(\vartheta/2))) \cdot z} \tag{2.20}$$

$$D^{dielectric}_{TOTAL}(z) = A + Bz + \frac{\left(V - V_{sp}\right)^2 \cdot \pi\varepsilon_0 R^2 \cdot (1 - \sin(\vartheta/2))}{k \cdot (z + R\,(1 - \sin(\vartheta/2)) + h/\varepsilon_r) \cdot (z + h/\varepsilon_r)} \tag{2.21}$$

Eq.2.20and 2.21 represent the static deflection of the tip on electrode and on thin dielectric film, where h is the film thickness, z is the tip-film distance, ε_0 is the vacuum dielectric constant, ε_r is the relative dielectric constant of the film, R is the tip radius of curvature, ϑ is the tip cone angle, A represents all the static contributes that don't vary with z. In agreement with [182] a linear correction parameter B that take in to account the linearized medium and long range forces is taken into account. The dielectric constant is calculated by data fitting in analogy to 2-steps NIM measurements. Eq.2.20 is used to calibrate the radius of electric contact of the tip, while Eq.2.21 is used to obtain the h/ε_r ratio and finally to calculate ε_r.

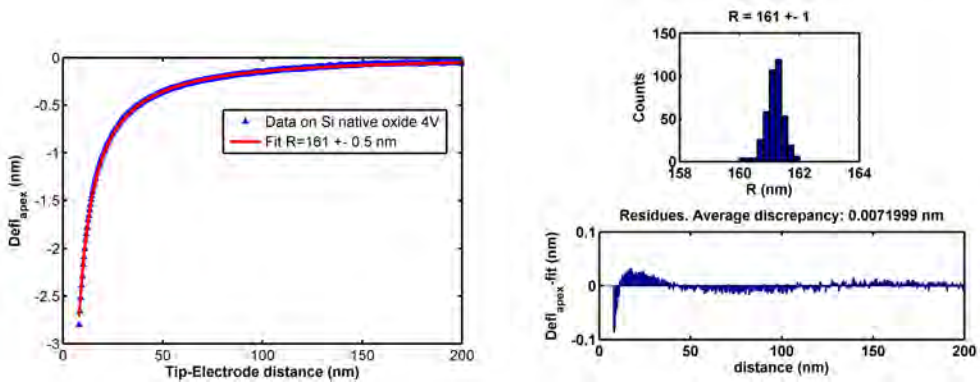

Figure 2.35: (left)Contribution from the tip apex, it is clear the curvature trend of deflection at small distances induced by the electric field. The fit is shown in red while in blue experimental values obtained through average process. (right) Distribution of the R values extracted from the fit of the experimental data and diagram of the discrepancy between experimental data and fit.

A similar test of measurements was carried on analyzing the static deflection of the tip when a DC bias is applied between the conductive tip and the sample. Also in this case the experimental setup and measurement protocol was characterized on thermal silicon oxide layer (thickness 38nm); the fit follows very well the experimental values calculated using the radius of the electrode. The dielectric constant ε_r =3.9 $\pm$ 0.2 is in good agreement with AC previous values and also independent from the value of potential applied to the tip.

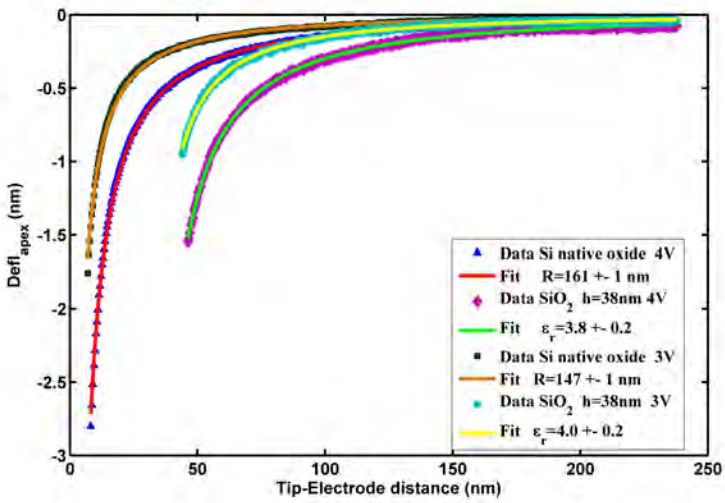

Figure 2.36: Fit of the static deflection experimental data obtained on electrode with native oxide and SiO_2 film thickness of 38 nm using different potentials applied between tip and sample.

Beyond the analysis of DC static deflection suffered by the biased tip, in a recent work [183] was developed a method to obtain capacitive forces and dielectric constants of ultra-thin films on metallic substrates using multifrequency non-contact atomic force

microscopy with amplitude feedback in air. Capacitive forces are measured via cantilever oscillations induced at the second bending mode and dielectric constants are calculated by fitting an analytic expression for the capacitance [179] to the experimental data. When a conducting AFM cantilever and a metallic substrate are brought close to each other, they form a capacitor with the thin film acting as a dielectric medium between the two conductors. When an AC potential is applied to the cantilever with respect to the substrate, the cantilever experiences an oscillating electric force. If the frequency of the applied AC potential (V_{AC}) is ω, then the resulting electric force between the cantilever tip and the sample has three components: one DC component and two oscillating components of frequencies ω and 2ω. The $D_{2\omega}$ component of the total deflection (proportional to the exerted force) depends on the local capacitive coupling between the cantilever tip and the sample as:

$$D_{2\omega}(z) = -\frac{1}{4k}\frac{\partial C_{TOT}}{\partial z}\left(V_{AC}\right)^2 \cos(2\omega t). \tag{2.22}$$

where C and V_{AC} are the capacitance and applied AC potential between the cantilever tip and the substrate, respectively, and z is the tip–sample distance. This equation (eq. 2.22)suggests that the capacitance gradient can be obtained also by measuring the $D_{2\omega}$(z) component of the capacitive force.

I-V spectroscopy with conductive AFM

The circuit described in the section 2.2.6 allows us to detect DC current continuously. This is compatible with the imaging, so, by applying a DC bias to the tip, it is possible to acquire simultaneously the morphological and the electrical maps. In addition it is possible to acquire the I-V characteristics of the sample by ramping the bias. It is convenient to have a I-V characteristics with the tip at rest with respect to the sample surface in order to avoid morphological contribution to the current variation. There are two main modalities of electrical contact to get an I-V characteristic: contact mode imaging and force curve approach. The first method is performed controlling the deflection of the tip, keeping it at constant value while it is in contact with the sample, adjusting the applied force in order to ensure a better electrical contact, especially if the tip is moving laterally on the sample [176]. This mode is good for homogeneous material though while scanning the surface, the conductive layer can wear off from the apex, it can becomes dirty due to particle sticking, or it can get oxided. The second mode is the force curves approach or spectroscopy mode, where the tip is approached vertically in selected locations. This is the way to investigate the heterogeneous layers of ionic liquid avoiding lateral erosion, especially after imaging procedures in ContactMode. In order to acquire the I-V curves we used NI PCI-6251 board, controlled by data acquisition software, developed in Labview environment. A necessary condition in order to have sensitivity to the electrical properties of the sample surface is the good state of the conductive tip coating and the DC amplifier of current [177] described in section 2.2.6. A critical point for this kind of measurements is the applied force during the electrical measurement: high enough to ensure electrical contact without damaging the surface and the tip coating. A W_2C coated tip mounted on a force modulation cantilever (k = 3N/m) was used.

2.3 Electrochemical methods

Three complementary electrochemical techniques have been used in this study: rapid cyclic voltammetry (RCV), out-of-phase alternating current voltammetry (ACV), and

electrochemical impedance spectroscopy (EIS). Electrochemical techniques are very powerful tools for monitoring structural changes of Hg-supported phospholipid layers because these structural changes are reflected in capacitance discontinuities at specific applied potentials. In the next section will be presented these techniques, with experimental comparison between DOPC coated and uncoated mercury film electrode. Accordingly, with its extreme sensitivity, the supported model monolayer system is shown to be a suitable platform for developing toxicity sensors [126; 127]. Recently using the technique, interactions with biomembrane-active compounds[184; 185] polymers [128] and nanoparticles [129] have been also investigated.

2.3.1 Rapid Cyclic Voltammetry RCV

In rapid cyclic voltammetry (RCV) the current at the working electrode is plotted versus the applied voltage to give the cyclic voltammogram trace that can visualize the conformational change of the phospholipids at the Hg/electrolyte interface. For RCV measurements, the wafer-based electrode was installed inside a flow cell. From a reservoir, a constant flux of PBS was passed over the electrode surface. A flow rate of $5-10$ cm^3 min^{-1} pumped by a peristaltic pump with pumpsil 913 A016.016 peristaltic tubing (Watson Marlow, UK) was used. The flow cell contained a sampling port for the injection of phospholipid and testing compound solutions. The electrodes were connected to the Autolab PGSTAT 30 potentiostat (Ecochemie, Utrecht, Netherlands) and all RCV measurements were carried out with a PowerLab 4/25 signal generator (AD Instruments Ltd.) which was controlled by Scope software (AD Instruments Ltd.). The RCV voltage excursion was from -0.4 to -1.8 V at a scan rate (ν) of 40 V s^{-1}. The integrity and recovery of each deposited DOPC layer was determined by applying repetitive RCV from -0.4 to -1.8 at 40 V s^{-1} scan rate and monitoring the capacitance peaks characteristic of successive electrically induced phase transitions in the DOPC monolayers[124; 186; 187]. This scan rate was chosen because the resulting currents as capacitance currents were significant enough to be recorded at a good resolution while maintaining a good signal-to-noise ratio. C_{sp} was calculated from the RCV current (I) using equation C_{sp} = I/(ν $\times$ A_0) where A_0 is the electrode area. Before each measurement the Hg electrode was cleaned by cycling the potential between -0.4 V and -2.8 V and a fresh DOPC deposition was performed.

2.3.2 Alternating Current Voltammetry ACV

To compare and confirm the RCV measurements(Figure 3.5), an out-of-phase alternating current voltammetry (ACV) technique has been carried out in this work to study the monolayer capacitance following the interaction of the ILs with the monolayer. An important advantage of ACV over RCV is that since it is essentially a measure of impedance, a more accurate value of capacitance of the interface can be estimated. ACV was carried out using an Autolab PGSTAT 30 potentiostat to obtain the capacitance$-$ potential profiles at negative potentials from -0.4 to -1.6 V in response to an applied AC wave of frequency (f) of 75 Hz and a voltage amplitude (ΔV) of 5 mV. Specific capacitance was calculated from C_{sp} = I*($\omega\Delta VA_0$)$^-1$ where ω is the angular frequency (ω = 2πf) and I* is the imaginary current. Alterations of the DOPC monolayer structure by the ionic liquids near the potential of zero charge (PZC) are detected as modifications of the relative permittivity (ε_r) and/or thickness (d) of the hydrocarbon fraction of the monolayer, as extrapolated from the formula C_{sp} = $\varepsilon_r\varepsilon_0$/d where ε_0 is the permittivity of a vacuum. An example of this technique is the differential capacity of a spread layer of DOPC onto

Hg was measured for ACV cathodic scans (Figure 3.9). All ACV and subsequent EIS experiments were performed in a three-electrode static cell containing a MFE working electrode, prepared as described in the previous section, a 3.5 mol dm^{-3} KCl Ag/AgCl reference electrode, and a Pt counter electrode. Prior to each experiment, the electrolyte was deaerated and all measurements were performed under a protective argon blanket above the electrolyte.

After transferring the DOPC monolayer to the electrode surface, ionic liquids solutions in Milli-Q water, prepared in the same way as described in the previous sections, were added with a micropipette to the electrolyte solution in the measurement cell and then stirred for 15 min prior to ACV measurement. Similarly to the RCV case, this time interval turned out to facilitate equilibration of the IL−lipid system.

2.3.3 Electrochemical Impedance Spectroscopy EIS

Electrochemical impedance spectroscopy (EIS) is a very sensitive way to measure the frequency dependent response at the lipid interface and to gain additional new information about changes in the structure and properties of the DOPC layer on Hg interacting with ionic liquids[128; 186]. All the measurements were carried out using the same experimental conditions and setup described previously for ACV measurements. The electrochemical impedance of the coated electrodes was measured using an Autolab system composed of frequency response analyzer (FRA) and PGSTAT 30 interface (Ecochemie, Utrecht, Netherlands) controlled by Autolab software. Measurements of the complex impedance (Z*(ω)) versus frequency using frequencies logarithmically distributed from 65 kHz to 0.1 Hz, with ΔV = 2 mV in 0.1 mol dm^{-3} KCl at the potential of -0.4 V, were carried out on the supported monolayer systems.

The Z*(ω) versus f plot of the supported DOPC monolayer was recorded as a control prior to the addition of each IL. The experimental conditions for the measurement of Z*(ω) were used exactly as described in other works[124]. For operations, impedance data were currently transformed to the complex capacitance plane using Matlab program and presented using the admittance Y* = 1/Z*, obtaining C′(ω) = Im(Y*/ω) and C″(ω) = −Re(Y*/ω). $-C''_{sp}$ vs C'_{sp} was plotted in the unit of μF cm^{-2} where $-C''_{sp}$ and C'_{sp} are the imaginary and real specific capacitances, respectively. The impedance data of the DOPC monolayer (specifically to take into account the presence of ILs) was analyzed with a more accurate impedance model describing a constant phase element[188] (CPE) which undergoes a Debye type relaxation[124; 186; 187]

$$Y = \frac{1}{R + \frac{1}{(i\omega)^{\beta}\left(\frac{A_S - A}{1+(i\omega\tau)^{\alpha}} + A\right)}} \tag{2.23}$$

where R is the uncompensated solution resistance, ω is the angular frequency, β is the CPE exponent relating to the homogeneity of the CPE (in this case the supported monolayer), τ is the time constant of the secondary Debye relaxation, and α is the coefficient describing the dispersion of τ. A and As are the values of the CPE constants before and after the Debye relaxation.

The capacitance before and after relaxation can be extracted from the equations [124] $A = C^{\beta}\ R^{-}(1-\beta)$ and $C_s = A_s\tau^{(}1-\beta)$. In this fitting the value C is equivalent to the ZFC and can be divided by the electrode area A_0 to give C_{sp}. The fitting of the EIS data was performed with IGOR Pro (Wavemetrics, Inc.).

CHAPTER 3

Results and discussion

3.1 Electrical properties of solid-supported thin films of Ionic liquids

3.1.1 Structural resistance to large electrical fields

We have checked the resistance of $[C_4MIM][NTf_2]$ ordered structures to intense electric fields. Such fields (in order of 10^9 V/m) are known to displace loosely bound ions and detach them from the bulk liquid, a phenomenon called electrospray [189; 190]. In turn, ions arranged in a solid-like structure, like that of conventional crystalline salts, are not expected to be displaced. We have scanned the sample in tapping mode several times applying a potential difference between the conductive tip and the n^+ doped silicon substrate shorted to ground. The small distance between the 2 electrodes (from a few nm down to less than 1 nm), leads to the development of very strong electric fields, $E \approx 10^9$ V/m. If the ions in the ordered layers, as suggested by morphological and mechanical characterization, were more tightly bound than in the liquid droplets, a different behavior under the action of the electrostatic field would be expected, as will be shown in the following. The study of the effect of strong electrostatic fields on the ionic liquid deposition, was usually performed in this way: first, both the tip and the sample were grounded and one or more topographic maps were acquired; then, a scan was performed applying a potential difference (ΔV = +8 V) and a subsequent scan was acquired again with both electrodes grounded. The cycle was iterated using a negative potential difference (ΔV = -8 V). A scan with the tip and the sample grounded is usually performed after the application of the potential, because for high potentials the long-range electrostatic force between the tip and the sample leads to a decrease in the lateral resolution that does not allow to fully appreciate any possible modification in the morphology.

In Figure 3.1, 3 topographic maps show the behavior of ordered ionic liquid layers under the influence of a strong electrostatic field. The map A is the first of the series and has been acquired with both the tip and the sample grounded. The second image B has been again acquired with tip and sample grounded, but after a previous scan performed applying a ΔV=+8V between the tip and the sample. In the same way, image C has been acquired after a scan at ΔV=-8V. The histograms of the heights reported in Figure 3.1 show that, a part from a small broadening of some peaks, possibly due to a slight decrease in the quality of the morphologies because of a dirtier tip, the envelopes overlap, meaning that the structure of the ordered layers has not been substantially modified by the electrostatic field.

In Figure 3.2, 4 AFM topographies acquired in tapping mode using a conductive tip (the conductive coating is Cr-Pt and typical tip radius is around 25nm) on a sample deposited on doped silicon are shown. The image A has been acquired in neutrality conditions and show an area where the IL is structured in both liquid and highly ordered

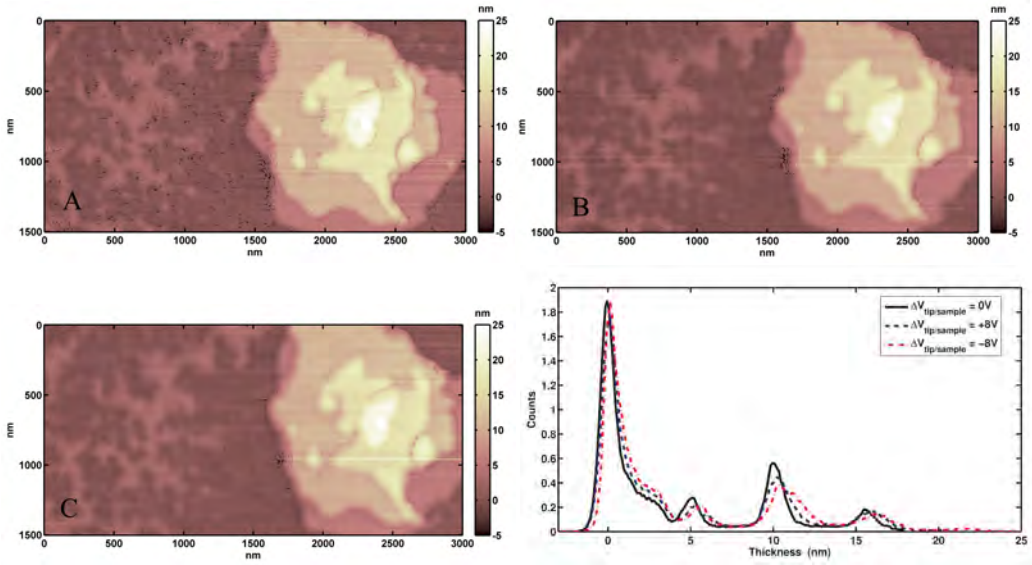

Figure 3.1: Effect of strong electric fields on a thin [C_4MIM][NTf_2] deposition. All the images have been acquired in neutrality conditions. The image A is initially acquired in tapping mode. Second image B has been acquired after a scan in tapping mode applying ΔV=+8V. Third image C has been acquired after a scan at ΔV=-8V. The graph shows the histograms of the heights demonstrating that no quantitative changes in the structure of the ordered layers took place.

form. The image B is the third image after A acquired in neutrality conditions, and illustrates how the ordered layers, but also the droplets are stable against scanning. After acquisition of B, a scan has been performed applying a ΔV =+4 V between the tip and the substrate and image C shows the effect of electric field . The image D of Figure 3.2 has been acquired, again in neutrality conditions, after a scan performed applying a ΔV =+8 V. There is a clear difference in the behavior of ordered layers and liquid droplets. In fact, while the layers, even if damaged, are still there and kept their shapes, the droplets disappeared almost completely from the scanned area. This is clearly an effect of the applied electric field, because it is not observed in figure 3.2 A and B. In this experiments also the height of solid-like islands decrease, probably due to local melting of structure thanks to liquid layer adsorbed on the tip. Another interesting feature to note, is the texturing of the areas of the sample between the terraces, where evidently there was a uniformly distributed sublayer. This effect is clearly visible in histogram of Figure 3.2, in fact a peak at negative height appears. The sublayer of IL is probably less bound and stable than ordinary flat layers.

In Figure 3.3 it is interesting to note that passing from picture A to B, i.e. after a scan applying -8V the droplets disappeared again, but furthermore a small flat layer was grown: this growing was probably due to a deposition of a very small quantity of ionic liquid that was on the tip from previous scans, showing how small amount of IL can spontaneously rearrange in the form of an ordered layer, rather than of a droplet (green square in Figure 3.3). This effect is similar to that obtained by K. Kaisei et al. in ref. [191], who succeeded in fabrication of [C_4MIM][BF_4] film of 4 nm on platinum using electrified AFM cantilever tip used as a nano-inkjet printer. The new layer formed was not as stable as the rest of the islands in the scanned area, because it disappeared after a

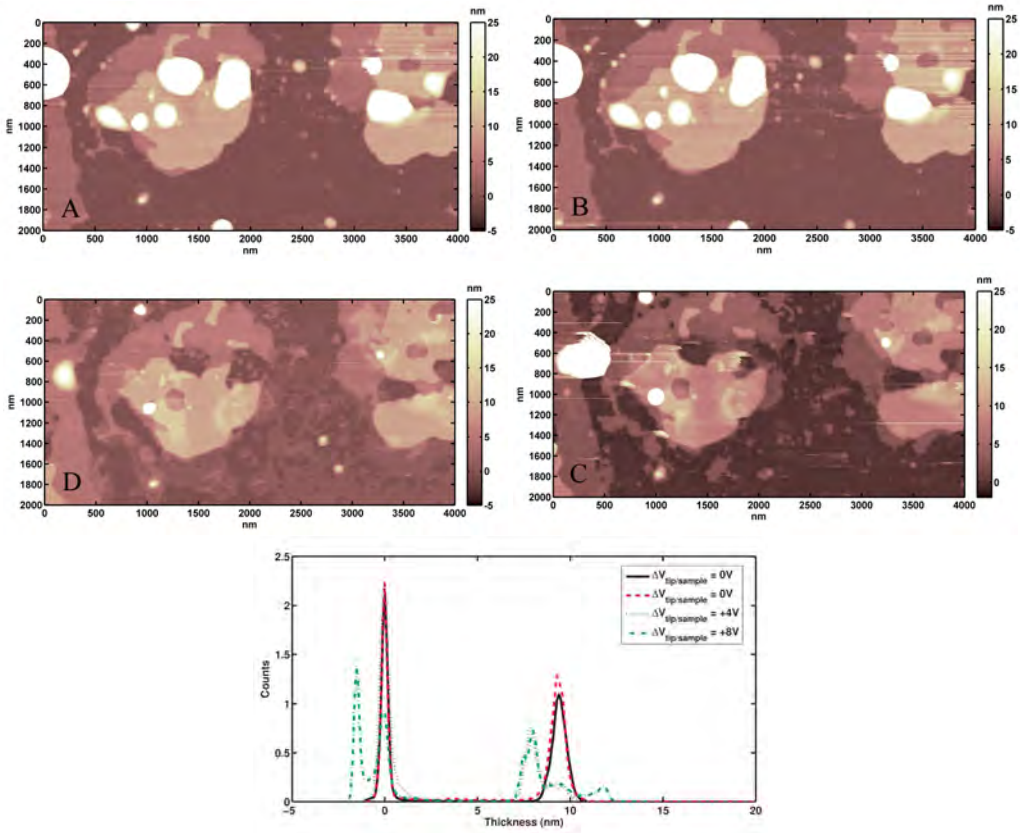

Figure 3.2: Effect of strong electric fields on a thin $[C_4MIM][NTf_2]$ deposition. All the images have been acquired in neutrality conditions. Image A is the first image. Image B has been acquired after 3 scans in neutrality conditions. Image C shows the stability of the ordered layers compared to the liquid droplets after a scan of ΔV =+4 V.The graph shows the histograms of the heights showing small changes due to delamination of structures and

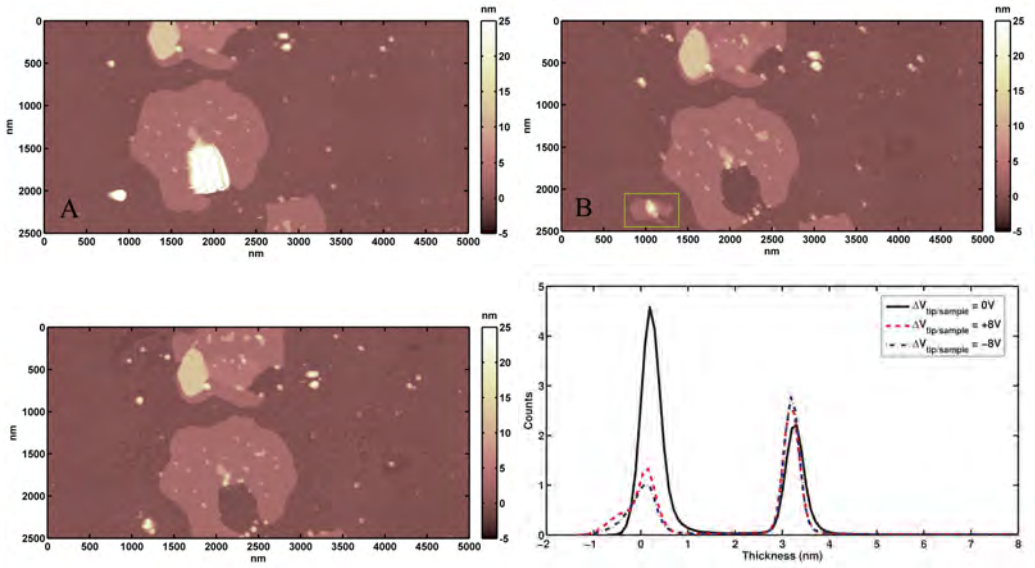

Figure 3.3: Effect of strong electric fields on thin IL deposition. A is the first image acquired in neutrality conditions. B Has been acquired after a scan at -8V, green square indicates a new layer formation. C is the morphology after another scan at +8V. The application of a potential difference between a conductive tip and the substrate, can lead to the uptake and subsequent deposition of small quantities of ionic liquid. Such small quantities can rearrange as ordered layers, even if they do not appear as stable as the others.

subsequent scan at +8V, as can been seen in Figure 3.3 C.

The stability of the ordered domains under strong electric fields evidences how the ions of the ionic liquids are tightly bound in a stable structure. This is a further indication of the fact that IL islands are not only structurally ordered in the vertical direction, as witnessed by the layered morphology [62; 63], but also possess as expected ([64]) a solid-like mechanical character. This observation suggests that ordered [C_4MIM][NTf_2] domains may possess electric/dielectric properties analogous to those of standard solid salts, i.e they may be insulators and dielectrics. The next experimental results strongly support this hypothesis.

3.1.2 DC conductivity of solid-like [C_4MIM][NTf_2]omains

The electrical conductivity of [C_4MIM][NTf_2] films was quantitatively investigated by measuring the local current -versus- voltage (I-V) characteristics. The technique and methods are previously explained in section 2.2.6. The conductivity measurements were carried on 3 different samples: a conductive sample composed by Au-Cu micro-patterns in series with 100MΩ resistor to avoid excessive current flow; a heavy doped n^+ silicon with native oxide layer; a 5nm thick layer of [C_4MIM][NTf_2] deposited on the previous surface.

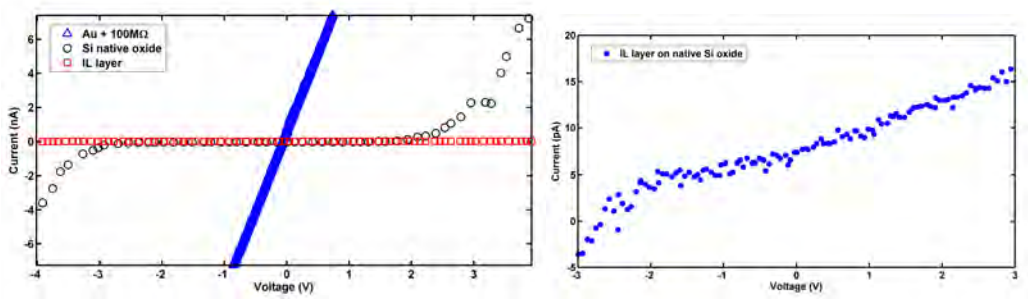

Figure 3.4: (left)I-V curves acquired in spectroscopy mode in the nA range on Au + 100MΩ (blue triangles), n^+ doped silicon with native oxide (black circles), 5 nm thick $[C_4MIM][NTf_2]$ layer (red squares). (right) Zoom of I-V curves acquired in spectroscopy mode in the pA range on 5 nm thick $[C_4MIM][NTf_2]$ layer

As shown in Fig 3.4 the behavior of Au micro-contacts is mainly ohmic with a slope consistent with the resistance placed in series with the micro-contact (100MΩ). The doped silicon with native oxide (1.5-2 nm thick) shows the typical diode-like behavior of a junction metal-oxide-semiconductor, having an exponential increase of current after a critical voltage dependent on thickness and type of oxide material. If the negative potential exceeds the break-down fields the electrons are injected from the tip to the sample; if the bias is positive the electrons flow from the sample to the tip. The break-down field for SiO_2 is 13MV/cm [169], leading to 2.6 V for 2nm thick oxide, a value in complete agreement with that shown in Figure 3.4. The I-V characteristics on an IL layer is a flat horizontal line, showing no conduction and insulator behavior in nA range within the $\pm$4 V window. A conductive behavior of layered $[C_4MIM][NTf_2]$ would have determined an overlap, also an augment due to increased contact area, of the diode-like trend of n^+ doped silicon. In the pA range we can measure a linear trend buried in noise with a slope resistance of 400-500 GΩ (see Figure 3.4 right). Considering the height of IL film (5nm) and the underlying native oxide layer, the resistivity is in the order of 10^{16}-10^{18} Ω/cm demonstrating and ensuring the insulating behavior of IL thin film.

3.1.3 Nanoscale dielectric analysis: AC capacitive measurements (C vs. z curves)

Nanoscale impedance measurements on ionic liquid layers were carried out in a point&shoot method (See section 2.2.3), so initially we run a contact-mode imaging, then points on the image, where the tip was approached, were selected in correspondence of IL islands as well as of bare substrate. Generally, the procedure tested on thin layers of silicon thermal oxide (See section 2.2.6) may fail because the IL sample has a lot of liquid drops that affect negatively the measurement. In figure 3.5 a scheme of layers adsorbed on tip is presented. This situation could induce difficult imaging and force curves acquired during P&S with anomalous behavior.

When the tip is several nanometers away from the top of ILs layer, the probe collapses on surface showing huge adhesion. It seems that a 70 nm thick layer of IL is adsorbed on the tip apex, affecting the tip-sample adhesion force. In this situation several problems arise: the effective electrical radius of the tip is dramatically modified, the super-linear part of C vs. distance curve near the surface, where apex capacitance contribution is emphasized, is masked by adhesion and the effective force applied by the tip is increased. The capacitance curves show only the linear part of the parasitic capacitance in the non-contact region, while the capacitance signal saturates after contact with layer.

Even in conditions in which it is possible to scan correctly and it is possible to perform C vs. distance curves, the curves obtained are sometimes problematic. The fit is executed correctly, but provides not good dielectric values or negative h/ε_r ratios.

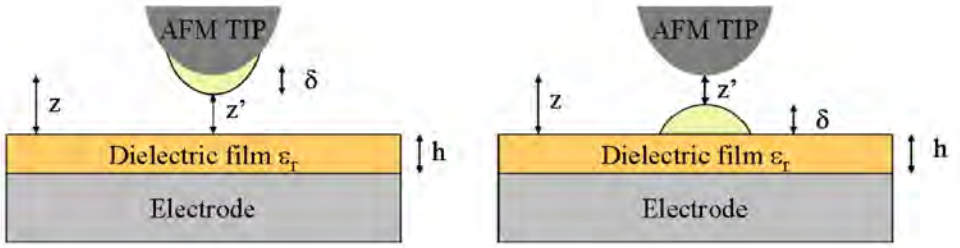

Figure 3.5: Schematic representation of the measurement process of solid-like layers when the liquid material is interposed between the tip and the surface. The liquid can be adsorbed on the tip (left) or on the surface (right). In both cases, h is the thickness of the dielectric film, δ is the thickness of the liquid material between the tip and film, z is distance tip-film real while z' is the distance measured during fictitious approaching curves.

Also in this situation a possible explanation can be tip modification, adsorbing IL in the vicinity of the apex and affecting the applicability of the fit model (i.e. determines a distance effective z' łz). The same phenomenon may appear if a liquid-like drop is on the top of solid-like IL layer, decreasing the effective tip-electrode separation to that determined by deflection vs. distance approaching curve. In fact, the presence of a liquid layers on the tip does not produce appreciable changes during The 'deflection vs. distance' curves. Considering z instead of z' = z-δ in the equations 2.17 and 2.18 is an error, equivalent to move the entire axis of the distances of a quantity δ. The fit provides therefore a (h/ε_r)* value erroneous, in fact: z' + h/ε_r = z - δ + h/ε_r = z + (h/ε_r - δ) = z + (h/ε_r)*. If δ is large enough, (h/ε_r)* values may result negative, without physical meaning because there is no way to know exactly δ. In some situations it may happen that the tip scratches and ruins the solid-like layers by large adhesion while it retracts from surface. Also if the piezoelectric crystal is out of the equilibrium there are considerable thermal drift causing not precise positioning of the tip. These problems are solvable stabilizing the piezo and using small offset. Moreover, after the contact mode image, very fast force curves are performed on clean substrate to clean up the tip apex. The cleaning quality is checked analyzing the adhesion shape of the curves. As mentioned in section 2.1.2 the sample consists in a thin strip of silicon large 1-2 mm with [C_4MIM][Tf_2N]/methanol drop-coating deposition performed on the native oxide substrate. On the same sample, silicon surface with native oxide layer (calibration electrode) and thicker silicon thermal oxide (dielectric layer test) are present. Here calibrations, tests and measurements on ILs layers can be performed in a quick and clean way.

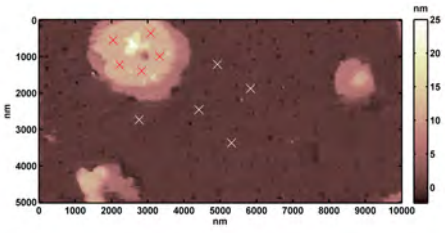
nm
nm
nm

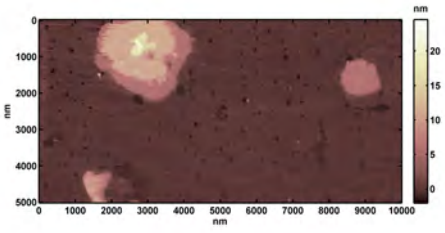
nm
nm
nm

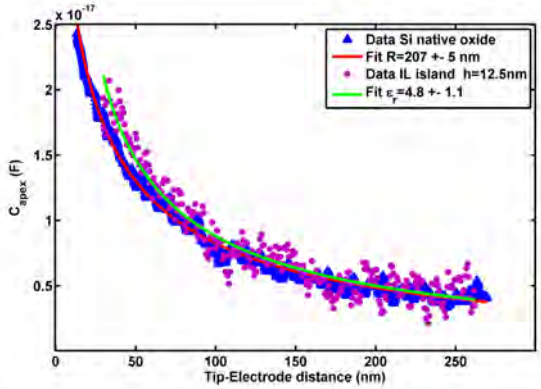
x 10^-17
Data Si native oxide
Fit R=207 +- 5 nm
Data IL island h=12.5nm
Fit ε_r=4.8 +- 1.1
C_apex (F)
Tip-Electrode distance (nm)

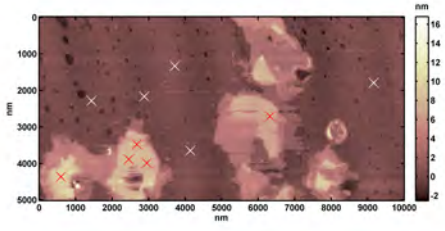
nm
nm
nm

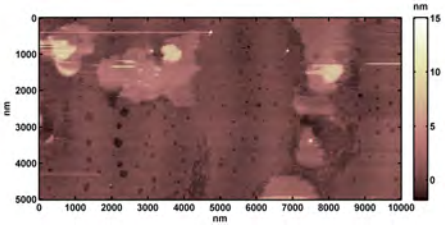
nm
nm
nm

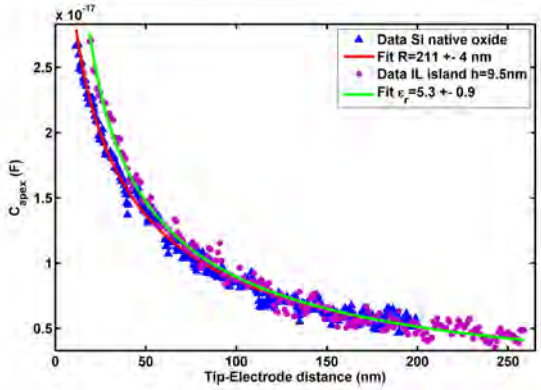
x 10^-17
Data Si native oxide
Fit R=211 +- 4 nm
Data IL island h=9.5nm
Fit ε_r=5.3 +- 0.9
C_apex (F)
Tip-Electrode distance (nm)

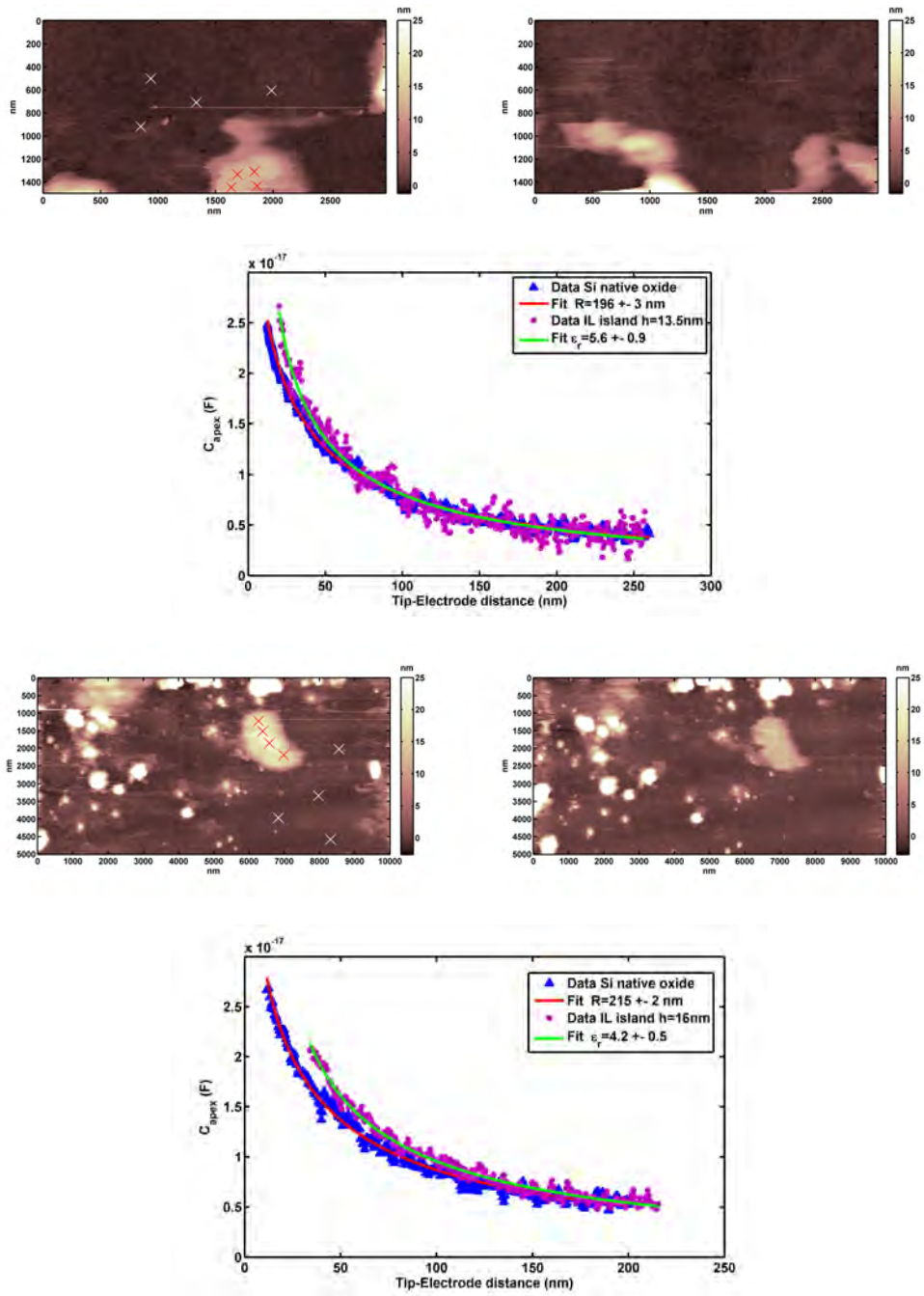

Figure 3.4: Example of P&S executed on islands of $[C_4MIM][NTf_2]$ (See Tab. 3.1 for info). The first image A represents the first scan before P&S. The curves were acquired on substrate for radius calibration (white crosses) and on the layer to measure the dielectric constant from C vs. d curves (red croses). The second image B is obtained after P&S procedure, showing the integrity of IL layer and the correct re-positioning of the scanner (no thermal or piezo drift). The graph shows the apex capacitance acquired on a $[C_4MIM][NTf_2]$ solid-like island (purple circles for experimental data and green line for fit) compared with curves acquired on bare electrode (blue triangles for experimental data and red line for fit) for radius calibration purpose.

The aF capacitance resolution was achieved by applying standard NIM parameters described in section 2.2.6 in Table 2.1: AC input voltage of 500mV amplitude and 90kHz frequency, and with a lock-in time constant τ = 30ms in order to minimize the noise. A force measurement was simultaneously performed to monitor the tip-surface distance. Results of the simultaneous measurements of force and capacitance are presented in Fig. 3.4. The experimental data are obtained by averaging on 100 curves sparse on substrate (for radius calibration)and on surface of IL island. We consider as distance zero the position at the top of IL layer. Then the distance from the film surface is calculated from the force plot curve by considering the jump-in point as the zero distance between the tip apex and the surface and then rescaling the distance from the piezo displacement taking in to account the cantilever deflection. The figure 3.4 clearly show, after a subtraction of a constant capacitance slope due to an increase in stray capacitance, a faster logarithmic increase in the surface proximity. The 2-steps procedure to obtain the dielectric constant (described in section 2.2.6) consists, firstly, in the electrical radius calibration using C vs. z curves on substrate near flat islands and marked with white crosses. The radius R_1 (See Tab. 3.1) is calculated fitting the experimental data using Eq. 2.17. The second step consists in the analysis of C vs. curves acquired on the top of IL layer. Knowing the radius R_1, the ratio h/ε_r and consequently ε_r are calculated fitting the experimental data using Eq. 2.18.

After the point-shoot data acquisition, a second contact-mode image is collected to check the conditions of the IL layer. If topographical deformation, delamination and ruptures are detected in the second image, the measured values are considered unreliable. With the same severity, thermal or piezoelectric drifts are checked and validated. Finally, to complete the set of measurements, the value of electric contact radius R_2(nm) is re-calibrated on the bare electrode to see changes of tip apex state (See Tab. 3.1). These modifications generally occur if the conductive coating is damaged or if material (ionic liquid or dirt particles) is adsorbed on the tip. If also the re-measured value of the radius is well within experimental error, we can fully confirm the validity of measurements. In case of small discrepancies, the average value of radii is used.

R_1(nm)	R_2(nm)	h(nm)	h/ε_r(nm)	ε_r
207 ± 11	210 ± 8	12.5 ± 0.2	2.6 ± 0.9	4.8 ± 1.1
211 ± 6	206 ± 5	9.5 ± 0.1	2.0 ± 0.6	5.3 ± 0.9
196 ± 5	201 ± 7	13.5 ± 0.2	2.3 ± 0.5	5.6 ± 0.9
215 ± 4	217 ± 5	10.6 ± 0.2	2.5 ± 0.4	4.2 ± 0.5

Table 3.1: Summary of experimental data obtained with capacitive AC sensing measures. R_1 is the radius of the calibration before the measurement on IL, while R_2 represents the calibration after the measurements, h is the thickness of the island calculated with topographical analysis before and after P&S. Finally we present the values of h/ε_r and ε_r obtained from the fit procedure described in section 2.2.6.

The final value at 90 kHz frequency is obtained by a weighted average of all the measures in Tab 3.1: $\varepsilon_r = 4.8 \pm 0.8$. It is noticeable that dielectric constant of thin IL layers is similar to the conventional insulating material one, like SiO_2 (ε_r = 3.9) or NaCl(ε_r = 5.3). This value confirms again the dielectric nature of ILs solid layers, and in the next section we have had ulterior confirm, carrying on similar measurements but using a different technique[168].

3.1.4 Nanoscale dielectric analysis: electric force measurements (F_{el}s. z curves)

A simple method to measure the static dielectric constant of thin films with nanometric spatial resolution consists in monitoring the static deflection of the cantilever induced by the capacitive electrostatic force, according to equation for the deflection 2.19. The dielectric constant is extracted also from DC electrostatic force measurements by fitting data with eq. 2.21 [168] exposed in section 2.2.6. As in the previous AC measurements, the method was validated here on thin silicon dioxide films (section 2.2.6) and then applied on IL layers. All the static deflection measures are carried on with the same strategy discussed previously. After checking the status of sample, the experimental data are considered for final analysis. After a contact-mode measure, we select points on the image where the DC polarized tip will approach the surface. Measurements on ionic liquid layers were carried out always in a point&shoot method.

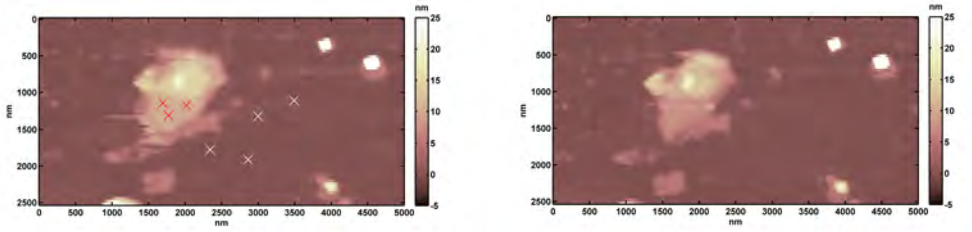

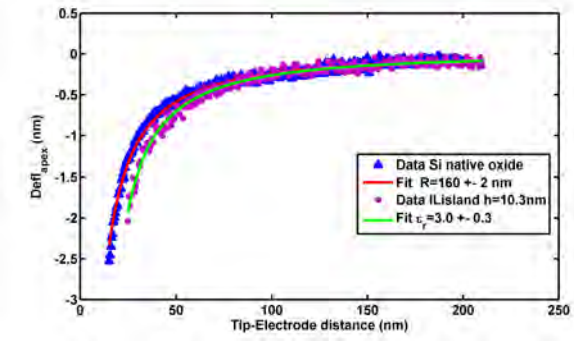

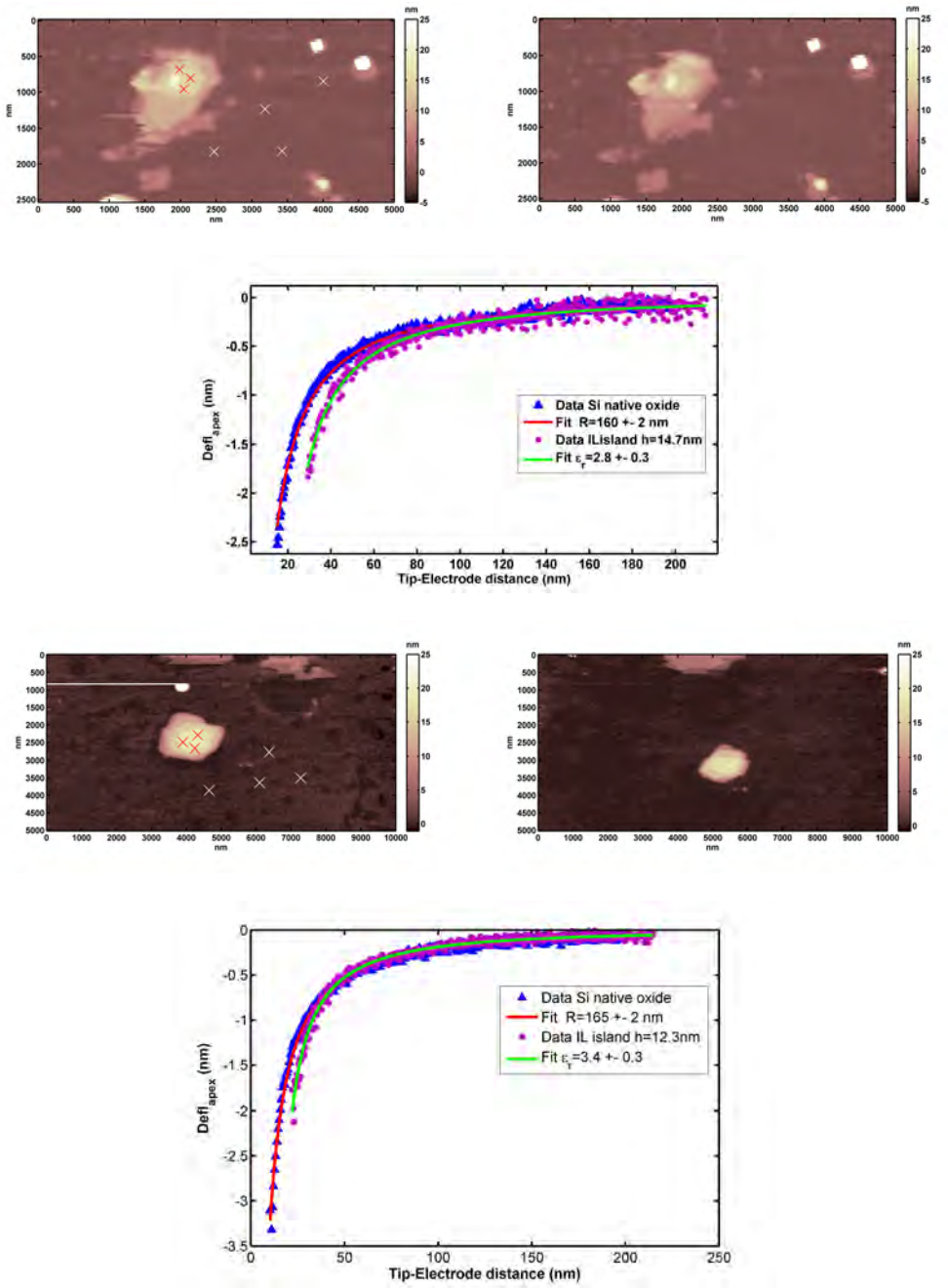

Figure 3.4: Example of P&S executed on islands of $[C_4MIM][NTf_2]$ with DC polarized tip (See Tab. 3.2 for info). The first image A represents the first scan before P&S. The curves were acquired on substrate for radius calibration (white crosses) and on the layer to measure the dielectric constant from Defl vs. d curves (red crosses). The second image B is obtained after P&S procedure, showing the integrity of IL layer and the correct re-positioning of the scanner (no thermal or piezo drift). The graph shows the electrostatic deflection curves acquired on a $[C_4MIM][NTf_2]$ solid-like island (purple circles for experimental data and green line for fit) compared with curves acquired on bare electrode (blue triangles for experimental data and red line for fit) for radius calibration purpose.

The dielectric constant is extracted also from DC electrostatic force measurements by fitting data with eq. 2.21 [168] exposed in section 2.2.6. As in the previous AC measurements, the method was validated here on thin silicon dioxide films (section 2.2.6) and then applied on IL layers. All the static deflection measures are carried on with the same strategy discussed previously. After checking the status of sample, the experimental data are considered for final analysis. After a contact-mode measure, we select points on the image where the DC polarized tip will approach the surface. Measurements on ionic liquid layers were carried out always in a point&shoot method.

R_1(nm)	R_2(nm)	h(nm)	h/ε_r(nm)	ε_r
160 ± 2	164 ± 3	10.3 ± 0.2	3.5 ± 1.7	3.0 ± 0.4
160 ± 2	164 ± 3	14.7 ± 0.1	5.3 ± 0.8	2.8 ± 0.3
165 ± 2	167 ± 2	12.3 ± 0.1	3.7 ± 0.8	3.4 ± 0.3

Table 3.2: Summary of experimental data obtained with capacitive DC sensing measures. R_1 is the radius of the calibration before the measurement on IL, while R_2 represents the calibration after the measurements, h is the thickness of the island calculated with topographical analysis techniques. Finally we present the values of h/ε_r and ε_r obtained from the fit procedure described in section 2.2.6.

Weighting the values reported in Tab 3.2, we have obtained : ε_r = 3.1 $\pm$ 0.2. The DC static dielectric constant is smaller than AC value acquired at 90 KHz (ε_r = 4.8 $\pm$ 0.8) during this study.

The local dielectric constant values measured are significantly lower than values (ε_r = 9-14) found in the literature and extrapolated from impedance spectroscopy at high frequency (between 1 MHz and 20 GHz) on bulk ionic liquid [16; 17; 20–22]. Low values of ε_r (typically between 3 and 6) are measured on insulating solid salts like NaCl (see for example tab. 1.2). This behavior is justified by the fact that the mobility of ions in the terraces is small compared to the bulk liquid ions. The compact structure of IL layers, mechanically and electrically tested here, is a clear indication that ions in the islands are 'trapped' in a structure more bound and tight compared to the liquid phase. The dielectric spectroscopy, accomplished by Sangoro et al. [19], of ionic liquid [C_4MIM][BF_4] at temperatures close to the gelation (188K) further confirms this hypothesis because, at fixed frequency, there is a noticeable decrease of the dielectric constant, going towards the gel state. In a more recent paper, Iacob, Sangoro et al. [192] explore the electrical properties of [C_6MIM][PF_6] interacting with silica nanoporous membranes (average diameter of pores 7.5 nm). The differences of diffusivity and conductivity in the pores compared to the bulk are explained within a model that considers, in addition to the bulk response, the contribution from a compact layer of reduced mobility at the pore–matrix interface. An order of magnitude decrease in diffusivity and conductivity of the untreated, hydrophilic membrane is observed, due to affinity between the ionic liquid and the silanol groups. In agreement with the nanopores layering model, a remarkable increase of the diffusion coefficient of the ionic liquid is observed if, upon silanization, the affinity between IL and silica membranes is nullified. Although diffusion coefficient, charge transport rate, dc conductivity and dielectric loss are distinguishable for different systems (membranes treated and untreated, bulk), unfortunately in this study, the total dielectric constant is dominated by the contribution from the SiO_2 membrane, thereby leading to the absence of deviation and identification of the compact layer role. The geometrical confinement inside nanopores is very similar to surface layer confinement

induced by charged surface after drop coating deposition. AFM allows the characterization of dielectric constant for this layered system and direct comparison with extrapolated bulk system. Roling et al. [193] presented EIS results for the interface between [C_4MPyrr]FAP and Au(111). The fast capacitive process was attributed to charge redistributions at the interface which do not require activation energy in excess of that for ion transport in the IL. A low-frequency relaxation was observed in a frequency range from about 20 Hz to about 0.1 Hz. This underlying slow capacitive process was attributed to charge redistributions in the innermost ion layer in proximity of electrode surface. In this layer, the ions are strongly bound to the electrode, and thus charge redistributions require a higher amount of activation energy. Moreover, in complete agreement with mechanical experiments performed on [C_4MIM][NTf_2] in [64], force–distance curves obtained by in situ AFM measurements [193]revealed that at any electrode potential, there is a multi-layer structure next to the Au(111) surface. Increasing the potential in the cathodic direction leads to an increase of the number of detectable layers and to an increase of the mechanical breakthrough forces indicating that the layers become more strongly bound to the charged surface.

Another confirm of dielectric constant lowering is depicted by Senapati et al. [194] studying the equilibrium and dynamical properties of Stockmayer liquids (dipolar solvents) in confined spherical cavity. Clearly, the system under study, shows that confinement leads to a noticeable lowering of the dielectric constant. First of all, the density profiles in the cavity are found to be highly nonuniform; a similat behavior is fond for simulated IL in ref. [63]. Pronounced orientational order is found for the dipolar molecules which are seen to align parallel to the cavity wall [194]. More importantly, orientational ordering leads to a lowering of the dielectric constant of the dipolar solvent in a cavity as compared to its bulk value. The translational motion of the confined molecules is calculated in directions perpendicular and parallel to the surface tangent. It is found that the perpendicular diffusion is hindered and the lateral diffusion is enhanced compared to diffusion in the bulk phases. The dipolar orientational relaxation in a cavity is also found to be slower than that in the bulk phase and the extent to slowing down is found to increase with decreasing cavity size, so enhancing the system confinement. It may be speculated that surface or cavity confinement effects on highly correlated ionic systems, like ILs, can be more influential than dipolar solvents. A theoretical paper by Kornishev [23] highlights how the static dielectric constant ε_r represents an important parameter which sets the scale of the electrostatic interactions and capacitance in ionic liquids. He considers also the total capacitance of electrode/ILs interface, in the absence of specific adsorption, and when the diameters of anions and cations are similar, composed of the compact- and diffuse-layer parts in series, like in the Gouy-Chapman-Stern theory. For the compact-layer an effective dielectric constant similar to optical dielectric value ($\varepsilon_r \approx 4$), was introduced to describe the capacitance behavior. For a dense, but compressible, IL the capacitance should go up with the electrode polarization as long as it draws more counterions to the electrode surface, filling the voids in the IL and thereby achieving denser packing. Once the packing is complete (all the voids filled), the capacitance will start decreasing, with counterions lining up near the electrode. There will be a maximum in between. However, in dense Coulombic systems, where the effects of ionic correlations and overscreening are important, [195] the response cannot be rationalized solely in terms of "filling voids" and "coming closer" of one sort of ion to the electrode. The system response is determined by the formation of standing charge density waves, made possible by collective rearrangement of counterions and their coions. Also in another theoretical work performed by Kisza [196], the dielectric constant of the compact layer is considered lowered by the vicinity with the electrode surface. For example, us-

ing ethylammonium nitrate ionic liquid, the static dielectric constant (calculated in [197] ε_r =24.5), is expected to fall down to ≈ 6 at the outer Helmoltz plane.

3.2 Ionic liquids interacting with biological membranes a models living cells

In the next section I will show how ionic liquids interact with biological material by means of AFM and electrochemical methods. First, I will present phospholipid monolayers adsorbed on Hg electrodes interacting with various ILs and investigated with electrochemical techniques. Second, I will perform morphological and nanomechanical experiments by AFM on phospholipid bilayers supported on solid surface interacting with ILs. In the end, directly connected to the interaction with model cell membranes, I will explore the nanomechanical and morphological properties of live cells always interacting with different ILs.

3.2.1 Ionic liquids interacting with biomembrane models: electrochemical study

For electrochemical measurements, the experimental setup and the technique is explained in the section 2.1 and 2.3. All the results that I am going to present are published in ref. [198]

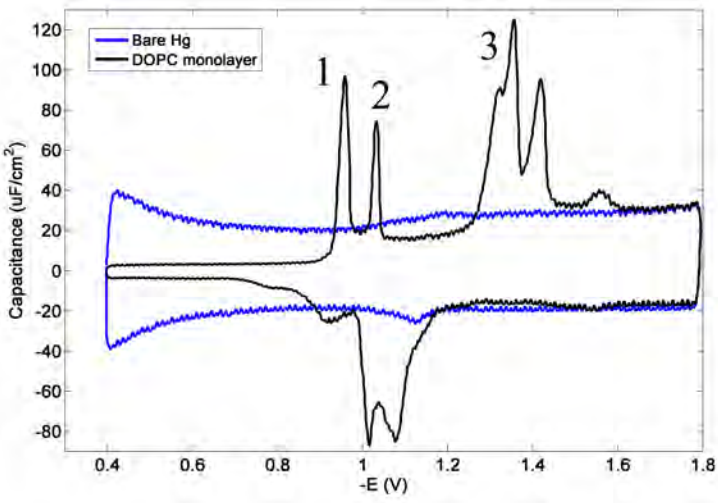

Figure 3.5: Capacitance versus potential profiles of uncoated (blue line) and DOPC monolayer coated MFE (black line), using RCV voltage sweep between 0.40 and 1.80 V. Experiment was carried out in pH 7.4 PBS buffer solution

When the electrode potential is rapidly cycled over a defined potential range, the DOPC-coated Hg shows characteristic voltammetric current peaks that correspond to processes of DOPC phase transition, desorption, and respreading at the mercury surface. At potentials around -0.40 V (circa position of zero charge (PZC) of mercury), DOPC is oriented with its hydrophobic tails toward the Hg surface and forms a dielectric insulating layer. At more negative potentials, the monolayer begins to be permeable

to ions until a phase transition (peak 1 in Figure 3.5) occurs at -0.94 V, leading to the formation of a porous monolayer fully permeable to ions [126]. The second phase transition (peak 2 in Figure 3.5) at -1.04 V proceeds by the growth of defects or inhomogeneities in the layer, leading to the formation of porous bilayer in the potential range between $-1.1$and -1.3 V. At potential around -1.35 V a third phase transition (peak 3 in Figure 3.5) is detected highlighting desorption process of the DOPC and its replacement with electrolyte on the Hg surface. The three consecutive transitions are the result of the increasing negative charge at the surface of the electrode, providing a change in affinity of the phospholipid headgroups, phospholipid hydrocarbon chains, and electrolyte in proximity to the interface.

Subsequently, sample solutions of ILs in logarithmic concentration from 0.01 μmol dm^{-3}to 10 mmol dm^{-3} for hydrophobic ILs, and from 1 μmol dm^{-3} to 1 mol dm^{-3} for hydrophilic ILs, were prepared in pH 7.4 PBS buffer solution and injected in the flow cell. The IL$-$phospholipid system was kept at rest for 5 min before the RCV experiments were started, in order to allow for equilibration of the interface, as witnessed by the stabilization of voltammograms. The interaction of the compound with the DOPC was monitored while cycling the electrode potential from -0.4 to -1.8 at 40 V s^{-1}. In these RCV experiments a fabricated rectangular Pt electrode was employed as a counter electrode and a 3.5 mol dm^{-3} KCl Ag/AgCl was used as reference electrode. All potentials are quoted versus this reference electrode.

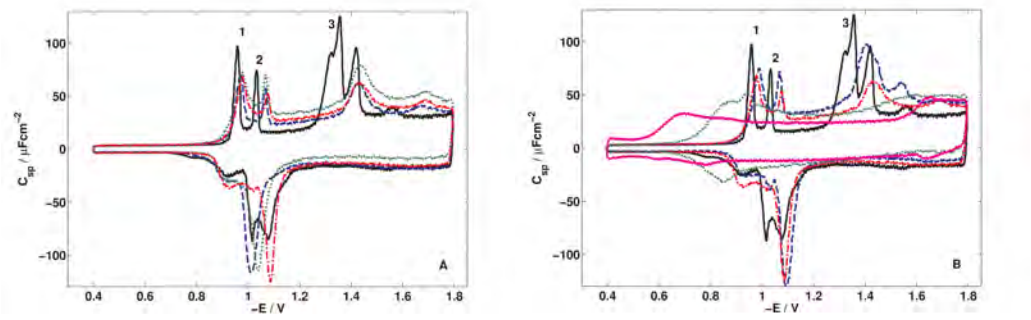

Figure 3.6: RCVs of a DOPC-coated Pt/Hg electrode in 0.1 mol dm^{-3} PBS standard electrolyte interacting with different ionic liquids at the same concentration 0.5 mmol dm^{-3}. For comparison, in both diagrams (A,B), the black flat line represents the RCV of non-interacting DOPC monolayer. Transitions peaks are labeled as follows: (1) formation of porous monolayer, (2) nucleation and growth of defects, and (3) desorption. (A) DOPC interacting with [C_4MIM][X] where X = Cl (blue dashed line), BF_4 (green dotted line), and NTf_2 (red dash-dotted line), highlighting the effect of anion. (B) DOPC interacting with [C_nMIM][NTf_2] with n = 2 (blue dashed line), 4 (red dash-dotted line), 8 (green dotted line), and 12 (pink flat line), highlighting the effect of lateral chain.

Ionic liquids dissolved in water interact with the adsorbed layer with varying degrees of affinity and these interactions can be observed in the current response of the RCV. Interaction is manifest as suppression, broadening, and shift of the voltammetric peaks corresponding to the phase transitions. Enhanced depression of the DOPC peaks following IL addition is correlated with a stronger DOPC$-$ILs interaction. Figure 3.6 A and B show the effect of the 0.5 mmol dm^{-3} ILs solution in 0.1 mol dm^{-3} PBS in a RCV experiment carried out on a DOPC layer performed in the flow cell apparatus. The data for each sample and each concentration have been acquired after flushing the cell with the IL solution for 10 min, during which the effects on the monolayer reach saturation.

Generally for all ILs, when the Hg electrode coated with DOPC is polarized at negative potentials, the positive cations in solution migrate toward the coated electrode and interact with the DOPC monolayer by forming a double layer with anions. The effect of each individual cation is critical and dominant in comparison with that of the anion[90; 199]. The secondary effect of the anion is well shown in Figure 3.6 A where [C_4MIM][X] (X = Cl, BF_4, NTf_2) are used. For these IL interactions the shape of the resultant RCV is similar: peak 1 is suppressed and broadened and reflects a general interaction of the IL with the monolayer. The capacitance minimum of DOPC in the potential range between -0.4 and -0.8 V remains unchanged after ILs$-$monolayer interaction. Only small variations were observed when altering the anionic species in solution. These variations were mainly exemplified in the height of the capacitance current peaks 1, 2, and 3 values during reorientation and desorption processes. Interestingly, using C_4MIM cation species the reaction with DOPC is reversible as shown in the figure 3.7.

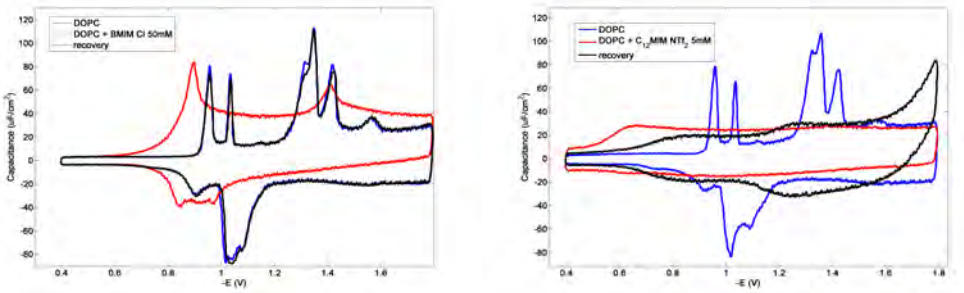

Figure 3.7: RCVs of a DOPC-coated Pt/Hg electrode in 0.1 mol dm^{-3} PBS standard electrolyte interacting with 0.1 mol dm^{-3} [C_4MIM][Cl] (A) and [C_{12}MIM][NTf_2] (B). For comparison, in both diagrams (A,B), the black flat line represents the RCV of non-interacting DOPC monolayer, red dashed line represents RCV of interaction with ILs and the blue dotted line represents the recovery process after 10 min flushing of pure PBS.

After exposure of DOPC monolayers to ILs, PBS electrolyte is flushed through the cell, the applied potential is scanned between -0.4 and -1.8 V and the characteristic capacitance$-$potential profile of the DOPC monolayer is recovered (fig.3.7 A). This information suggests that C_4MIM-based ILs may adsorb onto the DOPC monolayer and/or penetrate tail-first into the layer without significantly disrupting it (as observed in molecular simulation studies focusing on cholesterol and POPC bilayers [93; 94]). Simulations [94] show that anions interact rather weakly with the lipid layers; this is consistent with the minimal effect of the anion on the capacitance minimum observed in RCV experiments. The effect of the side lateral chain of cation is analyzed and compared in Figure 3.6 B where [C_nMIM][NTf_2] (n = 2, 4, 8, 12) are used. The behavior of [C_2MIM] is very similar to [C_2MIM]. The interaction with DOPC is stronger if the lateral chain is increased to 8 and 12 carbon atoms, as demonstrated by the increase in the monolayer capacitance and enhanced suppression/alteration of the capacitance peak current values. Compounds with long hydrocarbon structure are more lipophilic, leading to an aggressive reaction with phospholipid layers [200]. The increase of the DOPC monolayer capacitance probably suggests the decrease in dielectric spacing (monolayer rupture) and the simultaneous increase in relative dielectric constant resulting from monolayer disruption and the insertion of ILs molecules in DOPC. This strong interaction (especially for [C_{12}MIM]) was found to be irreversible (fig.3.7 B) in contrast to that of the

C_4MIM cation and DOPC and leads to the destruction of the monolayer and substitution of phospholipids by IL cations on the Hg. This suggests that, during the effective monolayer interaction, the short tail ILs do not solubilize the phospholipids through micellization, nor through irreversible monolayer replacement at the concentrations investigated. Instead, the long tail ILs and phospholipid form some complex conformations during the interaction, presumably between the hydrophobic domains of the polymers and the hydrophobic tails of the phospholipid. Similar RCV recovery behavior is experimented by Zhang et al. [128] in the analysis of membrane activity of hydrophobic modified Poly(L-lysine isophthalamide) (PLP).

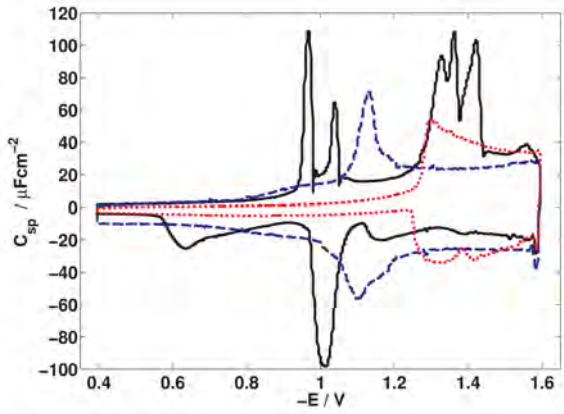

Figure 3.8: RCVs of DOPC monolayer on Hg in 0.1 mol dm^{-}3 KCl electrolyte interacting with a high concentration emulsion of [C_{12}MIM][NTf_2]. The black flat line represents the RCV of non-interacting DOPC monolayer. After a few minutes of interaction [C_{12}MIM] cations substitute completely the lipid monolayer forming a new compact layer without defined capacitive peaks (red dotted line). During the transition from DOPC monolayer to ILs monolayer a complex structure is formed (blue dashed line).

The transition from DOPC monolayer to [C_{12}MIM][NTf_2] layer is highlighted in RCV diagrams in Figure 3.8. The hydrophobic and lipophilic character of long-tail ILs promotes the formation of an IL layer on Hg. Similar to the compact layer formed on standard metallic electodes; recent studies [201; 202] using pure ILs as electrolyte confirm indeed the formation of compact IL layers in contact with Hg surface during electrochemical measurements. To check the hypothesis that ILs form compact layers at the Hg surface we have repeated the experiment using a concentrated (0.1 mol dm^{-3}) emulsion of [C_{12}MIM][NTf_2] in 0.1 mol dm^{-3} KCl water solution and a stable and compact layer readily formed on Hg (Figure 3.8). This layer shows a lowering in capacitance compared with DOPC, underlining the compact character of this structure. A broad transition peak around -1.3 V is evidence for the replacement and/or permeabilization of the IL layer by the base electrolyte at this negative potential.

Similarly to RCV scans, the DOPC monolayer displays a low-capacity region (1.85 μFcm^{-2}), two sharp pseudocapacitance peaks, (peaks 1 and 2 at -0.94 and -1.02 V, respectively), and a further broader pseudocapacitance peak (peak 3 at -1.275 V) at more negative potentials. Peaks 1, 2, and 3 correspond to structural reorientations of the monolayer and peaks 1 and 2 represent phase transitions 1 and 2, respectively, of the lipid monolayer.

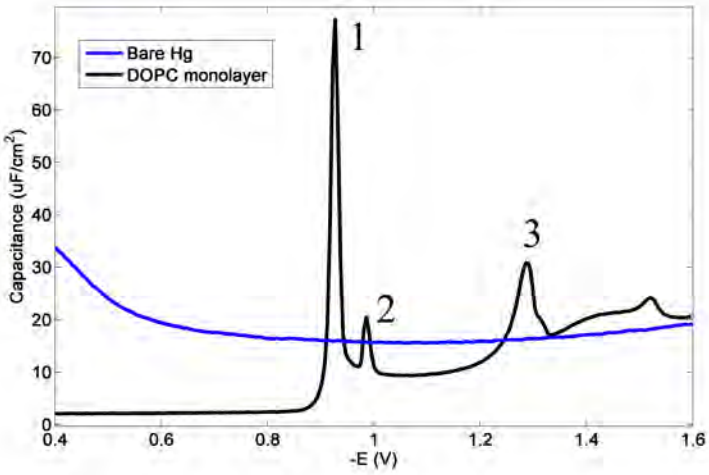

Figure 3.9: Capacitance versus potential profiles of uncoated (blue line) and DOPC monolayer coated MFE (black line), using an ACV cathodic voltage sweep between 0.40 and 1.60 V. Experiment was carried out in pH 7.4 PBS buffer solution

The activity of ILs on the DOPC monolayer has been further investigated by means of more sensitive out-of-phase ACV and subsequently EIS in a 3-electrode electrochemical cell (as described in section 2.3) validating the results obtained by RCV using the flow cell.

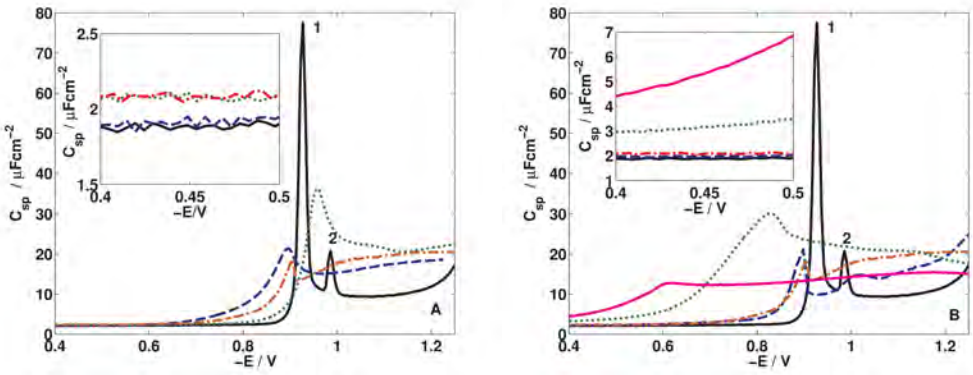

Figure 3.10: Capacitance versus potential profiles of DOPC monolayer coated MFE in 0.1 mol dm^{-3} KCl interacting with different ionic liquids at the same concentration 1 mmol dm^{-3} using an ACV cathodic voltage sweep between −0.40 and −1.25 V. For comparison, in both A and B, the black flat line represents the ACV of non-interacting DOPC monolayer. Transitions peaks are labeled as follows: (1) formation of porous monolayer and (2) nucleation and growth of defects. (A) DOPC interacting with [C_4MIM][X] where X = Cl (blue dashed line), BF_4 (green dotted line), and NTf_2 (red dash-dotted line). (B) DOPC interacting with [C_nMIM][NTf_2] with n = 2 (blue dashed line), 4 (red dash-dotted line), 8 (green dotted line), and 12 (pink flat line). The insets in (A) and (B) represent a magnification between −0.40 and −0.5 V highlighting the effect on monolayer capacitance.

Figure 3.10 shows the effect of anion (A) and the effect of lateral chain (B) using ACV. When changing the anions of ILs (Figure 3.10 A), the capacitance of the lipid layer after IL interaction remains the same as that shown in the DOPC control. From $C_{sp} = \varepsilon_0 \varepsilon_r / d$, a constant capacitance suggests negligible structural modification to DOPC monolayer. However, the presence of ILs alters the phase transition processes of the lipid monolayer: peak 1 was significantly suppressed and peak 2 became very broad and decreased in significance. In contrast, when changing the chain length of the cations, the monolayer activities of the ILs are more systematic and significant. The insets in Figure 3.10 show the capacitance minimum of the supported DOPC monolayer around PZC (ca. -0.4 V) before and after the IL interactions. [C_4MIM] and [C_2MIM] cations (independent from the anions) only cause a small increase of the monolayer capacitance ($\Delta C_{sp} \approx 10\%$), probably due to the rare events of reversible and partial penetration of butyl and ethyl tails of cations into DOPC monolayer [94]. Cations [C_8MIM] and [C_{12}MIM] are more lipophilic and cause significant capacitance minimum increases of ΔC_{sp}=57% and ΔC_{sp} = 113%, respectively, at -0.4 V. The increased capacitance can be attributed to the complete penetration of hydrocarbon tails into the lipid monolayer, which leads to the formation of holes and channels for ions in the electrolyte in the otherwise impermeable lipid layer. In summary, as shown in Figure 3.10, substantial structural modifications of DOPC monolayers can be observed upon increasing of the chain length of the cations, while changing the anions of [C_4MIM][X] leads to small unsystematic variations in the capacitance−potential plot.

In Figure 3.11 is possible to see the ideal behavior of capacitance (real part and phase) for MFE interface coated and uncoated by DOPC. These interfaces could correctly described with a simple model of RC circuit.

EIS measurements have been carried out immediately following ACV measurements using ILs at the same concentration of 1 mmol dm^{-3}. The extrapolated zero frequency capacitance (ZFC_{sp}) values for the DOPC layers after the ILs interactions are in approximate agreement with the ACV results presented as insets of Figure 3.10 A and B.

From EIS spectra in Figure 3.12, two noticeable modifications to the impedance profile of the monolayer can be extrapolated following the IL−DOPC interactions: the increase of the ZFC_{sp}, and the additional capacitive elements at low frequencies. This low frequency 'tail' is caused by dielectric relaxation induced by the movement of large ions within the Debye length at the electrode interface. These modifications to the impedance profiles of supported DOPC monolayer are related to the change in the structural properties of the monolayer, arising from the adsorption/penetration of ILs cations into the lipid monolayer. As demonstrated in Figure 3.12 A, [C_4MIM][X] with different anions does not modify the supported monolayer significantly. More extensive monolayer interactions have been observed by increasing the chain length of the cations (Figure 3.12 B), as demonstrated by the increase of monolayer capacitance and an enhanced low-frequency secondary element. In particular, the extra low-frequency capacitance suggests the formation of an ILs/DOPC complex (see Figure 3.8), caused by the insertion of hydrocarbon tails into the well oriented DOPC monolayer. The fitting procedure was carried out using the eq 1 previously described. The most significant effect of the IL interaction on the fitting parameters is the interaction of DOPC with [C_8MIM][NTf_2] and [C_{12}MIM][NTf_2]. In this case the C_{sp} increases from 1.9 to 2.5 and to $\approx$4 μF cm^{-2}, respectively, and there is a decrease in the value of β from 0.985 to 0.970. The decrease in β, indicating a roughening of the monolayer− electrolyte interface, is caused by the strong interaction of [C_{12}MIM][NTf2] with the lipid layer. The low-frequency relaxations that appear in the capacitance plot as a 'tail' near semicircle have been usually attributed to Maxwell−Wagner effects, i.e. to electric charge buildup in dielec-

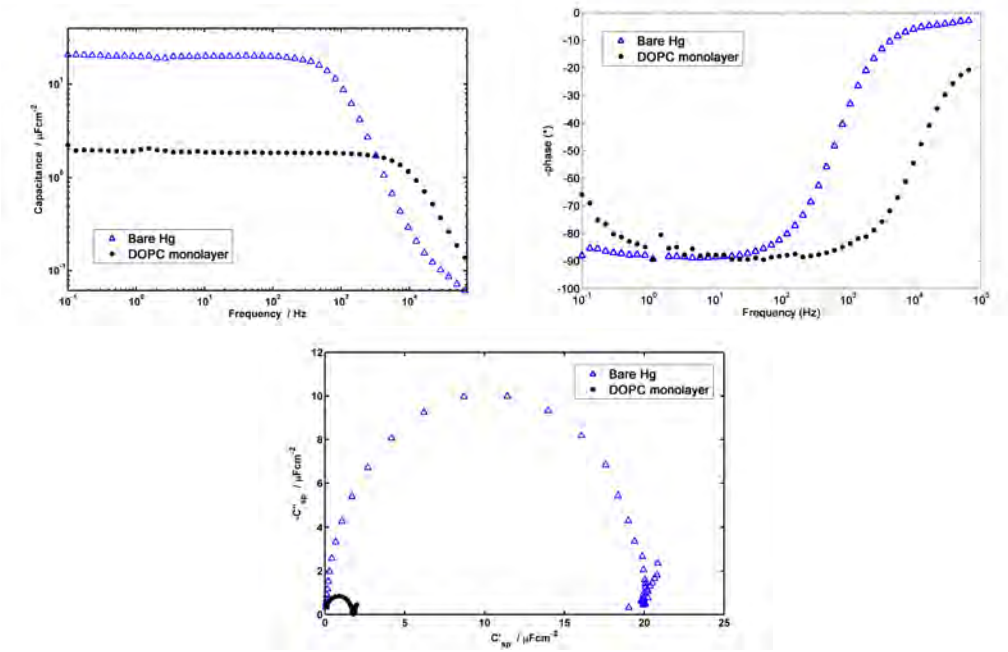

Figure 3.11: Real capacitance (left) and phase (right) of uncoated (blue triangles) and DOPC monolayer coated MFE (black circles) varying the frequency in 0.1 mol dm-3 KCl at -0.4V potential. The third diagram (down) shows the complex capacitance derived from impedance data uncoated and DOPC monolayer coated MFE.All this data are derived from EIS spectra

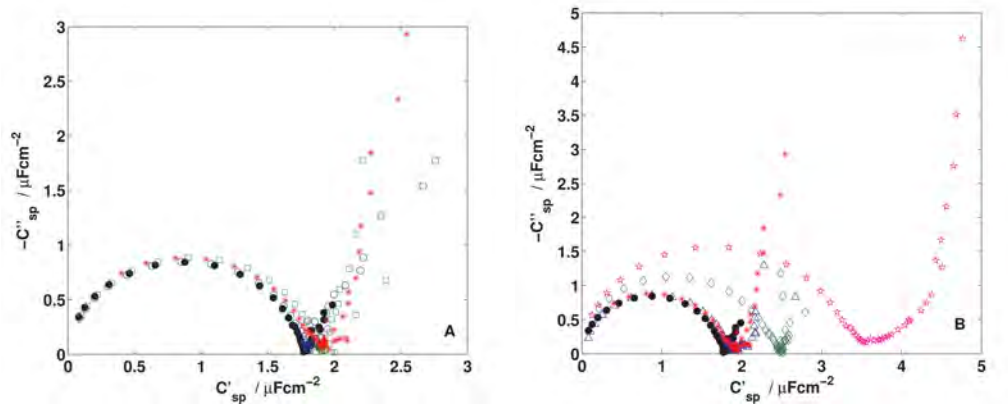

Figure 3.12: Impedance data presented as imaginary specific capacitance $-C''_{sp}$ = Re($Y^*/\omega A_0$) versus real specific capacitance C'_{sp} = ($Y^*/\omega A_0$) of DOPC monolayer-coated Hg electrode in 0.1 mol dm^{-3} KCl at -0.40 V vs Ag/AgCl interacting with different ionic liquids at the same 1 mmol dm^{-3} concentration. For comparison, in both A and B, the black full dots represent the EIS of non interacting DOPC monolayer. (A) DOPC interacting with [C_4MIM][X] where X = Cl (blue circles), BF_4 (green squares), and NTf_2 red asterisks). (B) DOPC interacting with [C_nMIM][NTf_2] with n = 2 (blue triangles), 4 (red asterisks), 8 (green diamonds), and 12 (pink stars).

tric layered materials,[186][203; 204] charge-carrier movement[185; 186] and counterion relaxation[186; 205]. The evidence from this and previous studies[128; 184–187; 206] indicates that the low-frequency effects observed in the DOPC−mercury system interactions with ILs are caused by defects in monolayer allowing entry of ions. The relaxation phenomena represent the response of these systems to a low frequency AC field. To summarize, two distinct monolayer activities can be discerned for the ILs tested in this study. Cations with short lateral chains of 2 and 4 carbon atoms weakly adsorb on the DOPC monolayer, causing negligible or very low level of penetration. This is demonstrated by the negligible increase of monolayer capacitance and the insignificant decrease of 'roughness' parameter β. Modifications of the secondary low frequency capacitance are noticeable. It may be presumed that a double layer, composed of ILs cations and anions, forms on the DOPC monolayer and is dominant against the standard electrolyte species (PBS). The physisorption of short chain cations is confirmed by the fact that a DOPC monolayer can be restored after IL interaction following flushing DOPC layer with PBS concurrent with RCV scanning. An additional evidence of this physisorption is probably the broadening of peak 1 in Figure 3.10 A; such peak is related to the transition from an ordered lipid monolayer to a porous bilayer [124] and this process is likely to be influenced by the presence of an adsorbed IL layer. In contrast, exposure to cations with longer lateral chains (8 or 12 carbon atoms) causes them to be incorporated into the DOPC monolayer, partially disrupting it. This is reflected by the increase of monolayer capacitance by more than 100% in addition to a decrease of parameter β and increasing significance of a secondary low-frequency element. The IL's hydrocarbon chains which have penetrated inside the monolayer cause an increase of DOPC permeability to standard electrolyte ions. Due to the intercalation of long chain inside the DOPC monolayer, it is difficult to desorb the IL from the DOPC layer, and consequently, impossible to restore a characteristic DOPC monolayer.

An important part of electrochemical results is the relationship with toxicity. One screening method commonly used to assess the toxicity of chemicals to living organisms is the standard ecotoxicological bioassay (ISO 11348), which correlates the reduction of luminescence in cultures of Vibrio fischeri (Gram-negative bacteria) with cellular toxicity defined by EC_{50} values [91]. EC_{50} represents the concentration of the substance under investigation that induces the maximum effect in 50% of the sample. EC_{50} data for imidazolium-based ionic liquids (exposure time of 30 min) reinforced the idea that their toxicity, higher than that of selected conventional organic solvents, is controlled by the cation lipophilicity (i.e., alkyl chain length), with a contributing secondary role from the anion and cation headgroup [84]. As a result, it becomes relevant to select numerical parameters describing the lipophilicity of ionic liquids, such as the octanol/water partition coefficient (K_{ow}). Parameters describing the direct interaction with lipid membranes are required. To this purpose and to numerically quantify the interaction of ionic liquids with the DOPC monolayer on Hg electrode, the detection limit (LOD) of IL in water was estimated. The LOD is the lowest concentration of a substance that can be distinguished from the absence of that substance (blank value) within a confidence limit of three times the standard deviation of the control response. LOD has been estimated from our data as follows. We have calculated the relative capacitance of peak 1 in RCV experiments as the ratio of the capacitances of peak 1 of IL-modified and of pure DOPC layers, respectively.

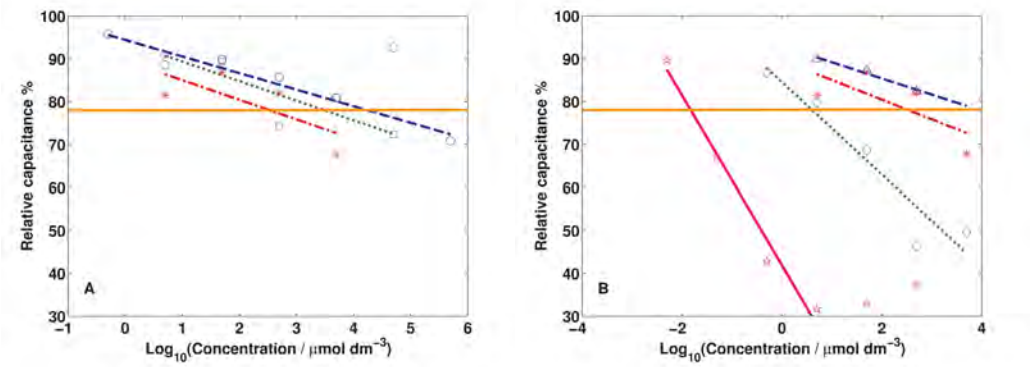

Figure 3.13: Characterization of the detection limit (LOD) for the interaction of DOPC with ILs with different anions and cation lengths. The orange horizontal line represents three times the standard deviation of the capacitance of peak 1 from RCV of pure DOPC. Assuming a linear correlation between the relative capacitance of peak 1 and the logarithmic IL concentration in μmol dm^{-3}, the LOD is determined as the concentration at which the straight line intersects the control value line. (A) [C4MIM][X] where X = Cl (data blue circle, fit dashed line), BF4 (data green square, fit dotted line), and NTf2 (data red asterisks, fit dash-dotted line). (B) [CnMIM][NTf2] with n = 2 (data blue triangles, fit dashed line), 4 (data red asterisks, fit dash-dotted line), 8 (data green diamonds, fit dotted line), and 12 (data pink stars, fit thick line).

As shown in Figure 3.13 A (effect of the anion) and Figure 3.13 B (effect of the lateral chain) the relative capacitance of peak 1 of modified DOPC monolayers and the logarithm of the IL concentration are decently linearly correlated; the estimated LOD is therefore calculated as the concentration at which the linear fit intercepts the line representing the control value. The logarithmic values of LOD are listed in Table 1 and plotted in Figure 3.14 as a function of (A) reported $\log_{10}(EC_{50})$ toxicity values for Vibrio fischeri, and (B) octanol/water partition coefficient $\log_{10}(K_{ow})$; linear correlation coefficients r = 0.97 and r = 0.87 are found for $\log_{10}(EC_{50})$ Vibrio fischeri and for $\log_{10}(K_{ow})$, respectively.

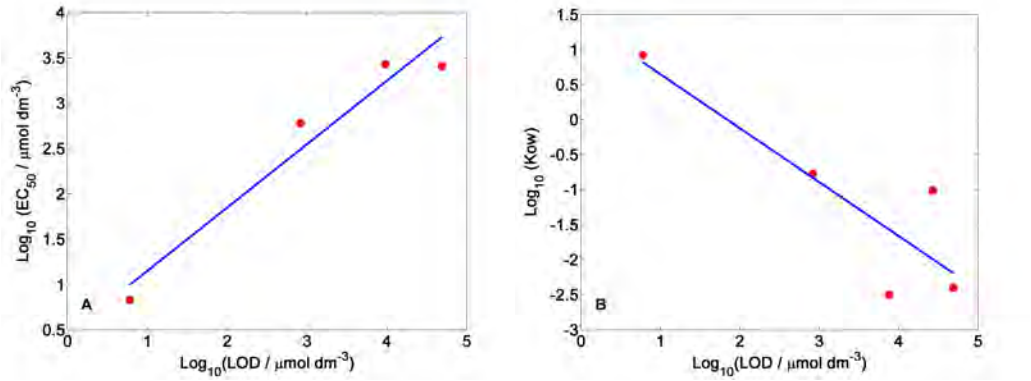

Figure 3.14: Correlation of (A) toxicity values $\log_{10}(EC_{50})$ for Vibrio fischeri marine bacteria, and (B) octanol/water partition coefficient $\log_{10}(K_{ow})$, with $\log_{10}$(LOD) (data filled red circles, linear fit thick lines).

Despite the fact that phospholipid monolayers are model systems compared to the complex cell membranes of living organisms, the correlation between the toxicity of ILs to organisms and their effect on the DOPC phospholipid monolayer is demonstrated here. This suggests that the phospholipid membrane is the primary target of toxic action of ionic liquids. When short-chain ILs are adsorbed on the membrane, the toxic effect can be explained as due to an influence on phospholipid fluidity seen as a suppression and broadening of the current peaks corresponding to the phase transitions. This effect has been seen and imaged previously for SiO_2 particles on DOPC monolayers and bilayers [129]. The stronger toxic effects of aggressive long-chain ILs is explained by phospholipid layer breakdown leading to ions permeability. In order to confirm interactions of ILs with cell membrane, Cornmell et al. [207] analyzed bacterial phospholipid membranes after exposure to phosphonium based IL. Therefore, they grew Escherichia coli in the presence of extremely low concentration of trihexyltetradecyl phosphonium bis(trifluoromethylsulfonyl)imide, harvested the cells and fractionated them into cytoplasmic and membrane fractions. The residual buffer from the washing step was also collected, to check for leakage of ILs. Then, they measured the FT-IR spectra of the subcellular fractions and compared them with fractions from cells that had not been exposed to IL. Remarkably, the ionic liquid could only be detected in the cell membranes, and not in the cytoplasmic fraction or the extracellular wash fraction. It seems that hydrophobic IL is lipophilic enough to accumulate in the membranes, even though it causes relatively little growth inhibition. Even though cytototoxicity mechanism of ILs is not fully understood yet,it has been proposed that the mode of toxic action for ionic liquids takes place through membrane disruption because of the structural similarities of imidazolium-based ILs to detergent, pesticides and antibiotics [208].

3.2.2 Ionic liquids interacting with model membranes: AFM study of lipid bilayers

In the next section I'm going to investigate the properties of ionic liquids interacting with DOPC bilayers supported on solid surface by means of AFM. In the first paragraph I will focus on the time-lapse morphological analysis following the contamination varying the interaction time and concentration. In the second paragraph I will present the combined morphological and nanomechanical analysis to deeply investigate the effect of ILs on DOPC model membranes.

Interaction with biomembranes: time-lapse AFM

Morphological and structural analysis of lipid bilayers supported on mica surface was performed with AFM in PeakForce Tapping (See for technical specifications section 2.2.2 and section 2.2.4). For hydrophobic ionic liquid the most common phenomenon is represented by the deposition of segregated nano-droplets on the top of phospholipid blayers. The deposition of droplets of ionic liquid $[C_4MIM][NTf_2]$ on lipid layers is clearly visible from analysis of sequences image in Figure 3.15, especially after 100 μmol dm^{-3}, image D, E, F. These drops seem to vary their size as a function of concentration, in fact they tend to increase as a function of the amount of IL present in solution. In this regard, an important aspect to be emphasized is that this behavior was observed only in the presence of hydrophobic ionic liquids (see also next Fig. 3.17).

This phenomenon is somehow related to the effects of segregation that have hydrophobic ionic liquids in solution. A confirmation of the behavior of ILs interacting with DOPC bilayers is evidenced in the computational analysis performed with molecular dynamics simulations by Bingham et.al.[94]. The phenomena described in these

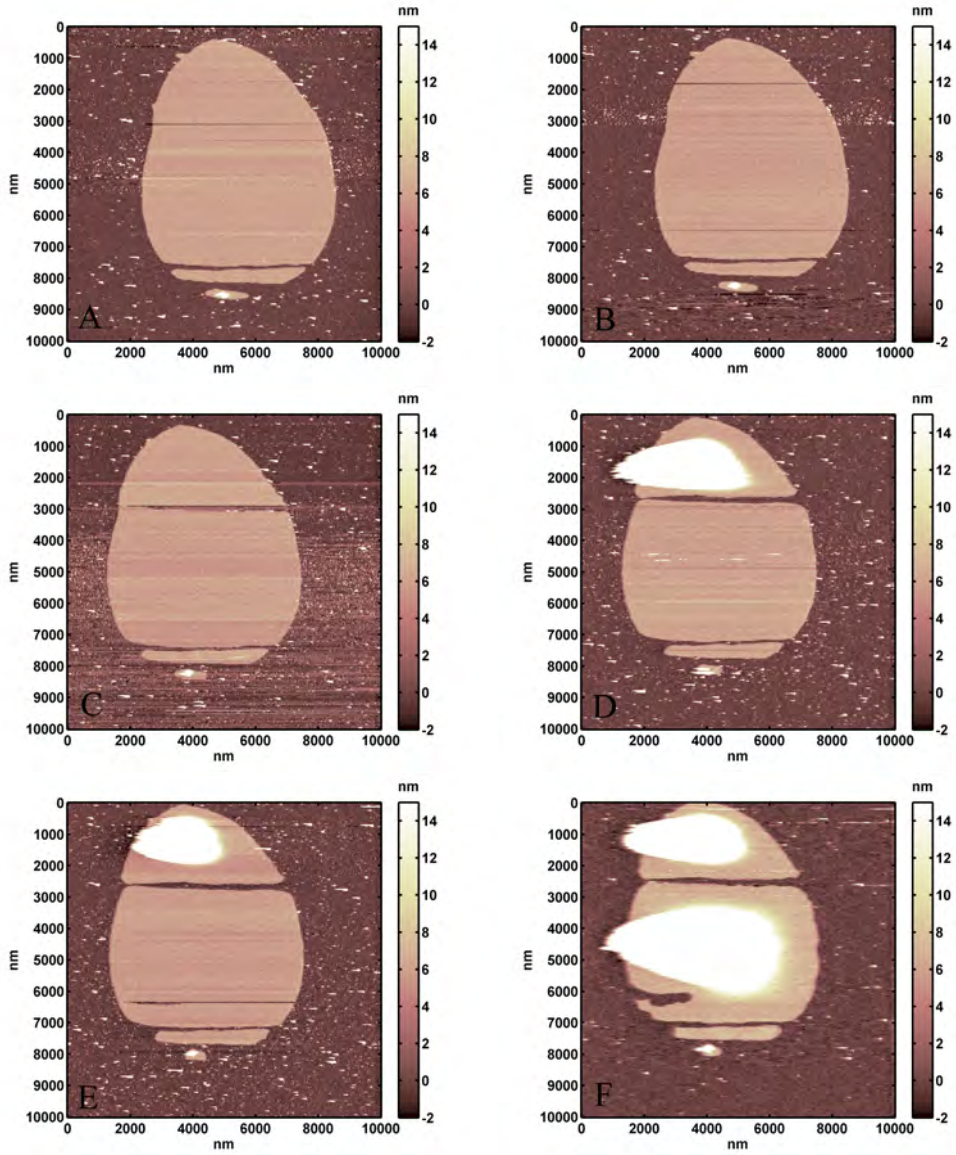

Figure 3.15: The figure shows the evolution of a DOPC bilayer as a result of adding progressive concentrations of $[C_4MIM][NTf_2]$ at different time T of measurements. Image A represents the non-interaction situation, while B (T = 4 min) and C (T = 8 min) represent interaction at 10 μmol dm^{-3} concentration. Image D (T = 4 min) and E (T = 8 min) represent interaction at 100 μmol dm^{-3} concentration. Image E depicts the interaction of 1000 μmol dm^{-3} concentration at T = 4 min. The deposition of the droplets of segregated ionic liquid is easy detectable in D,E,F.

simulations relate to the interaction between membranes of POPC and different ionic liquids including [C_4MIM][Cl], [C_4MIM][PF_6], [C_4MIM][NTf_2] present in solution at concentrations of 500 mmol dm^{-3}. Working well beyond the solubility limit, it is simulated and experimented that the [C_4MIM][NTf_2] segregate in solution forming drops with tendency to deposit on lipid membranes.

Another characteristic behavior observed is the progressive growth of lipid structures after the addition of ILs contaminant. The phenomenon is evident from qualitative analysis of time-lapse images, especially for hydrophilic ILs like [C_4MIM][BF_4] in Figure 3.16. This effect seems to be in contrast to the results reported in the literature [95][96][97], where ILs strongly interact with membranes creating holes and depletion. The lipid structures are expanded and in many cases even after a substantial addition of IL, the sample was completely covered by a reconstructed layer (see Fig. 3.16 and Fig. 3.17). Moreover, ionic liquid seems to interact easier with lipids in the amorphous phase rather than with structured bilayers. Following the contamination in time-lapse, new structures very similar to the lipid bilayer are formed, but characterized by a greater roughness. These new layers can be distinguished thanks to irregularities, maybe due to ILs inclusions and DOPC/ILs complexes, that are absent in original and pure lipid bilayers.

As expected, the most active action is given by [C_{12}MIM][NTf_2] ionic liquid, with the longest side chain in these experiments. The observed phenomenon is generally composed by a first phase in which this hydrophobic IL is deposited on the top of DOPC bilayer forming drops as those shown by [C_4MIM][NTf_2] in Fig. 3.15. These drops, then, break and go to form rapidly structured layers with topographic characteristics similar to as-deposited lipid bilayers. As in the case of [C_4MIM][BF_4] these new layers are characterized by small irregularities and increased roughness. The complete behavior is examined in the time-lapse sequence of images in Fig. 3.17.

Another example of rough layers formation after [C_{12}MIM][NTf_2] IL contamination is presented in Fig. 3.18. In this case a double packed bilayer grows, almost covering all the mica substrate.

Finally, to better investigate the mechanisms of interaction between the contaminant and the lipid membrane an additional experiment with [C_{12}MIM][NTf_2] IL was performed, trying to decrease the contamination at minimum concentrations. Based on the results of electrochemical experiments (see section 3.2.1 and ref. [198]) an ionic liquid with the lowest limit of detection (LOD) on DOPC membranes, is just the [C_{12}MIM][NTf_2]. The intent is to drastically slow down the kinetics of interaction reducing the number of particles of ionic liquid present in solution in order to better observe interaction phenomena. A contamination of 0.1 μmol dm^{-3} concentration was injected in the DOPC sample. The sequence of images acquired in PeakForce tapping is shown in Fig 3.19.

After the addition of the IL, the appearance of holes was noticed in the lipid bilayer although after few minutes they closed immediately, see Figure 3.19 B. Continuing the experiment after repairing of holes, it has witnessed the occurrence of new filamentous structures, possessing a thickness twice that of single lipid bilayer. These dendritic structures grows preferentially in horizontal direction, because the tip, moving fast in horizontal direction, could drive the interaction and the subsequent formation. It is plausible to think these new membranes are able by coalescence to restructure forming uniform layers. The formation of new layers in this sense it would be one of the late interaction effects of ionic liquids incorporated into lipid membrane. Schaffran et al. in [209] observe, with cryo-TEM experiments, the reorganization of liposomes in solution after ILs contamination. Depending by alkyl tail, ionic liquids promotes the reorganization of unilamellar liposomes in extended bilayer sheets (short tail) and multilamellar lipo-

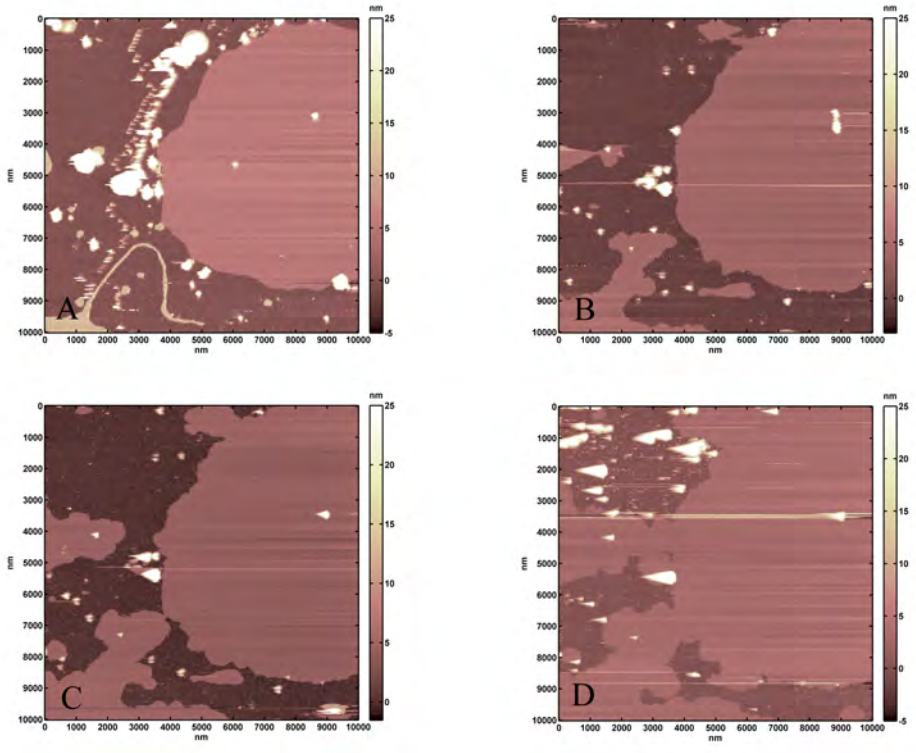

Figure 3.16: The figure shows the evolution of a DOPC bilayer as a result of adding progressive concentrations of $[C_4MIM][BF_4]$ at fixed time of measurements T = 4 min. Image A represents the non-interaction situation, while B is acquired at 1 mmol dm^{-3} concentration, C at 10 mmol dm^{-3} concentration and D at 100 mmol dm^{-3} concentration. In this sequence is evident the growing of lipid bilayers thanks to ILs interaction

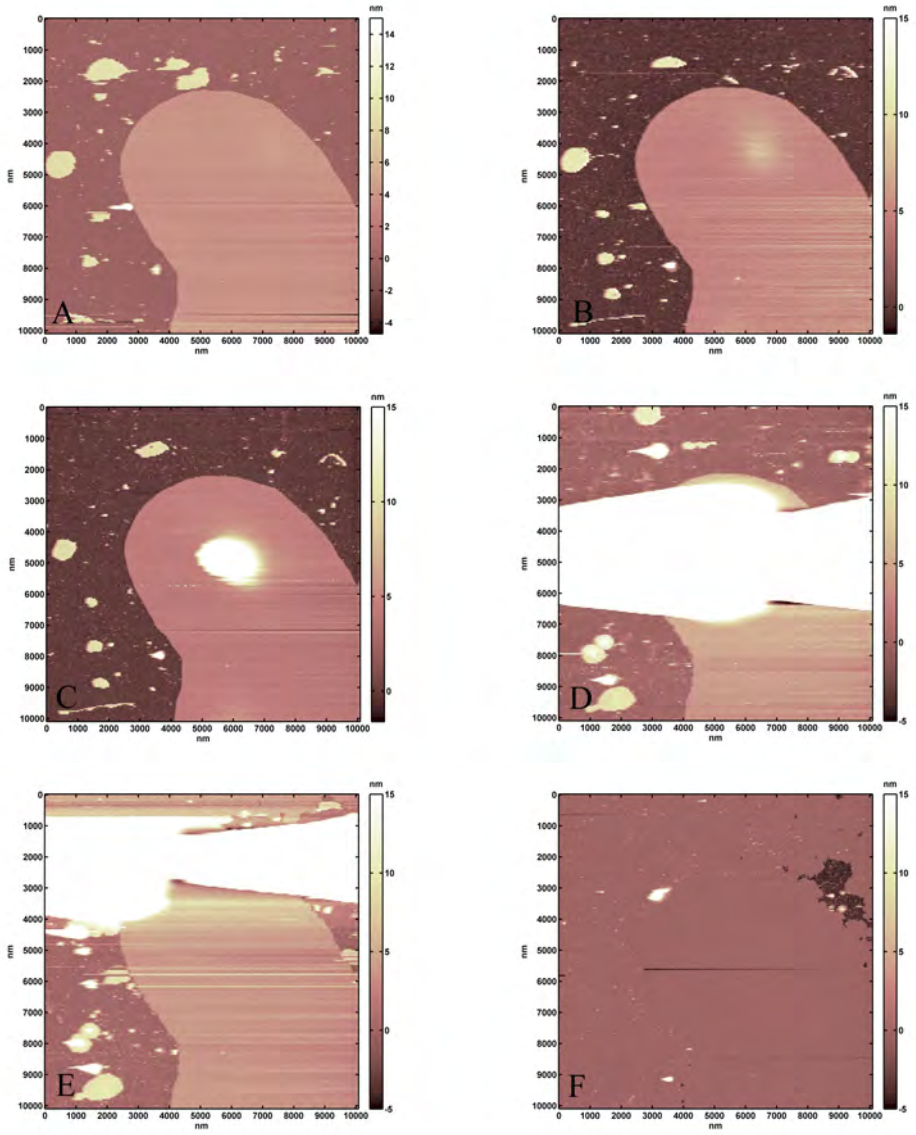

Figure 3.17: The figure shows the evolution of a DOPC bilayer as a result of adding progressive concentrations of $[C_4MIM][NTf_2]$ at different time T of measurements. Image A represents the non-interaction situation, while B (T = 4 min) and C (T = 4 min) represent interaction at 10 μmol dm^{-3} and 100 μmol dm^{-3} concentration. Image D (T = 4 min), E (T = 8 min), F (T = 16 min) represent interaction at 1 mmol dm^{-3} concentration, at increasing interaction time. The deposition of the droplets of segregated ionic liquid is easy detectable in B, C, D; while in E and F ILs drops disappear and the substrate is completely covered.

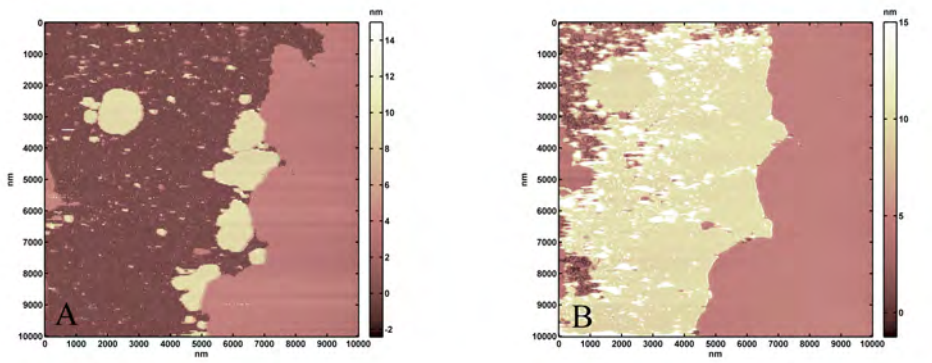

Figure 3.18: The figure shows the time evolution of the sample as a result of adding $[C_{12}MIM][NTf_2]$ at 100 μmol dm^{-3} concentration. Image A represents the non-interaction status, while B shows the effect of interaction after 5 consecutive scans (T = 20 min).

somes onion-like (long tail). The authors explain this fact as the short tail molecule inserts into liposomal membranes, and may, at sub-solubilizing concentrations, induce a range of structural transformations of the liposomes. Commonly the surfactants act as "edge-actants" and stabilize open membrane structures. Long tail molecules form a well defined compound layer around a liposome and that repulsion forces might prevent a closer approach of the liposomal membranes, forming regular onion-like structures.

The important experimental phenomenon observed is a progressive increase of lipid membranes extension following the addition of the ionic liquid. This result is not in agreement with literature. In fact, according to the work of Evans [95][96][97] in which has been studied the interaction of DEPC lipid bilayer with various ILs, using AFM in TappingMode, showed the tendency of the ionic liquid to interact with the membrane opening little holes in the case of $[C_8MIM][Cl]$, and creating an overlayer of ionic liquid deposited on the lipid layer in the case of $[C_4MPyr][NTf_2]$. The same molecular dynamics simulation work carried out by Bingham et.al.[94], show the tendency of the cations $[C_4MIM]^+$ to partially penetrate into the lipid membrane altering the structure. This would suggest a tendency of the cationic part to interact with the lipid membrane fluidizing and restructuring the lipids detached from it in solution. With electrochemical analysis, exposed previously in 3.2.1 and ref. [198], the results obtained are similar. The general increase of capacitance signal is due to the ability of the ionic liquid to pierce the membrane, partially eroding the lipid coating of the electrode. Beyond trivial explanation regarding differences in experimental configurations, the opposite effect seen by Evans is due to different scanning mode; in fact PeakForce tapping is more gentle than contact mode used by Evans, and the fast vertical approach favor an instantaneous (see Fig. 3.19) refill of eventual holes. The creation of new structure similar to original bilayers, but more disordered highlights the idea of a lipid membrane that can be modified and restructured in a complex ILs/DOPC.

This effect is evident also with electrochemical methods, where high concentration of hydrophobic IL $[C_{12}MIM][NTf_2]$, also during DOPC deposition on Hg electrodes, promotes the formation of new RCV spectrum (See previous Fig. 3.8). This new RCV seems to be really a complex ILs/DOPC because it has an averaged behavior between pure DOPC and pure $[C_{12}MIM][NTf_2]$ RCV fingerprints.

Another morphological effect concerns the fluctuation of height values after contami-

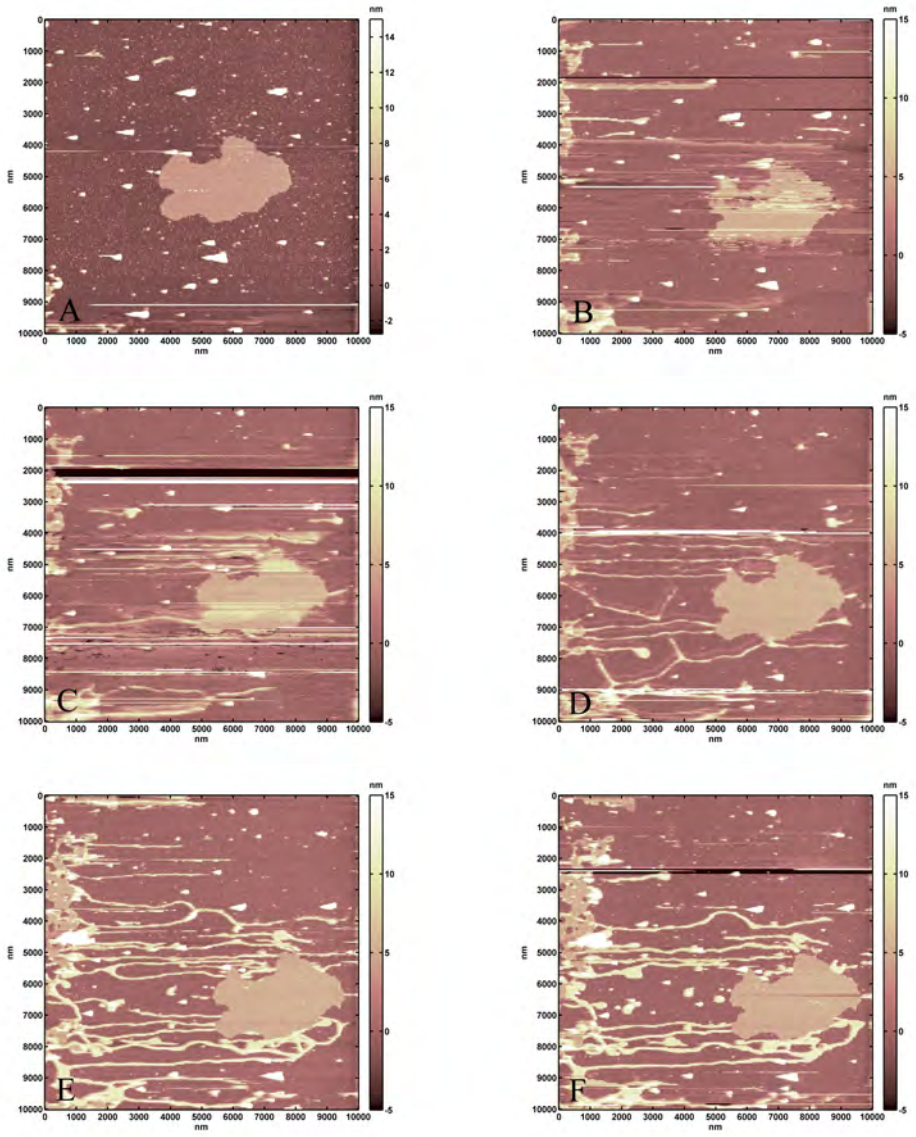

Figure 3.19: The figure shows the time evolution of the sample as a result of $[C_{12}MIM][NTf_2]$ at very low concentration (0.1 μmol dm^{-3}), with a frame rate every 4 min. Image A represents the non-interaction status. A first phase with appearance of holes and increase of experimental noise is noticeable in frame B, while the progressive formation of new dendritic structures is depicted in C, D, E and F.

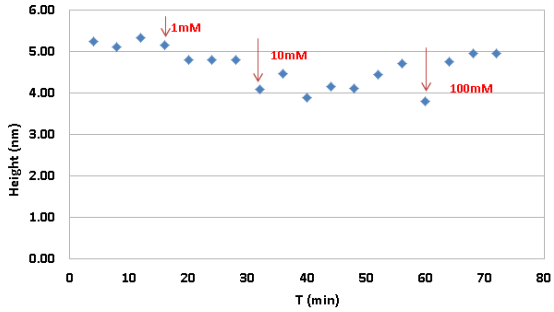

Figure 3.20: The graph refers to one of the experiments conducted with $[C_4MIM][BF_4]$, red arrows indicate the images acquired immediately after the addition of the contaminant for 1 mmol dm^{-3}, 10 mmol dm^{-3}, 100 mmol dm^{-3} concentrations.

nation (see for Fig. 3.20). At first the ionic liquid interacts with the membrane depositing on polar heads of phospholipids and increasing their height value. Subsequently, as a result of the incorporation of alkyl tail the membrane experienced a decrease in the lipid layers thickness. This effect is due thanks to variation of the consistency of the membrane that becomes softer and more sensitive to the pressure exerted by the tip during PeakForce Tapping imaging. Keeping constant the value of the applied force is visible a relaxation of the structure that causes the microscope to record minor height values. At this point, a nanomechanical investigation by AFM is required to see how DOPC bilayers respond to mechanical stress after interaction with ILs

Interaction with biomembranes: nanomechanical study

Nanomechanical properties of DOPC bilayers supported on mica interacting with ILs at various concentrations were investigated using techniques and methods explained in section 2.2.4. Only hydrophilic ILs were analyzed in FV to avoid formation of segregated ILs drops on topo of DOPC bilayers. A tip immersed in IL can be irremediably (at least during experiment section) covered by a considerable layer that can negatively affect all measurements. As explained in previous section the strong affinity of IL with lipid membranes can dynamically promote the attachment and detachment of complex ILs/DOPC on the tip apex. For this reason many sets of nanomechanical data are completely unstable and unusable. An example of bad measurements is reported in Fig. 3.21

Moreover the FV procedure is slow and, using high force trigger, the real-time morphology is precluded. For these reason only one set of data in the measurements campaign shows acceptable morphology. A possible method to avoid bad measurements is a chemical treatment of the tip surface. For example Vakurov et al. in ref. [210] treated the probe, prior to the experiment, with dichlorodimethylsilane (DCDMS) for 30 s. The silanization routine was found operationally to give reproducible force-distance curves presumably because it prevented lipid from adhering to the tip.

Analyzing the electrostatic and mechanical interaction in the force curves inside a FV, the thickness of phospholipid bilayers is obtained with extreme precision. In this situation the morphology is equivalent to the thickness map.

The variation of lipid membrane thickness is a secondary effect produced by nano-

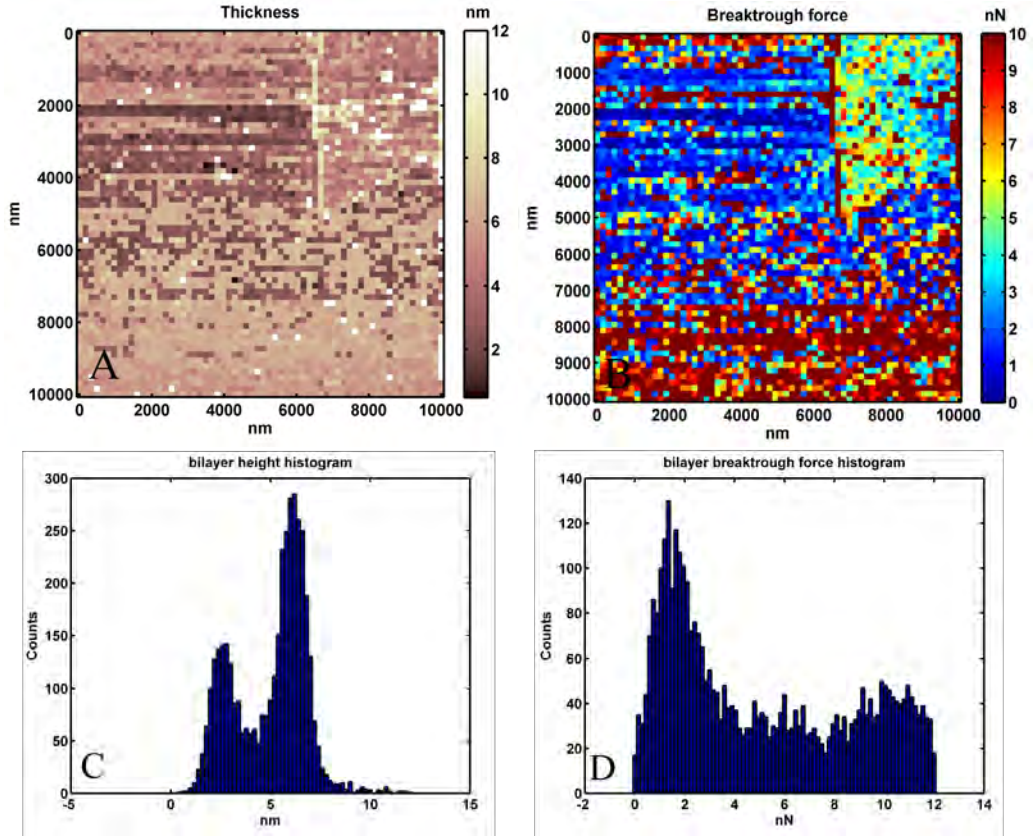

Figure 3.21: Example of bad FV measurements. Image A represents the thickness of DOPC supported bilayer at 100 μmol dm^{-3}concentration of contaminant [C_8MIM][Cl]. Image B represents thebreaktrough force map correnspondent to image A. The quantitative histograms C and D are representative of height and force respectively. Grains in both maps suggest presence of soft material attaching/detaching from the tip

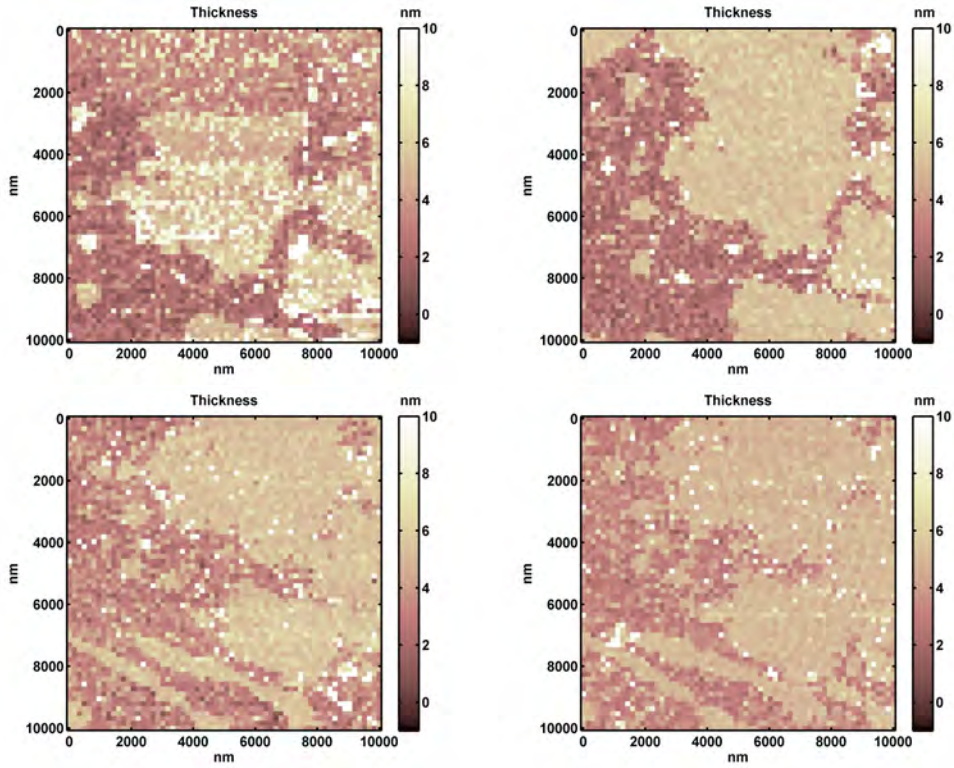

Figure 3.22: Analysis of the evolution of morphology (thickness) of DOPC supported bilayer varying the concentration of contaminant [C_4MIM][Cl]. Image A represents the thickness map before contamination, while image B, C, D represent thickness after 15 min interaction with 1 mmol dm^{-3}, 10 mmol dm^{-3}, 100 mmol dm^{-3} concentration rispectively.

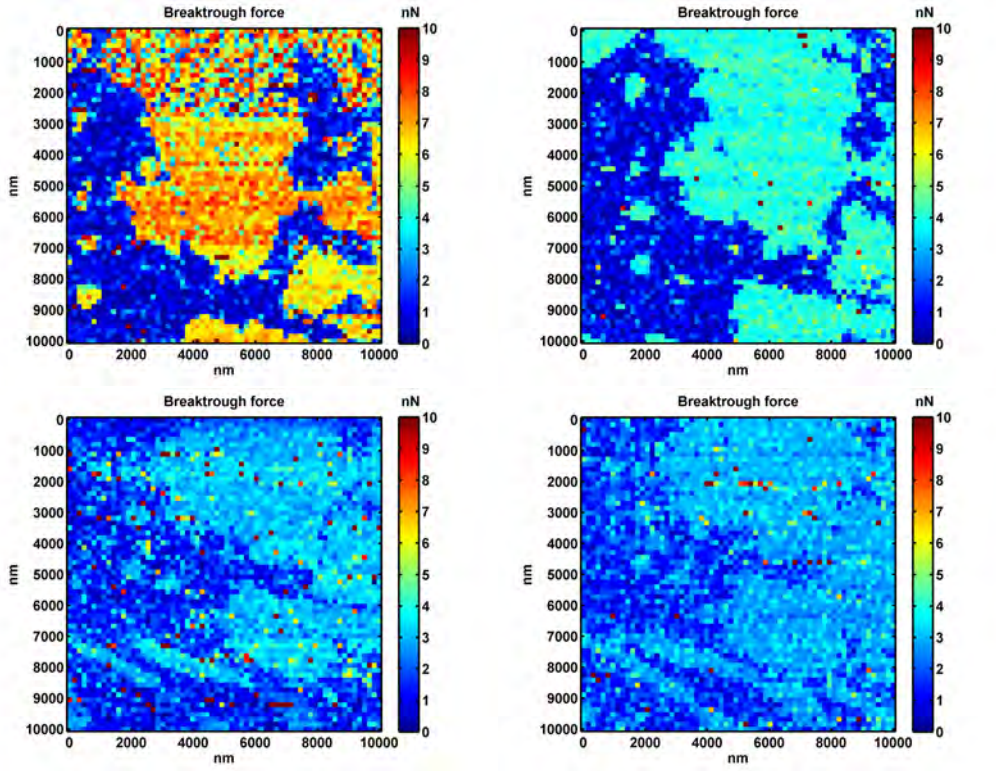

Figure 3.23: Analysis of the evolution of breaktrough force of DOPC supported bilayer varying the concentration of contaminant [C_4MIM][Cl]. Image A represents the breaktrough force map before contamination, while image B, C, D represent breaktrough force after 15 min interaction with 1 mmol dm^{-3}, 10 mmol dm^{-3}, 100 mmol dm^{-3} concentration rispectively.

mechanical modifications. It is a natural consequence to continue in this direction performing AFM force spectroscopy on lipid membranes exposed to ionic liquid. The results confirm the height variations of the lipid layer as a result of the contamination and show a decrease of the force of breakthrough. Even with an ionic liquid in the side chain is relatively short as the [C_4MIM][Cl], the interaction with the lipid membrane appears to be an established fact. Probably as a result of the butyl tail inside the bilayer there is a relaxation of the structure that makes the layer softer and vulnerable to penetration effect of the tip. This produces a decrease in the force required to break trough the lipid layer, see Figure 3.23.

For example a similar effect was observed by Dante et al. [211], investigating the structural and mechanical effects of beta-amyloid on phospholipid membranes. The thickness of the lipid bilayer increases in the presence of beta-amyloid by about 0.4 nm. This concomitant effects reveal that beta-amyloid is capable of penetrating the double layer, increasing the thickness of the membrane. AFM force spectroscopy has shown that the mechanical properties of the membrane are different depending on the substrate. On mica the force necessary to punch through the double layer is lowered in presence of beta-amyloid, meaning that the structural changes upon interaction with the peptide have a softening effect on the bilayer. The force necessary to penetrate the double layer

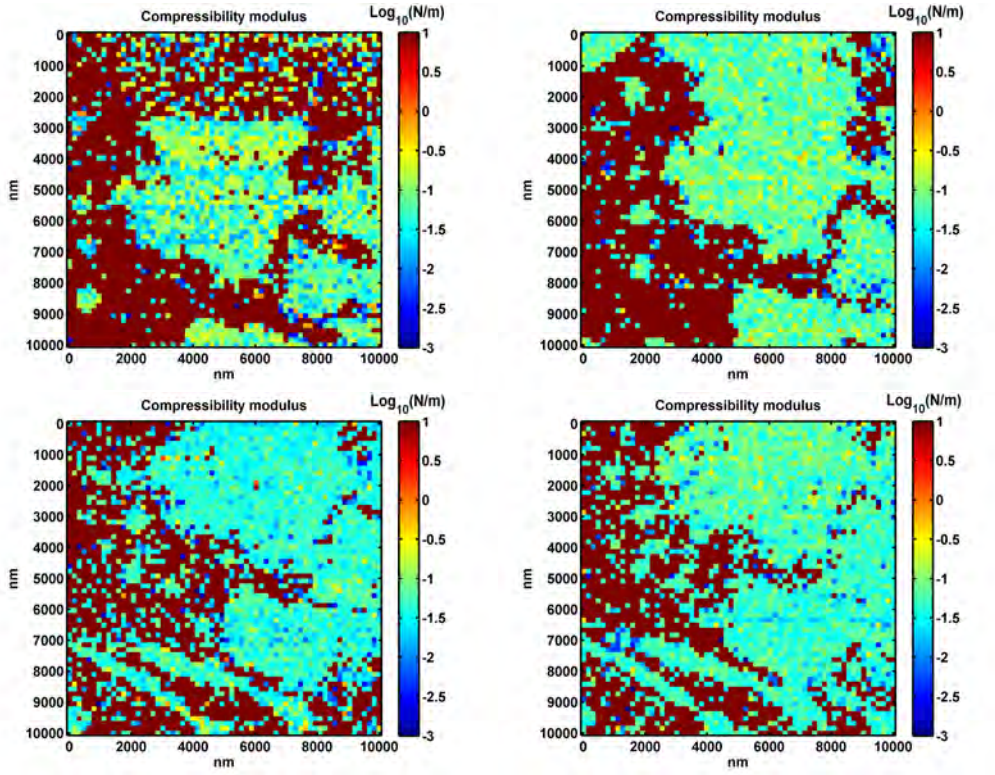

Figure 3.24: Analysis of the evolution of logarithmic compressibility modulus κ_A of DOPC supported bilayer varying the concentration of contaminant [C_4MIM][Cl]. Image A represents the compressibility modulus map before contamination, while image B, C, D represent modulus after 15 min interaction with 1 mmol dm^{-3}, 10 mmol dm^{-3}, 100 mmol dm^{-3} concentration rispectively.

decreases noteworthy after interaction with beta-amyloid.

A confirm of the compressibility modulus modification after interaction with dispersed IL is evidenced in the simulation work carried out by Bingham et.al.[94]. The POPC bilayer in pure water, for instance, has a computed area compressibility modulus κ_A of 0.590 $\pm$ 0.005 N/m. It is definitely higher than the experimental value for POPC (κ_A = 0.231 $\pm$ 0.020 N/m from ref. [157]) and DOPC system (See section 2.2.4). More importantly, adding [C_4MIM][Cl] (500 mmol dm^{-3}) to the solution, the decrease of κ_A (-15%) is in agreement with the trend of results obtained here. The same behavior, in simulations, is observed in the [C_4MIM][PF_6] case, but the effect are quantitatively more important, with the κ_A variation reaching -45%. The effect of [C_4MIM][NTf_2] is the smallest among the systems considered in simulation. The stronger effect of [C_4MIM][PF6] as compared to that of [C_4MIM][Cl], in particular, reflects the accumulation of both cations and anions within or at least close to POPC, whereas the limited effect of [C_4MIM][Tf2N] reflects its extensive segregation and only partial wetting of the bilayer by the compact IL droplets, in which cations and anions are closely interacting with each other.

From each FV map, final values with errors are obtained using histograms and Gaussian fits as explained in section 2.2.4. Final values are presented in graphs of Figure

3.25.

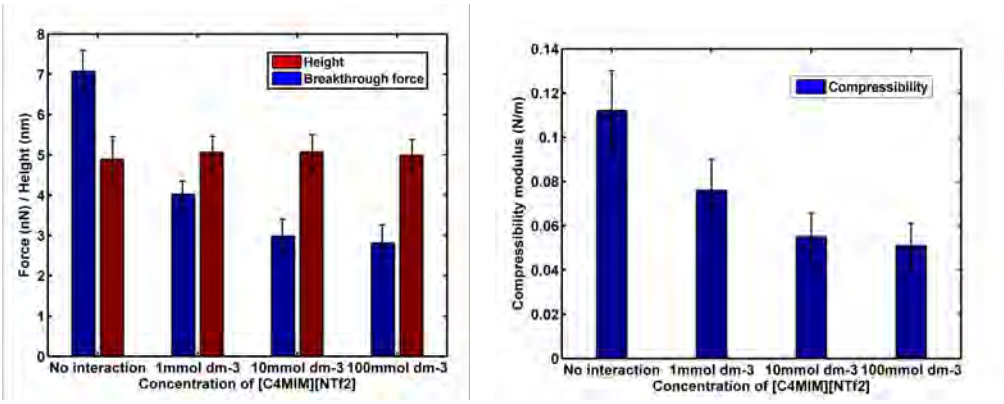

Figure 3.25: Force diagram for a breakthrough force (left) and compressibility modulus (right) of phospholipid bilayer interacting with [C_4MIM][Cl] at increasing concentration.

The most interesting consideration that emerges from these results regards the experimental agreement of decreasing trend of breaktrough force and compressibility modulus κ_A, varying the concentration of contaminant during the experiment. From Fig. 3.25 seems that breakthrough force and compressibility modulus for 10 mmol dm^{-3} and 100 mmol dm^{-3} concentration is comparable, maybe because the interaction reaches saturation. The lowered mechanical stability of the lipid membrane found by AFM force spectroscopy is in agreement with the results obtained with electrochemistry. Inclusions of IL tails inside the lipid layer destabilize the compact structure. This effect causes an augment of monolayer capacitance and broadening of voltammetric peaks using electrochemical methods. A noticeable decrease of breakthrough force and compressibility modulus indicate a lowering in mechanical stability but also the bilayer is much more compliant. This finding is important in the toxicity scenario, since it means that ionic liquids interact with the cell membrane, depending on their concentration and lateral chain length, by changing its structure, and especially by softening it. This may increase/change membrane permebility and eventually disrupt it completely. Also a plethora of complementary biophysical and microscopy techniques performed by Gal et al. [212] highlights aspects pertaining to the membrane activity of the ILs. They carried out a differential scanning calorimetry (DSC) analysis using DMPC/DMPG (98:2 mole ratio) vesicles. DSC interrogates the thermodynamic profile of lipid bilayers and constitutes a highly sensitive tool for determining the effects of membrane-active species upon organization and cooperative properties of the bilayer. The DSC trace of the unperturbed vesicles (prior to their incubation with ILs) shows the phospholipid pre-transition at around 15 °C, and the major gel–fluid transition at 24 °C. For example there is a dramatic change in heat absorption after incubation with [C_{12}MIM][Br] following almost complete elimination of the gel–fluid phase transition. Similar modifications in transitions peaks, modifying the temperature, are shown in section 3.2.1 modifying the electric field applied at the Hg electrode. This result is a strong indication for a marked reduction of phospholipid ordering and corroborates our data, indicating substantial bilayer disruption induced by cation tails. Importantly, the experiments of Gal et al. [212] show that all the ILs tested exhibit membrane interactions. The experiments reveal distinct differences among the compounds in terms of their association with- and effects upon

lipid bilayers, and also point to a relationship between the extent of membrane disruption/permeation and biological activities of the ILs. The experimental data also underscore the significance of structural features within ILs, particularly the head-groups, in determining the biological/toxic profiles of the molecules. This correlation is important, since it indicates that membrane interactions of ILs are most likely universal phenomena, even for ILs that are patently hydrophilic. Distinct membrane interactions and biological activity profiles were found for the oxygenated ILs, displaying similar membrane interaction profiles with the lowest bilayer activity among the compounds studied.

3.2.3 Ionic liquids interacting with living cells

The last part of my thesis consisted in the execution and interpretation of morphological and nanomechanical experiments aimed at studying the interactions of ILs with living cells. These experiments completed those carried out on phospholipid layers as models of biomembranes by AFM and electrochemcal tools. All the data were acquired and treated with statistical analysis with the procedures described in paragraph 2.2.5. The ionic liquids used in this experiments are [C_4MIM][Cl] and [C_4MIM][BF_4] representative of short tail cation, and [C_8MIM][Cl] representative for long tail cation.

The first visible effect observed in topographic maps is the change of cell morphology (size and shape) for varying concentration of ionic liquid. This effect is evident using all the ionic liquids, with enhancement produced by [C_8MIM]$^+$ cation, i.e. by the IL with the longest chain. Cells, in fact, withdraw lamellar protrusive areas assuming a more compact configuration which is a prelude to an apoptotic phenomenon (see for example the effect of [C_4MIM][Cl] in Fig. 3.26). Another noticeable phenomenon, observed at higher IL concentration, is the increase of amorphous material present in cell culture, which makes it more difficult measuring operations. Both behaviors could qualitatively confirm the hypothesis of gradually destructive interaction of ionic liquids towards the outer layers of the cell bodies.

In Figure 3.26 is showed the effect of [C_4MIM][Cl] at increasing concentration. The inverted optical microscope allows to follow the same cell.

Along with morphological modifications, the Young's modulus maps in Fig. 3.27 are built considering the experimental methods and analysis discussed in section 2.2.5. In this analysis, the finite thickness correction is always taken in consideration to deconvolve the hardening effect of substrate. To focus the nanomechanical analysis on the external layers of cell structure a low indentation range is used in the fit. The mechanical contribution of the phospholipid membrane is however convoluted to the more external actin layer.

The histograms in Fig. 3.28 represent the quantitative analysis derived from Young's modulus map and subjected to Gaussian fit analysis.

For each configuration (type of IL and respective concentration) a population of 6-8 cells is measured. The average values and errors presented in Tab. 3.3 and Fig. 3.29 are calculated considering the method explained in section 2.2.5. Using a mask built on morphology map, it is also possible to separate the contribution of lamellipodium (at low heights) and cell body. In Tab. 3.3 also the effective Young's modulus at high indentation range, correspondent to deep cytoskeletal layers is presented.

Log_{10}(Young's modulus / Pa)				
Conc (mmol dm-3)	Cell body L range	lamellipodia L range	Cell body H range	lamellipodia H range
0	2.63 ± 0.22	2.92 ± 0.18	2.57 ± 0.20	2.56 ± 0.15
1	2.56 ± 0.16	2.84 ± 0.14	2.47 ± 0.12	2.38 ± 0.10
10	2.76 ± 0.18	2.95 ± 0.23	2.68 ± 0.14	2.58 ± 0.22
100	3.39 ± 0.28	3.28 ± 0.30	3.25 ± 0.24	2.94 ± 0.22

Table 3.3: Summary of experimental data obtained on Young's modulus obtained on samples cell MDA-MB-231 interacting with [C_4MIM][Cl].

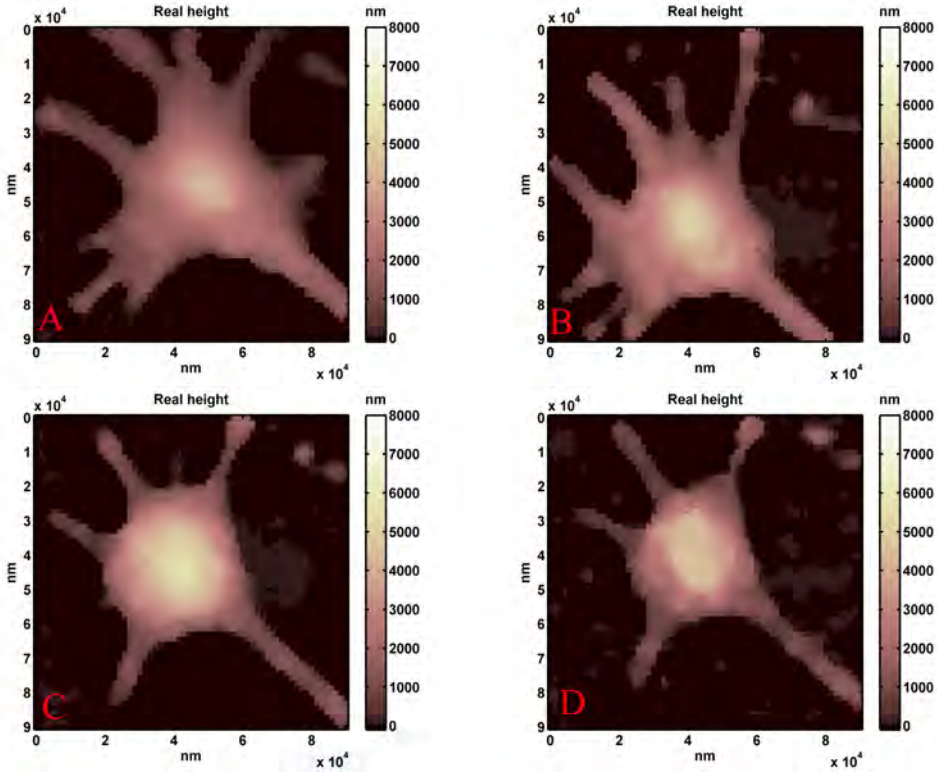

Figure 3.26: Real topography of typical MDA-MB-231 cell with increasing concentration of [C_4MIM][Cl]. Image A represents the initial situation without interaction. Image B represents the cell contaminated with 1 mmol dm^{-3} of [C_4MIM][Cl] after 40 min. Image C represents the cell contaminated with 10 mmol dm^{-3} of [C_4MIM][Cl] after 20 min. Image D represents the cell contaminated with 100 mmol dm^{-3} of [C_4MIM][Cl] after 20 min.

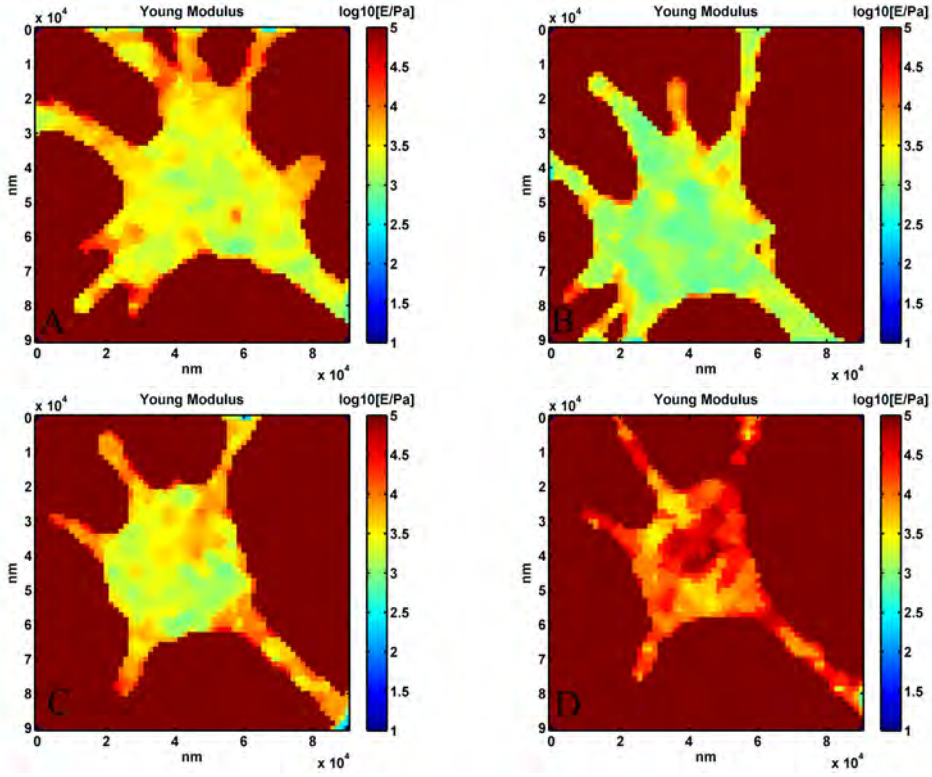

Figure 3.27: Young's modulus map at low indentation range for MDA-MB-231 cell in Fig 3.26 with increasing concentration of $[C_4MIM][Cl]$. Image A represents the initial situation without interaction with IL. Image B represents the cell contaminated with 1 mmol dm^{-3} of $[C_4MIM][Cl]$ after 20 min. Image C represents the cell contaminated with 10 mmol dm^{-3} of $[C_4MIM][Cl]$ after 20 min. Image D represents the cell contaminated with 100 mmol dm^{-3} of $[C_4MIM][Cl]$ after 20 min.

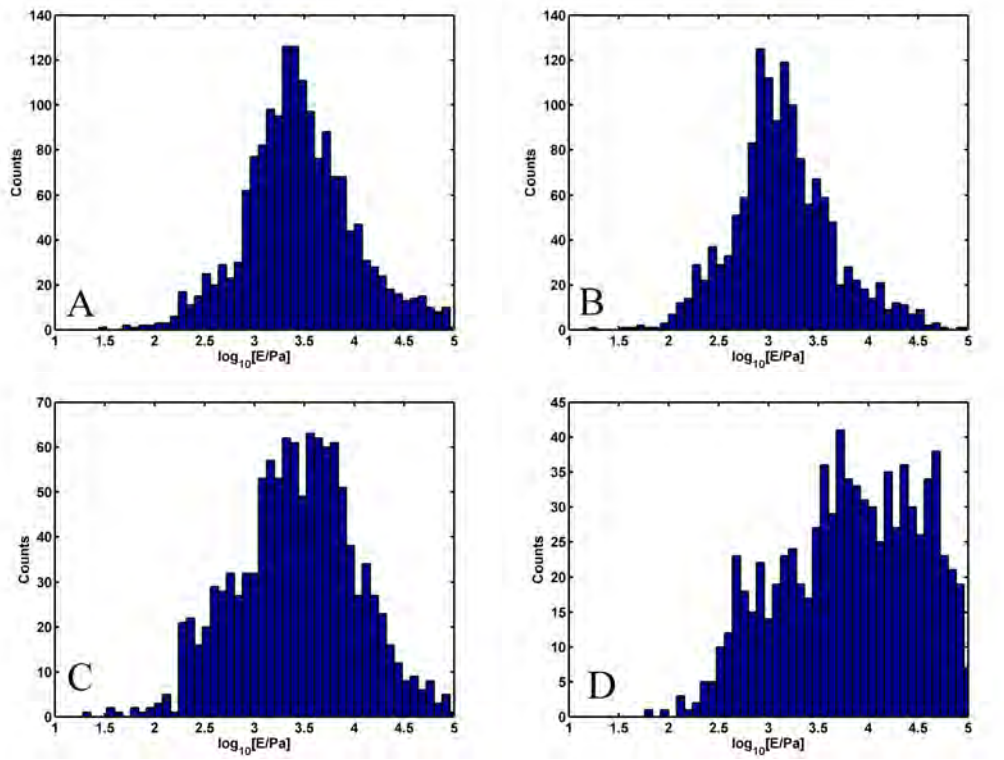

Figure 3.28: Quantitative histograms of Young's modulus at low indentation range for MDA-MB-231 cell in Fig 3.27 with increasing concentration of [C_4MIM][Cl]. Graph A represents the initial situation without interaction with IL. Graph B represents the cell contaminated with 1 mmol dm^{-3} of [C_4MIM][Cl] after 20 min. Graph C represents the cell contaminated with 10 mmol dm^{-3} of [C_4MIM][Cl] after 20 min. Graph D represents the cell contaminated with 100 mmol dm^{-3} of [C_4MIM][Cl] after 20 min.

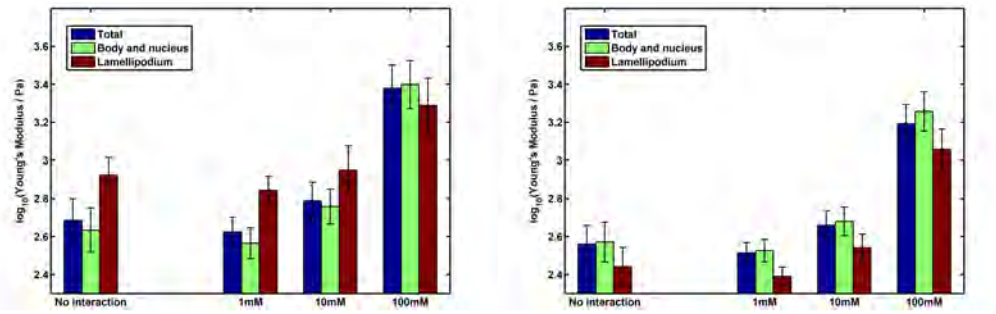

Figure 3.29: Behavior of the Young modulus of cells MDA-MB-231 varying the concentration of [C_4MIM][Cl]. In the graph are taken into account data referring to low indentation range (left) and high indentation range (right)

As shown by the graph in figure 3.29, the Young's modulus vary with the concentration. The aging effects in the time of experiments are completely escluded from ILs effect as shown in the section in Fig. 2.22. Contaminating the sample solution with IL at low concentrations of [C_4MIM][Cl], the cellular system is affected. The [C_4MIM]$^+$, in fact, thanks to the lipophilic properties of the lateral chain, is supposed to interact with the cell membrane that responds to mechanical stresses similarly to phospholipid layers model investigated previously. In agreement with the idea that alkyl chains are incorporated in the complex system of the membrane, the structure of the cell membrane is modified starting to affect the equilibrium that regulate the external defense of the cell. For this reason at low concentrations, a softening of the cell structure, more evident in the region of lamellipodium, is evidenced by Young's modulus lowering. The lamellipodium, in fact, is presented as a compact and ordered layers of cytoskeletal protein filaments that induces an hardening in the effective Young's modulus, compared to the YM relative to cell body and nucleus regions. As explained before, with this experimental approach it is impossible to define a value of the elastic modulus focused only on the outer phospholipid membrane. The thickness of membrane is around 4-5 nm and also restricting the measurements on very low indentation range the YM of membrane is always convoluted with deeper actin layers. However, considering a low indentation range, i.e. 30 nm on lamellipodium and 300 nm on cell body and nucleus, the mechanical study will be focused on the membrane and external layer of actin filaments directly connected to the cell membrane[158]. At low concentration, the gradually destructive action of the cation is not sufficiently strong to pierce the cell membrane causing big damage but it undermines the compact network of lipid molecules in the external layers. In this way the elastic contribution of the inner zone of the cytoskeleton remains almost unchanged, while the contribution of the external zones is more marked. this phenomenon can be seen in Figure 3.29, where the Young's modulus for indentation on the inner layers of the cell is not greatly modified.

Increasing the concentration of [C_4MIM][Cl] in MDA-MB-231 cell culture (up to 10 mmol dm^{-3} concentration) an opposite phenomenon takes place. From data presented in figure 3.27 and 3.29, it can be observed that the entire cell starts hardening with maximum value reached at maximum concentration 100 mmol dm^{-3}. A possible explanation of this unexpected YM behavior is that, after the initial interaction and destabilization of membrane, the ionic liquid ions penetrate within the cellular structure, interacting with the cytoplasmic area and causing the stiffening. The reasons for this phenomenon are

not entirely clear, but it can be assumed that the main reasons are two: first, penetrating within the cell body, the ions of the contaminant interact directly with protein filaments of the cytoskeleton, binding their components and promoting a cross-linking of proteins. This behavior is due to a polymerization of protein fibers, characteristic of other phenomena related to the fixation of biological material such as treatment in formalin. Second, the ILs molecules interact indirectly with the cytoskeleton, inducing the production of particular substances able to polymerize the cytoskeletal proteins. A similar behavior, in fact, has been studied by Majewski et al.[213] who discovered the potential of ionic liquids as fixing agent for embalming and preservation of biological tissues. Using pure ILs, the amount of water molecules in the cytoplasm can vanish, replaced by a solution with great abundance ions. In that work, [C_4MIM][BF_4] shows improved performance, compared to standard formaldehyde, in terms of quality of optical images and eco-friendly properties. In our work must be emphasized that, at 100 mmol dm^{-3} concentration, it is easy to observe cells in advanced apoptosys status leading to a percentage of samples, suitable for a measurement with AFM, dramatically lower compared to situation at lower concentration.

As expected, the evolution of the system is similar if [C_4MIM][BF_4] is used to contaminate the MDA-MB-231 cell culture. In perfect analogy with [C_4MIM][Cl] experiments, morphological effects (Fig. 3.30) and mechanical effects 3.31 are presented for [C_4MIM][BF_4].

Log_{10}(Young's modulus / Pa)				
Conc (mmol dm-3)	Cell body L range	lamellipodia L range	Cell body H range	lamellipodia H range
0	2.62 ± 0.10	3.02 ± 0.12	2.60 ± 0.08	2.66 ± 0.25
1	2.68 ± 0.08	3.00 ± 0.20	2.63 ± 0.09	2.61 ± 0.14
10	2.64 ± 0.09	2.82 ± 0.18	2.59 ± 0.09	2.44 ± 0.11
100	3.77 ± 0.16	3.38 ± 0.20	3.70 ± 0.19	3.09 ± 0.15

Table 3.4: Summary of experimental data obtained on Young's modulus obtained on samples cell MDA-MB-231 interacting with [C_4MIM][BF_4].

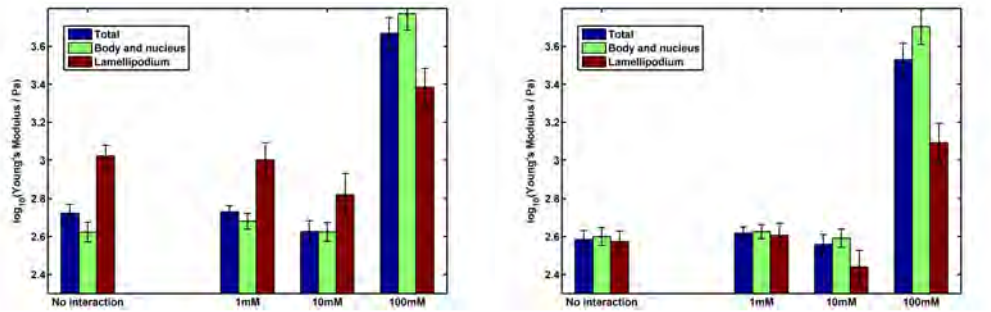

Figure 3.33: Behaviour of the Young modulus of cells MDA-MB-231 varying the concentration of [C_4MIM][BF_4]. In the graph are taken into account data referring to low indentation range (left) and high indentation range (right)

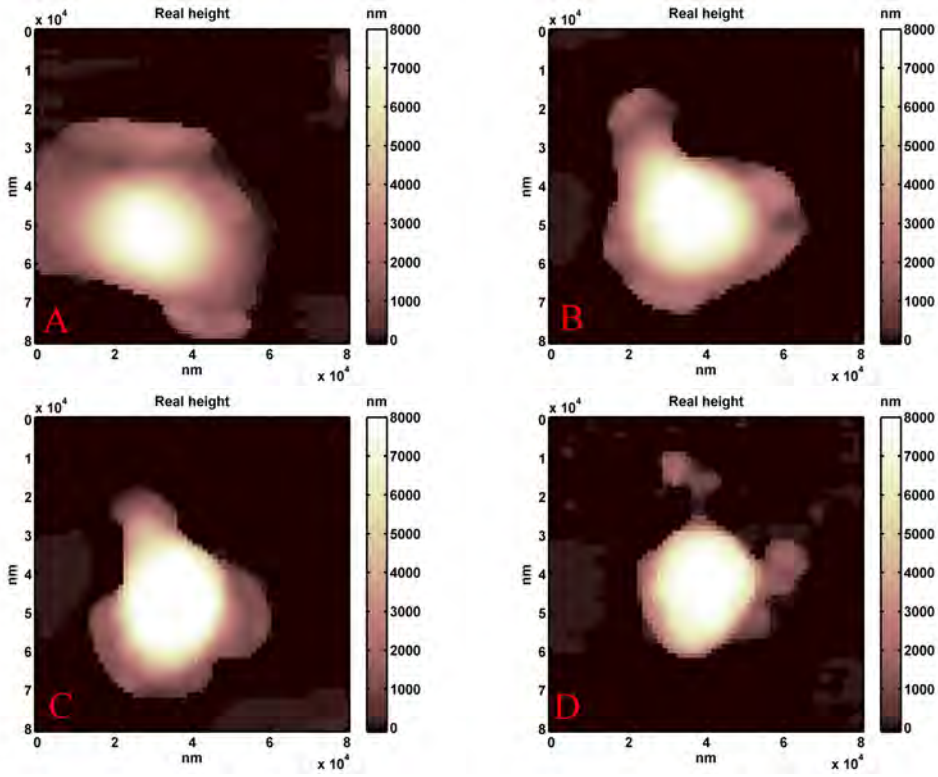

Figure 3.30: Real topography of typical MDA-MB-231 cell with increasing concentration of $[C_4MIM][BF_4]$. Image A represents the initial situation without interaction. Image B represents the cell contaminated with 1 mmol dm^{-3} of $[C_4MIM][BF_4]$ after 20 min. Image C represents the cell contaminated with 10 mmol dm^{-3} of $[C_4MIM][BF_4]$ after 20 min. Image D represents the cell contaminated with 100 mmol dm^{-3} of $[C_4MIM][BF_4]$ after 20 min.

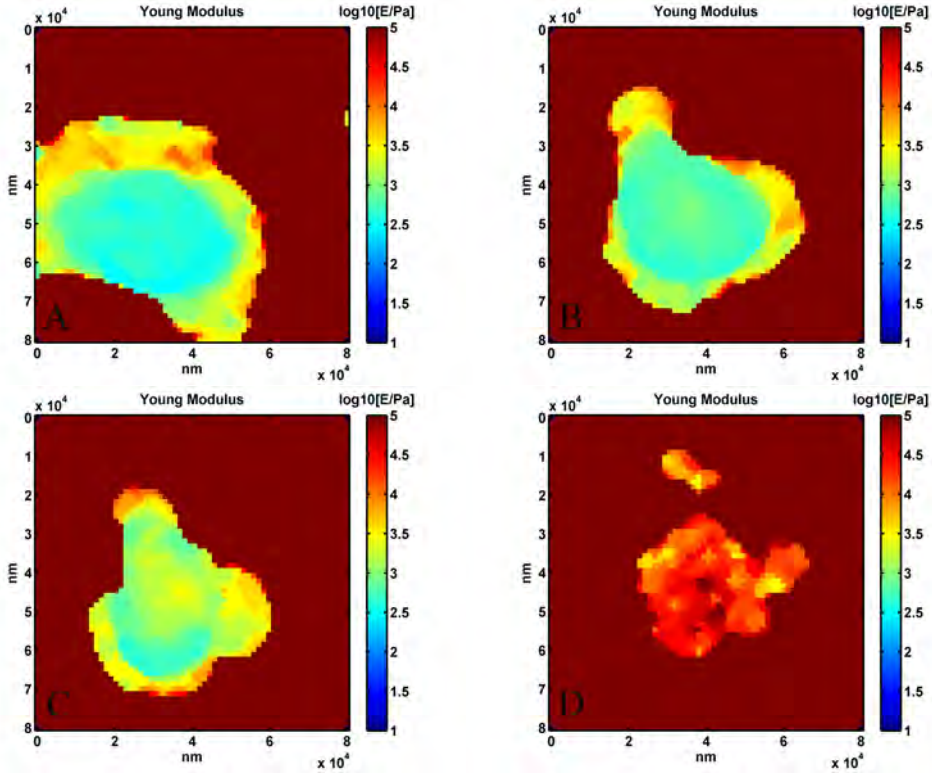

Figure 3.31: Young's modulus map at low indentation range for MDA-MB-231 cell in Fig 3.30 with increasing concentration of $[C_4MIM][BF_4]$. Image A represents the initial situation without interaction with IL. Image B represents the cell contaminated with 1 mmol dm^{-3} of $[C_4MIM][BF_4]$ after 20 min. Image C represents the cell contaminated with 10 mmol dm^{-3} of $[C_4MIM][BF_4]$ after 20 min. Image D represents the cell contaminated with 100 mmol dm^{-3} of $[C_4MIM][BF_4]$ after 20 min.

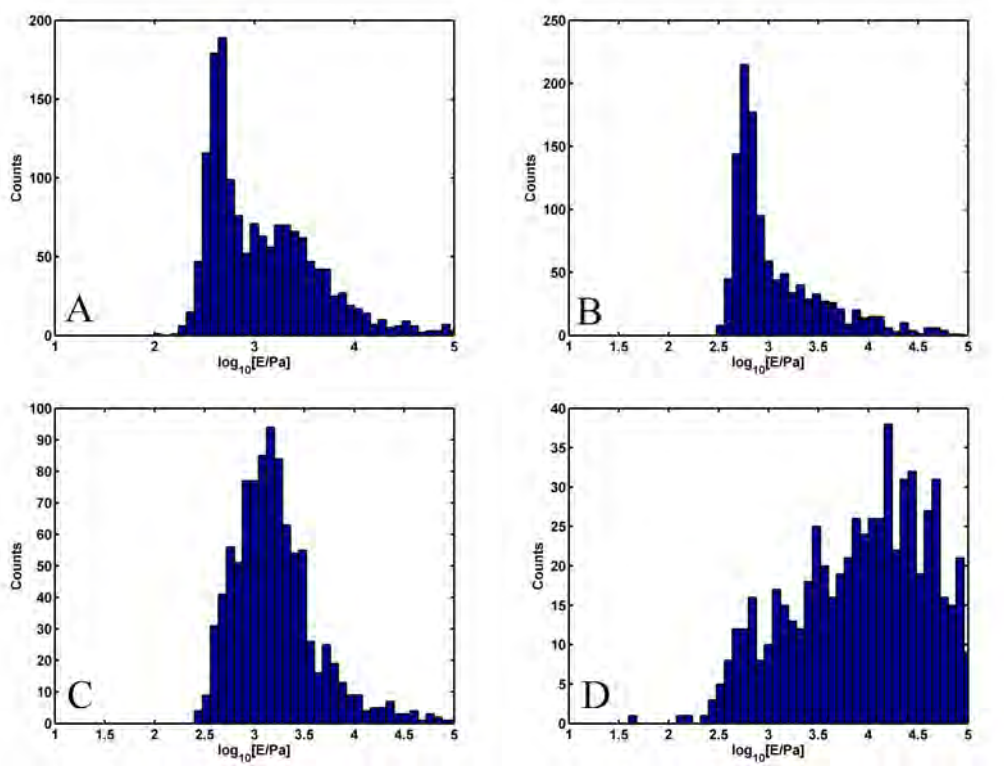

Figure 3.32: Quantitative histograms of Young's modulus at low indentation range for MDA-MB-231 cell in Fig 3.31 with increasing concentration of $[C_4MIM][BF_4]$. Graph A represents the initial situation without interaction with IL. Graph B represents the cell contaminated with 1 mmol dm^{-3} of $[C_4MIM][BF_4]$ after 20 min. Graph C represents the cell contaminated with 10 mmol dm^{-3} of $[C_4MIM][BF_4]$ after 20 min. Graph D represents the cell contaminated with 100 mmol dm^{-3} of $[C_4MIM][BF_4]$ after 20 min.

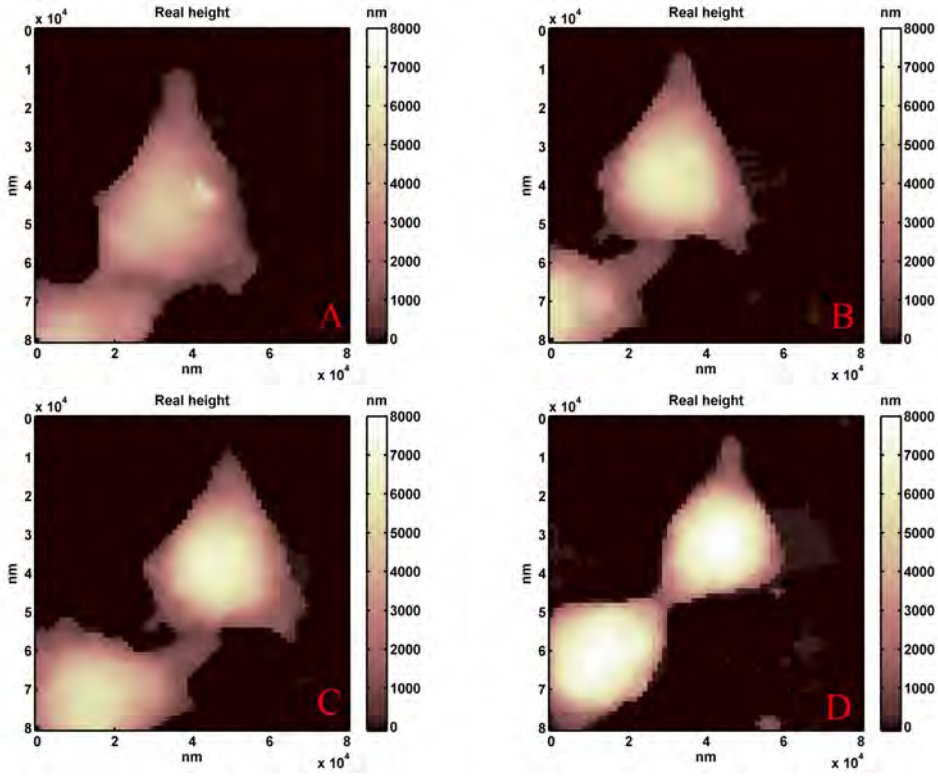

Figure 3.34: Real topography of typical MDA-MB-231 cell with increasing concentration of [C_8MIM][Cl]. Image A represents the initial situation without interaction. Image B represents the cell contaminated with 1 μmol dm^{-3} of [C_8MIM][Cl] after 20 min. Image C represents the cell contaminated with 10 μmol dm^{-3} of [C_8MIM][Cl] after 20 min. Image D represents the cell contaminated with 100 μmol dm^{-3} of [C_8MIM][Cl] after 20 min.

After quantitative mechanical analysis depicted in Fig. 3.32, the data contained in Table 3.4 and reported also in the graph in Figure 3.33, show the trend of the mechanical properties of the cellular system and highlight the same trend observed with interaction with [C_4MIM][Cl].

The mode of interaction change radically with the use of [C_8MIM][Cl]. As already stated several times in the introductory part of this thesis, the length of the alkyl side chain ([C_8MIM]$^+$ has 8 carbon atoms in the tail) is in some way proportional to the toxic character of ionic liquid. Considering the higher lipophilic character the concentration used in new experiments was three orders of magnitude lower than those used for the other sets of data. Measurements were performed, in fact, with 1 μmol dm^{-3}, 10 μmol dm^{-3} and 100 μmol dm^{-3}. Above this threshold, the number of cells attached to the substrate, that can be used in nanomechanical experiments was negligible, quantitatively less than 5% of the total, and then also inconsistent for statistical analysis. In perfect analogy with previous experiments, morphological effects (Fig. 3.34) and mechanical effects 3.35 are presented for [C_8MIM][Cl].

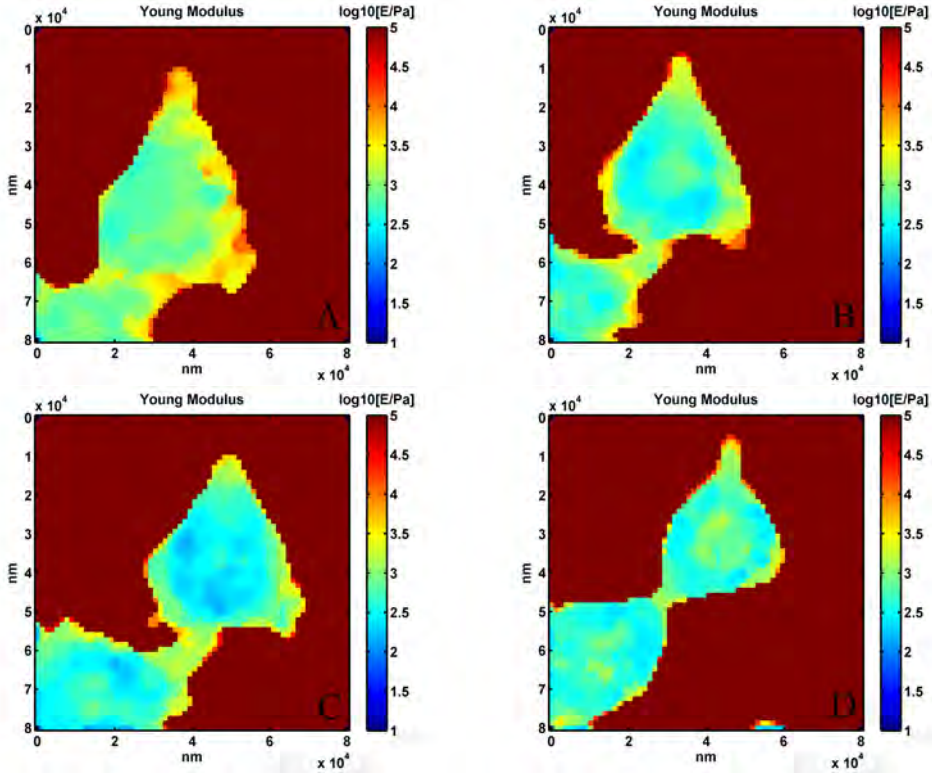

Figure 3.35: Young's modulus map at low indentation range for MDA-MB-231 cell in Fig 3.34 with increasing concentration of $[C_8MIM][Cl]$. Image A represents the initial situation without interaction with IL. Image B represents the cell contaminated with 1 μmol dm^{-3} of $[C_8MIM][Cl]$ after 20 min. Image C represents the cell contaminated with 10 μmol dm^{-3} of $[C_8MIM][Cl]$ after 20 min. Image D represents the cell contaminated with 100 μmol dm^{-3} of $[C_8MIM][Cl]$ after 20 min.

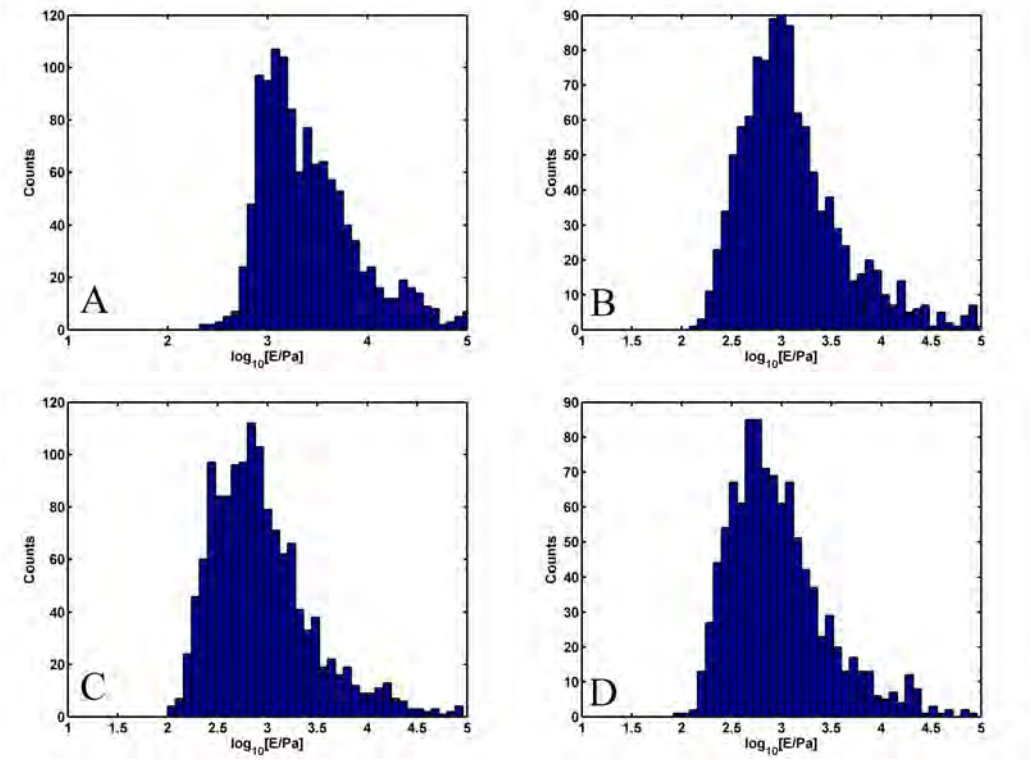

Figure 3.36: Quantitative histograms of Young's modulus at low indentation range for MDA-MB-231 cell in Fig 3.35 with increasing concentration of [C_8MIM][Cl]. Graph A represents the initial situation without interaction with IL. Graph B represents the cell contaminated with 1 μmol dm^{-3} of [C_8MIM][Cl] after 20 min. Graph C represents the cell contaminated with 10 μmol dm^{-3} of [C_8MIM][Cl] after 20 min. Graph D represents the cell contaminated with 100 μmol dm^{-3} of [C_8MIM][Cl] after 20 min.

Log_{10}(Young's modulus / Pa)				
Conc (μmol dm-3)	Cell body L range	lamellipodia L range	Cell body H range	lamellipodia H range
0	2.93 ± 0.16	3.31 ± 0.14	2.88 ± 0.11	2.81 ± 0.13
1	2.72 ± 0.10	3.00 ± 0.09	2.63 ± 0.11	2.55 ± 0.08
10	2.64 ± 0.07	2.92 ± 0.11	2.57 ± 0.07	2.49 ± 0.10
100	2.59 ± 0.04	2.83 ± 0.09	2.60 ± 0.07	2.51 ± 0.09

Table 3.5: Summary of experimental data obtained on Young's modulus obtained on samples cell MDA-MB-231 interacting with [C_8MIM][Cl].

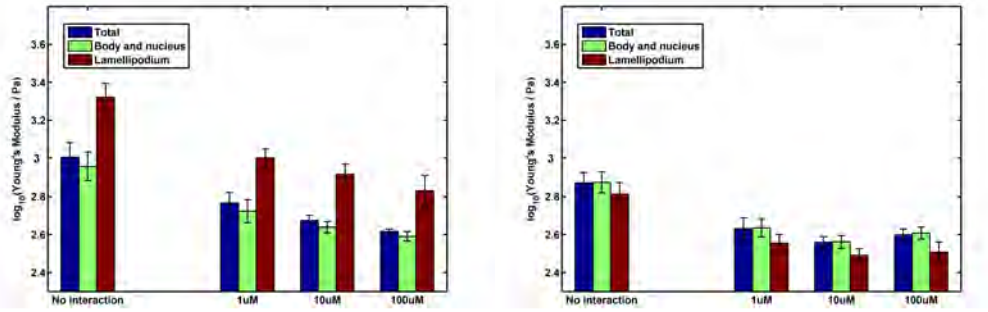

Figure 3.37: Behaviour of the Young modulus of cells MDA-MB-231 varying the concentration of [C_8MIM][Cl]. In the graph are taken into account data referring to low indentation range (left) and high indentation range (right)

From Table 3.5 and the graph in Figure 3.37 we observe the modifications in Young's modulus varying the concentration of [C_8MIM][Cl] in the micro-molar range. The systematic trend of the elastic modulus is compatible with softening obtained at low concentrations of short tail ionic liquids. In fact, a decrease of Young's modulus of the cell in accordance with the softening of the external membrane area is observed in μmol dm^{-3} range. At concentrations higher than 100 μmol dm^{-3}, the most effective action of the cation readily triggered the apoptotic process probably caused by the big damage caused to the external membrane.

This effect is confirmed in a very recent work of Radosevic et al. [214] who observed that treatment with various imidazolium ILs decreased CCO cell viability on dose-dependent manner and showed dependency on anion and alkyl chain length. Morphological alterations observed by fluorescence microscopy are related to the structure and concentration of tested IL while flow cytometry results showed that ILs with longer alkyl chain increased the proportion of necrotic and apoptotic cells. Complementary use of WST-1 cell proliferation assay, fluorescent microscopy and flow cytometry can provide better insight into interrogation of biological impact of ILs in(fish) cell lines. By such approach we can study in more details the alterations in cells and their membranes, which are probably related to the mechanism of actions of ILs.

Another cytotoxicity study performed by Li et al. [215] confirms that ILs with long lateral tails induce apoptosis. They studied the cytotoxicity of alkyl methylimidazolium-based ILs on rat pheochromocytoma (PC12) cells. The results showed dose-dependent

cytotoxicity of ILs on PC12 cells, and the ionic liquids with longer lateral chains had stronger cytotoxicity. Additionally, they found that exposure to [C_8MIM][Br] IL provoked cellular lactate dehydrogenase (LDH) release, increased mitochondrial depolarization, nuclear shrinkage and DNA fragmentation, and promoted caspase-3 (cysteine proteases that mediate cell death) activity and reactive oxygen species (ROS) levels in PC12 cells. These results suggest that [C_8MIM][Br] may induce PC12 cell apoptosis triggered by excessive ROS and mediated by mitochondrial depolarization and permeability transition. Another similar study performed by Jing et al. [216] evaluates the cytotoxicity and responses of the cellular antioxidant system of [C_8MIM][Cl] on human hepatocarcinoma QGY-7701 cells. In this study, nuclear morphology observation reveals that [C_8MIM][Cl] exposure has induced typical apoptosis of QGY-7701 cells, which has also been verified by the results of caspase-3 activity assays and overproduction of cellular ROS. Caspase-3 has been shown to be an important regulator of apoptosis, because caspase-3 is usually cleaved and activated during the final step of apoptosis. Liver is the most important organ involved in the redox metabolism, where the key enzymes and some small molecules responsible for ROS clearance are synthesized. All these parameters of the defense system have been considered as valuable biomarkers of pro-oxidant situations in mammals [217]. Under normal physiological conditions, these enzymes or molecules maintain a dynamic balance in cells while the remaining one will be destroyed by excessive ROS induced by exogenous chemicals. In this study, the results of biochemical assays reveal that [C_8MIM][Cl] exposure inhibits enzymes activities, decreasing the capacity to scavenge ROS in a cell, which finally induces apoptosis. Therefore, the results of this study indicate that ROS and oxidative stress may be responsible for the apoptosis induced by [C_8MIM][Cl] in QGY-7701 cells. A particular molecule, malondialdehyde (MDA), increases after interaction. MDA is the product of reaction between free radicals and unsaturated fatty acids in cellular membrane, which may react with the free amino ends of proteins to form inter- and intramolecular protein cross-link, resulting in disorder and injury in cellular structure and function [218]. As the metabolic product of lipid peroxidation in organisms, an increase in the cellular MDA content can be a representation of lipid peroxidation. Hence, it has now become a sensitive biomarker to judge cellular oxidative injury [219]. In this study, the increase in the MDA level indicates that lipid peroxidation occurs in QGY-7701 cells after [C_8MIM][Cl] exposure and this result also suggests that the cellular antioxidant system fails to eliminate excessive ROS.

CHAPTER 4

Conclusions

In the first part of my PhD work I investigated the electrical properties of thin ionic liquid layers on solid surfaces by atomic force microscopy. Atomic force microscopy has been chosen since it allows to acquire morphological maps with nanometer resolution along vertical direction and of the order of few nanometers in the lateral direction. Furthermore simultaneously to the topography, other maps of the physico-chemical properties can be acquired, with the same or comparative lateral resolution. A morphological investigation of $[C_4MIM][NTf_2]$ thin films deposited on different solid surfaces confirms that IL exists in the form of micro- and nano- -droplets and flat ordered solid-like domains behaving like solids under the AFM tip. Investigating the resistance to normal loads, penetration steps in nano-indentation experiments (force vs. distance curves) have been found [64]. The first part of the mechanical interaction has been treated as an elastic compression, leading to Young modulus E $\approx$ 1.8 GPa, similar to that of some plastic material like nylon.

The nanomechanical investigation suggests that solid-like layers, in comparison with bulk IL, possess different electrical properties. In fact, another evidence to the solid-like character of IL layering, was the observation that islands were not disrupted by intense electric fields up to 10^8-10^9 V/m (applied biasing the AFM with respect to sample during imaging). Even in this case, unlike liquid drops, that are strongly influenced by the applied electric field, the structures are not changed demonstrating that the ions are tightly bound in a stable structure. I-V characteristics, by means of conductive AFM, performed on solid-like layer deposited on doped silicon with native oxide, show an insulating behavior with resistivity is in the order of 10^{16}-10^{18} Ω/cm. Starting from this assumption, an insulating and dielectric character was hypothesized for these layers.

Nanoscale impedance microscopy and electric force detection methods have been developed to measure local static dielectric constant by means of atomic force microscopy. Using alternating voltages applied on conductive substrate with thin IL solid-like layer, the capacitive component of the tip-sample system is analyzed. This method allows to measure the dielectric constant of the layer between the tip and the conductive sample; ε_r = 4.8 $\pm$ 0.9 was measured. Electric force detection techniques was performed using constant voltage applied between the tip and the conductive sample. Considering that static deflection of electrified tip is proportional to the derivative of capacitance, the dielectric constant of solid-like layers is extrapolated; ε_r = 3.1 $\pm$ 0.2.

Insulating character of the ordered domains (ε_r = 3-5 was measured) is consistent with the idea that IL ordered domains behave as solid materials in which the ions are tightly bound. The dielectric constant values measured on solid-like terraces seems to be significantly lower than values (ε_r = 9-14) found in the literature [16; 17; 20–22]. Low values of ε_r (typically between 3 and 6) are measured on insulating solid salts like NaCl. This atypical behavior could be justified by confinement in a 2D layered system

(graphite-like) induced by decrease of the degrees of freedom during electric polarization. The formation of ordered insulating structures can have a crucial influence in the performances of photo-electrochemical devices. Especially for new generation devices, where nanostructured electrodes enhance the surface effects, the confinement and ordering of electrolyte inside nanopores could negatively influence the energy efficiency of the devices. This study could provide useful information to prepare optimized interfaces in devices application, but also to deeply understand the structure and behavior of ionic liquids near a charged interface.

In the second part of my thesis the surface interaction of ILs with biological membranes and live cells was studied by means of electrochemical tools and AFM morpho-mechanical combined investigation. A series imidazolium-based ionic liquids in aqueous solutions interacting with phospholipid monolayers of DOPC was analyzed, these results were published in ref. [198]. The strength of interaction is related to the length of carbon chain of the cation and is not systematically related to the nature of the anion. With 2 and 4 carbons in the lateral chains, IL cations adsorb reversibly on the phospholipid monolayer. The presence of 8 and 12 carbons in the lateral chain of IL cations causes stronger irreversible interaction, leading to eventual replacement of DOPC by IL on the electrode surface. The linear correlation (R = 0.97) between the detection limit (LOD) of RCV to ILs and the toxicity of ILs to Vibrio fisheri suggests that the toxic mechanism of ILs in unicellular organisms is underwritten by a biomembrane mechanism.

To deeply investigate this mode of interaction, AFM morphological and mechanical measurements were performed on membrane model, consisting of DOPC phospholipid bilayers supported on solid surface interacting with ILs. In this study it was possible to obtain AFM morphology and elasticity maps of the samples, along with histograms for quantitative analysis. The information that has been acquired has yielded interesting results, confirming the behavior observed with electrochemical methods. In general, the main observation that can be seen from morphological analysis is the strong affinity of ionic liquids with phospholipid membranes; this leads to rupture, modifications and reorganizations of lipid materials supported on surface. From the mechanical point of view, a general softening of membranes was experimented with increasing contaminant concentration. Inclusions of IL tails inside the lipid layers destabilize their compact structure. This effect causes an augment of monolayer capacitance and broadening of voltammetric peaks using electrochemical methods. A noticeable decrease of breakthrough force and compressibility modulus indicate a lowering in mechanical stability but also that bilayers are much more compliant. This finding is important in the toxicity scenario, since it means that ionic liquids interact with the cell membrane, depending on their concentration and lateral chain length, by changing its structure, and especially by softening it. Living cells maintained at 37°C were investigated using a combined morphological and nanomechanical analysis by AFM. A decrease of Young's modulus, in the low indentation regime, was observed only for low concentrations of ionic liquid (up to 1mM). This effect probably coincides with the direct interaction of ILs and external layers of membrane, suggesting a progressive inclusion of ionic liquid molecules within the phospholipid structure. At higher concentration different phenomena were seen depending from the length of the alkyl side chain of the cation. In the case of $[C_4MIM][Cl]$ and $[C_4MIM][BF_4]$ a considerable increase of Young's modulus of the cytoskeletal structure is evidenced, while in the case of $[C_8MIM][Cl]$ late apoptosis processes are triggered, making the system unsuitable for measurements with scanning probe. At high concentrations seems that ionic liquids penetrates the cell membrane interacting, with different aggression strength, also with internal structures and organelles. Biological methods will be required to deeply investigate internal mechanism involved in that reactions.

The results obtained in this thesis provide information about the biomembrane activity of widely used and investigated imidazolium-based ILs, relating their structure to different degree of interaction. They could provide strategic directions in the design of new ILs to satisfy environmental sustainability. Tuning the interaction with biomembrane, by modifying the chemical structure of ions, the particular properties of ILs could also match the field of biomedical applications.

Appendices

APPENDIX A

Interaction with nanostructured materials

A.1 The ns-surface/ionic liquid interface

The study of the role of the substrate roughness is important in order to understand how surface topography affects the morphology of the interfacial layers of ionic liquid. Flat surfaces are fundamental to understand the behavior of thin IL layers because they are easier to study with many experimental techniques as well as theoretically, but nanostructured surfaces, with increased specific area, are used in devices like Graetzel cells or electrochemical capacitors. For those reasons, preliminary studies of the interaction of ILs are performed on these particular surfaces. SiO_2 nanoparticles of were deposited on oxidized silicon, giving the possibility to study the effect of roughening on a deeply investigated substrate. A sub-monolayer of SiO_2 particles has been deposited on the first clean substrate, whereas another substrate has been covered by a 32 ± 2nm thick nanostructured film.

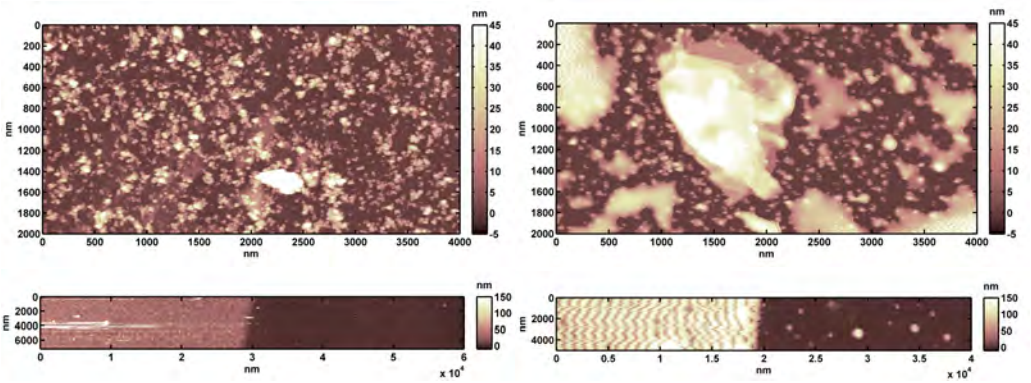

Figure A.1: A: sub-monolayer deposition of silicon oxide nanoparticles on silicon; B: $[C_4MIM][NTf_2]$/methanol on the sample represented in A; C: step in a 32nm thick deposition of ns-SiOx on silicon (vertical scale 155nm); D: $[C_4MIM][NTf_2]$/methanol on the sample imaged in C: the regular pattern in the left of the image is due to an unstable imaging induced by the ionic liquid that permeate completely the nanostructured film.

As it can be seen in Figure A.1 A and B, the presence of nanoparticles on the surface of silicon does not prevent the formation of highly ordered structures, that are found to be densely distributed on the surface. Analyzing the liquid part of the deposition, it can be noticed that the shape of the droplets is very irregular and determined (pinned) by the silica nanoparticles distribution. This is not surprising because the $[C_4MIM][NTf_2]$ wets

very well the silica surface (direct measurements of contact angle of $[C_4MIM][NTf_2]$ on different substrates by AFM imaging have been performed in [64]); for the same reason, in samples where thick layers of silica nanoparticles has been deposited, it is not possible to acquire meaningful AFM images. In Figure A.1 C it is possible to see the nanoparticle film on the left and the substrate on the right and in Figure A.1 D the same sample has been observed after IL deposition: the nanoporous matrix is completely permeated by the IL, and the strong interaction between the IL and the tip avoids a stable imaging, as evidenced by the regular noise in the left part of the image, whereas on the right side is possible to observe the usual morphology.

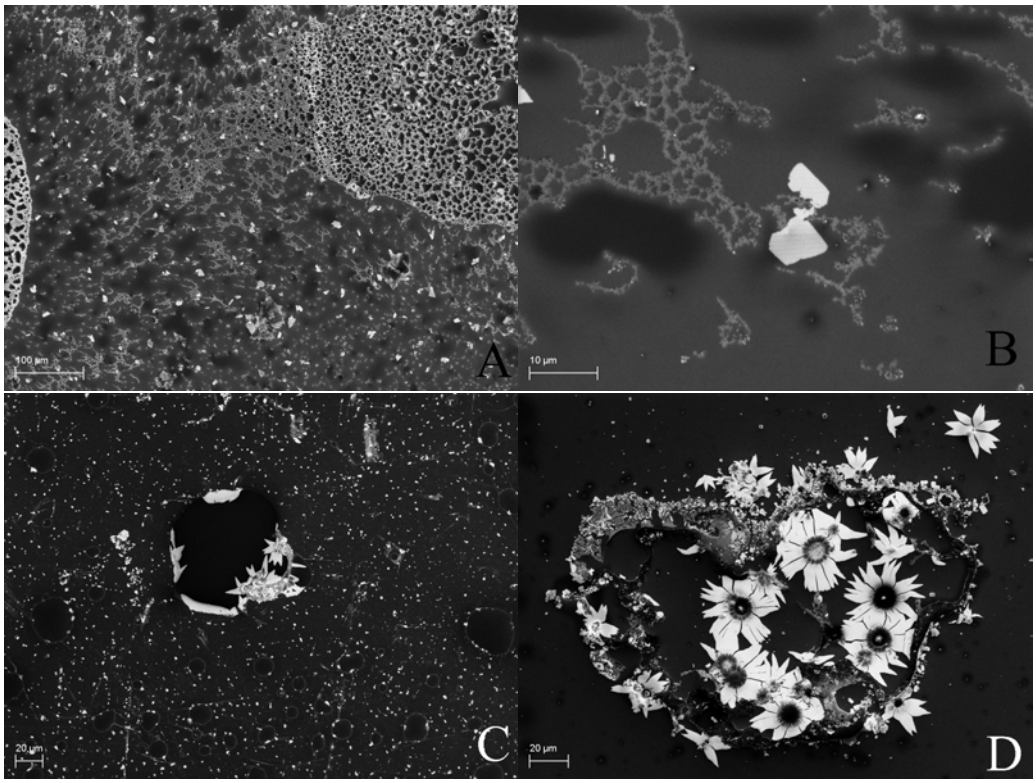

Figure A.2: SEM morphology of $[C_4MIM][NTf_2]$ nanostructured silica on oxidised silicon. Images A and B are relative to IL deposited on a sub-monolayer of silica nanoparticles. In images C and the IL was on top of a 32nm thick layer of ns-Si. In the last image D can be noticed beautiful flower-like structures, whose origin is still unclear.

Images A and B of Figure A.2 show, as AFM investigation evidenced, that solid-like domains can form even if a flat surface is covered by a sub-monolayer layer of nanometric silica nanoparticles [64]. Something similar can be observed even on a thicker deposition of silica nanoparticles, as shown in Figure A.2 C, where the with spots are solid-like layers. Figure A.2 D has been collected on the same sample as C. Beautiful flower-like structures are found to sit on top of the 32nm thick nanostructured film of silica. Those structures could be another form of the solid-like terraces, but can also be formed by the aggregation of silica particles detached from the substrate by action of the ionic liquid. In fact, due to the high affinity of $[C_4MIM][NTf_2]$ with silica and to the

possible solvation effect of the particles in ionic liquid (as it has been actually seen in colloidal suspension of silica particles in ionic liquids [220]), silica clusters can detach and aggregate at the surface. Those structures are still not fully understood and a more detailed investigation is required.

As already remarked, the optimal use of nanostructured surfaces in contact with ionic liquids in many applications would requires an extensive study of the interface between the IL and the solid. During this work I have focused my attention on the mechanical and electrical properties of ILs interacting with flat surfaces like silica as a preliminary step before the investigation of ILs deposited on nanostructured surfaces. The roughening of the substrate surface can be expected to lead to two opposite effects: on one hand a rougher surface introduces some degree of disorder that can inhibit the formation of well ordered structures; on the other hand, since with a nanostructured deposition the surface area is greatly increased respect to a flat substrate, if the affinity between the ionic liquid and the material composing of the nanoparticles is high, the formation of solid-like structures could be enhanced.

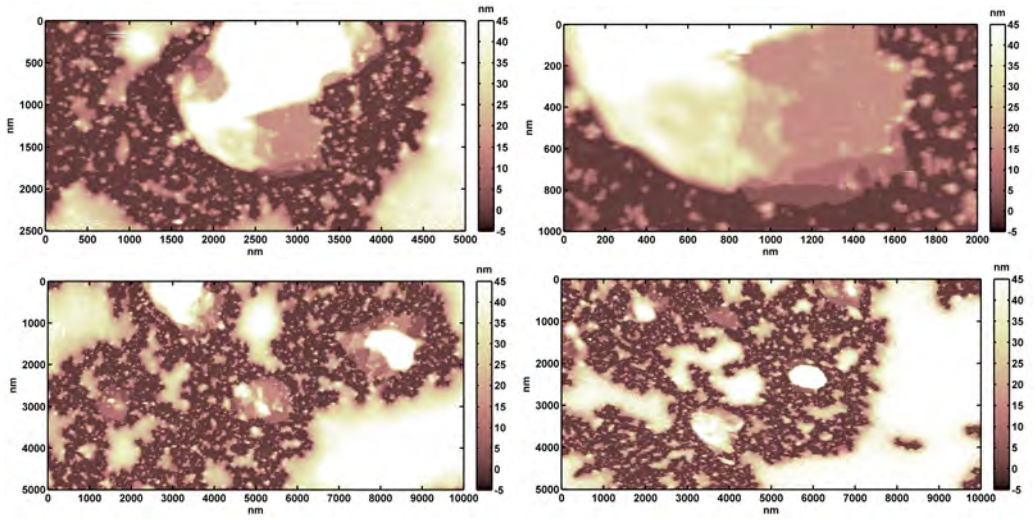

Figure A.3: Collection of AFM morphologies of $[C_4MIM][NTf_2]$ deposited with methanol on a sub-monolayer coating of silica nanoparticles on oxidised silicon. The images allow to appreciate the thickness and density of the terraced structures, whose formation is not prevented by the presence of silica clusters. Vertical scales 50nm.

Figure A.3, as well as the previously reported Figure A.1, shows the result of a first approach to the study of a rough surface. For the AFM investigation it is of particular interest the case of a sub-monolayer deposition of nanoparticles on a at surface, in this case silica nanoparticles, because this represents a first step toward a nanostructured surface and also it should be easier to observe the effects of the IL/solid interaction, if any. From the figures it is possible to observe that the affinity between the silica nanoparticles and the IL is actually high. As can be noticed in fact, the shape of the liquid domains in no more that of rounded droplets, but the IL lies more at on the surface and every droplet looks pinned to some silica nanoparticles. The morphology of the droplets remember that of a liquid experiencing dewetting for minimize its free energy, but it is not allowed to a further reduction of its interface because it is trapped on the surface be localized points acting as pinning elements, the same effect that happens when a drop of IL

solution is deposited onto a small substrate and pins to the borders. Actually the affinity of the [C_4MIM][NTf_2] with the silica surface is witnessed by the low contact angle ($\approx 11°$) [C_4MIM][NTf_2] on silica calculated by the shape of nano-droplets in AFM topographic map, reported in [64]. Figures A.1 and A.3 evidence that the presence of a dense distribution of nanoparticles on the surface of oxidized silicon actually doesn't prevent the growth of multilayered solid-like domains, that are as thick as on flat surfaces and densely distributed. The fact that, at least on substrates where it is still feasible an AFM investigation, the introduction of nanoparticles still doesn't prevent IL ordering phenomena, leads us to think that if an ionic liquid would be confined into a nanoporous matrix, where in each pore the surface to volume ratio for the IL is high, the ordered, solid-like phase, can still develop. When considering the effect of confinement on melting point of a substance, in general a reduction respect to the bulk can be observed. A simple argument can be used in order to predict the effect of confinement on ILs. The predicting behavior for melting point is opposite to what we have seen on flat and rough surfaces as well as to that we guess can be seen into nanopores. Considering a particle, a reduction in size induces an increase in the ratio of surface atoms to volume atoms. Surface atoms have a lower number of nearest neighbors than bulk atoms and so if the surface to volume ratio increases, the cohesive energy correspondingly decreases. The decrease in the cohesive energy leads to a decrease in the melting point of the particle. The same argument is still applicable to confined systems, in which the melting point reduction is described by the Gibbs-Thomson equation. The Gibbs-Thomson equation analyze the behavior of a solid confined into a nanopore in contact with its own liquid and allows to calculate the melting temperature as a function of the pore diameter as:

$$T_m(d) = T_{mb}\left(1 - \frac{4\sigma_{sl}}{d\Delta H_f \rho_s}\right) \tag{A.1}$$

where T_{mb} is the bulk melting temperature, σ_{sl} is the interfacial tension between the liquid and the solid phase of the confined material, ΔH_f is the bulk enthalpy of fusion and ρ_s is the density of the solid phase [221]. While this equation describes the behavior of many confined liquids, i.e. in general a lowering of T_m and confinement-induced fluidification. In many studies (reported in the review in Ref. [221]), ΔH_f if found to decrease with d. Furthermore, not only pore size but also pore shape influences the behavior of Tm as a function of d. Some studies on the variation of the melting point of ILs upon confinement in nanoporous matrices, actually show that Tm follow the behavior predicted by equation A.1. In particular Konakubo et al. [222] studied, by density scanning calorimetry (DSC) the behavior of the melting point for several imidazolium-based ionic liquids confined in a controlled porous glass (CPG) matrix on both the slightly hydrophilic native matrix and on a methyl-modified hydrophobic one. In both cases a marked decrease of T_m is observed for all the ILs. Liu et al.[223] studied by DSC the variation in the melting point of several imidazolium-based ILs in ILs/silica nanoparticles mixtures. They found, as Konakubo, a depression in the melting point for all the ionic liquids studied. Anyway, it is interesting to note that the authors argue that the depression in T_m is due to the immobilisation of imidazolium cations at the surface of the hydrophilic silica particles. In this confined geometry part of the ions are then freezes in an high entropic state that breaks the symmetry in the liquid and leads to a decrease in the melting point. Despite the prediction of the Gibbs-Thomson equation, there are other studies that underline ordering and layering effects upon confinement. In particular ordering-immobilisation of ionic liquid ions at the pore interface is thought to be responsible for a decrease in conductivity in a study conducted by Iacob et. al [192]. In this study the conductivity of the IL [C_6MIM][PF_6] confined in nanopores,

with an average diameter around 7nm, is measured. A decrease of an order of magnitude in the conductivity respect to the bulk is observed when hydrophilic silica, i.e. with an hydroxilated surface, is used. If the internal surface of the pores is modified by silanisation, adding trimethylsilyl inert groups, the conductivity in the membrane is almost the same as in the bulk. The authors suggest that the decrease in conductivity for non-treated silica is due to the formation of a bound surface layer on the internal surface of the pores. In another study performed by the group of Graetzel [224], silica nanoparticles are used to induce a gelation in a ionic liquid-based electrolyte for a DSSC solar cell. Only 5 wt% or 3 vol % of nanoparticles having an average diameter of 12nm added to two IL-based electrolytes (composed of 0.5M iodine and 0.45M of N-methyl-benzimidazole in either pure $[C_3MIM][I]$ or a mixture of $[C_3MIM][I]$ and 3-methoxypropionitrile (volume ratio 13:7), respectively) is needed to realize a gel. 3% in volume roughly means that the distance between the surface of neighboring nanoparticles is around 20nm, but nevertheless a stable gel can be realized. This may happen because each particle is surrounded by a bonded layer of ionic liquid molecules increasing their actual diameter and leading to the gelation. The fact that the gelation influences only weakly the conductivity of the electrolyte could mean that the volume is not filled completely by immobilized layers, but some channels are formed, allowing for ionic liquid ions redox couple flowing. Ueno et al.[220] show the formation of gels by adding to different ionic liquids hydrophilic or hydrophobic silica nanoparticles. In particular the addition of hydrophilic particles lead to the formation of stable colloidal suspension and ionogels. The authors relate this stability with the development of solvation layers that prevent the particle aggregation and lead to the formation of a stable structure. Li et al. [225] studied the influence of different types of solid walls on the structural and dynamic properties of confined $[C_4MIM][NTf_2]$. The electrostatic interaction drives the structuring near the silica walls and causes realignment of the cation ring and alkyl chains, which is not the case for $[C_4MIM][NTf_2]$ near carbon walls. It can be noted that alkyl chains diffuse deeper into the cavities in silica, which restrains the access of the relatively big cation rings. For carbon mesopores, in that MD simulations, only relatively weak van der Waals forces between ions and carbon walls contribute to the structuring of $[C_4MIM][NTf_2]$. They noted that diffusion coefficients of $[C_4MIM][NTf_2]$ confined in silica and carbon mesopores exhibited dissimilar temperature dependence as the loading fraction changed; complicated interfacial microstructures of $[C_4MIM][NTf_2]$ near solvophilic silica mesopores were observed; an oscillatory interaction potential profile near the silica surface was revealed, in contrast to a non-oscillatory potential profile near a smooth carbon surface; and both surface heterogeneity and features of the interaction potential for silica mesopores (i.e., electrostatic interaction) might contribute to the distinctive interfacial microstructure and weakened temperature dependence of diffusion. The observed oscillatory interaction potential profile near the silica surface coincides with the measured force profile from AFM measurements.

A.2 ILs on nanostructured carbon

To complete and apply this study, the electric double layer capacity of ns-C films (thickness variable in the range of 140-500 nm) was investigated by electrochemical impedance spectroscopy and cyclic voltammetry employing four different hydrophobic ILs featuring the same anion and with different cations as electrolyte [226]. Electrochemical impedance spectroscopy and cyclic voltammetry highlighted a quasi-ideal capacity response revealing that the surface chemistry and morphology of the nanostructured carbon allows the penetration and the reversible ion adsorption in the ns-C porous matrix

of RTILs ions over a wide range of ns-C thickness. These evidences clearly show that the nanometric structure of the ns-C, which is fundamental for the double layer formation mechanism, is characterized by an open porosity, easily wettable and accessible by RTILs.

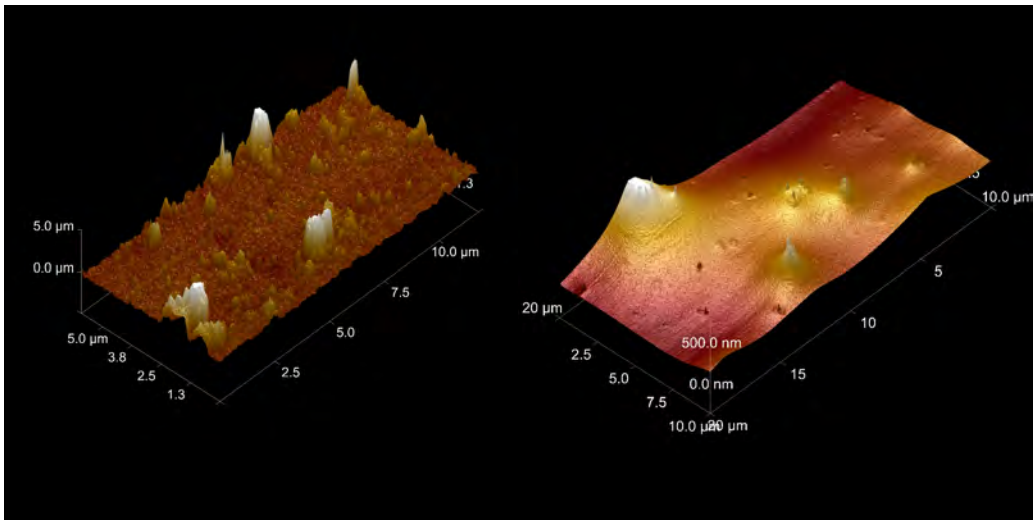

Figure A.4: AFM 3D image of a ns-C electrode before (left) and after (right) the immersion in ionic liquid [C_4MIM][NTf_2] showing a complete coverage of nanostructured surface.

The fact that no ordered layering on HOPG graphite could be found [64], tells that surface chemistry is probably an important factor inducing the ordering of IL molecules. On noncharged, nonpolar surfaces, like graphite, the alkyl tails of the cations very likely interact with the surface, hampering the stable ordering of correlated positively and negatively charged layers, therefore favoring the liquid phase. Carbon material is suggested to be a very promising material to develop high performance electrodes.

Electrochemical stability window was higher than 3 V for all the RTILs tested. The highest EDL capacity, 75 F/g, was obtained by using [C_4MIM][NTf_2], the IL with short alkyl chain. Using [C_4MIM][NTf_2] a supercapacitor with single electrode area of 0.2 cm^2 and specific capacity of 80 $\mu F/cm^2$ was obtained. A possible device could be easily implementable on a wide range of different substrates (e.g. glass, SiO_2, polymers) and compatible with planar technology. The measured performances in terms of energy and power density, together with the intrinsic versatility of SCBD in producing patterned depositions on virtually any kind of substrate by using a stencil mask approach, are appealing for the fabrication of thin electrodes for microscale energy storage devices to be integrated with MEMS. Aqueous electrolytes, such as acids (e.g., H_2SO_4) and alkalis (e.g., KOH), are widely employed as standard electrolytes in supercapacitors mainly thanks to their high ionic conductivity (up to 1 S/cm) and low cost. However, they have the inherent disadvantage of a relatively low electrochemical stability window of ca. 1 V that harshly limits the amount of energy storage in the EDL to few watt hours per kilogram. Enhancing the voltage of the device is viable route to overcome this problem. Non-aqueous electrolyte mixtures such as propylene carbonate or acetonitrile, containing dissolved quaternary alkyl ammonium salts, are employed in many commercial supercapacitors, particularly those targeting higher energy applications [227]. Commercially available supercapacitors based on organic electrolytes easily

reach operating voltages up to 2.5 V but suffer of limitations associated with the operating temperature making these devices unsafe at 50-60°C. In this context the employment of room temperature ionic liquids (RTILs) as electrolytes may significantly increase the specific energy of the device, owing to the significant increase in their electrochemical stability window that can exceeds 5V. Moreover, RTILs are excellent ionic conductors, virtually non volatile and thermally stable up to 300° C, and are therefore considered the key toward the development of green, safe and high specific energy supercapacitors [37; 228]. However, the development of RTIL based supercapacitors is still in its infancy and further advance is needed to ensure their full exploitation. The challenge is in the choice of ionic liquids that feature wide electrochemical stability windows combined with high ionic conductivity, as well as in the design of electrode nanostructures capable of assuring proper wettability by the ionic liquid [229].

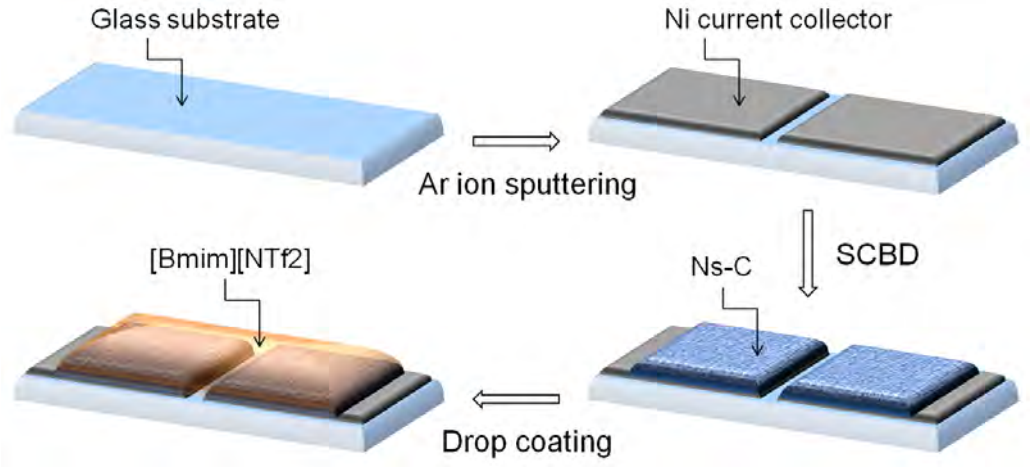

Figure A.5: Sketch of the fabrication process of the planar ns-C based supercapacitor. Electrodes have a thickness of 200 nm, an area of 0.2 cm^2 and are separated by a non conductive gap of 0.6 mm. [C_4MIM][NTf_2] is employed as electrolyte.

Besides the technological potential, ILs have been recently demonstrated to be unique and innovative probes for the structural characterization of porous electrode material [230–232]. Indeed, as room temperature molten salts, they are entirely composed by anions and cations that can directly interact with the electrode surface without the mediation of the solvent. This offers the advantage of a well identified ion size, which can be crucial not only in providing information about the electrode porosity but also in understanding the EDL charge storage mechanism in nanoporous materials. In this section we present and discuss the characterization of the electrochemical capacitive behavior of cluster assembled carbon thin films soaked in room temperature ionic liquids. We investigated the EDL capacitance of the interface between ns-C electrodes and four different RTILs ([C_4MIM][NTf_2], [C_2MIM][NTf_2], [C_{12}MIM][NTf_2] and [C_4MPyr][NTf_2]) featuring the same anion, which provides hydrophobic character, and different cations, so to disentangle the role of electrode material and the influence of ionic liquid nature from the interface properties. We found evidence of good impregnation of the ns-C nanoporous matrix by the different RTILs, suggesting that the ns-C has an open porosity easily accessible by the tested ionic liquids, and we measured an electrochemical stability window higher than 3V for all the RTILs employed. Furthermore, we observed

an increase in the interfacial EDL capacity moving from a RTIL featuring larger cation as the [C_{12}MIM] to RTILs featuring smaller cation as the [C_2MIM] and the [C_4MIM], suggesting that in the latter case the porosity of the ns-C is better exploited due to an optimized match between the size of the ns-C pores and the dimension of the electrolyte ions. [C_4MIM][NTf_2] provided the highest EDL capacity: ca. 75 F/g. These features, together with the intrinsic versatility of SCBD in producing patterned depositions on virtually any kind of substrate by using a stencil mask approach and its compatibility with standard planar microtechnology processes, inspired the fabrication of a thin film planar ns-C based supercapacitor.

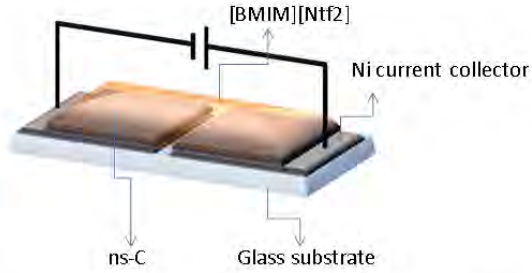

Electrode area	20 (5x4)	mm^2
ns-C thickness	200	nm
Separator gap	0.6	mm
Total weight (nsC+Ni)	7.5E-05	g
Voltage	3	V
Capacity	3.3E-05	F
ESR	1E04	Ohm
Power	2.3E-04	W
Energy	1.5E-04	J=W*s
Power density*	2986	W/Kg
Energy density*	0.5	W*h/Kg

*normalized by the total weight of the device (nsC+Ni)

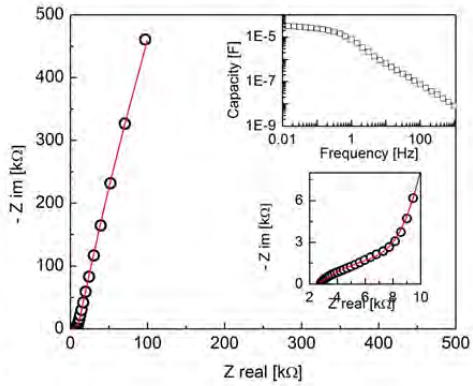

Figure A.6: Scheme of planar supercapacitor imbedded with [C_4MIM][NTf_2] and presentation of electrochemical performances

Bibliography

[1] Wilkes J.S. A short history of ionic liquids—from molten salts to neoteric solvents. *Green Chemistry*, 4:73–80, 2002. doi:10.1039/B110838G.

[2] Seddon K. R. Holbrey J. D. Ionic liquids. *Clean Products and Processes*, 1:223–236, 1999. doi:10.1007/s100980050036.

[3] Freemantle M. Basf's smart ionic liquid. *Chem. Eng. News*, 81(9), 2003. doi:10.1021/cen-v081n013.p009.

[4] Wasserсheid P. Welton T. *Ionic liquids in synthesis*. Wiley-VCH, Weinheim, 2003.

[5] Torimoto T. Tsuda T. Kuwabata S. New frontiers in materials science opened by ionic liquids. *Adv. Mater.*, 22:1196–1221, 2010. doi:10.1002/adma.200902184.

[6] Fischer L. Falta T. Koellensperger G. Stojanovic A. Kogelnig D. Galanski M. Krachler R Keppler B. K. and Hann S. Ionic liquids for extraction of metals and metal containing compounds from communal and industrial waste water. *Water Res.*, 45: 4601–4614, 2011. doi:10.1016/j.watres.2011.06.011.

[7] Zhang H. and Cui H. Synthesis and characterization of functionalized ionic liquid-stabilized metal (gold and platinum) nanoparticles and metal nanoparticle/carbon nanotube hybrids. *Langmuir*, 25:2604–2612, 2009. doi:10.1021/la803347h.

[8] Greaves T.L. and Drummond C.J. Ionic liquids as amphiphile self-assembly media. *Chem. Soc. Rev.*, 37:1709–1726, 2008. doi:10.1039/B801395K.

[9] Mu T. Li Z., Jia Z. Luan Y. Ionic liquids for synthesis of inorganic nanomaterials. *Current Opinion in Solid State and Materials Science*, 12:1–8, 2008. doi:10.1016/j.cossms.2009.01.002.

[10] Endres F. Ionic liquids: Solvents for the electrodeposition of metals and semiconductors. *Chem. Phys. Chem.*, 3:144–154, 2002. doi:10.1002/1439-7641(20020215)3:2<144::AID-CPHC144>3.0.CO;2-#.

[11] Welton T. Room-temperature ionic liquids. solvents for synthesis and catalysis. *Chem. Rev.*, 99:2071–2083, 1999. doi:10.1021/cr4004314.

[12] Sun N. Rodriguez H. Rahmana M. and Rogers R. D. Where are ionic liquid strategies most suited in the pursuit of chemicals and energy from lignocellulosic biomass? *Chem. Comm.*, 47:1405–1421, 2011. doi:10.1039/C0CC03990J.

[13] Canongia Lopes J. N. Costa Gomes M. F. and Padua A. A. H. Nonpolar, polar and associating solutes in ionic liquids. *J. Phys. Chem. B*, 110:16816–16818, 2006. doi:10.1021/jp063603r.

[14] Triolo A. Russina O. Bleif H.J. and Di Cola E. Nanoscale segregation in room temperature ionic liquids. *J. Phys. Chem. B*, 111:4641–4644, 2007. doi:10.1021/jp067705t.

[15] Triolo A Russina O. Fazio B. Triolo R. and Di Cola E. Morphology of 1-alkyl-3-methylimidazolium hexafluorophosphate room temperature ionic liquids. *Chem. Phys. Lett.*, 457:362–365, 2008. doi:10.1016/j.cplett.2008.04.027.

[16] Wakai C. Oleinkova A. How polar are ionic liquids? determination of the static dielectric constant of an imidazolium-based ionic liquid by microwave dielectric spectroscopy. *J. Phys. Chem. B*, 109:17028–17030, 2005. doi:10.1021/jp053946+.

[17] Nakamura K. Shikata T. Systematic dielectric and nmr study of the ionic liquid 1-alkyl-3-methyl imidazolium. *Chem. Phys. Chem.*, 11:285–294, 2010. doi:10.1002/cphc.200900642.

[18] Rivera A. Brodin A. Orientational and translational dynamics in room temperature ionic liquids. *J. Phys. Chem.*, 126:114503, 2007. doi:10.1063/1.2712184.

[19] Sangoro J. Iacob C. Electrical conductivity and translational diffusion in the 1-butyl-3-methylimidazolium tetrafluoroborate ionic liquid. *J. Phys. Chem.*, 128: 214509, 2008. doi:10.1063/1.2921796.

[20] Leys J. Wubbenhorst M. Temperature dependence of electrical conductivity of imidazolium ionic liquids. *J. Phys. Chem.*, 128:064509, 2008. doi:10.1063/1.2827462.

[21] Golley A. Vass A. Apparatus and method to measure dielectric properties of ionic liquids. *Rev. Sci. Instrum.*, 80:044703, 2009. doi:10.1063/1.3117352.

[22] Singh T. Kumar A. Static dielectric constant of room temperature ionic liquids: internal pressure and cohesive energy density approach. *J. Phys. Chem B*, 112(41): 044703, 2008. doi:10.1021/jp8059618.

[23] Kornyshev A.A. Double-layer in ionic liquids: paradigm change? *J. Phys. Chem.B*, 111(194):5545–5557, 2007. doi:10.1021/jp067857o.

[24] Galinski M. Lewandowski A. Ionic liquids as electrolytes. *Electrochimica Acta*, 51: 5567–5580, 2006. doi:10.1016/j.electacta.2006.03.016.

[25] Mermin N.D. Ashcroft N.W. *Solid State Physics*. Rinehart and Winston, Holt, 1976.

[26] Rice M.J. Strassler S. Toombs G.A. Superionic conductors: theory of the phase transition to the cation disordered state. *Phys. Rev. Lett.*, 32:113, 1974. doi:10.1103/PhysRevLett.32.596.

[27] Jong-Taek K. Kiung-Bum L. Fabrication of beta-alumina films as a thermoelectric material by thermal plasma processing. *Surf. Interface Anal.*, 35:658–661, 2003. doi:10.1002/sia.1586.

[28] Fuller R.G. Reilly M.H. Anion contribution to the electrical conductivity of alkali chlorides. *Phys. Rev. Lett.*, 19:113, 2003. doi:10.1103/PhysRevLett.19.113.

[29] Sato T. Masuda G. Takagi K. Electrochemical properties of novel ionic liquids for electric double layer capacitor applications. *Electrochimica Acta*, 49:113, 2004. doi:10.1016/j.electacta.2004.03.030.

[30] Ye C. Liu W. Chen Y and Yu L. Room-temperature ionic liquids: a novel versatile lubricant. *Chem. Commun.*, pages 2244–2245, 2001. doi:10.1039/B106935G.

[31] Bhushan B. Palacio M. Kinzig B. A review of ionic liquids for green molecular lubrication in nanotechnology. *J. Coll. and Inter. Sci.*, 317:275–287, 2008. doi:10.1007/s11249-010-9671-8.

[32] Jimenez A.E. Bermudez M.D. Iglesias P. Carrilon F.J. and Martinez-Nicolas G. 1-n-alkyl-3-methylimidazolium ionic liquids as neat lubricants and lubricant additives in steel-aluminum contacts. *Wear*, 260:766–782, 2006. doi:10.1016/j.wear.2005.04.016.

[33] Minami I. Kamimura H. and Mori S. Thermo-oxidative stability of ionic liquids as lubricating fluids. *J. Synthetic Lubrication*, 24:135–147, 2007. doi:10.1002/jsl.36.

[34] Conway B.E. *Electrochemical supercapacitors: scientific fundamentals and technological applications*. New York: Kluwer, Academic/Plenum, 1999.

[35] Kotz R. Carlen M. Principles and applications of electrochemical capacitors. *Electrochim Acta*, 45:2483–98, 2000. doi:10.1016/S0013-4686(00)00354-6.

[36] Simon P. Gogotsi Y. Materials for electrochemical capacitors. *Nat. Mat.*, 7:845–854, 2008. doi:10.1038/nmat2297.

[37] Burke A. R and d considerations for the performance and application of electrochemical capacitors. *Electrochim Acta*, 53:1083–1091, 2007. doi:10.1016/j.electacta.2007.01.011.

[38] Lazzari M. Soavi F. and Mastragostino M. Mesoporous carbon design for ionic liquid-based, double layer supercapacitor. *Fuel Cells*, 10:840–847, 2010. doi:10.1002/fuce.200900198.

[39] Helmholtz H. Ueber einige gesetze der vertheilung elektrischer strome in korperlichen leitern mit anwendung auf die elektrischen versuche. *Pogg.Ann. LXXXIX*, 211, 1853. doi:10.1002/andp.18531650603.

[40] Bolt G.H. Analysis of the validity of the gouy-chapman theory of the electric double layer. *Journal of Colloid Science*, 10:206–218, 1955. doi:10.1016/0095-8522(55)90027-1.

[41] Aliaga C. Santos C. S. Surface chemistry of room-temperature ionic liquids. *Phys. Chem. Chem. Phys.*, 9:3683–3700, 2007. doi:10.1039/B703574H.

[42] Zhang L.L. and Zhao X.S. Carbon-based materials as supercapacitor electrodes. *Chem. Soc. Rev.*, 38:2520–2531, 2009. doi:10.1039/B813846J.

[43] O'Regan B. and Gratzel M. A low-cost, high-efficiency solar cell based on dye-sensitized colloidal tio2 films. *Nature*, 353:737–739, 1991. doi:10.1038/353737a0.

[44] S. Aliaga C. Baldelli. Surface chemistry of room-temperature ionic liquids. *J. Phys. Chem. C*, 112:3064–3072, 2008. doi:10.1039/B703574H.

[45] Baldelli S. Bao J. Wu W. Pe S.-S. Sum frequency generation study on the orientation of room-temperature ionic liquid at the graphene–ionic liquid interface. *Chemical Physics Letters*, 516:171–173, 2011. doi:10.1016/j.cplett.2011.09.084.

[46] S. Baldelli. Interfacial structure of room-temperature ionic liquids at the solid−liquid interface as probed by sum frequency generation spectroscopy. *J.Phys.Chem.Lett.*, 4:244−252, 2013. doi:10.1021/jz301835j.

[47] Mezger M. Schroder H. Reichert H. Schramm S. Okasinski J. S. Schoder S. J. and Rohwerder. Layering of bmim-based ionic liquids at a charged sapphire interface. *Science*, 322:424–428, 2008. doi:10.1063/1.3212613.

[48] Mezger M. Ocko B.M. Reichert H. and Deutsch M. Surface layering and melting in an ionic liquid studied by resonant soft x-ray reflectivity. *Science*, 322:424–428, 2008. doi:10.1073/pnas.1211749110.

[49] Druschler M. Borisenko N. Wallauer J. Winter C. Huber B. Endres F. and Roling B. New insights into the interface between a single-crystalline metal electrode and an extremely pure ionic liquid: slow interfacial processes and the influence of temperature on interfacial dynamics. *Phys. Chem. Chem. Phys.*, 14:5090–5099, 2012. doi:10.1039/C2CP40288B.

[50] Ueno K. Kasuya M. Watanabe M. Mizukami M. and Kurihara K. Resonance shear measurement of nanoconfined ionic liquids. *Phys. Chem. Chem. Phys.*, 12:4066–4071, 2010. doi:10.1039/b923571j.

[51] Hayes R. Warr G. G. and Atkin R. At the interface: solvation and designing ionic liquids. *Phys. Chem. Chem. Phys.*, 12:1709–1723, 2010. doi:10.1039/B920393A.

[52] Cremer T. Stark M. Deyko A. Steinruck H.P. and Maier F. Liquid/solid interface of ultrathin ionic liquid films: [c1c1im][tf2n] and [c8c1im][tf2n] on au(111). *Langmuir*, 27:3662–3671, 2011. doi:10.1021/la105007c.

[53] Cremer T. Wibmer L. Krick Caldero S. Deyko A. Maier F. and Steinruck H.-P. Interfaces of ionic liquids and transition metal surfaces—adsorption, growth, and thermal reactions of ultrathin [c1c1im][tf2n] films on metallic and oxidised ni(111) surfaces. *Phys. Chem. Chem. Phys.*, 14:5153–5163, 2012. doi:10.1039/c2cp40278e.

[54] Deyko A. Cremer T. Rietzler F. Perkin S. Crowhurst L. Welton T. Steinruck H.-P. Maier F. Interfacial behavior of thin ionic liquid films on mica. *J. Phys. Chem. C*, 117:5101−5111, 2013. doi:10.1021/jp3115397.

[55] Zhang X. and Cai Y. Ultralow voltage electrowetting on a solidlike ionic-liquid dielectric layer. *Angew. Chem. Int. Ed.*, 52:2289–2292, 2013. doi:10.1002/anie.201207857.

[56] Gong X. Frankert S. Wang Y. Li L. Thickness-dependent molecular arrangement and topography of ultrathin ionic liquid films on a silica surface. *Chem. Commun.*, 49:7803, 2013. doi:10.1039/c3cc43392g.

[57] Atkin R. and Warr G. G. Structure in confined room-temperature ionic liquids. *J. Phys. Chem. C*, 111:5162–5168, 2007. doi:10.1021/jp067420g.

[58] Atkin R. Borisenko N. Druschler M. El Abedin S. Z. Endres F. Hayes R. Huber B. and Roling B. An in situ stm/afm and impedance spectroscopy study of the extremely pure 1-butyl-methylpyrrolidinium tris(pentafluoroethyl)trifluorophosphate/au(111) interface: potential dependent solvation layers and the herringbone reconstruction. *Phys. Chem. Chem. Phys.*, 13:6849–6857, 2011. doi:10.1039/c0cp02846k.

[59] Atkin R. Borisenko N. Druschler M. Endres F. Hayes R. Huber B. and Roling B. Structure and dynamics of the interfacial layer between ionic liquids and electrode materials. *Journal of molecular liquids*, XXX:XXX, 2013. doi:10.1016/j.molliq.2013.08.006.

[60] Yokota Y. Harada T. and Fukui K. Direct observation of layered structures at ionic liquid/solid interfaces by using frequency-modulation atomic force microscopy. *Chem. Commun.*, 46:8627–8629, 2010. doi:10.1039/C0CC02643C.

[61] Liu Y. Zhang Y. Wu G. and Hu J. Coexistence of liquid and solid phases of bmimpf6 ionic liquid on mica surfaces at room temperature. *J. Am. Chem. Soc.*, 128: 7456–7457, 2006. doi:10.1021/ja062685u.

[62] Bovio S. Podestà A. Lenardi C. Milani P. Evidence of extended solid-like layering in [bmim][ntf2] ionic liquid thin film at room temperature. *J. Phys. Chem. B*, 113: 6600, 2009. doi:10.1021/jp9022234.

[63] Bovio S. Podestà A. Milani P. Ballone P. Del Popolo M. G. Nanometric ionic liquid films on silica: a joint experimental and computational study. *J. Phys.: Condens. Matter*, 21:00000, 2009. doi:10.1088/0953-8984/21/42/424118.

[64] Bovio S. *Investigation of morphological and structural properties of ionic liquid thin layers on solid surfaces by Scanning Probe Microscopy*. Phd dissertation, Università degli Studi di Milano, 2011.

[65] Ballone P. Del Popolo M.G. Bovio S. Podesta A. Milani P. and Manini N. Nanoindentation of a room-temperature ionic liquid film on silica: a computational experiment. *Phys. Chem. Chem. Phys.*, 14:2475–2482, 2012. doi:10.1039/c2cp23459a.

[66] Anastas P. T. and Kirchhoff M. M. Origins, current status and future challenges of green chemistry. *Acc. Chem. Res.*, 35:686–694, 2002. doi:10.1021/ar010065m.

[67] Sheldon R. A. The e factor: fifteen years on. *Green Chem.*, 9:1273–1283, 2007. doi:10.1021/la400923d.

[68] Deetlefs M. and Seddon K. R. Assessing the greeness of some typical laboratory ionic liquids preparations. *Green Chem.*, 12:17–30, 2010. doi:10.1039/B915049H.

[69] Zhang Y. Bakshi B. R. Demessie E. S. Life cycle assessment of an ionic liquid versus traditional solvents and their applications. *Environ. Sci. Technol.*, 42:1724–1730, 2008. doi:10.1039/B713736M.

[70] Latala A. Stepnowski P. Nedzi M. Mrozik W. Marine toxicity assessment of imidazolium ionic liquids: acute effects on the baltic algae ooctis submarina and cyclotella meneghiniana. *Aquat. Toxicol.*, 73:91, 2005. doi:10.1016/j.aquatox.2005.03.008.

[71] Jastorff B. Stormann R. Ranke J. Molter K. Stock F. Oberheitmann B. Hoffmann W. Hoffmann J. and Filser J. How hazardous are ionic liquids? structure–activity relationships and biological testing as important elements for sustainability evaluation. *Green Chem.*, 5:136–142, 2003. doi:10.1039/B211971D.

[72] Zhao D. Liao Y. Zhang D. Toxicity of ionic liquids. *Clean*, 35:42–48, 2007. doi:10.1002/clen.200600015.

[73] Nealson K. Platt T. Hastings J.W. The cellular control of the synthesis and activity of the bacterial luminescent system. *Journal of Bacteriology*, 104:313–322, 1970.

[74] J. Stolte S. Matzke M. Arning J. Boschen A. Pitner W.-R. Welz-Biermann U. Jastorff B. Ranke. Effects of different head groups and functionalized side chains on the aquatic toxicity of ionic liquids. *Green Chem.*, 9:1170–1179, 2007. doi:10.1039/B711119C.

[75] Ranke J. Molter K. Stock F. Bottin-Weber U. Poczobutt J. Hoffmann J. Ondruschka B. Filser J. Jastorff B. Biological effects of imidazolium ionic liquids with varying chain lengths in acute vibrio fischeri and wst-1 cell viability assays. *Ecotoxicol. Environ. Saf.*, 13:396−404, 2004. doi:10.1016/S0147-6513(03)00105-2.

[76] Romero A. Santos A. Tojob J. Rodrıguez A. Toxicity and biodegradability of imidazolium ionic liquids. *Journal of Hazardous Materials*, 151:268–273, 2008. doi:10.1016/j.jhazmat.2007.10.079.

[77] Matzke M. Stolte S. Thiele K. Juffernholz T. Arning J. Ranke J. Welz-Biermann U. Jastorff B. The influence of anion species on the toxicity of 1-alkyl-3-methylimidazolium ionic liquids observed in an (eco)toxicological test battery. *Green Chem.*, 9:1198–1207, 2007. doi:10.1039/B705795D.

[78] B. Ranke J. Stolte S. Stormann R. Arning J. Jastorff. Design of sustainable chemical products: The example of ionic liquids. *Chem. Rev.*, 107:2183−2206, 2007. doi:10.1021/cr050942s.

[79] Stolte S. Arning J. Bottin-Weber U. Muller A. Pitner W.-R. Welz-Biermann U. Jastorff B. Ranke J. Effects of different head groups and functionalised side chains on the cytotoxicity of ionic liquids. *Green Chem.*, 9:760–767, 2007. doi:10.1039/B615326G.

[80] Bernot R.J. Brueseke M.A. Evans-White M.A. Lamberti G.A. Acute and chronic toxicity of imidazolium-based ionic liquids on daphnia magna. *Environ. Toxicol. Chem.*, 24:87–92, 2005. doi:10.1897/03-635.1.

[81] Couling D.J. Bernot R.J. Docherty K.M. Dixon J.K. Maginn E.J. Assessing the factors responsible for ionic liquid toxicity to aquatic organisms via quantitative structure-property relationship modeling. *Green Chem.*, 8:82–90, 2006. doi:10.1039/B511333D.

[82] Thuy Pham T. P. Cho C. W. Yun Y. S. Environmental fate and toxicity of ionic liquids: A review. *Water Res.*, 44:352–372, 2010. doi:10.1016/j.watres.2009.09.030.

[83] Ranke J. Muller A. Bottin-Weber U. Stock F. Stolte S. Arning J. Stormann R. Jastorff B. Lipophilicity parameters for ionic liquid cations and their correlation to in vitro cytotoxicity. *Ecotox. Environ. Saf.*, 67:430–438, 2007. doi:10.1016/j.ecoenv.2006.08.008.

[84] Stolte S. Arning J. Bottin-Weber U. Matzke M. Stock F. Thiele K. Uerdingen M. Welz-Biermann U. Jastorff B. Ranke J. Anion effects on the cytotoxicity of ionic liquids. *Green Chem.*, 8:621−629, 2006. doi:10.1039/B602161A.

[85] Kumar R.A. Papaiconomou N. Lee J.-M. Salminen J. Clark D.S. Prausnitz J.M. In vitro cytotoxicities of ionic liquids: effect of cation rings, functional groups, and anions. *Environ. Toxicol.*, 24:388–395, 2009. doi:10.1002/tox.20443.

[86] Garcia-Lorenzo A. Tojo E. Tojo J. Teijeira M. Rodriguez-Berrocal F.J. Gonzalez M.P. Martinez-Zorzano V.S. Cytotoxicity of selected imidazolium-derived ionic liquids in the human caco-2 cell line. sub-structural toxicological interpretation through a qsar study. *Green Chem.*, 10:508–516, 2008. doi:10.1039/B718860A.

[87] Stepnowski P. Skadanowski A.C. Ludwiczak A. Laczynska E. Evaluating the cytotoxicity of ionic liquids using human cell line hela. *Hum. Exp. Toxicol*, 23:513–517, 2004. doi:10.1191/0960327104ht480oa.

[88] Petkovic M. Seddon K. R. Rebelo L. P. N. Pereira C. S. Ionic liquids: A pathway to environmental acceptability. *Chem. Soc. Rev.*, 40:1383−1403, 2011. doi:10.1039/C004968A.

[89] Yang Z. H. Zeng R. Wang Y. Li X. K. Lv Z. S. Lai B. Yang S. Q. Liao J. G. Tolerance of immobilized yeast cells in imidazolium-based ionic liquids. *Food Technol. Biotechnol.*, 47:62−66, 2009.

[90] Cho C. W. Thuy Pham T. P. Jeon Y. C. Vijayaraghavan K. Choe W. S. Yun Y. S. Toxicity of imidazolium salt with anion bromide to a phytoplankton selenastrum capricornutum: Effect of alkylchain length. *Chemosphere*, 69:1003−1007, 2007. doi:10.1016/j.chemosphere.2007.06.023.

[91] Alvarez-Guerra M. Irabien A. Design of ionic liquids: An ecotoxicity (vibrio f ischeri) discrimination approach. *Green Chem.*, 13:1507−1516, 2011. doi:10.1039/C0GC00921K.

[92] Ranke J. Cox M. Muller A. Schmidt C. Beyersmann D. Sorption, cellular distribution, and cytotoxicity of imidazolium ionic liquids in mammalian cells - influence of lipophilicity. *Toxicol. Environ. Chem.*, 88:273−285, 2006. doi:10.1080/02772240600589505.

[93] Cromie S. R. T. Del Popolo M. G. Ballone P. Interaction of room temperature ionic liquid solutions with a cholesterol bilayer. *J. Phys. Chem. B*, 113:11642−11648, 2009. doi:10.1021/jp904060y.

[94] Bingham R. J. Ballone P. Computational study of roomtemperature ionic liquids interacting with a popc phospholipid bilayer. *J. Phys. Chem. B*, 116:11205−11216, 2012. doi:10.1021/jp306126q.

[95] Evans K. O. Room-temperature ionic liquid cations act as shortchain surfactants and disintegrate a phospholipid bilayer. *Colloids Surf.*, 274:11−17, 2006. doi:10.1016/j.colsurfa.2005.10.007.

[96] Evans K. O. Supported phospholipid bilayer interaction with components found in typical room-temperature ionic liquids - a qcm-d and afm study. *Int. J. Mol. Sci.*, 9:498−511, 2008. doi:10.3390/ijms9040498.

[97] Evans K. O. Supported phospholipid membrane interactions with 1-butyl-3-methylimidazolium chloride. *J. Phys. Chem. B*, 112:8558−8562, 2008. doi:10.1021/jp7116592.

[98] Jeong S. Ha S. H. Han S.-H. Lim M.-C. Kim S. M. Kim Y.-R. Koo Y.-M. So J.-S. Jeon T.-J. Elucidation of molecular interactions between lipid membranes and ionic liquids using model cell membranes. *Soft Matter*, 8:5501−5506, 2012. doi:10.1039/C2SM25223F.

[99] Mammoto T. Ingber D.E. Mechanical control of tissue and organ development. *Development*, 137:1407–1420, 2010. doi:10.1242/dev.024166.

[100] Schiller H.B. Fassler R. Mechanosensitivity and compositional dynamics of cell–matrix adhesions. *EMBO reports*, 14(6):509, 2013. doi:10.1038/embor.2013.49.

[101] Batchelder E. Hollopeter G. Campillo C. Mezanges X. Jorgensen E.M. Nassoy P. Sens P. and Plastino J. Membrane tension regulates motility by controlling lamellipodium organization. *PNAS*, 108(28):11429–11434, 2011. doi:10.1073/pnas.1010481108.

[102] Gauthier N.C. Masters T.A. and Sheetz M.P. Mechanical feedback between membrane tension and dynamics. *Trends in Cell Biology*, 22(10):527, 2012. doi:10.1016/j.tcb.2012.07.005.

[103] Diz-Munoz A. Fletcher D.A. and Weiner O.D. Use the force: membrane tension as an organizer of cell shape and motility. *Trends in Cell Biology*, 23(2):47, 2013. doi:10.1016/j.tcb.2012.09.006.

[104] Lafaurie-Janvore J. Maiuri P. Wang I. Pinot M. Manneville J-P. Betz T. Balland M. Piel M. Escrt-iii assembly and cytokinetic abscission are induced by tension release in the intercellular bridge. *Science*, 339(6127):1625–1629, 2013. doi:10.1126/science.1233866.

[105] Discher D. E. Janmey P. Wang Y. Tissue cells feel and respond to the stiffness of their substrate. *Science*, 310:1139–1143, 2005. doi:10.1126/science.1116995.

[106] Tee S. Fu J. Chen C. Janmey P. Cell shape and substrate rigidity both regulate cell stiffness. *Biophysical Journal*, 100:25–27, 2010. doi:10.1016/j.bpj.2010.12.3744.

[107] Lamour G. Eftekhari-Bafrooei A. Borguet E. Souès S. Hamraoui A. Neuronal adhesion and differentiation driven by nanoscale surface free-energy gradients. *Biomaterials*, 31:3762–3771, 2010. doi:10.1016/j.biomaterials.2010.01.099.

[108] Tedeschi G. Maffioli E. Forti S. Negri A. Lenardi C. Milani P. Nanostructured titanium oxide as substrate for pc12 cell differentiation. *FEBS J.*, 278:428, 2011.

[109] Cross S.E. Jin Y. Rao J. Gimzewski J.K. Nanomechanical analysis of cells from cancer patients. *Nature Nanotechnology*, 2:780–783, 2007. doi:10.1038/nnano.2007.388.

[110] Plodinec M. Loparic M. Monnier C. A. Obermann E. C. Zanetti-Dallenbach R. Oertle P. Hyotola J.T. Aebi U. Bentires-Alj M. R. Lim Y.H. Schoenenberger C. The nanomechanical signature of breast cancer. *Nature Nanotechnology*, 7:757–765, 2012. doi:10.1038/nnano.2012.167.

[111] Darling E. M. Zauscher S. Block J. A. Guilak F. A thin layer model for viscoelastic, stress-relaxation testing of cells using atomic force microscopy: do cell properties reflect metastatic potential? *Biophysical Journal*, 92:1784–1791, 2007. doi:10.1529/biophysj.106.083097.

[112] Houk A.R. Jilkine A. Mejean C.O. Boltyanskiy R. Dufresne E.R. Angenent S.B. Altschuler S.J. Wu L.F. andnWeiner O.D. Membrane tension maintains cell polarity by confining signals to the leading edge during neutrophil migration. *Cell*, 148:175–188, 2012. doi:10.1016/j.cell.2011.10.050.

[113] Sinha B. Koster D. Ruez R. Gonnord P. Bastiani M. Nassoy P. Cells respond to mechanical stress by rapid disasembly of caveolae. *Cell*, 144:402–413, 2011. doi:10.1016/j.cell.2010.12.031.

[114] Lieber A.D. Yehudai-Resheff S. Barnhart E.L. Theriot J.A. Keren K. Membrane tension in rapidly moving cells is determined by cytoskeletal forces. *Current Biology*, 23:1409–1417, 2013. doi:10.1016/j.cub.2013.05.063.

[115] Fletcher D.A. Mullin R.D. Cell mechanics and the cytoskeleton. *Nature*, 463:485, 2010. doi:10.1038/nature08908.

[116] Cheeseman I.M. and Desai A. Molecular architecture of the kinetochore–microtubule interface. *Molecular cell biology*, 9:33, 2008. doi:10.1038/nrm2310.

[117] Radmacher M. Studying the mechanics of cellular processes by atomic force microscopy. *Nano/Micro Biotechnology*, 83:347–372, 2007. doi:10.1016/S0091-679X(07)83015-9.

[118] Ikai A. A review on: Atomic force microscopy applied to nano-mechanics of the cell. *Nano/Micro Biotechnology*, 119:47–61, 2010. doi:10.1007/10_2008_41.

[119] Muller D. J. and Dufrene Y. F. Force nanoscopy of living cells. *Current Biology*, 21: 347–372, 2010. doi:10.1016/j.cub.2011.01.046.

[120] Muller D. J. and Dufrene Y. F. Atomic force microscopy: a nanoscopic window on the cell surface. *Trends in Cell Biology*, 21, 2011. doi:10.1016/j.tcb.2011.04.008.

[121] Hassan E-A. Heinz W.F. Antonik M.D. D'Costa N.P. Nageswaran S. Schoenenberger C-A. and Hoh J.H. Relative microelastic mapping of living cells by atomic force microscopy. *Biophysical Journal*, 74:1564–1578, 1998. doi:10.6122/CJP.

[122] Radmacher M. Fritz M. Kacher C.M. Cleveland J.P. and Hansma P.K. Measuring the viscoelastic properties of human platelets with the atomic force microscope. *Biophysical Journal*, 70:556–567, 1996. doi:10.1016/S0006-3495(98)77868-3.

[123] Rotsch C. Radmacher M. Drug-induced changes of cytoskeletal structure and mechanics in fibroblasts: An atomic force microscopy study. *Biophysical Journal*, 78: 520–535, 2000. doi:10.1016/S0006-3495(00)76614-8.

[124] Nelson A. Electrochemistry of mercury supported phospholipid monolayers and bilayers. *Curr. Opin. Colloid Interface Sci.*, 15:455−466, 2009. doi:10.1016/j.cocis.2010.07.004.

[125] Gomila G. Toset J. Fumagalli L. Nanoscale capacitance microscopy on thin dielectric films. *J. Appl. Phys.*, 104:024315, 2008. doi:10.1063/1.2957069.

[126] Coldrick Z. Steenson P. Millner P. Davies M. Nelson A. Phospholipid monolayer coated microfabricated electrodes to model the interaction of molecules with biomembranes. *Electrochim. Acta*, 54:4954−4962, 2009. doi:10.1016/j.electacta.2009.02.095.

[127] Coldrick Z. Penezic A. Gasparovic B. Steenson P. Merrifield J. Nelson A. High throughput systems for screening biomembrane interactions on fabricated mercury film electrodes. *J. Appl. Electrochem.*, 41:939−949, 2011. doi:10.1007/s10800-011-0319-7.

[128] Zhang S. Nelson A. Coldrick Z. Chen R. The effects of substituent grafting on the interaction of ph-responsive polymers with phospholipid monolayers. *Langmuir*, 27:8530−8539, 2011. doi:10.1021/la105125d.

[129] Vakurov A. Brydson R. Nelson A. Electrochemical modelling of the silica nanoparticle−biomembrane interaction. *Langmuir*, 28:1246−1255, 2012. doi:10.1021/la203568n.

[130] Scheuring S. Muller D.J. Ringler P. Heymann J.B. and Engel A. Imaging streptavidin 2d crystals on biotinylated lipid monolayers at high resolution with the atomic force microscope. *Journal of Microscopy*, 193:28–35, 1999. doi:10.1046/j.1365-2818.1999.00434.x.

[131] Richter R.P. and Brisson A.R. Following the formation of supported lipid bilayers on mica: A study combining afm, qcm-d, and ellipsometry. *Biophysical Journal*, 88: 3422–3433, 2008. doi:10.1529/biophysj.104.053728.

[132] Reviakine I. and Brisson A.R. Formation of supported phospholipid bilayers from unilamellar vesicles investigated by atomic force microscopy. *Langmuir*, 16:1806–1815, 2000. doi:10.1021/la9903043.

[133] Indrieri M. Podesta A. Suardi M. Ranucci E. Ferruti P. Milani P. Quantitative investigation by atomic force microscopy of supported phospholipid layers and nanostructures on cholesterol-functionalized glass surfaces. *Langmuir*, 24:7830–7841, 2008. doi:10.1021/la703725b.

[134] Cailleau R. Breast tumor cell lines from pleural effusions. *J Natl Cancer Inst*, 53: 661–674, 1974. doi:10.1093/jnci/53.3.661.

[135] Cailleau R. Long-term human breast carcinoma cell lines of metastatic origin: preliminary characterization. *In Vitro*, 14:911–915, 1978. doi:10.1007/BF02616120.

[136] Binnig G. Rohrer H. Gerber C. and Weibel E. Surface studies by scanning tunneling microscopy. *Phys. Rev. Lett.*, 49:57, 1982. doi:10.1103/PhysRevLett.49.57.

[137] Binning G. Quate C. F. Gerber C. Atomic force microscope. *Phys. Rev. Lett.*, 56:930, 1986. doi:10.1103/PhysRevLett.56.930.

[138] Jarvis M.R. Perez R. Payne M.C. Can atomic force microscopy achieve atomic resolution in contact mode? *PHYSICAL REVIEW LETTERS*, 86, 2001. doi:10.1103/PhysRevLett.86.1287.

[139] San Paulo A. and Garcia R. Tip-surface forces, amplitude, and energy dissipation in amplitude-modulation tapping mode force microscopy. *PHYSICAL REVIEW B*, 64:193411, 2001. doi:10.1103/PhysRevB.64.193411.

[140] San Paulo A. and Garcia R. Unifying theory of tapping-mode atomic-force microscopy. *PHYSICAL REVIEW B*, 66:041406R, 2002. doi:10.1103/PhysRevB.66.041406.

[141] Kappl M. Butt H.-J., Cappella B. Force measurements with the atomic force microscope: Technique, interpretation and applications. *Surface Science Reports*, 59: 1–152, 2005. doi:10.1016/j.surfrep.2005.08.003.

[142] Burnham N. A. Chen X. Hodges C.S. Matei G.A. Thoreson E.J. Roberts C.J. Davies M.C. and Tendler S.J.B. Comparison of calibration methods for atomic-force microscopy cantilevers. *Nanotechnology*, 14:1–6, 2003. doi:10.1088/0957-4484/14/1/301.

[143] Hutter J. Bechhoefer J. Calibration of atomic force microscope tips. *Review of Scientic Instruments*, 64:7, 1993. doi:10.1063/1.1143970.

[144] H. J. Butt and Jaschke M. Calculation of thermal noise in atomic force microscopy. *Nanotechnology*, 6:1–7, 1995. doi:10.1088/0957-4484/6/1/001.

[145] Sader J.E. Chon J.W.M. and Mulvaney P. Calibration of rectangular atomic force microscope cantilevers. *Review of Scientic Instruments*, 70:3967, 1999. doi:10.1063/1.4757398.

[146] van der Werf K.O. Putman C.A.J. de Grooth B.G. and Greve J. Adhesion force imaging in air and liquid by adhesion mode atomic force microscopy. *Appl. Phys. Lett.*, 65:2159–2165, 1994. doi:10.1063/1.112106.

[147] Radmacher M. Cleveland J. P. Fritz M. Hansma H. G. and Hansma P. K. Tapping mode atomic force microscopy in liquids. *Biophysical Journal*, 66:2159–2165, 1994. doi:10.1063/1.111795.

[148] Sababi M. Kettle J. Rautkoski H. Claesson P.M. and Thormann E. Structural and nanomechanical properties of paperboard coatings studied by peak force tapping atomic force microscopy. *ACS Appl. Mater. Interfaces*, 4:5534−5541, 2012. doi:10.1021/am301439k.

[149] Alsteens D. Dupres V. Yunus S. Latge J-P.Heinisch J.J: and Dufrene Y.F. High-resolution imaging of chemical and biological sites on living cells using peak force tapping atomic force microscopy. *Langmuir*, 28:16738−16744, 2012. doi:10.1021/la303891j.

[150] Walczyk W. Schon P.M. and Schonherr H. The effect of peakforce tapping mode afm imaging on the apparent shape of surface nanobubbles. *J. Phys.: Condens. Matte3*, 25:184005, 2013. doi:10.1088/0953-8984/25/18/184005.

[151] Morandat S. Azouzi S. Beauvais E. Mastouri A. El Kirat K. Atomic force microscopy of model lipid membranes. *Anal Bioanal Chem*, 10:117, 2012. doi:10.1007/s00216-012-6383-y.

[152] Das C. Sheikh K.H. Olmsted P.D. and Connell S.D. Nanoscale mechanical probing of supported lipid bilayers with atomic force microscopy. *PHYSICAL REVIEW E*, 82:041920, 2010. doi:10.1103/PhysRevE.82.041920.

[153] Alessandrini A. Facci P. Nanoscale mechanical properties of lipid bilayers and their relevance in biomembrane organization and function. *Micron*, 43:1212–1223, 2012. doi:10.1016/j.micron.2012.03.013.

[154] Leonenko Z. V. Finot E. Ma H. Dahms T. E. S. and Cramb D. T. Investigation of temperature-induced phase transitions in dopc and dppc phospholipid bilayers using temperature controlled scanning force microscopy. *Biophysical Journal Volume*, 86:3783–3793, 2004. doi:10.1529/biophysj.103.036681.

[155] Garcia-Manyes S. Oncins G. Sanz F. Nanomechanics of lipid bilayers by force spectroscopy with afm: A perspective. *Biochimica et Biophysica Acta*, 1798:741–749, 2010. doi:10.1016/j.bbamem.2009.12.019.

[156] G.U. Lee J. Schneider, W. Barger. Nanometer scale surface properties of supported lipid bilayers measured with hydrophobic and hydrophilic atomic force microscope probes. *Langmu03*, 19:1899–1907, 2003. doi:10.1021/la026382z.

[157] Nagle J.F. Tristram-Nagle S. Structure of lipid bilayers. *Biochimica et Biophysica Acta*, 1469:159–195, 2000. doi:10.1.1.65.6945.

[158] Puricelli Luca. Studio delle proprieta meccaniche di singole cellule in risposta a stimoli esterni ed alterazioni del terreno di coltura mediante microscopia a forza atomica. master thesis, Università degli Studi di Milano, 2013.

[159] Indrieri M. Podesta A. Bongiorno G. Marchesi D. Milani P. Adhesivefree colloidal probes for nanoscale force measurements: Production and characterization. *Review of Scientific Instruments*, 82:023708, 2011. doi:10.1063/1.3553499.

[160] Johnson K.L. *Contact Mechanics*. Cambridge University Press, 1985.

[161] Dimitriadis E.K. Horkay F. Maresca J. Kachar B. Chadwick R. S. Determination of elastic moduli of thin layers of soft materials using the atomic force microscope. *Biophysical Journal*, 82:2798–2810, 2002. doi:10.1016/S0006-3495(02)75620-8.

[162] Kasas S. Wang X. Hirling H. Marsault R. Huni B. Yersin A. Regazzi R. Grenningloh G. Riederer B. Forro L. Dietler G. Catsicas S. Superficial and deep changes of cellular mechanical properties following cytoskeleton disassembly. *Cell Motility*

and the Cytoskeleton, 62:124–132, 2005. doi:10.1002/cm.20086.

[163] Cassina V. *Characterization of electrical properties of nanostructured interfaces by advanced atomic force microscopy*. Phd dissertation, Università degli Studi di Milano, 2006.

[164] Sorokina K. and Tolstikhina A.L. Atomic force microscopy modified for studying electric properties of thin films and crystals. review. *Crystallography Reports*, 49: 541, 2003. doi:10.1134/1.1756648.

[165] Jacobs H. Knapp H. and Stemmer A. Practical aspects of kelvin probe force microscopy. *Rev Sci.Instrum*, 70:1756, 1999. doi:10.1063/1.1149664.

[166] Takahashi T. and Ono S. Tip-to-sample distance dependence of an electrostatic force in kfm measurements. *Ultramicroscopy*, 100:287, 2004. doi:10.1016/j.ultramic.2004.01.017.

[167] Glatzel T. Sadewasser S. and Lux-Steiner M. Amplitude or frequency modulation-detection in kelvin probe force microscopy. *Appl. Surf. Sci.*, 210:84, 2003. doi:10.1016/S0169-4332(02)01484-8.

[168] Gramse G. Casuso I. Toset J. Quantitative dielectric constant measurement of thin films by dc electrostatic force microscopy. *Nanotechnology*, 20:395702, 2009. doi:10.1088/0957-4484/20/39/395702.

[169] O'Shea S. Atta R. Murrell M. and Wellland M. Conducting atomic force microscopy study of silicon dioxide breakdown. *J. Vac. Sci Technol.B*, 13:1945, 1995. doi:10.1116/1.588113.

[170] Xu D. Watt G. Harb J.N. and Davis R. Electrical conductivity of ferritin proteins by conductive afm. *Nano Let*, 5:571–577, 2005. doi:10.1021/nl048218x.

[171] Williams C. Two-dimensional dopant profiling by scanning capacitance microscopy. *Ann. Rev. Mater. Sci.*, 2:471, 1999. doi:10.1146/annurev.matsci.29.1.471.

[172] Barrett R. and Quate F.C. Charge storage in a nitride-oxide-silicon medium by scanning capacitance microscopy. *J. Appl. Phys.*, 70:2725, 1991. doi:10.1063/1.349388.

[173] Pingree L. and Hersam M. Bridge-enhanced nanoscale impedance microscopy. *Appl.Phys.Lett.*, 87:73509, 2005. doi:10.1063/1.2137874.

[174] Fumagalli L. Ferrari G. Sampietro M. Dielectric-constant measurement of thin insulating films at low frequency by nanoscale capacitance microscopy. *Appl. Phys.Lett.*, 91:243110, 2007. doi:10.1063/1.2821119.

[175] Fumagalli L. Ferrari G. Sampietro M. Quantitative nanoscale dielectric microscopy of single-layer supported biomembranes. *Nano Lett.*, 9:465503, 2009. doi:10.1021/nl803851u.

[176] Cassina V. Gerosa L. Podesta A. Ferrari G. Sampietro M. and Milani P. Nanoscale electrical properties of cluster-assembled palladium oxide thin films. *Phys. Rev. B*, 79:115422, 2009. doi:10.1103/PhysRevB.79.115422.

[177] Ferrari G. and Sampietro M. Wide bandwidth transimpedance amplifier for extremely high sensitivity continuous measurements. *Rev. Sci. Instrum.*, 78:094703, 2007. doi:10.1063/1.2778626.

[178] Fumagalli L. *Instrumentation for wide-bandwidth electrical characterization at the nanoscale using Atomic Force Microscopy*. Phd dissertation, Politecnico di Milano, 2006.

[179] Fumagalli L. Gomila G. Casuso I. Nondestructive thickness measurement of biological layers at the nanoscale by simultaneous topography and capacitance imaging. *Appl. Phys. Lett.*, 91:063111, 2007. doi:10.1063/1.2767979.

[180] Fumagalli L. Ferrari G. Sampietro M. Nanoscale capacitance imaging with attofarad resolution using ac current sensing atomic force microscopy. *Nanotechnology*, 17:4581–4587, 2006. doi:10.1088/0957-4484/17/18/009.

[181] Lybanon M. A better least-squares method when both variables have uncertainties. *Am. J. Phys.*, 84:22–26, 1984. doi:10.1119/1.13822.

[182] Rieutord F Law B M. Electrostatic forces in atomic force microscopy. *Phys. Rev. B*, 66:035402, 2002. doi:10.1103/PhysRevB.66.035402.

[183] Kumar B. Bonvallet C.J. Crittenden S.R. Dielectric constants by multifrequency non-contact atomic force microscopy. *Nanotechnology*, 23:025707, 2012. doi:10.1088/0957-4484/23/2/025707.

[184] Ringstad L. Protopapa E. Lindholm-Sethson B. Schmidtchen A. Nelson A. Malmsten M. An electrochemical study into the interaction between complement-derived peptides and dopc mono- and bilayers. *Langmuir*, 24:208−216, 2008. doi:10.1021/la702538k.

[185] Cohen-Atiya M. Nelson A. Mandler D. Characterization of nalkanethiol self-assembled monolayers on mercury by impedance spectroscopy and potentiometric measurements. *J. Electroanal. Chem.*, 593:227−240, 2006. doi:10.1016/j.jelechem.2006.04.018.

[186] Whitehouse C. O'Flanagan R. Lindholm-Sethson B. Movaghar B. Nelson A. Application of electrochemical impedance spectroscopy to the study of dioleoyl phosphatidylcholine monolayers on mercury. *Langmuir*, 20:136−144, 2004. doi:10.1021/la035259k.

[187] Whitehouse C. Gidalevitz D. Cahuzac M. Koeppe R. E. Nelson A. Interaction of gramicidin derivatives with phospholipid monolayers. *Langmuir*, 20:9291−9298, 2004. doi:10.1021/la048797l.

[188] Macdonald J. R. New model for nearly constant dielectric loss in conductive systems: Temperature and concentration dependencies. *J. Chem. Phys.*, 116: 3401−3409, 2002. doi:10.1063/1.1434953.

[189] Dyson P.J. McIndoe J.S. and Zhao D. Direct analysis of catalysts immobilised in ionic liquids using electrospray ionisation ion trap mass spectrometry. *CHEM. COMMUN.*, 11:508–509, 2003. doi:10.1039/B211669C.

[190] Alfassi Z. B. Huie R. E. Milman B. L. Neta P. Electrospray ionization mass spectrometry of ionic liquids and determination of their solubility in water. *Anal. and Bioanal. Chem.*, 2003. doi:10.1007/s00216-003-2033-8.

[191] Kaisei K. Kobayashi K. Matsushige K. Yamada H. Fabrication of ionic liquid thin film b ynano-inkjet printing method using atomic force microscope cantilever tip. *Ultramicroscopy*, 12:733–736, 2010. doi:10.1016/j.ultramic.2010.02.041.

[192] Iacob C. Sangoro J.R. Papadopoulos P. Schubert T. Naumov S. Valiullin R. Karger J. and Kremer F. Charge transport and diffusion of ionic liquids in nanoporous silica membranes. *Phys. Chem. Chem. Phys.*, 12:13798–13803, 2008. doi:10.1039/c004546b.

[193] Roling B. Dreuschler M. and Huber B. Slow and fast capacitive process taking place at the ionic liquid/electrode interface. *Faraday Discuss.*, 154:303–311, 2012. doi:10.1039/C1FD00088H.

[194] Senapati S. Chandra A. Molecular dynamics simulations of simple dipolar liquids in spherical cavity: Effects of confinement on structural, dielectric, and dynamical properties. *JOURNAL OF CHEMICAL PHYSICS*, 11:1223, 1999. doi:10.1063/1.479307.

[195] Fedorov M.V. Kornyshev A.A. Ionic liquid near a charged wall: Structure and

capacitance of electrical double layer. *J. Phys. Chem.B*, 112:11868–11872, 2008. doi:10.1021/jp803440q.

[196] Kisza A. The capacitance of the diffuse layer of electric double layer of electrodes in molten salts. *Electrochimica Acta*, 51:2315–2321, 2006. doi:10.1016/j.electacta.2005.03.093.

[197] Weingaertner H. Knocks A. Schrader W. Kaatze U. Dielectric spectroscopy of the room temperature molten salt ethylammonium nitrate. *J. Phys. Chem.A*, 105:8646, 2001. doi:10.1021/jp0114586.

[198] Galluzzi M. Zhang S. Mohamadi S. Vakurov A. Podesta A. and Nelson A. Interaction of imidazolium-based room-temperature ionic liquids with dopc phospholipid monolayers: Electrochemical study. *Langmuir*, 29:6573−6581, 2013. doi:10.1021/la400923d.

[199] Ventura S. P. M. Marques C. S. Rosatella A. A. Afonso C. A. M. Goncalves F. Coutinho J. A. P. Toxicity assessment of various ionic liquid families towards vibrio fischeri marine bacteria. *Ecotoxicol. Environ. Saf.*, 76:162−168, 2012. doi:10.1016/j.ecoenv.2011.10.006.

[200] Ropel L. Belveze L. S. Aki S. N. V. K. Stadtherr M. A. Brennecke J. F. Octanol-water partition coefficients of imidazoliumbased ionic liquids. *Green Chem.*, 7:83−90, 2005. doi:10.1039/B410891D.

[201] Costa R. Pereira C. M. Silva F. Double layer in room temperature ionic liquids: Influence of temperature and ionic size on the differential capacitance and electrocapillary curves. *Phys. Chem. Chem. Phys.*, 12:11125−11132, 2010. doi:10.1039/c003920a.

[202] Alam M. T. Islam Md M Okajima T. Ohsaka T. Ionic liquid structure dependent electrical double layer at the mercury interface. *J. Phys. Chem. C*, 112:2601−2606, 2008. doi:10.1021/jp7098043.

[203] Lu C. Y. D. Yu J. W. Dielectric response of a dilute oil-in-water emulsion solution. *Chin. J. Phys.*, 40:60–68, 2002. doi:10.6122/CJP.

[204] Kuang W. Nelson S. O. Low-frequency dielectric dispersion from ion permeability of membranes. *J. Colloid Interface Sci.*, 193:242–249, 1997. doi:10.1006/jcis.1997.5073.

[205] Martinsen O. G. Grimnes S. Karlsen J. Low frequency dielectric dispersion of microporous membranes in electrolyte solution. *J. Colloid Interface Sci.*, 193:107–110, 1998. doi:10.1006/jcis.1997.5331.

[206] Hernandez V. A. Scholz F. The lipid composition determines the kinetics of adhesion and spreading of liposomes on mercury electrodes. *Bioelectrochemistry*, 74: 149−156, 2008. doi:10.1016/j.bioelechem.2008.06.007.

[207] Cornmell R.J. Winder C.L. Tiddy G.J.T. Goodacre R. and Jill S. Accumulation of ionic liquids in escherichia coli cells. *Green Chem.*, 10:836–841, 2008. doi:10.1039/B807214K.

[208] Docherty K.M. and Kulpa C. Toxicity and antimicrobial activity of imidazolium and pyridinium ionic liquids. *Green Chem.*, 7:185–189, 2005. doi:10.1039/B419172B.

[209] Schaffran T. Li J. Karlssonb G. Edwardsb K. Winterhalterc M. Gabela D. Interaction of n,n,n-trialkylammonioundecahydro-closo-dodecaborates with dipalmitoyl phosphatidylcholine liposomes. *Chemistry and Physics of Lipids*, 163:64–73, 2010. doi:10.1016/j.chemphyslip.2009.09.004.

[210] Vakurov A. Galluzzi M. Podesta A. Gamper N. Nelson A. and Connel S. Afm study of fluid lipid assemblies in electric fields. *JACS nano*, submitted:1–10, 2013.

[211] Dante S. Hauss T. Steitz R. Canale C. Dencher N. A. Nanoscale structural and mechanical effects of beta-amyloid (1–42) on polymer cushioned membranes: A combined study by neutron reflectometry and afm force spectroscopy. *Biochimica et Biophysica Acta*, 1808:2646–2655, 2011. doi:10.1016/j.bbamem.2011.07.024.

[212] Gal N. Malferarri D. Kolusheva S. Galletti P. Tagliavini E. Jelinek R. Membrane interactions of ionic liquids: Possible determinants for biological activity and toxicity. *Biochimica et Biophysica Acta*, 1818:2967–2974, 2012. doi:10.1016/j.bbamem.2012.07.025.

[213] Majewski P. Pernak A. Grzymislawsk M. Iwanik K. and Pernak J. Ionic liquids in embalming and tissue preservation. *Acta Histochemica*, 105:135–142, 2003. doi:10.1078/0065-1281-00707.

[214] Radosevic K. Cvjetko M. Kopjar N. Novak R. Dumic J. Srcek V.G. In vitro cytotoxicity assessment of imidazolium ionic liquids: Biological effects in fish channel catfish ovary (cco) cell line. *Ecotoxicology and Environmental Safety*, 92:112–118, 2013. doi:10.1016/j.ecoenv.2013.03.002.

[215] Li X.-Y. Jing C.-Q. Lei W.-L. Li J. Wang J.-J. Apoptosis caused by imidazolium-based ionic liquids in pc12 cells. *Ecotoxicology and Environmental Safety*, 83:102–107, 2012. doi:10.1021/la400923d.

[216] Jing C. Li X. Zhang J. and Wang J. Responses of the antioxidant system in qgy-7701 cells to the cytotoxicity and apoptosis induced by 1-octyl-3-methylimidazolium chloride. *J BIOCHEM MOLECULAR TOXICOLOGY*, 0:1–7, 2010. doi:10.1016/j.ecoenv.2012.06.013.

[217] Pinho G.L. Da Rosa C.M. Maciel F.E. Bianchini A. Yunes J.S. Proenca L.A. Monserrat J.M. Antioxidant responses and oxidative stress after microcystin exposure in the hepatopancreas of an estuarine crab species. *Ecotoxicol Environ Saf.*, 61:353–360, 2005. doi:10.1016/j.ecoenv.2004.11.014.

[218] Li X.Y. Luo Y.R. Yun M.X. Wang J. Wang J.J. Effects of 1-methyl-3-octylimidazolium bromide on the antioxidant system of earthworm. *Chemosphere*, 78:853–858, 2010. doi:10.1016/j.chemosphere.2009.11.047.

[219] Grundy J.E. Storey K.B. Antioxidant defenses and lipid peroxidation damage in estivating toads, scaphiopus couchii. *J Comp Physiol B*, 168:132–142, 1998. doi:10.1007/s003600050129.

[220] Ueno K. Watanabe M. From colloidal stability in ionic liquids to advanced soft materials using unique media. *Langmuir*, 27:9105–9115, 2011. doi:10.1021/la103942f.

[221] Alcoutlabi M. and McKenna G. B. Effects of confinement on material behaviour at the nanometre size scale. *J. Phys. Condens. Matter*, 17:R461–R524, 2005. doi:10.1088/0953-8984/17/15/R01.

[222] Kanakubo M. Hiejima Y. Minami K. Aizawa T. and Nanjo H. Melting point depression of ionic liquids confined in nanospaces. *Chem. Commun.*, 29:1828–1830, 2006. doi:10.1039/B600074F.

[223] Liu Y. Wu G. Fu H. Jiang Z. Chena S. and Sha M. Immobilization and melting point depression of imidazolium ionic liquids on the surface of nano-siox particles. *Dalton Trans.*, 39:3190–3194, 2010. doi:10.1039/b924042j.

[224] Zakeeruddin S. M. and Gratzel M. Solvent-free ionic liquid electrolytes for mesoscopic dye-sensitized solar cells. *Adv. Funct. Mater.*, 19:2187–2202, 2009. doi:10.1002/adfm.200900390.

[225] Li S. Han K. S. Feng G. Hagaman E.W. Vlcek L. and Cummings P.T. Dynamic and structural properties of room-temperature ionic liquids near silica and carbon surfaces. *Langmuir*, 29:9744−9749, 2013. doi:10.1021/la401172z.

[226] Bettini L.G. Galluzzi M. Podesta A. Milani P. Piseri P. Planar thin film supercapacitor based on cluster-assembled nanostructured carbon and ionic liquid electrolyte. *Carbon*, 59:212–220, 2013. doi:10.1016/j.carbon.2013.03.011.

[227] Frackowiak E. and Beguin F. Carbon materials for the electrochemical storage of energy in capacitors. *Carbon*, 39:937–50, 2001. doi:10.1016/S0008-6223(00)00183-4.

[228] Arbizzani C. Lazzari M. Soavi F. Mastragostino M. and Conte M. Ilhypos ionic liquid-based supercapacitors. *Fuel Cells*, 25:25–30, 2010. doi:10.1149/1.3328508.

[229] Armand M. Endres F. MacFarlane D.R. Ohno H. and Scrosati B. Ionic liquid materials for the electrochemical challenges of the future. *Nature Materials*, 8:621–629, 2009. doi:10.1038/nmat2448.

[230] Frackowiak E. Supercapacitors based on carbon materials and ionic liquids. *Journal of the Brazilian Chemical Society*, 17:1074–1082, 2006. doi:10.1590/S0103-50532006000600003.

[231] Largeot C. Taberna P.L. Gogotsi Y. and Simon P. Microporous carbon-based electrical double layer capacitor operating at high temperature in ionic liquid electrolyte. *Electrochemical and Solid-State Letters*, 14:A174–A176, 2011. doi:10.1149/2.013112esl.

[232] Merlet C. Rotenberg B. Madden P.A. Taberna P.-L. Simon P. Gogotsi Y. and Salanne M. On the molecular origin of supercapacitance in nanoporous carbon electrodes. *Nature Materials*, 11:306–310, 2012. doi:10.1038/nmat3260.

List of Publications

Refereed publications

- M. Galluzzi, S. Zhang, S. Mohamadi, A. Vakurov, A. Podesta' and A. Nelson. 'Interaction of imidazolium-based room-temperature ionic liquids with DOPC phospholipid monolayers: Electrochemical study' Langmuir 29, 6573−6581 (2013) http://dx.doi.org/10.1021/la400923d
- Ajay V. Singh, M. Galluzzi, F. Borghi, M. Indrieri, V. Vyas, A. Podesta', and W. N. Gade 'Interaction of Bacterial Cells with Cluster-Assembled Nanostructured Titania Surfaces: An Atomic Force Microscopy Study' J. Nanosci. Nanotechnol. 13, 77-85 (2013) http://dx.doi.org/10.1166/jnn.2013.6727
- Luca G. Bettini, M. Galluzzi, A. Podesta' , P. Milani, P. Piseri 'Planar thin film supercapacitor based on cluster-assembled nanostructured carbon and ionic liquid electrolyte' Carbon Available online 16 March 2013 http://dx.doi.org/10.1016/j.carbon.2013.03.011
- Ajay V. Singh, A. Rahman, N.V.G. Sudhir Kumar, A.S. Aditi, M. Galluzzi, S. Bovio, S. Barozzi, E. Montani, D. Parazzoli 'Bio-inspired approaches to design smart fabrics' Materials and Design 36 (2012) 829–839. http://dx.doi.org/10.1016/j.matdes.2011.01.061

Summer schools

- "Quantum wires, boxes and molecules", Transalp Nano-2010, Varese, Italy, 30/05-02/06 2010.
- "Theory and practice of AFM in life sciences and medicine" AFMBioMed 2011, Marcoule, France, 28/08- 02/09 2011.

Presentations at international meeting: posters

- XII International Symposium on Polymer Electrolytes, Padova, 2010-08-29 "Investigation of interfacial properties of supported [Bmim][NTf2] ionic liquid layers by Scanning Probe Microscopy" S. Bovio, A. Podesta', M. Galluzzi, C. Lenardi, G. Losacco, M. Del Popolo, P. Ballone, P. Milani.
- Faraday discussion: ionic liquids, Belfast, 2011/08/22 "Investigation of morphological and mechanical properties of [bmim][Tf2N] thin layers on solid surfaces by Scanning Probe Microscopy" S. Bovio, M. Galluzzi, A. Podesta', C. Lenardi, P. Milani.
- Faraday discussion: ionic liquids, Belfast, 2011/08/22 "Characterization of electrical properties of thin films of [bmim][Tf2N] using Atomic Force Microscopy " M. Galluzzi, S. Bovio, A. Podesta', P. Milani.
- Nanotechitaly 2012, Venezia, 2012/11/21 "Morphological, structural, mechanical and electrical properties of thin ionic liquid films characterized by Atomic Force Microscopy: an integrated experimental approach based on a multi-purpose nanoscale characterization tool" M. Galluzzi, S. Bovio, A. Podesta', P. Milani.
- EUPOC 2013 (polymers and ionic liquids), Gargnano, 2013/09/01 "Interaction of imidazolium-based ionic liquids with single cells and model cell membranes" M. Galluzzi, S. Bovio, A. Podesta', P. Milani.

Other scientific activities

- From 03/2012 to 09/2012 participation to Erasmus placement program at Leeds University, School of Chemistry: Centre for Molecular Nanoscience; project for the characterization of the interaction of biological membranemodels with ionic liquids.
- From 29/07/2013 to 10/31/2013 stage at E.N.I. S.p.A. S.Donato (Mi); project for development of methodology for the evaluation of ICNIRP (according to the EU-Directive 2013-35) starting from the harmonic spectrum of magnetic field sources (single or multiple). Implementation of a calculation method for the assessment of electric currents induced in the human body from external electric fields using analytical models (spheroid) and numerical (axisymmetric) 2D.

Acknowledgments

Finally, I am arrived to acknowledgments! First of all, I would like to thank Alessandro P., who made this PhD thesis possible since the beginning and greatly supported me throughout all this period.

A special thank goes to the colleagues of today and of the past from CIMaINa group with whom I spent precious moments. Starting from the boss Paolo M. and other profs. Paolo P. and Cristina L. a great thank to have sustained me and for scientific discussion. All the people in AFM lab: a great thank to Simone B. who worked with me very closely and taught me a lot as far as AFM and ionic liquids, Marco for advices and help using Matlab and AFM, Francesca B. for useful discussion and supports, Luca P. for Matlab programs and measurements on cells. A great thank to all other people of the group: Luca B. (my office mate) for collaboration and realization of planar supercapacitor with ILs, Carsten S. who cultured and provided all the cells used in experiments and useful discussion about biology. I would like to thank also all the people of the lab in all this period for discussions, precious moments and help: Cristian G., Andrea B., Claudio P., Tommaso S., Flavio D., Marta F., Michele D., Alice M., Yan L., Ajay V., Varoun V., Nunzia T. I will not forget all the students passed the lab, in particular who worked with me with AFM, lipids and cells: Federico F., Nicolò T. and Davide P.

For the beginning of my work, I want to thank also P. Ballone and M. Del Popolo for discussions and suggestions, K. Seddon and M. Deetlefs for having provided the ILs used, and and M. Perego for the XPS analysis of ILs samples. A big thank to Davide M. for extended SEM analysis at the Filarete foundation facility.

I would like to thank the group of electronic engineers of Politecnico di Milano, in particular: Marco S., Giorgio F. and Marco V. for all the advices and for teaching me how to perform and improve the electrical measurements with AFM.

An enormous thank must be devoted to the people of Centre for Molecular Nanoscience in Leeds University, School of Chemistry during my Erasmus placement program in 2012 for project for the characterization of the interaction of biological membrane models with ionic liquids. In particular Prof. Andrew N. for his hospitality and great support; Alex V. for electrochemical and AFM combined measurements and discussions; Ann Z., Ashi R., Shahrzad M. for helping, discussions and for teaching me about electrochemical measurements.

A big thank is dedicated to the people in E.N.I. S.p.A. S.Donato (Mi) RADI division, that welcomed me for a stage project. In particular Alex S. and Roberto F. who made it possible, fighting all bureaucracy problems.

Last but not less important, a huge thank also goes to my family and all my friends to have always believed in me and for giving me the strength to continue even in the most difficult moments.